Probabilistic Nonlinear Seismic Analysis of AAR-Affected Dams

by

Golsa Mahdavi

B.S., K. N. Toosi University of Technology, 2014

M.S., K. N. Toosi University of Technology, 2017

M.S., University of Colorado, Boulder, 2023

A thesis submitted to the

Faculty of the Graduate School of the

University of Colorado in partial fulfillment

of the requirements for the degree of

Doctor of Philosophy

Department of Civil, Environmental and Architectural Engineering

© 2023

Committee Members:

Victor E. Saouma, Chair

Shideh Dashti

Mija Hubler

Srikanth S.C. Madabhushi

Larry Nuss

Jeong-Hoon Song

Mahdavi, Golsa (Ph.D., Civil, Environmental and Architectural Engineering)

Probabilistic Nonlinear Seismic Analysis of AAR-Affected Dams

Thesis directed by Prof. Victor E. Saouma

Many dams worldwide suffer from alkali aggregate reaction (AAR). This nefarious and irreversible phenomenon causes concrete deterioration through expansion resulting in cracking and deformation. Most, if not all, numerical simulations of dam in the U.S. have relied on simplistic approaches that seek to match dam's irreversible displacements without explicit recognition of the kinetics of the reaction. This was achieved by either modifying the elastic properties and/or including a temperature field. At best, simplified AAR models were used.

In this thesis, a systematic approach is followed. First a detailed thermal analysis including the effect of solar radiation is performed. Next, a comprehensive finite element model of the dam-foundation coupled system is developed including material and joint nonlinearities, and the AAR simulations are conducted using an advanced model which accounts for the kinetics of reaction as well as material degradation. In the absence of reliable accelerated expansion tests representative of the dam, a parameter identification framework is developed. The process seeks to determine those parameters through an optimization procedure that minimizes the error between measurements and numerical predictions.

Recognizing the uncertainties associated with many of the input parameters, the thesis pursues an uncertainty quantification approach to provide a probabilistic assessment. Finally, dynamic analysis of the coupled dam-foundation system is performed using a series of innovative intensifying artificial accelerations. Both the AAR-affected dam and its (imaginary) non-AAR-affected counterpart are evaluated to determine the potential reduction in seismic capacity of the structure.

Dedication

To my beloved parents, your unwavering love and encouragement have been the bedrock of my academic journey, supporting and shaping my aspirations at every turn.

To my husband, whose patience, understanding, and constant motivation have been my source of strength throughout this scholarly pursuit.

To the memory of my beloved grandmother, whose support and belief in my academic endeavors remain an eternal guiding light.

Acknowledgements

The author would like to acknowledge and thank the financial support of the Bureau of Reclamation through the cooperative agreement R18AC00055, and the technical support of Dr. Jerzy Salamon.

The additional financial support from the Civil, Environmental and Architectural Engineering is also acknowledged.

The author would also like to acknowledge the assistance of Dr. M. Amin Hariri-Ardebili for his assistance in key aspects of her research.

Finally, she would like to thank the support of her advisor Prof. Victor Saouma for his continuous technical support, encouragement and dedication to perfection.

Acknowledgment is also extended to her thesis committee for the numerous constructive comments made.

Disclaimer

The views and opinions expressed in this thesis are solely those of the author and do not necessarily reflect those of any other entity.

Contents

Chapter

1 Introduction **1**

1.1 Motivation 1

1.2 Ultimate Goal 2

1.3 Literature Review; Advancecd AAR Analysis of Dams 2

1.4 The "Big-Picture" 22

I THEORY **25**

2 Alkali Aggregate Reaction **26**

2.1 Finite element modeling of AAR in dams 26

2.1.1 State of the practice 30

2.1.1.1 AAR Modeling 30

2.1.1.2 Failure Criterion 32

2.1.2 State of the Art 33

2.1.2.1 AAR Modeling 34

2.2 AAR model 34

2.2.1 Premises 34

2.2.2 Kinetics 35

2.2.3 Volumetric Expansion 38

2.2.4 AAR Strain Redistribution 40

2.2.5 Degradation 46
2.2.6 Interaction with Creep 47

3 Methodology for Thermal Analysis with Solar Radiation 48

3.1 Preliminaries 48
3.1.1 Units 48
3.1.2 Conversions for selected quantities 48
3.1.3 Concrete Thermal Properties 50
3.2 Solar Radiation 52
3.2.1 Preliminary Definitions 52
3.2.1.1 Solar Time 52
3.2.1.2 Solar Angles 53
3.2.1.3 Zenith Angle 54
3.2.1.4 Incidence Angle 55
3.2.1.5 Plane azimuth angle 55
3.2.1.6 Sun azimuth angle 55
3.2.2 Solar Flux 55
3.2.2.1 Horizontal Surfaces 55
3.2.2.2 Inclined Surfaces 56
3.2.3 Discussion 56
3.2.3.1 Incidence angle 56
3.2.3.2 Roles of various solar radiation forms 57
3.2.4 Algorithms 59
3.2.4.1 Solar Flux 59
3.2.4.2 Finite element determination of ϕ_p 60
3.2.4.3 Temperature Variation Due to Solar Radiation 65
3.3 Conclusion 68

4 System Identification **69**

4.1 Theory . . . 69

4.1.1 Overview of Algorithms . . . 71

4.1.2 Trust Region . . . 72

4.1.2.1 Algorithm . . . 75

4.2 Implementation . . . 76

4.2.1 Matlab® Formulation . . . 76

4.2.2 Matlab® code . . . 78

4.2.2.1 Function definition . . . 78

4.2.2.2 Real time visualization . . . 79

5 Seismic Analysis **81**

5.1 Fluid Structure Interaction; Westergaard's model . . . 81

5.1.1 Theoretical Model . . . 81

5.1.2 Added Mass . . . 94

5.2 Dynamic Soil Structure Interaction . . . 96

5.2.1 Lysmer Model . . . 97

5.2.2 Other SSI Models . . . 99

5.2.3 Miura-Saouma (MS) Model . . . 101

5.2.3.1 Disclaimer . . . 101

5.2.3.2 Introduction . . . 101

5.2.3.3 Model Description . . . 103

5.2.3.4 Finite Element Formulation . . . 110

5.2.3.5 Finite Element Implementation . . . 115

5.2.4 Validation Problems . . . 118

5.3 Nonlinear Analysis Methods . . . 124

5.3.1 Cloud Analysis (CLA) . . . 125

5.3.2 Endurance Time Analysis (ETA); Fundamentals . . . 125
5.3.3 Intensifying Artificial Accelerations; Advances . . . 128
5.3.4 Generation of Intensifying Artificial Acceleration (IAA); Implementation . . . 131
5.4 Damage Index . . . 134
5.4.1 Probability of Exceedance . . . 135

II APPLICATION **138**

6 Physical Properties **139**
6.1 Properties . . . 139
6.1.1 Thermal Analysis . . . 139
6.1.1.1 Concrete Material Properties . . . 139
6.1.1.2 Film Coefficient . . . 140
6.1.1.3 Air Temperature . . . 140
6.1.1.4 Solar Radiation . . . 141
6.1.1.5 Water Temperature . . . 141
6.1.1.6 Water Elevation . . . 143
6.1.2 AAR Analysis . . . 143
6.1.2.1 Concrete and AAR Properties . . . 143
6.1.2.2 Joint Properties . . . 144
6.2 Analysis Procedures . . . 144
6.2.1 Procedure for Thermal Analysis . . . 144
6.2.2 Procedure for Uncertainty Quantification and Stress Analysis . . . 149

7 Physical Modeling **151**
7.1 Physical Model . . . 151
7.2 Geometry Model . . . 152
7.3 Stage Construction . . . 156

7.3.1 Proposed methodology . . . 159
7.3.2 Verification Study . . . 160
7.3.3 Verification . . . 160
7.4 Hydrostatic Load . . . 161
7.5 Foundation Modeling . . . 167

8 Deterministic Thermal Analysis 171

8.1 Analysis Procedure . . . 171
8.2 Comparison with Hatch (2015) . . . 171
8.3 Impact of Time Step . . . 172
8.4 Impact of Solar Radiation . . . 173
8.5 Comparison of Convection and Conduction . . . 173
8.6 Internal Temperatures . . . 174

9 Deterministic Stress Analyses Results 181

9.1 Parameter Identification Procedure . . . 181
9.2 Parameter Identification for Linear Concrete Model . . . 182
9.2.1 Control Parameters . . . 182
9.2.2 Measured displacements . . . 183
9.2.3 Results . . . 187
9.3 Deterministic Analysis with Nonlinear Concrete Model . . . 189
9.3.1 Displacements . . . 189
9.3.2 Stress Distribution . . . 193
9.3.2.1 Stress and Strains . . . 193
9.3.2.2 Crack Pattern . . . 194
9.3.2.3 Simulation Results . . . 194
9.3.2.4 Sectional Cuts of Principal Stresses Over Time . . . 196
9.3.3 Downstream Observations . . . 203

9.3.3.1 Crack Mapping 204
9.3.3.2 LIDAR observations 205

10 Uncertainty Quantification **207**
10.1 Thermal Analysis 207
10.1.1 Procedure 209
10.1.2 Observations 209
10.2 Stress Analysis 215
10.2.1 Results 221
10.2.1.1 Displacements 221
10.2.1.2 Stresses 222
10.2.1.3 Probability of Exceedance 227
10.2.1.4 Comparison of 3 sample sizes 231

11 Seismic Analyses Results **235**
11.1 Intensifying Artificial Acceleration 235
11.2 Seismic Analyses Results 238
11.2.1 Seismic Response of the Dam; Effect of AAR 240
11.2.2 Comparison of Different SSI Models 247
11.2.3 Dam Deformed Shape 247

12 Conclusion and Recommendation for Future Work **261**
12.1 Conclusion 261
12.2 Recommendation for Future work 263

References **263**

Appendix

A Thermal Load; Verification **276**

A.1 Pool Temperature 276

A.1.1 Heat conduction in a semi-infinite plate 277

A.1.2 Pool water temperature distribution 278

A.1.2.1 Empirical Solution 278

A.1.2.2 Model comparisons 278

A.1.2.3 Application 280

A.2 Numerical Solution with Merlin; Concrete 281

A.2.1 Stability Condition 281

A.2.2 Verification Problems 281

A.2.2.1 Temperature 282

A.2.2.2 Flux 291

A.3 Solar radiation 292

A.4 Conclusion 296

B Verification Study for Pool and Concrete Temperatures **297**

C Complementary Figures **299**

D Additional Uncertainty Quantification Results **302**

E Modeling Dam-Foundation **306**

F Fourier Transform **313**

F.1 Basic Equations 313

F.2 Butterworth Filter 313

F.3 Transfer Function 314

G Wave Equation **316**

G.1 Deconvolution 318

G.1.1 Introduction 318

G.1.2 Algorithm 319

G.1.2.1 One-Dimensional 319

G.1.2.2 Three-Dimensional 320

G.1.2.3 Simplification 321

Tables

Table

2.1 Side-b-Side Comparison of the State-of-the-Practice and the State-of-the-Arth methodologies to analyze dams with AAR 27
2.2 Variation of $\epsilon(\infty)$, τ_c and τ_l for 4 specimens, (Larive, 1998) 38
2.3 Triaxial weights 44

3.1 Thermal Analysis 49
3.2 Stress Analysis 50
3.3 Concrete thermal properties; * From (Hatch, 2015) ** From (Malm, Hassanzadeh, and Hellgren, 2017) 51
3.4 Reflectivity of selected surfaces (Kreider and Rabl, 1994) 56

5.1 Numerical Results Corresponding to the Period, $T = \frac{4}{3}$ second 90

6.1 Concrete material Properties used in thermal analysis * From (Hatch, 2015) 140
6.2 Air and water film coefficients 140
6.3 Concrete Material Properties 144
6.4 Initial AAR Properties 145
6.5 Rock Material Properties 145
6.6 Joint Properties 146

7.1 The comparison of the execution time for the full and reduced mesh 169

9.1 Data preparation for parameter identification 183

9.2 Displacement instrumentation coordinates 185

9.3 T_3B Measurements (Dressel, 2011) 186

10.1 Water temperature (Hatch, 2015) 209

A.1 CFL conforming and non-conforming conditions 291

B.1 Temperature data fitting 298

B.2 Temperature data fitting for the case study dam 298

Figures

Figure

1.1 FE model and calibration results; Curtis et al. (2005) 3
1.2 Results for the ASR simulation: gel pressure for 40 years and the displacements at the crest of the dam; Fairbairn et al. (2006) 4
1.3 Comparison of yearly vertical displacement, and principal stress fields in two models; Saouma and Perotti (2006b) 5
1.4 Comparison between first guess analysis and final analysis with optimized parameters (left), Internal AAR-induced maximum principal stresses in MPa (right); Saouma, Perotti, and Shimpo (2007b) 7
1.5 Reaction extent and damage during AAR development in Koyna Dam; Comi, Fedele, and Perego (2009a) 8
1.6 Reaction extent and damage during AAR development in Fontana Dam; Comi, Fedele, and Perego (2009a) 9
1.7 Principle of chemical advancement assessment; Sellier et al. (2009a) 10
1.8 Views of the mesh, and Downstream displacement at the crest of the Dam; Leroy et al. (2011) 11
1.9 Patterns of the reaction extent and damage after (a) 3, (b) 6 and (c) 60 years; Comi, Kirchmayr, and Pignatelli (2012) 12
1.10 Gel pressure evolution in the concrete wall via the uncoupled (above) and the coupled (below) models; Ferreira, Farage, and Barbosa (2013) 13

1.11 Volumetric expansion applied to the model; Amberg, Stucchi, and Brizzo (2013) . . 14
1.12 Displacement and stress vs. time before and after sawing; Metalssi et al. (2014) . . . 15
1.13 Finite element model and calibration; Cima and Reinicker (2015) 16
1.14 Comparison of displacements at crest of the Dam; Lamea and Mirzabozorg (2015) . 17
1.15 Maximum major principal stresses contour; Nik-Azizan et al. (2017) 18
1.16 Comparison of measured and computed deformations in 3D modeling; Chulliat, Grimal, and Bourdarot (2017) 19
1.17 Linear model and nonlinear model with concrete-to-rock joint on a swelling arch dam with thrust blocks; Stress reorientation and modification on the upstream face; Coubard and Sausse (2017) 20
1.18 Finite element analysis: (a) real crack pattern, (b) stresses in the diaphragm, and (c) crack pattern of the model; Blanco et al. (2018) 21
1.19 Outline of a comprehensive analysis (Adapted from Saouma and Hariri-Ardebili (2021c)) 24

2.1 A clouded approach 27
2.2 AAR FEA models 27
2.3 Spatial and temporal partitioning 31
2.4 Mapping of recovered core test results (E, f_c, f_t) measurement into finite element mesh 32
2.5 Spatial and temporal fitting for concrete mechanical properties based on limited cores and observations (courtesy Y. Gakuhari) 33
2.6 Assessment paradigms for AAR affected structures 34
2.7 ASR expansion curve 36
2.8 Environmental factors affecting AAR expansion 39
2.9 Stress induced cracks with potential gel absorption 39
2.10 Graphical representation of Γ_c and Γ_t 40

2.11 Effect of confinement on AAR strain redistribution 41
2.12 Weight of volumetric aar redistribution in selected cases 42
2.13 Weight regions 45
2.14 Degradation of E and f'_t 46
2.15 Effect of creep (Saouma and Hariri-Ardebili, 2021c) 47

3.1 Solar declination 53
3.2 Solar characteristic angles 54
3.3 Seasonal impact on incidence angle for different plane orientations ϕ_p 58
3.4 Solar fluxes at latitude 42.1558° and longitude -106.908° 61
3.5 Solar radiation and solar angles for a vertical surface at at latitude 42.1558° and longitude -106.908° 62
3.6 Algorithm to determine the solar radiation intensity 63
3.7 Solar radiation on a concrete dam surface 63
3.8 Algorithm to determine ϕ_p for a mesh element 64
3.9 Mean annual temperature variation due to solar radiation for surfaces with various orientations and inclinations adopted from Bureau of Reclamation (1981) 66
3.10 Comparison of temperature variation due to solar radiation at latitude 42.1558° and longitude -106.908° 67
3.11 Average monthly temperature increase due to solar radiation for upstream face of the dam from Bureau of Reclamation (1981) 67
3.12 Comparison of solar radiation and the resulting temperature increase from Bureau of Reclamation (1981) and equation 3.26 68

4.1 Principle of the system identification approach 70
4.2 Trust region algorithm 73
4.3 System identification procedure flow chart 79
4.4 Graphical user interface for AAR parameter identification 80

5.1 Pressures on the dam due to dynamic action of the water (Westergaard, 1933) . . . 88
5.2 Approximate distribution of pressures (Westergaard, 1933) 91
5.3 Body of water which may be considered to move with dam. (Westergaard, 1933) . . 95
5.4 Comparison of the approximate and exact solutions for a hypothetical dam; Adapted from Saouma and Hariri-Ardebili (2021c) 96
5.5 Elastic waves in an infinite medium 98
5.6 Lysmer Modeling for Lateral Excitation 99
5.7 Viscous elements (dash-pots) 99
5.8 Conceptual Model 103
5.9 2D Idealization and Γ_x Plane 106
5.10 Foundation boundary conditions for radiating flexible foundation 110
5.11 Finite element discretization of the free field 113
5.12 Discretization of 2D dam foundation with free field velocities 114
5.13 2D Finite Element Modeling 115
5.14 3D extension; procedure outline 116
5.15 Boundary conditions for free field modeling 117
5.16 Free field analysis flowchart 119
5.17 Free field modeling 119
5.18 Free field boundaries and meshes 120
5.19 Selected results for 2D analyses with free boundaries; Crest accelerations, deformed shapes with contour lines of V_X and V_Y 121
5.20 Selected results for 2D Lysmer analyses; Crest accelerations, deformed shapes with contour lines of V_X and V_Y 122
5.21 Selected results for 2D Miura-Saouma analyses; Crest accelerations, deformed shapes with contour lines of V_X and V_Y 123

5.22 Selected results for 3D Lysmer analyses; Crest accelerations, accelerations at $h = 0$, h/8, h/4, 3h/8, h/2, 5h/8, 3h/4, 7h/8 and h; deformed shapes with contour lines of V_X 123

5.23 Selected results for 3D Miura-Saouma analyses; Crest accelerations, accelerations at $h = 0$, h/8, h/4, 3h/8, h/2, 5h/8, 3h/4, 7h/8 and h; deformed shapes with contour lines of V_X 123

5.24 Comparison of various analysis methods (Saouma and Hariri-Ardebili, 2021c) 125

5.25 Cloud Based Analysis(Hariri-Ardebili and Saouma (2016)) 126

5.26 ETA-based capacity function generation (Hariri-Ardebili and Saouma, 2017) 128

5.27 Target acceleration response spectra used in different IAA generations(Adapted from Hariri-Ardebili and Sattar (2023)). 129

5.28 Variation of time- and period-dependent acceleration response spectra in IAAs. The horizontal axis represents time, and the vertical axis represents vibration period. The contour lines and colorbar represent the $S_a(T, t)$ in g. A 2.5% damping ratio is considered for all cases.(adapted from Hariri-Ardebili and Sattar (2023)) 131

5.29 Generation of target response spectra for different time intervals using linear interpolation 133

5.30 Input and output intensifying acceleration acceleration 134

5.31 Calculated vs target response spectra before and after optimization 135

5.32 Schematic curve fitting procedure 137

6.1 The dam air temperature 141

6.2 Dam reservoir temperature 142

6.3 Pool Elevations 143

6.4 Flowchart describing the thermal analysis input data preparation procedure 148

6.5 Flowchart of UQ Procedure 150

7.1 Geometry of the Dam; Redacted dimensions 152

7.2 Additional description of the dam (Salamon, Dressel, and Liechty, 2021) 153
7.3 Mathematical Modeling of the Dam 154
7.4 Matlab® based final model 154
7.5 Staged construction modeling plan the dam upstream 155
7.6 Finite element mesh 157
7.7 Development of Stresses through construction stages 158
7.8 Modeling of stage construction 159
7.9 Effect of modeling staged construction the dam Upstream; different stages 161
7.10 Effect of modeling staged construction vertical cut from middle of the dam; different stages 162
7.11 Effect of modeling staged construction the dam Downstream 163
7.12 Stress distribution; with vs. without Staged construction 163
7.13 Principal Stresses; With vs. without Staged construction 164
7.14 Stresse and displacements near Crest; With vs. without Staged construction 164
7.15 Four sections considered for stress integration and comparison with the self-weight . 165
7.16 Error comparison between the two self-weight analyses 165
7.17 Gradual application of hydrostatic load in 3 steps 166
7.18 Z direction Displacement contour plots 167
7.19 Maximum principal stresses after 40 years 168
7.20 The old versus New mesh where the foundation is shown in blue 168
7.21 Z direction Displacement contour plots, comparison of models with full and reduced foundation 169
7.22 Difference of the crest displacement for the 2 meshes with full and reduced foundation 170

8.1 Comparison of thermal analysis results with measured values 172
8.2 Comparison of thermal analysis results with measured values assuming 3 different time steps 173

8.3 Comparison of thermal analysis results with measured values with and without solar radiation . . . 173
8.4 Comparison of thermal analysis results with measured values assuming high values for film coefficients . . . 174
8.5 Temperature contour plots of various months throughout one year at a vertical section cut from the middle of the arch dam . . . 176
8.6 Temperature contour plots of various months throughout one year at a horizontal section cut from below the water level (Elevation 6243 [ft]) . . . 177
8.7 Temperature contour plots of various months throughout one year at a horizontal section cut from above the water level (Elevation 6348 [ft]) . . . 178
8.8 Temperature contour plots of various months throughout one year at the upstream face of the dam . . . 179
8.9 Temperature contour plots of various months throughout one year at the downstream face of the dam . . . 180

9.1 Principle of the system identification approach . . . 182
9.2 Instrumentation locations . . . 184
9.3 T3B Measurements and adjustments . . . 185
9.4 T3A Measurements and adjustments . . . 187
9.5 System Identification user interface . . . 188
9.6 Displacement comparison following system identification for T3B . . . 189
9.7 Displacement comparison following system identification for T3A . . . 190
9.8 Displacement comparison from linear and nonlinear analysis for T3B . . . 190
9.9 Displacement comparison from linear and nonlinear analysis for T3A . . . 190
9.10 Displacement plots after 50 years of Nonlinear analysis . . . 191
9.11 Radial displacement and deformations over time(side view) . . . 192
9.12 Dam deformed shape after 50 years of analysis; Nonlinear analysis . . . 193

9.13 Principal Stress and strain distributions after 50 years of Linear analysis 193
9.14 Smeared crack profile after 50 years of analysis 194
9.15 Smeared crack profile over the time compared to the maximum principal stresses . . 195
9.16 Development of Maximum principal stresses over time on the upstream 196
9.17 Maximum principal stresses at a section cut over time 197
9.18 Maximum principal stresses over summer and winter 198
9.19 Maximum principal stresses at different vertical sections in 2020 199
9.20 AAR development over the time 200
9.21 Development of AAR volumetric strain over time on the downstream 201
9.22 Maximum principal stress and vertical stress distribution after 80 years of analysis; Nonlinear analysis 202
9.23 Downstream crack pattern observation (Salamon, Dressel, and Liechty, 2021) 204
9.24 Selected views of the deformed shape 205
9.25 Comparison of computed results with LIDAR point clouds 206

10.1 Sources of uncertainty in thermal analysis 208
10.2 Monthly temperatures at PoI (Node 944), with mean and standard deviation 208
10.3 Uncertainty Quantification Flowchart 210
10.4 Correlation of nodal temperatures and variables at 6 different nodes in January and July 211
10.5 Monthly variation of temperature at 6 nodes throughout a year 212
10.6 Monthly air temperature correlation coefficients at node 944 (PoI) 213
10.7 Monthly mean and standard deviations histograms for temperatures inside entire mesh 214
10.8 Uncertainty in AAR modeling 215
10.9 Matrix plot of the 13 input variables 217
10.10 Flowchart of UQ Procedure 219
10.11 Location of recorded nodes 220

10.12 Crest Displacements (stream and vertical directions); (+ve is toward the upstream and upward) . . . 222
10.13 Maximum Principal Stress (+ve indicates tension); Downstream . . . 223
10.14 Maximum Principal Stres (+ve indicates tension)s; Upstream . . . 224
10.15 Normalized Maximum Principal Stress with respect to Tensile Strength(+ve indicates tension); Downstream . . . 225
10.16 Normalized Maximum Principal Stress with respect to Tensile Strength (+ve indicates tension); Upstream . . . 226
10.17 Schematic curve fitting procedure . . . 228
10.18 Probability of Exceedance; Downstream . . . 229
10.19 Probability of Exceedance; Upstream . . . 230
10.20 Standard Error and Standard deviation curves of T3A and T3B US-DS displacements 232
10.21 Standard Deviation; Downstream . . . 233
10.22 Standard Deviation; Upstream . . . 234

11.1 Intensifying Artificial Accelerations . . . 236
11.2 Intensifying artificial accelerations response spectra at different analysis equivalent times . . . 237
11.3 Matching PGA for different return periods . . . 238
11.4 Matching acceleration response spectra in [0.2T,1.5T] for different return periods . . 239
11.5 Different types of analyses . . . 241
11.6 Comparison of crest displacement with and without AAR for Free field model with respect to analysis time . . . 242
11.7 Comparison of Crest Displacements with and without AAR for Free field model with respect to PGA and Sa(T1) . . . 243
11.8 Comparison of joint opening displacement with and without AAR for Free field model versus PGA and Sa(T1) . . . 244

11.9 Comparison of maximum principal with and without AAR for Free field model with respect to PGA 245
11.10 Comparison of maximum principal with and without AAR for Free field model with respect to Sa(T1) 246
11.11 Comparison of crest displacement without AAR for three SSI models with respect to analysis time 248
11.12 Comparison of Crest Displacements without AAR for three SSI models versus PGA and Sa(T1) 249
11.13 Comparison of joint opening displacement without AAR for three SSI models versus PGA and Sa(T1) 250
11.14 Comparison of maximum principal stresses without AAR for three SSI model with respect to PGA 251
11.15 Comparison of maximum principal stresses without AAR for three SSI models with respect to Sa(T1) 252
11.16 Comparison of crest displacement with AAR for three SSI models with respect to analysis time 253
11.17 Comparison of Crest Displacements with AAR for three SSI models versus PGA and Sa(T1) 254
11.18 Comparison of joint opening displacement with AAR for three SSI models versus PGA and Sa(T1) 255
11.19 Comparison of maximum principal stresses with AAR for three SSI model with respect to PGA 256
11.20 Comparison of maximum principal stresses with AAR for three SSI models with respect to Sa(T1) 257
11.21 Comparison of Dam deformed shape at 3 and 5 seconds of equivalent time 259
11.22 Comparison of Dam deformed shape at 10 and 20 seconds of equivalent time 260

12.1 Earthquake occurring after substantial AAR expansion 263

A.1 Semi infinite plate subjected to surface harmonic temperature 277

A.2 Analytical and emperical solution for water temperature distribution 279

A.3 Fitted model of Ardito, Maier, and Massalongo (2008) 280

A.4 Recorded pool temperatures (Bureau of Reclamation, 1981) 283

A.5 Digitized data from Figure A.4 284

A.6 Fitted dam temperatures from (Model II) Figure A.5 285

A.7 Fitted dam temperature (from model II) for the case study dam 285

A.8 Thermal analysis results of constant temperature applied at the end of the column . 286

A.9 Verification procedure 287

A.10 Thermal analysis results of constant temperature applied at the end of the column . 287

A.11 Comparison of Analytical and Merlin solutions of constant temperature applied at the end of the column 288

A.12 Applied harmonic temperature 289

A.13 Thermal analysis results of harmonic temperature applied at the end of the column . 290

A.14 Comparison of Analytical and Merlin solutions of harmonic temperature applied at the end of the column 290

A.15 Comparison of results of CFL condition conforming and non conforming thermal analysis with harmonic temperature applied at the end of the column 290

A.16 Thermal analysis results of constant water temperature using flux applied at the end of the column 291

A.17 Thermal analysis results of harmonic water temperature using flux applied at the end of the column 292

A.18 Studied arch and cantilever located at dam upstream 293

A.19 Temperature variation due to solar radiation throughout the curved column within 1 year 294

A.20 Thermal analysis result for nodes on the central axis of the curved column considering solar radiation effect 294
A.21 Solar radiation calculation procedure for curved column 295

C.1 Monthly specific heat correlation coefficients at node 944 (PoI) 299
C.2 Monthly conduction correlation coefficients at node 944 (PoI) 300
C.3 Monthly top water temperature correlation coefficients at node 944 (PoI) 300
C.4 Monthly bottom water temperature correlation coefficients at node 944 (PoI) 301

D.1 Crest Displacements (Stream and vertical directions) 302
D.2 Maximum Principal Stress; Downstream 303
D.3 Ratio of Maximum Principal Stress to Tensile Strength; Downstream 303
D.4 Maximum Principal Stress; Upstream 304
D.5 Ratio of Maximum Principal Stress to Tensile Strength; Upstream 304
D.6 Probability of Exceedance; Downstream 305
D.7 Probability of Exceedance; Upstream 305

E.1 Concrete Rock interface crack opening displacements for 6 nodes from upstream to downstream for all increments 308
E.2 Concrete Rock interface crack opening displacements for 6 nodes from upstream to downstream for 5 different increments 309
E.3 Dam tilts 310
E.4 angles 311
E.5 Sliding; (+ve) Upstream 312

F.1 Comparison of filters 314
F.2 Transfer function 315

G.1 Infinitesimal element subjected to elastic wave 316
G.2 Seismic Attenuation/Amplification (Ake, Pires, and Munson, 2015) 318

G.3 Deconvolution 319

G.4 Deconvolution applied in finite element analysis 320

Chapter 1

Introduction

Abstract

This introductory chapter will provide contextual reference for this work, along with a brief outline of individual chapters.

1.1 Motivation

Mutliple dams, worldwide, are known to have been suffering from alkali silica reaction (ASR) (also known as alkali aggregate reaction, AAR) for many years. Many of them exhibit concerning cracking, and increased irreversible displacements.

As such, after many years of observations, regulators are increasingly confronted with critical decisions: a) Shall we wait, and continue to observe? or b) shall we initiate dismateling and possible replacement plans?

These are not easy questions, and they can be addressed by economic considerations backed by reliable scientific prediction as to the future damage to the dam.

This thesis presents a comprehensive framework designed for analyzing AAR-affected dams using state-of-the-art methodologies. An advanced AAR model has been employed to consider the kinetics of the AAR reaction, while integrating the effect of material degradation. An advanced finite element model involving different sources of nonlinearities have been developed and calibrated with the observations from the real dam conditions, using parameter identification processes.

A complicating factor is that a deterministic analysis is hardly credible. Numerous parameters affecting the analyses results can only be accurately described through a probability distribution function. Hence, in this research, deterministic analyses are succeeded by uncertainty quantification, offering decision-makers a more comprehensive understanding of the dam's potential response

The assessment of dams affected by AAR in their static state holds considerable value. However, delving into the aftermath of an earthquake following years of material degradation and irreversible displacements due to AAR bears even greater significance. To this end, a series of intensifying artificial accelerations are employed to assess the dam's response with reduced computational effort. Assessment of the dam response subject to dynamic motions will impose additional complexity to the modeling process to consider the dynamic dam-foundation interaction.

1.2 Ultimate Goal

Ultimately, this thesis could assist decision makers in conducting assessment of the dam's condition and its potential response to future possible earthquake events and ultimately performing the risk assessment of the structure. In such a study, a Probable Failure Mode would have to be identified, and the resulting uncontrolled release of water quantified, prior to the ultimate assessment of financial consequences.

As one would expect, there is not, and neither could there be, a clear-cut answer to many of the questions related to the dam safety. However this study provided as quantitative assessment as can be using modern analytical tools based on the State of the Art.

1.3 Literature Review; Advancecd AAR Analysis of Dams

Curtis et al. (2005) investigated AAR analysis in a 307-ft high concrete gravity dam using ANSYS software, employing a nonlinear stress-dependent concrete model and an enhanced creep model. A 3D linear elastic analysis was performed on the dam with a simple thermal expansion. Subsequently, remedial works were recommended including: post-tensioning of the dam, cutting of expansion joints in the bridge, and cutting of four transverse slots. Few

years later the time-dependent nonlinear concrete growth analyses were conducted. Figure 1.1 shows the calibration to the Block 14 plumb line data (top-right). The results of comparison between the measured and computed spillway closure is shown in the bottom-left plot. The slot closure measurements at Block 16/17 are also shown in the bottom-right figure. All of these results demonstrate a good agreement between the numerical model and the field measurements.

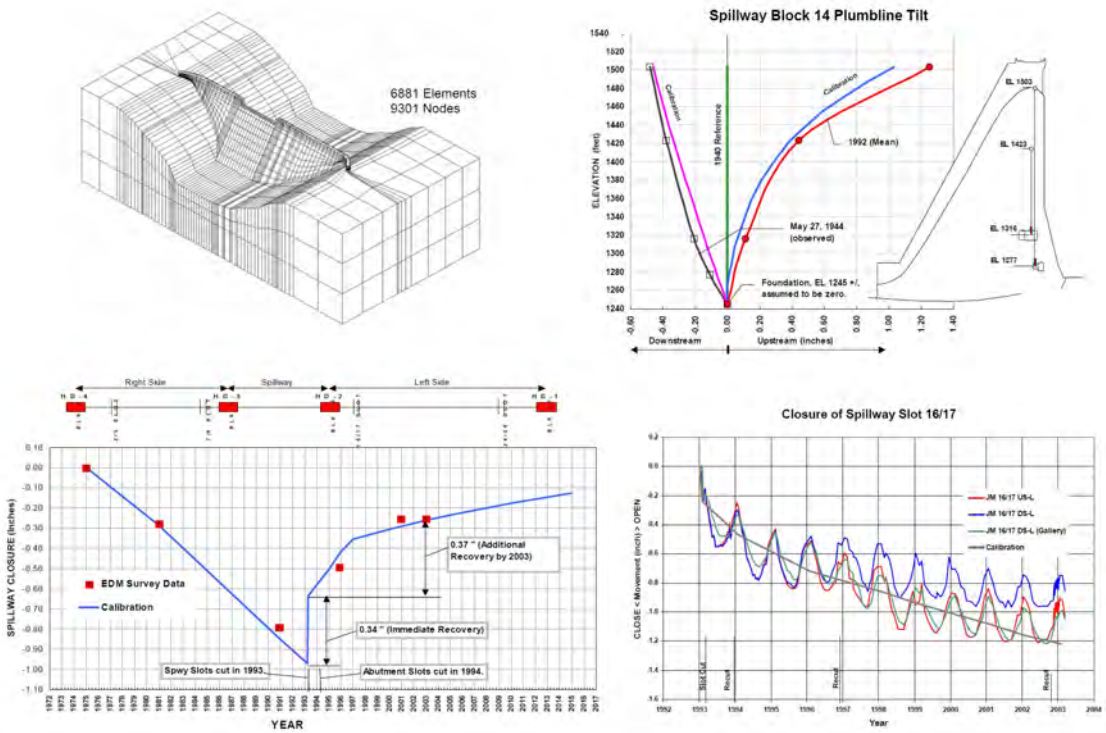

Figure 1.1: FE model and calibration results; Curtis et al. (2005)

Fairbairn et al. (2006) proposed an ASR thermo-chemo-mechanical expansion model with the main feature of representing the stress-induced anisotropy by means of a classical smeared cracking model. The model includes the influence of temperature and humidity. The model was applied to the 3D simulation of a real gravity dam located in the southeast region of Brazil. Determination of the thermal and humidity fields was based on simplified averaged assumptions. A constant ambient temperature and a constant reservoir level were assumed.

Figure 1.2 shows the vertical displacement of a point located at the top of the wall and its experimental counterpart monitored for the last 25 years which shows a good agreement between the measurements and simulation results.

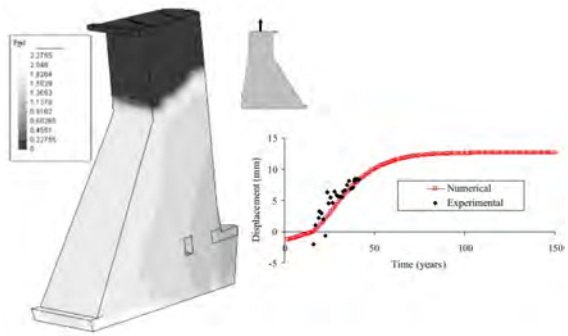

Figure 1.2: Results for the ASR simulation: gel pressure for 40 years and the displacements at the crest of the dam; Fairbairn et al. (2006)

Saouma and Perotti (2006b) proposed a new constitutive model for AAR expansion. This thermo-chemo-mechanical model was rooted in the chemistry, physics, and mechanics of concrete. This three-component model is an anisotropic model. A detailed 2D analysis of an arch gravity dam is presented. First, the seasonal pool elevation variation (for both thermal and stress analysis) and the stress free temperature (typically either the grouting temperature or the average yearly temperature) are identified. Next, a transient thermal analysis is performed for which only the heat transfer by conduction is accounted. Convection and radiation are approximated through an additional temperature. The total simulation time was 50 years with the selected incremental time of 2 weeks. Following the thermal analysis, the computed temperature must be transferred to another model (built for stress analysis) as, in general, we do not have the same finite element mesh (foundations, joints, and cracks are typically not modeled in the thermal analysis).

For the plane strain analysis, a 2D central section of the arch gravity dam is selected. Results are compared with the method proposed by Charlwood, Solymar, and Curtis (1992). To do so, final volumetric expansion was calibrated to yield identical vertical crest displacement after 50 years, Figure 1.3 (left), where the proposed model nonlinearity in the

crest displacement is caused by the kinetics model and its latency time in particular. Despite equal final crest displacements, internal field stresses are drastically different. Those determined from Charlwood's model are substantially lower than those predicted by the proposed model, Figure 1.3 (right). The large discrepancy in stresses is partially caused by the plane strain (which inhibits redistribution in the third direction) assumption of the proposed model.

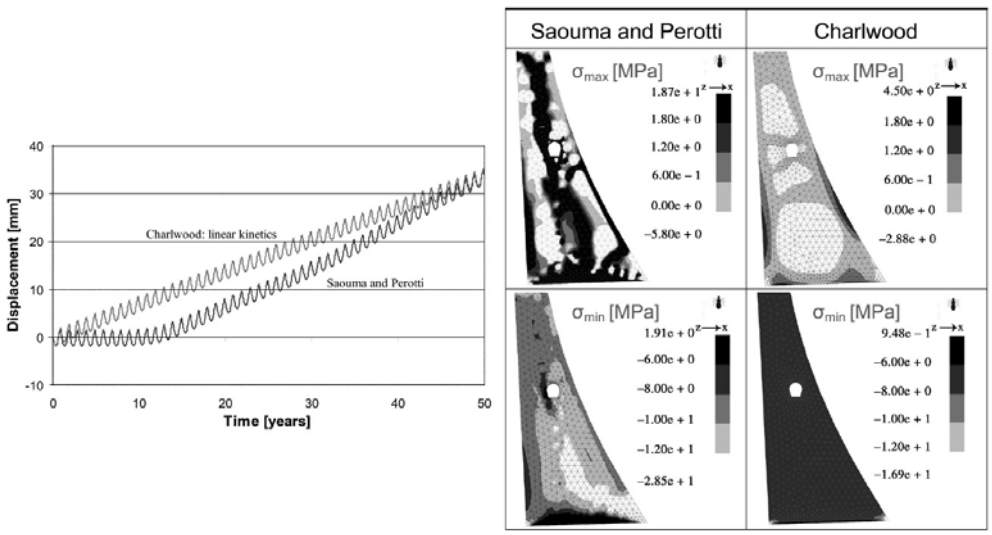

Figure 1.3: Comparison of yearly vertical displacement, and principal stress fields in two models; Saouma and Perotti (2006b)

Saouma, Perotti, and Shimpo (2007b) proposed a methodology for analysis and system identification of important AAR parameters which includes: 1) thermal analysis, 2) stress analysis, and 3) system identification.

- Thermal analysis:
  - ∗ Because of the temperature dependency, and to obtain a temporal map of the internal temperature, a transient thermal analysis must be performed.
  - ∗ At this stage, there is no need to model the rock base in such analysis.
  - ∗ Required data for this stage are:
    - – The air temperature variation (including the grouting temperature),

  - The spatial (along the depth) and temporal (at least 12 or 24 increments a year) variation of the water temperature,
  - The pool elevation variation during a typical year,
  - And the concrete thermal properties.

- Stress analysis:
  * The stress analysis is then performed, and an effective E_{eff} is used to account for long-term creep ($E_{eff} = \frac{E_i}{1+c_t}$, where c_t is the specific creep coefficient and E_i is the initial modulus).
  * Detailed FE model including the joints, foundation, etc. should be used.
  * It should be kept in mind that the stress analysis requires the temperature difference with respect to the stress-free temperature.
  * A correct pool elevation (upstream and downstream), uplift pressures, and internal nodal temperatures should be applied for each increment.

- System identification:
  * AAR problems are prime candidates for system identification.
  * The field recorded (usually crest) displacements are denoted by $u(t)$, the kinetic (and possibly other) parameters as x, the finite element operator $f(.)$, and computed results by $u(t, x)$.
  * Hence, $f(x) = u'(t, x) \neq u(t)$.
  * The goal is to minimize the objective function $\omega(x) = (u - u')^T(u - u')$. The trust region method can be used to solve the problem.
  * A weight function can be used to assign importance to the last data field which usually has a major absolute value and, thus, better represents the irreversible effect of the AAR expansion with respect to the effect of normal loads.

Figure 1.4 (left) shows that the computed crest displacement is well within the seasonal variations of the numerical final predictions. Figure 1.4 (right) shows the internal AAR induced maximum principal stresses. The maximum principal stress field inside the dam

can explain the cracks discovered along the upper gallery of the analyzed dam.

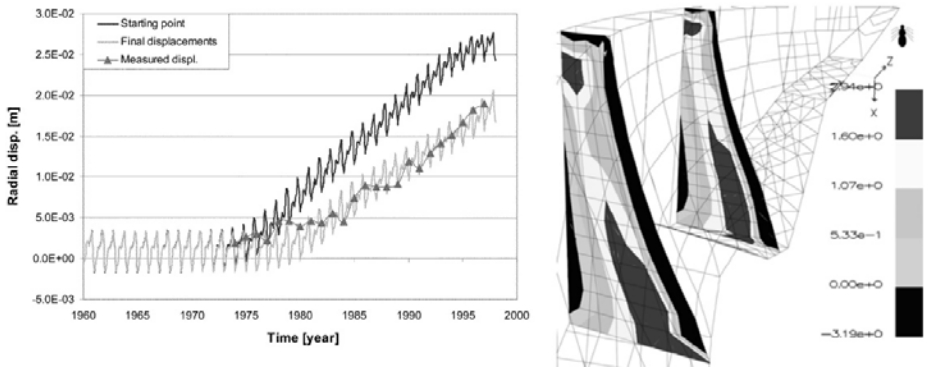

Figure 1.4: Comparison between first guess analysis and final analysis with optimized parameters (left), Internal AAR-induced maximum principal stresses in MPa (right); Saouma, Perotti, and Shimpo (2007b)

To the best of the author's knowledge, this is the most widely adopted model by other researchers. A non-comprehensive list of implementations includes:

(1) Rodriguez et al. (2011) implemented the model in Abaqus and analyzed an arch dam.

(2) El Mohandes and Vecchio (2013) in the Vector3 program and the analysis of reactive shear walls.

(3) Mirzabozorg (2013) in Iran for the analysis of Amir-Kabir arch dam in the NSAD-DRI code.

(4) Pan et al. (2013) from Tsinghua University for the analysis of Kariba dam.

(5) Huang and Spencer (2016) and Huang, Spencer, and Cai (2015) implemented this AAR model in the fully coupled Grizzly/Moose program.

(6) Ben-Ftima, Sadouki, and Bruhwiler (2016) Polytechnic of Montreal, and Swiss Federal Institute of Technology, as a model in Abaqus for the analysis of a hydraulic structure.

(7) Thonstad et al. (2021) implemented in LS-Dyna by NIST.

Comi, Fedele, and Perego (2009a) proposed a chemo-thermo-damage model to simulate the swelling and the deterioration of local stiffness and strength in concrete due to AAR in dams. AAR affected concrete is conceived as a two-phase heterogeneous material constituted by

the expanding gel and by the homogenized concrete skeleton. The micro-cracking produced by the gel expansion is taken into account by means of an isotropic damage model based on the definition of two scalar damage variables (tension and compression). The finite element code Abaqus was used to build a 2D plane strain model of two dams, Koyna Dam and Fontana Dam.

Koyna Dam was analyzed with and without AAR for 16 years under accelerated conditions. The dam body is assumed to have uniform moisture. Thus, the main factor driving the AAR is the temperature history. Harmonically varying temperature is assumed for air and water. Foundation temperature is kept constant. Figure 1.5 illustrates the development of the AAR and its mechanical consequences within the considered dam including the tensile damage. At the beginning of the AAR, the swelling is restricted to a thin "stripe" along the boundary exposed to air where the mean temperatures are higher. As a consequence of strain compatibility, the internal core of the dam is subjected to tensile stresses, whereas the external skin is compressed. After about 16 years of AAR activity, a macroscopic horizontal crack develops also in the lower part of the dam.

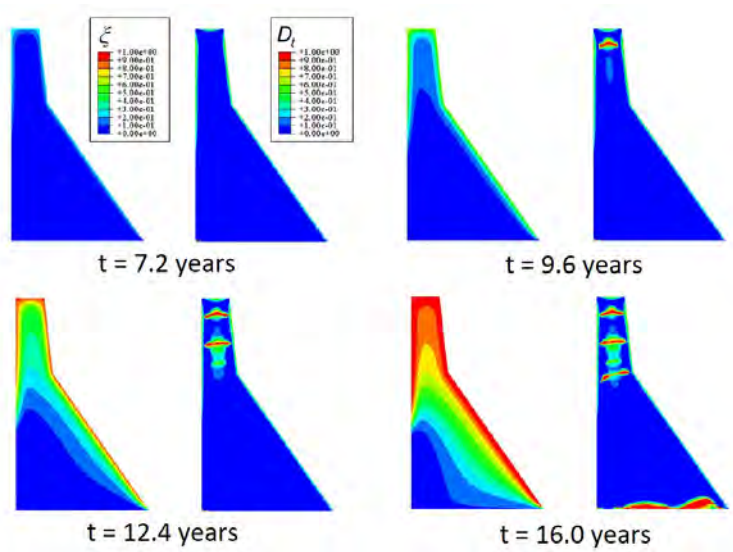

Figure 1.5: Reaction extent and damage during AAR development in Koyna Dam; Comi, Fedele, and Perego (2009a)

Fontana Dam was also modeled in a similar way to Koyna dam. Figure 1.6 shows the reaction extent and tensile damage pattern at different times of the analysis. At the third year, a highly localized damage zone forms at the high-left corner of the drainage gallery, and it develops quickly reaching the downstream face. Starting about at t = 4 years, this new crack rapidly extends through the whole dam thickness.

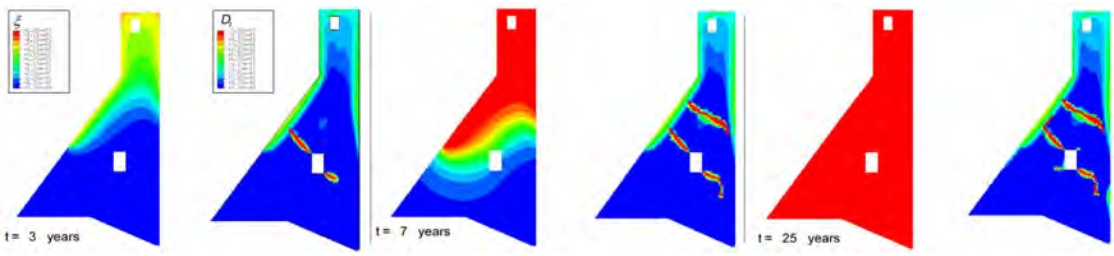

Figure 1.6: Reaction extent and damage during AAR development in Fontana Dam; Comi, Fedele, and Perego (2009a)

Sellier et al. (2009a) proposed a method including structural monitoring and laboratory tests for assessment of AAR swelling in gate structure dam. They used an old dam in France. This method first involved a laboratory test dealing with the silica consumption kinetics and, second, a numerical finite element inverse analysis of the dam which included the consumption kinetics measured in the laboratory. A procedure is proposed to assess the chemical advancement for each aggregate size of the concrete, Figure 1.7:

- Phase 1:
  - Aggregates of the affected concrete are first extracted by chemical attack and sifted.
  - Then, the residual reactive silica content is assessed for each reactive aggregate size.
  - Several types of mortar containing only one aggregate size from the dam concrete are cast.
  - The aggregates are crushed to obtain the same aggregate size distribution in each mortar.

  * A sufficient amount of alkali is added to the mortar cement paste to be sure that all the residual reactive silica contained in the crushed aggregates will be consumed during the tests.
  * The total swelling measured for each mortar depends only on the residual reactive silica contained in the reactive aggregate.

- Phase 2:
  * The constant representing the kinetics of in-place chemical advancement is deduced from both the chemical advancements measured for each aggregate size and the environmental conditions.

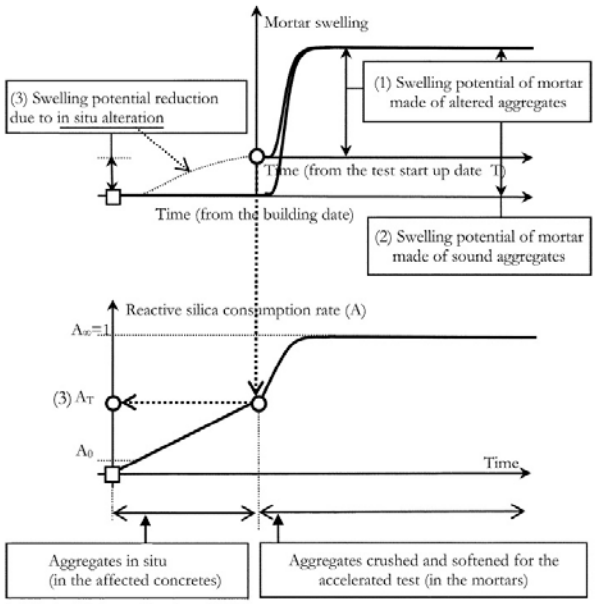

Figure 1.7: Principle of chemical advancement assessment; Sellier et al. (2009a)

For the case study, the variation of the lateral displacement of the dam was used to fit the unknown parameter. Then, the vertical and the horizontal displacement at other points could be simulated with good accuracy. A good agreement was found between the computed damage and the crack pattern with the lightest zones corresponding to the observed cracks.

Leroy et al. (2011) studied the abnormal crest displacements due to ASR in a gravity dam for over 50 years where the polygonal shape of the dam amplifies the effect of concrete expan-

sion. Both 2D and 3D numerical models were used to evaluate the dam response. Although the dam was built with different concrete mix-designs (with various cement quantities), the global behavior was best represented by considering a homogeneous expansion potential. The 3D mesh is composed of 28,589 quadratic elements, Figure 1.8. Model fitting to the monitoring data is used to determine the correct values for the three parameters: τ_l, τ_c and ε_∞. The temperature and moisture fields in the structure are considered as homogeneous. More than 30 parametric analyses are performed for 60 years of ASR expansion, and the computed crest displacement in blocks 13 and 23 are compared to the upstream-downstream displacements monitored on the Dam. The rehabilitation project is conducted on the Dam to reestablish an acceptable level of stress and deformation. Sawing the upper part of the dam to release stress and decrease the arching effect, which has been amplified by the Dam's elbow, is a good option to achieve this goal.

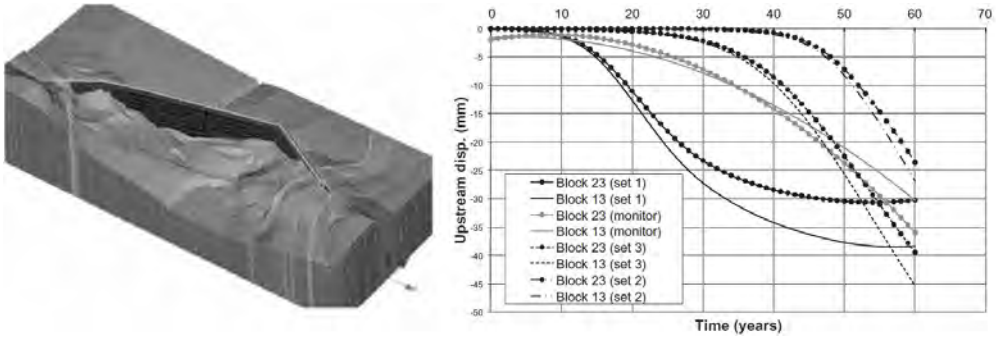

Figure 1.8: Views of the mesh, and Downstream displacement at the crest of the Dam; Leroy et al. (2011)

Comi, Kirchmayr, and Pignatelli (2012) conducted a similar research to their previous one where the concrete affected by ASR is represented as a two-phase material made of a solid skeleton and a wet expanding gel. The AAR mechanical degradation is described by an isotropic damage model. Again, the FE code Abaqus was used. They used the right gravity dam of the Beauharnois power plant (Québec, Canada) as case study which displayed cracks due to ASR. The chemical and mechanical properties of concrete are assumed homogeneously distributed in the dam. E, f_c, and f_t were determined from 45

years of field measurements. It is also assumed that f_c does not change over time. Since the final ASR expansion was unknown, various analyses were performed with variable values of the asymptotic axial ASR expansion. Figure 1.9 shows the reaction extent and the damage at three different time steps. At the beginning, the damage appears only on the external skin of the structure since it is the only area affected by the external humidity conditions. The first macroscopic crack in the body of the dam and visible on the surface of the structure appears six years post-construction.

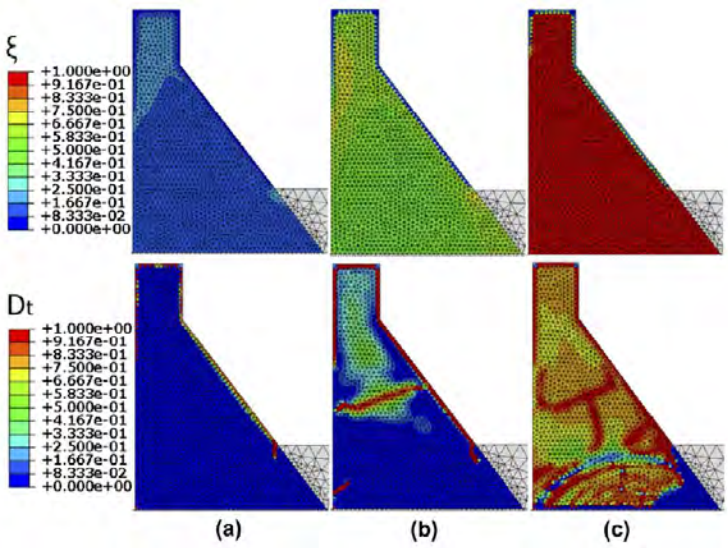

Figure 1.9: Patterns of the reaction extent and damage after (a) 3, (b) 6 and (c) 60 years; Comi, Kirchmayr, and Pignatelli (2012)

Ferreira, Farage, and Barbosa (2013) applied an AAR-stress model firstly proposed by Farage, Alves, and Fairbairn (2004) on gravity dams. A 2D nonlinear analysis was performed using triangular plane strain elements. The dam is fixed at the bottom, and a hydrostatic load is applied in the upstream face. The adopted AAR curve parameters are: $\varepsilon_\infty = 0.196$, $\tau_l = 3.34$ and, $\tau_c = 8.29$ years. Figure 1.10 compares the gel pressure evolution in the concrete wall evaluated via the uncoupled and the coupled models. The coupled model accounts for the reducing effect of confinement stresses on the reaction evolution as reflected by the lower gel pressure values in the confined regions and, as a consequence, by

a decrease on the amount of cracked finite elements. Cracking spreads more widely when the uncoupled model is applied. For the coupled model, cracking is mostly concentrated around the free surface.

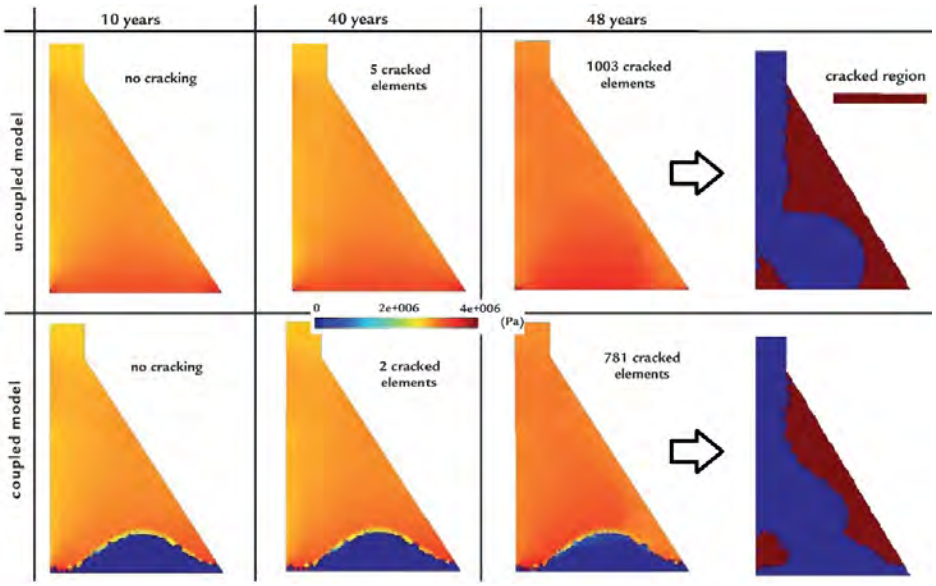

Figure 1.10: Gel pressure evolution in the concrete wall via the uncoupled (above) and the coupled (below) models; Ferreira, Farage, and Barbosa (2013)

Amberg, Stucchi, and Brizzo (2013) studied the effect of temperature on the development of the AAR at the Pian Telessio arch gravity dam. Approximately 20 years after its completion, the dam is showing an upstream drift caused by concrete expansion. In 2008, rehabilitation works by means of vertical slot cuttings in the upper half of the Dam were performed in order to reduce the effects of the concrete expansion.

In 2008, in order to evaluate the temperature effect on AAR, long term laboratory tests (2-3 years of duration) on concrete specimens (prism 7×7×28 cm) were performed. A back analysis was also performed aimed to identify the required parameters. The analysis focused on the three parameters (τ_l, τ_c, and ε_∞) leaving the others unchanged. The calibration is done on the permanent upstream displacement, recorded by four pendulums distributed along the Dam. The expansion distribution along the Dam's thickness is applied to a 3D model. Figure 1.11 shows the concrete expansion applied to the model as a function of the

Dam's elevation for the four reference dates.

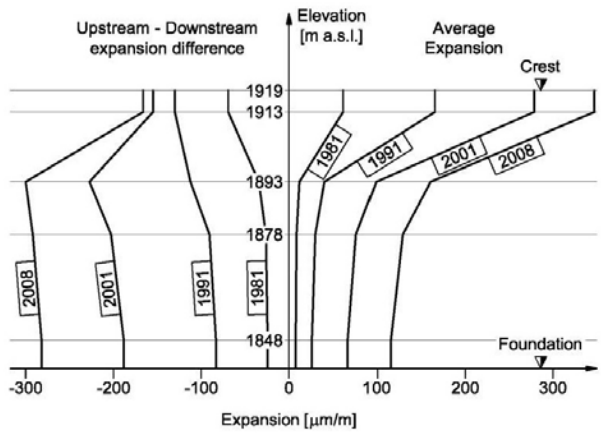

Figure 1.11: Volumetric expansion applied to the model; Amberg, Stucchi, and Brizzo (2013)

The nonuniform drift distribution observed for the Dam, which is more relevant at the crest than in the lower part. It is found that the expansion along the Dam's thickness is nonlinear. The highest expansion is observed along the downstream face as well as in the upper, thin Dam part.

Metalssi et al. (2014) investigated the AAR effect in a concrete dam including the nonlinearity and contact elements. Displacements and stresses at the contact elements zone were computed and compared with results of the dam computations without contact elements. The results show that the creation of the slot cutting leads to a decrease of the compressive stresses in the structure, confirming a favorable effect of this stress release technique to address AAR affected structures. Coulomb friction criterion is considered for shear response.

A simplified model, which might represent an idealized part of an AAR-affected gravity dam is used as case study. Displacement and stress at different points along the joint are shown in Figure 1.12. Results are presented for both before and after sawing. Transverse displacements are zero for points until 10 years for reasons of symmetry. After sawing ($e =$ 1 cm), the notch closes instantaneously due to the decompression of surrounding concrete, and cumulated displacements on both sides of this notch reach exactly the value of the

sawing thickness. The notch remains open only at point P6 (top). For the reference case, the transverse stress increases with time until its stabilization at a value of 45 MPa (the theoretical maximum stress). While in the case of the slot cutting, the stresses decrease instantaneously just after sawing but then increase again with time until stabilization at values of 30 to 35 MPa (the theoretical values calculated at the end of the swelling).

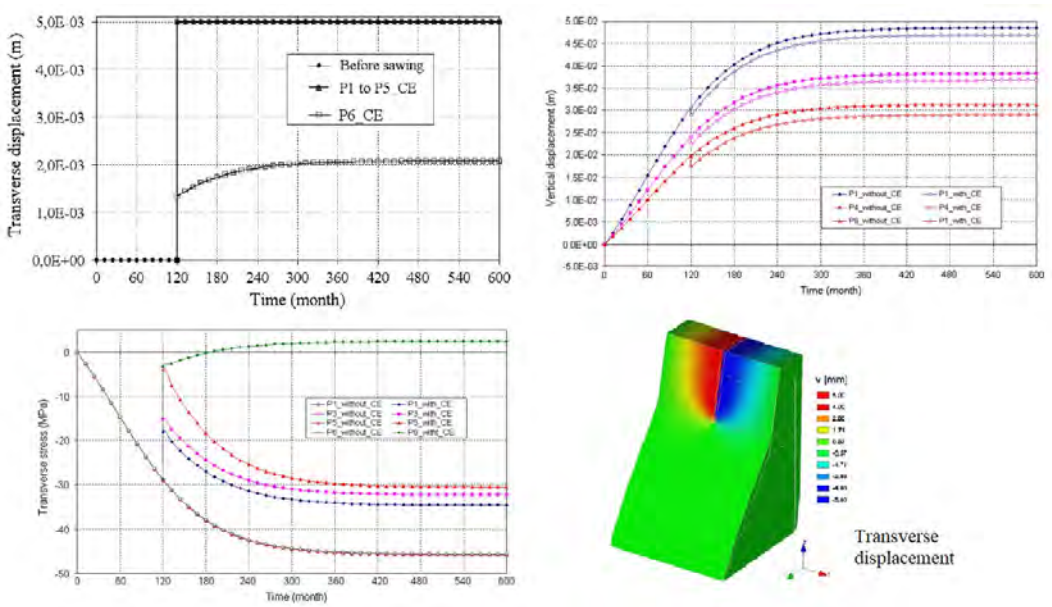

Figure 1.12: Displacement and stress vs. time before and after sawing; Metalssi et al. (2014)

Cima and Reinicker (2015) studied the ASR in Roanoke Rapids Dam, located in North Carolina and completed in 1955. Due to a concern that partial block movement could create additional damage during anchor installation and loading, grouting of the ASR cracking was the first step in the remediation design. A finite element model was also developed to better understand the behavior of the structure. The FEM model included several important and key features: (1) transient thermal analysis; (2) temperature-dependent ASR expansion rates; (3) anisotropic stress-dependent ASR expansion rates; (4) visco-elastic creep behavior with creep function and effective modulus of elasticity; and (5) separation/opening along preexisting cracks. Calibration of the model before and after post-tensioning is shown in Figure 1.13. It is evident that, since completion of the anchoring project, the trend

of rapidly increasing downstream movement has been arrested, and only smaller seasonal temperature variations are observed.

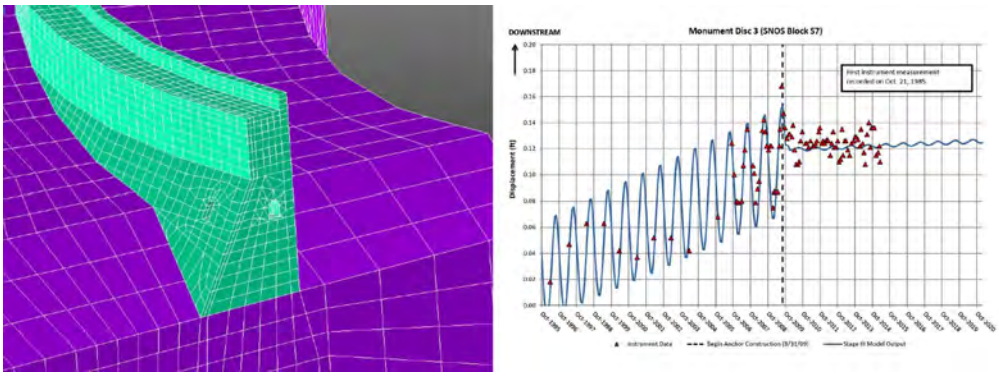

Figure 1.13: Finite element model and calibration; Cima and Reinicker (2015)

Lamea and Mirzabozorg (2015) studied the impact of AAR on static analysis of Dez arch dam. Concrete was assumed to be linear elastic. Contraction joints were modeled with node-to-node contact elements using ANSYS finite element code. Results of initial thermal analysis included the solar radiations effect as reported in Mirzabozorg et al. (2014). The displacement time history of the crest for different simulations is shown in Figure 1.14. It is observed that the solar radiation does not significantly affect crest displacements in US/DS direction. On the other side, joints tend to move the crest downstream. These effects are mitigated when AAR damages the Dam's body.

Solar radiation effect is not disregardable in the first half of the history duration pertinent to AAR-affected cases. In contrast to the horizontal displacements, in all of the AAR-affected cases, the vertical displacements are not considerably affected by modeling none of the solar radiation or the contraction joints.

Nik-Azizan et al. (2017) performed AAR damage analysis of Koyna gravity dam using two-dimensional plane strain simulation. The extent of damage in concrete was computed using the orthotropic damage index proposed by Ghrib and Tinawi (1995). Total porosity,

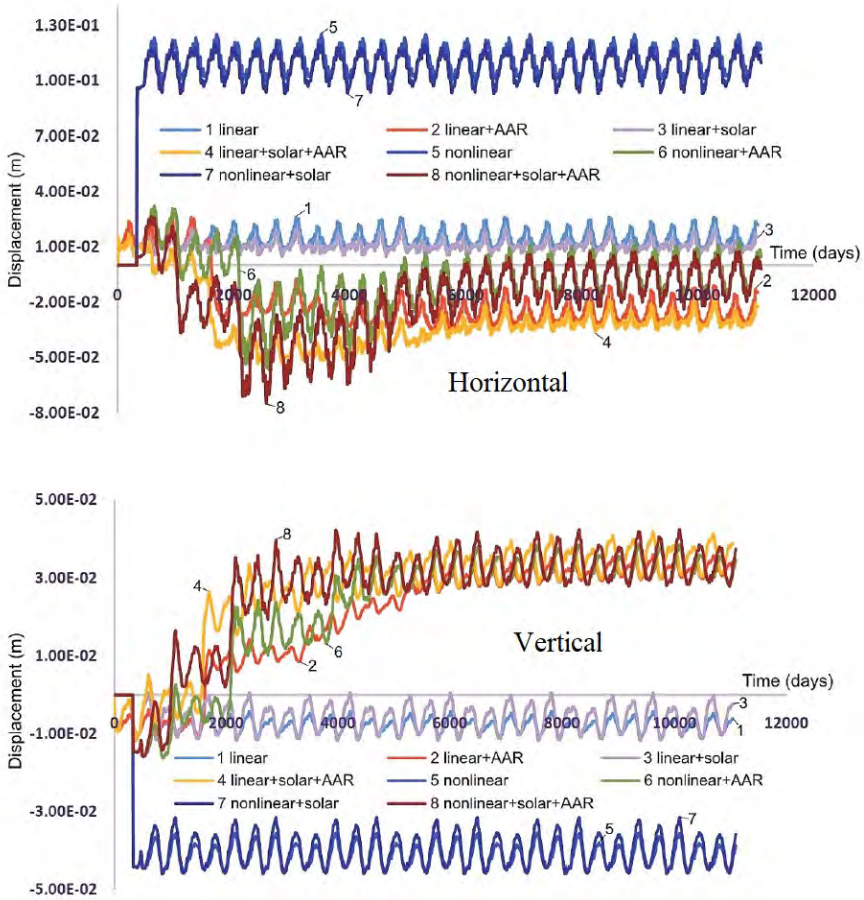

Figure 1.14: Comparison of displacements at crest of the Dam; Lamea and Mirzabozorg (2015)

ϕ, of concrete is considered as a measure to determine the degradation parameter:

$$\phi = \phi_0 + \phi_c + \phi_m \tag{1.1}$$

where ϕ_0 is the initial porosity, ϕ_c is the chemical porosity resulting from skeleton dissolution, and ϕ_m is the apparent mechanical porosity.

Larive curve was used to present the volumetric expansion. Degradation of E and f_t was considered explicitly. They also conducted seismic analyses using the rigid foundation assumption with empty reservoir. Three numerical simulations were conducted: after completion, 50 years later, and 100 years later. The contour plots revealed that the major principal stress at the neck reduced over time, Figure 1.15. These findings are attributed to the smaller modulus of elasticity in the aged dam and more flexible behavior.

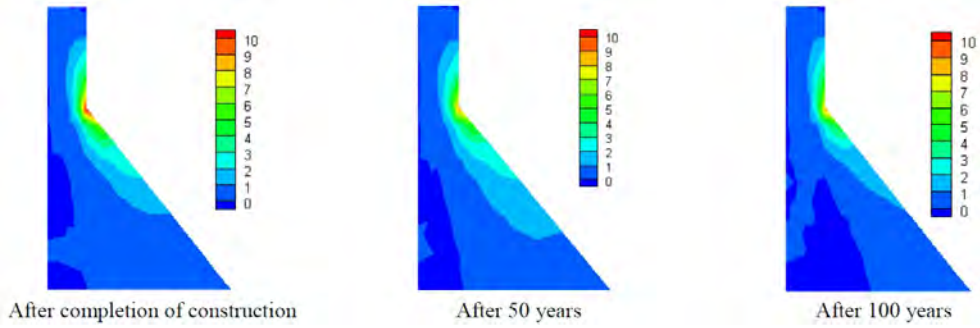

Figure 1.15: Maximum major principal stresses contour; Nik-Azizan et al. (2017)

Chulliat, Grimal, and Bourdarot (2017) studied AAR in Chambon Dam causing several pathologies, mainly resulting in shear stress zones in the structure and significant structural cracking, likely to affect its integrity under earthquake conditions. The new multi-scales swelling law for concrete implemented in ASTER computer code was used for numerical simulation. It provided a very good fitting with the monitored dam behavior, Figure 1.16. The FEM calculations showed that the benefits of the slot cuts done in the 1990's still remain in the upper part of the structure, confirmed by the monitoring of the deformations in the curved right wing. They, nevertheless, displayed noticeable stresses parallel to the abutments.

Coubard and Sausse (2017) investigated the safety reassessment of arch dams with thrust blocks subject to swelling phenomena. A methodology of calculation is made up of the following steps:

- Analysis of the initial design and associated loadings.
- Linear finite element model taking into account the arch and the thrust block. Simulation of concrete swelling by thermal analogy in a primary approach, accounting for a slight concrete creep due to swelling itself.
- Classical stability analysis of the thrust block with resultant forces determined using the linear model and conservative parameters (low shear strength, no lateral abutment).
- If a low stability coefficient is obtained, implementation of a nonlinear model with joint

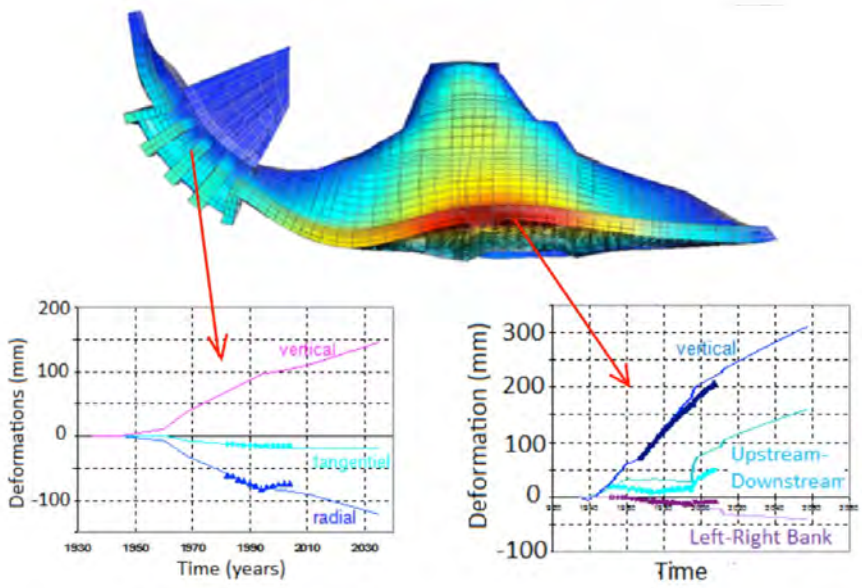

Figure 1.16: Comparison of measured and computed deformations in 3D modeling; Chulliat, Grimal, and Bourdarot (2017)

elements at the concrete-to-rock interface with a Mohr-Coulomb law. Evaluation of the irreversible displacements is obtained.

- Comparison of these irreversible displacements with monitoring measures.
- If necessary, monitoring device reinforcement of thrust block.
- If necessary, realization of site investigations in order to estimate the effectiveness of lateral abutment, shear strength and stress levels.
- If necessary, development of a more sophisticated non-linear model able to describe the behavior of swelling concrete.

Figure 1.17 shows the swelling response of an arch dam. For arch dams with thrust blocks submitted to swelling phenomena, the sum of actions highlights an increase in thrust block loading with time. Nonlinear models demonstrate that millimetric displacements of thrust blocks are sufficient to reach a new acceptable equilibrium state.

Gunn, Scrivener, and Leemann (2017) proposed a three-phase strategy for the investigation of AAR in existing dams:

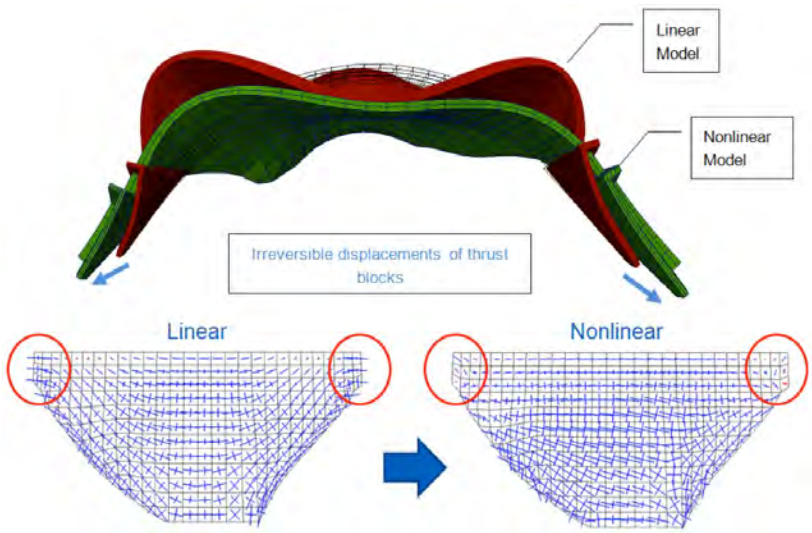

Figure 1.17: Linear model and nonlinear model with concrete-to-rock joint on a swelling arch dam with thrust blocks; Stress reorientation and modification on the upstream face; Coubard and Sausse (2017)

- Phase 1: AAR stage tests, material source(s) (e.g. quarries), visual inspection, and core sampling should cover all stages of the AAR process in the short, medium, and long term of the structures service life, including information needed for numerical modeling.
  - Classification of AAR tests by: category, location, phase, type, sample type, classification, reliability, quality of information, and sample preparation.
  - Influencing Factors: specimen size, quantity of cement, additives, relative humidity, temperature, time, and cost.
  - Results and Conclusions: Standard limits above which AAR is deemed to be potentially deleterious.
- Phase 2: AAR monitoring and data analysis. Using statistical, deterministic, and hybrid data analysis techniques to capture the potential zones of AAR swelling and, hence, perform analyses to assess the behavior and safety of the dam.
- Phase 3: AAR follow-up tests should be systematically performed every 5 years from the onset of AAR.

Blanco et al. (2018) studied an old concrete gravity dam with signs of deterioration due to expansive reactions. They collected evidences of damages in spillway, bridge, and dikes. Multiple tests were performed on the samples extracted from the dam, including X-ray diffraction, scanning electron microscope with energy dispersive spectroscopy mode, and petrography.

Next, a model based on finite differences was prepared to simulate heat transfer phenomena. The dam is modeled at a sectional level per length unit. The construction procedure is defined as casting of consecutive layers. Once cast, the layer is unprotected and exchanges with atmospheric air may occur, as well as the diffusion with the bottom and lateral layers. The results of the thermal modeling shows the maximum temperatures reached in the cross section of the dam. The highest temperature occurs in the center of each of the different layers.

Finally, they performed crack analysis of the dam in the finite element software ATENA using nonlinear fracture mechanics with the crack band method and smeared cracking. The reinforcement is modeled by a bilinear model. Figure 1.18 shows the crack pattern observed in the diaphragms. It suggests that the cause of the cracks may be a volumetric expansion in the spillway.

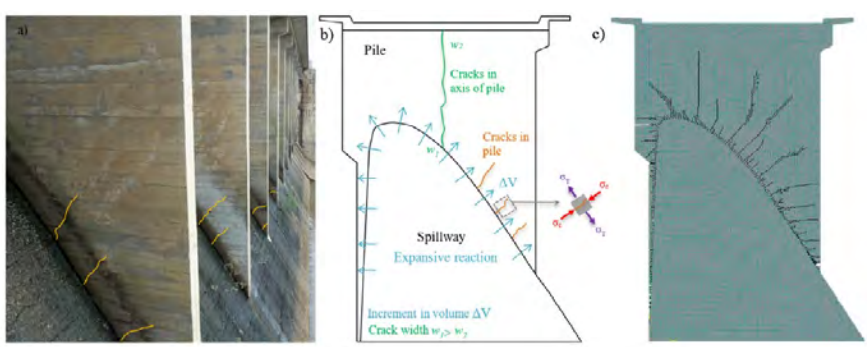

Figure 1.18: Finite element analysis: (a) real crack pattern, (b) stresses in the diaphragm, and (c) crack pattern of the model; Blanco et al. (2018)

Saouma, Hariri-Ardebili, and Graham-Brady (2020) presented an algorithm to model the dam inhomogeneity in terms of characteristic length and applied the algorithm to an arch

gravity dam.The impact of randomness in material properties on displacements, joint openings, and stresses were then investigated. They found that although the mean values of the responses were not impacted significantly, the standard deviations showed great variations. Furthermore, the safety assessment through fragility surfaces, and meta-modeling determined that whereas randomness may affect local results, their impact may be negligible for globally averaged responses.

1.4 The "Big-Picture"

Based on the provided literature review on the AAR analysis of the concrete dams, the big-picture of the proposed framework is demonstrated in figure 1.19.

- The first step, as for every finite element analysis, consists of gathering and preparing different data including:
  - The geometry of the dam
  - Meteorological data
  - Dam site seismic maps

    all of which will be used as inputs for the finite element code.
  - In addition, the long term field monitoring data being collected to validate the results of the numerical finite element analysis.

  Having the required input parameters in hand,
- appropriate constitutive models are then utilized to construct the model in the finite element code called Merlin which has the key feature to model:
  - The fluid structure interaction
  - The soil-structure interaction
  - Thermal Analysis
  - Dynamic Analysis
- In the next step in order to calibrate the input data with the field recordings, an iterative process of system identification based on the trust region methods, is being employed. More

precisely, input parameters describing the AAR expansion as well as strength and elasticity degradation are selected such that the resulting displacements match the field recordings.

- Extending the analysis one step further, an uncertainty quantification of the performed analysis will be conducted assuming various sources of uncertainties including epistemic uncertainties which is associated with the temporal material uncertainty, heterogeneity of the concrete material properties as well as the aleatory uncertainties associated with the ground motion selection will be considered through Latin hypercube sampling method and propagated into the finite element model.
- Finally, using the cloud analysis procedure a fragility curve will be derived which enables us to perform the risk assessement of the dam.

It should be noted that the author has on the one hand benefited from a vast body of previous work, (properly cited) and developed herself new ones. In either case, the author is fully confident in her understanding of all details.

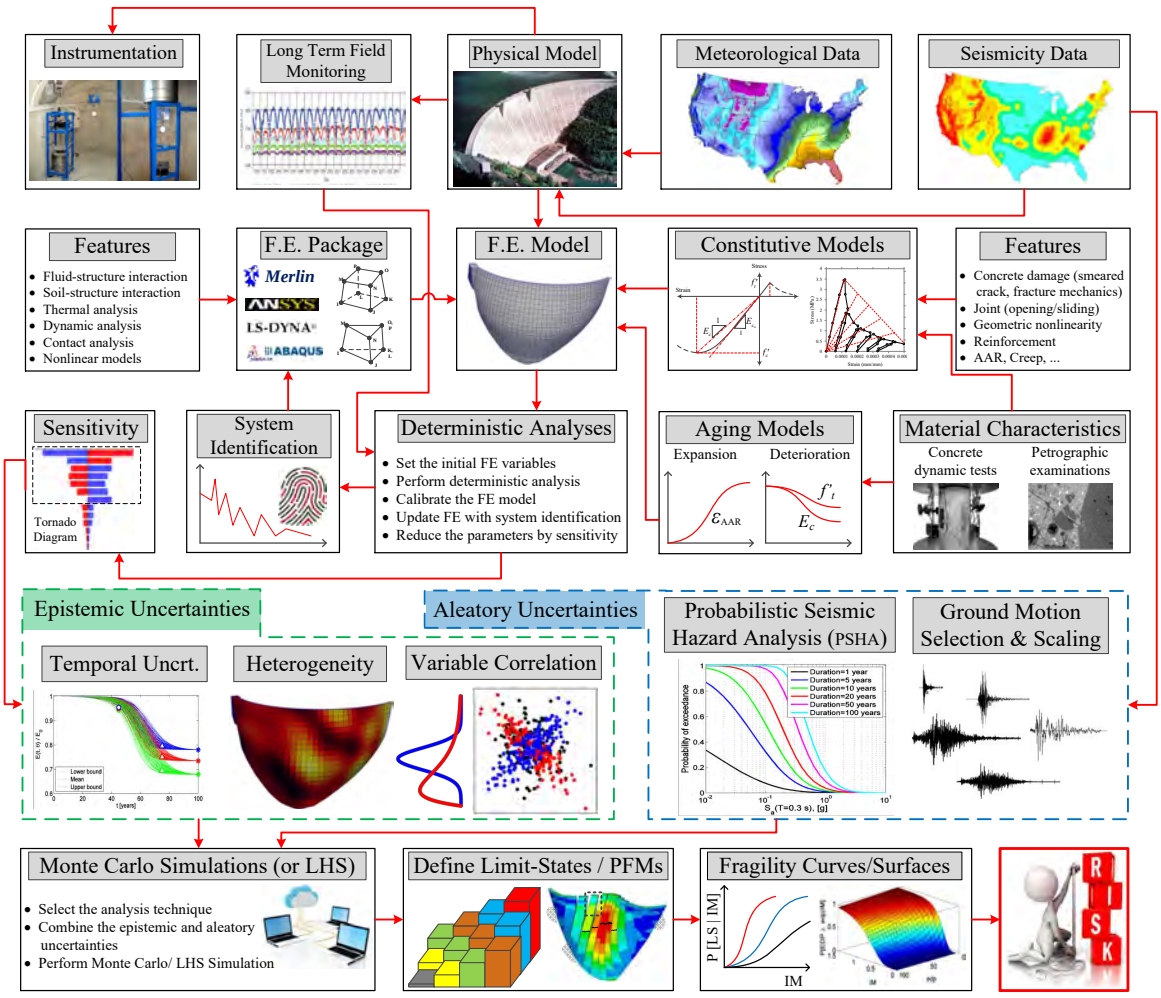

Figure 1.19: Outline of a comprehensive analysis (Adapted from Saouma and Hariri-Ardebili (2021c))

Part I

THEORY

Chapter 2

Alkali Aggregate Reaction

Abstract

The underlying mechanisms causing Alkali Aggregate Reactions (AAR) are by now well known. This chapter will limit itself to describe AAR in the context of the constitutive model developed by Saouma and Perotti (2006a) and implemented in the computer program Merlin used in the analyses.

2.1 Finite element modeling of AAR in dams

`Section Adapted from (Saouma and Hariri-Ardebili, 2021a)`

Prognosis of hydraulic structures suffering from AAR is notoriously difficult and for some impossible.

For the most part, current approach relies on one or more investigative tools, Fig. 2.1. Unfortunately those methodologies tend to be disjointed and difficult to directly relate to others. For example a petrographer may find the DRI (or other measure microscopically determined) too elevated, and hence consider the structure unfit. Expansion tests may be performed, but results are seldom fed into the finite element study. Finite element studies themselves may be conducted with unvalidated codes.

There are essentially two possible approaches to model AAR, Fig. 2.2. The first is represen-

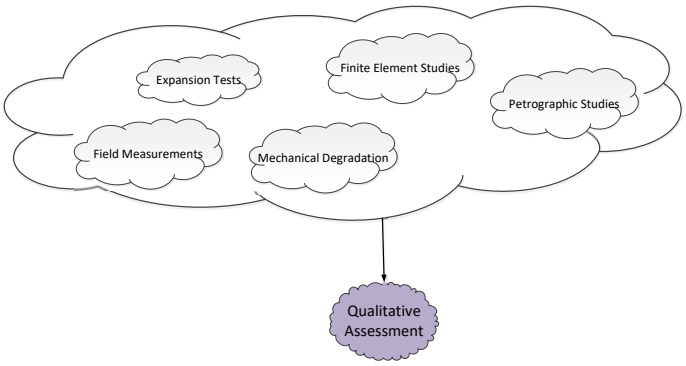

Figure 2.1: A clouded approach

tative of the State of the Practice, while the second captures the State of the Art in AAR.

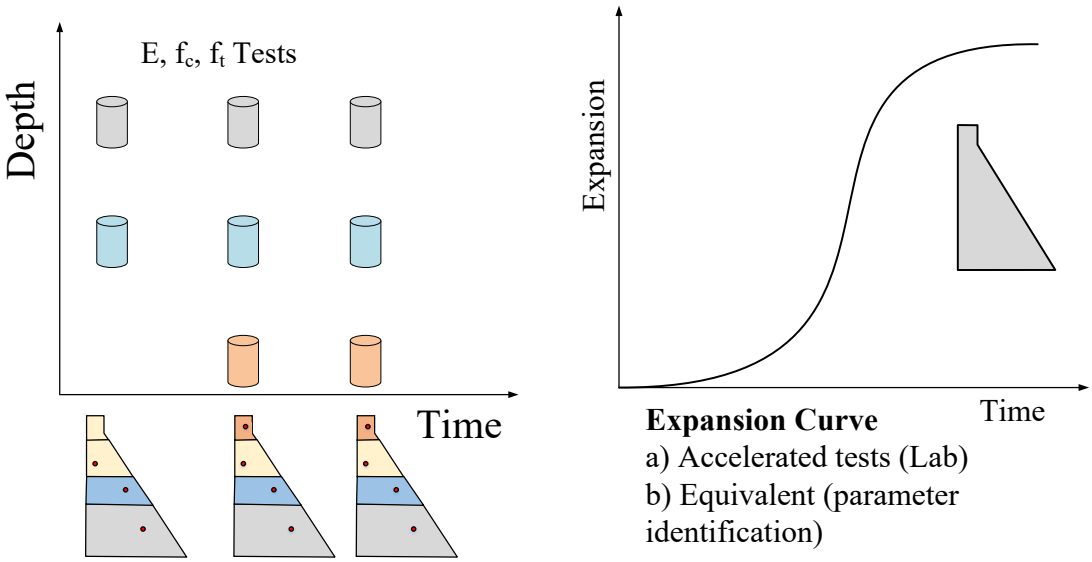

(a) State of the practice

(b) Proposed

Figure 2.2: AAR FEA models

A brief summary of the two methods is shown in Table 2.1.

Table 2.1: Side-b-Side Comparison of the State-of-the-Practice and the State-of-the-Arth methodologies to analyze dams with AAR

Methods	State of the Practice	State of the Art (e.g. Merlin)
# of Analyses	Multiple, one for each year we are interested in	Single analysis that starts at time 0 (dam construction) up till desired year
	Input data	
Parameters	Topological distribution of damaged concrete properties over the dam at the time of analysis	Characteristics of the concrete expansion to capture its kinetics (3 parameters)
How do we obtain them	Subdivide the dam in multiple regions; Extract sufficient representative cores from each one of them; perform tests (E and f_c primarily)	(1) Perform expansion and appropriate petrographic tests, determine the 3 parameters that characterize the concrete since time of construction (2) Same as above, without petrographic tests, characterization since date of core extraction (3) Perform a parameter identification based on the historical record of crest deflections
	Analysis	

Advantage	Easier to perform the analysis if one does not have a finite element code that can track the expansion with time.	Single analysis that capture the entire response (displacements and internal deterioration of concrete); Requires only three parameters that capture the cause of the expansion (as opposed to multiple tests that reflect the consequences of the reaction); Truly captures the complex response of a structure subjected to AAR (listed as disadvantage for Method 1 below).
Disadvantage	Approximate as we have to assign material properties over large zones, many input data coming from tests. May not be representative enough as it does not capture: 1) interaction of temperature with expansion; 2) effect of confinement on the anisotropic expansion;	Some numerical instability may occur in a nonlinear time history analysis
	Analysis Output	
Dislacements stresses	Yes, a snapshot at time t (of analysis), i.e. one single scalar quantity at time t	Yes, a "movie" that captures the evolution of the dam response, i.e. a vector for each response in terms of time
Concrete deterioration	No, that was part of the input	Yes as computed by the AAR model
	Future Prediction	

Possible	Will have to be based on the time dependent concrete deterioration	By just letting the analysis go beyond present date.
Reliability	Low would rely on the extrapolation of concrete damage measured in the laboratory and inputted in the mesh	High, embedded in the analysis are the expansion characteristics measured in the lab (or extracted from a parameter identification based on historical record of crest displacement)

2.1.1 State of the practice

A simpler approach, which is based on a mapping of the field determined concrete deterioration on the ensuing finite element mesh. The analysis, is then calibrated with some of the field measurements. Thus, a separate analysis will be conducted for each year of recorded mechanical properties.

2.1.1.1 AAR Modeling

One would start with testing cores (E, f_c and f_t, but not necessarily all three of them all the times) recovered from the dam at time t_i. Then, one would, semi-arbitrarily but certainly approximately, assign a representative region to each one of the cores. Within that region, elements of the mesh will be assigned the same mechanical properties.This method is explained in details in Saouma, Hariri-Ardebili, and Graham-Brady (2020) . It is noted that this has not been addresses in the current work.

Separately, at time t_i one would estimate the AAR expansion $\varepsilon^{\infty}(t_i)$, and its spatial distribution $\varepsilon^{AAR}(t_i, x, y)$.

Finally, combining those two, a finite element analysis is performed. However, this is very unlikely to yield good correlation with recorded field displacements. Hence, correction are made with *some* of the recorded data, and verification is made with the others. This is repeated until

adequate comparison at time t_i is achieved. Adjustments are for a given time t_i and are very unlikely to be the same for time t_j.

The outcome of such a calibration (for $E|f_t|f_c$) is a spatial and temporal partitioning shown below, Fig. 2.3

$$
\begin{aligned}
[E|f_t|f_c](h,t) &= \begin{cases}
a_1 f_1(h) \times f_2(t) & yr_1 \le t \le yr_2 \quad \& \quad h \ge h_1 \quad ① \\
a_2 f_2(t) & yr_1 \le t \le yr_2 \quad \& \quad h < h_1 \quad ② \\
a_3 f_1(h) & t < yr_1 \quad \& \quad h \ge h_1 \quad ③ \\
a_4 f_1(h) & t > yr_2 \quad \& \quad h \ge h_1 \quad ④ \\
a_5 & t < yr_1 \quad \& \quad h < h_1 \quad ⑤ \\
a_6 & t > yr_2 \quad \& \quad h < h_1 \quad ⑥
\end{cases} \\
f_1(h) &= b_1 + b_2 h + b_3 h^2 \\
f_2(t) &= c_1 + c_2 t + c_3 t^2
\end{aligned}
\tag{2.1}
$$

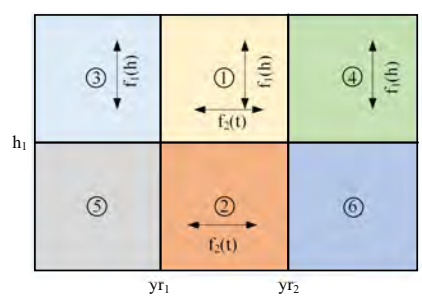

Figure 2.3: Spatial and temporal partitioning

The major (but not only) concern with this method, is that typically one would have not only very limited measurements but those are also widely spaced in times. This is further exacerbated by the seldom performance of tensile strength tests. This handicap is best illustrated by Fig. 2.4. One can readily note the very gross approximation one has to resort to in such an analysis[1] .

Typically, only few cores are drilled and tested during the life of the dam. Hence, mapping deterioration over the dam is at best approximate. Furthermore, the idiosyncrasies of the AAR

[1] Though an idealization, these curves are based on an actual study espousing this method.

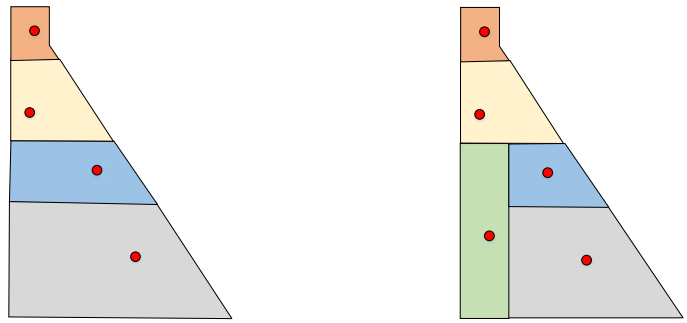

(a) Time t_1 (b) Time t_2

Figure 2.4: Mapping of recovered core test results (E, f_c, f_t) measurement into finite element mesh

(Saouma, V.E., 2014) are not captured.

This approach has been primarily used by consulting engineers.

2.1.1.2 Failure Criterion

Typically, the failure criterion is a post-processing of an otherwise linear elastic analysis (with possible exception for the contact elements). Those would include:

(1) Uniaxial compression failure criterion

(2) Uniaxial tension failure criterion

(3) Triaxial failure criterion

Also, a final '*concrete cracking analysis* may be performed using the so-called *smeared crack model*. This will inherently allow for internal stress redistribution and a corresponding increase in compressive stresses.

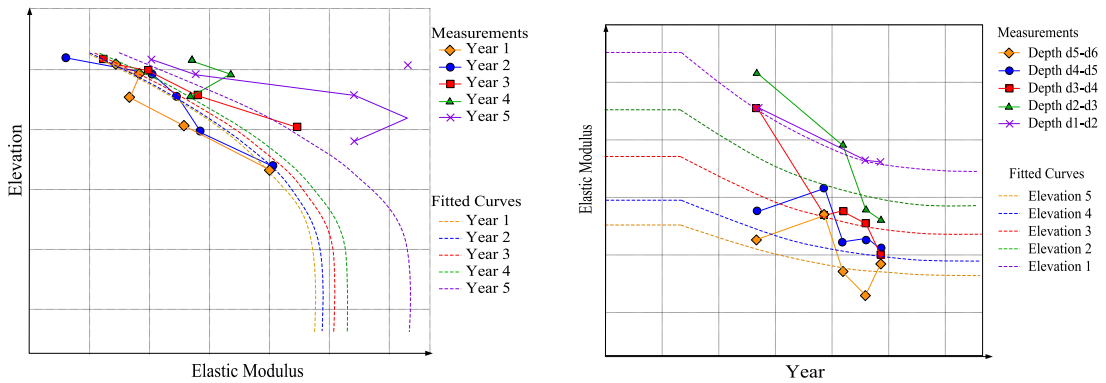

(a) Elastic modulus

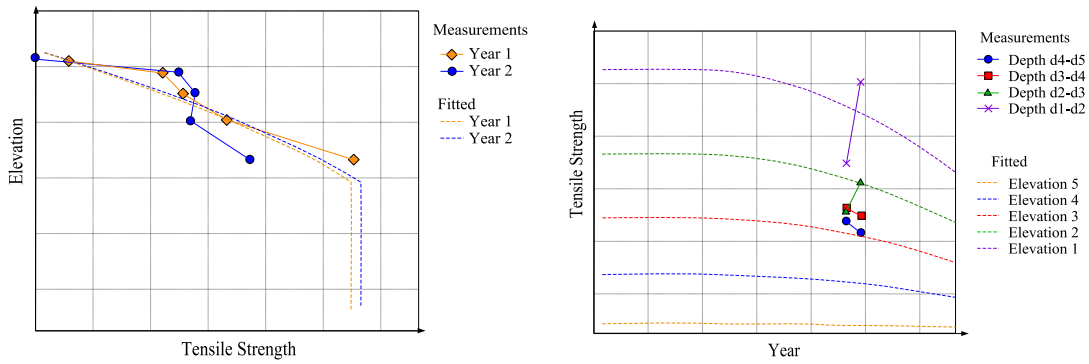

(b) Tensile strength

Figure 2.5: Spatial and temporal fitting for concrete mechanical properties based on limited cores and observations (courtesy Y. Gakuhari)

2.1.2 State of the Art

In this second approach, one that is rooted in the State of the Art, one would take into account apparent (or not so apparent) synergy between investigative tools, Fig. 2.6(a).

It should be noted that the approach about to be presented has been used by some researchers already, Saouma, Perotti, and Shimpo (2007a), Comi, Fedele, and Perego (2009b), Sellier et al. (2009b) and Huang and Spencer (2016) to name a few. The most recent, and comprehensive, study was recently presented by Joshi et al. (2021).

This approach consists of three major stages, each one will be described separately in the next section.

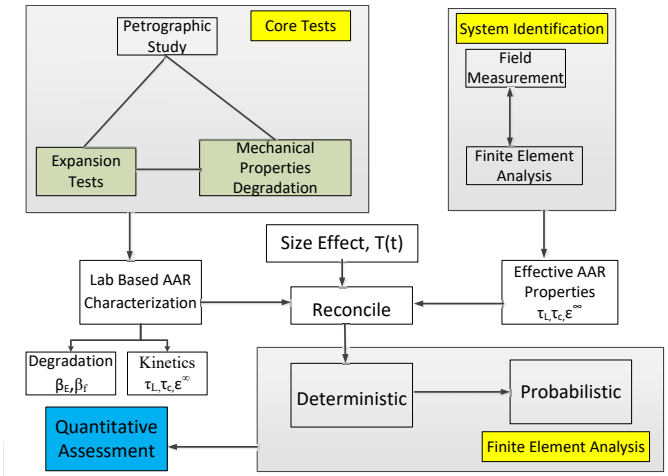

(a) Proposed

Figure 2.6: Assessment paradigms for AAR affected structures

2.1.2.1 AAR Modeling

It should be emphasized that, in this approach, any quantitative assessment will have to rely on a mathematical model for the concrete expansion. The model usually adopted is based on the one of Ulm et al. (2000) which is nearly universally accepted.

2.2 AAR model

This section describes the AAR model used in the thesis and is adapted from Saouma and Perotti (2006a) and Saouma (2013).

2.2.1 Premises

Two different aspects of mathematical modeling of AAR in concrete may be distinguished: 1) the kinetics of the chemical reactions and diffusion processes involved and 2) the mechanics of fracture that affects volume expansion and causes loss of strength, with possible disintegration of the material (Bažant, Zi, and Meyer, 2000). The proposed model (Saouma and Perotti, 2006a) (Saouma, 2013) is driven by the following considerations:

(1) AAR is a volumetric expansion, and as such can not be addressed individually along a

principal direction without due regard to what may occur along the other two orthogonal ones.

(2) The kinetics component is taken from the work of Larive (1998) and Ulm et al. (2000).

(3) AAR is sufficiently influenced by temperature to account for its temporal variation in an analysis.

(4) AAR expansion is constrained by compression and is redirected in other less constrained principal directions. This will be accomplished by assigning "weights" to each of the three principal directions.

(5) Relatively high compressive or tensile stresses inhibit AAR expansion due to the formation of micro or macro cracks which absorb the expanding gel.

(6) High compressive hydrostatic stresses slow down the reaction.

(7) Triaxial compressive state of stress reduces but does not eliminate expansion.

(8) Accompanying AAR expansion is a reduction in tensile strength and elastic modulus.

2.2.2 Kinetics

One of the most extensive and rigorous AAR investigations has been conducted by Larive (1998), who tested more than 600 specimens, Figure 2.7(a), with various mixes, ambient and mechanical conditions, and proposed a numerical model that governs concrete expansion. This thermodynamically-based, semi-analytical model was then calibrated using laboratory results in order to determine two key parameters: the latency time and characteristic times shown in Figure 2.7(b) for the normalized expansion.

$$\xi(t,T) = \frac{1 - e^{-\frac{t}{\tau_c(T)}}}{1 + e^{-\frac{(t-\tau_l(T))}{\tau_c(T)}}} \tag{2.2}$$

or in rate form

$$\dot{\xi}(t,T) = \frac{e^{t/\tau_c}\left(e^{\frac{\tau_l}{\tau_c}} + 1\right)}{\tau_c\left(e^{t/\tau_c} + e^{\frac{\tau_l}{\tau_c}}\right)^2} \tag{2.3}$$

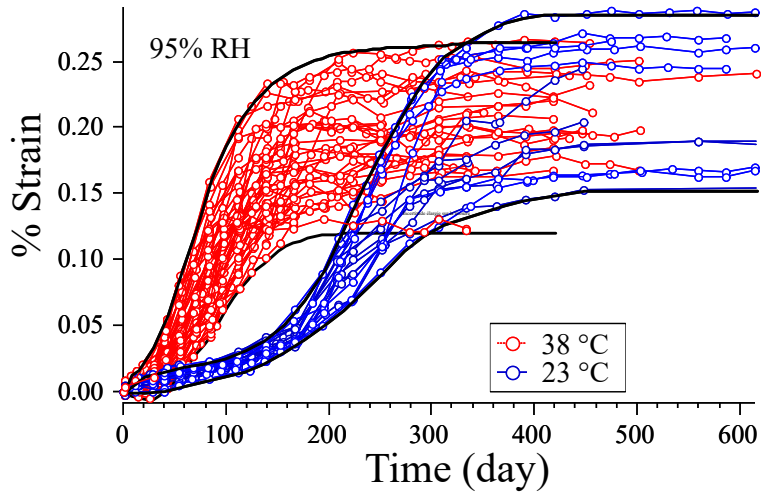

(a) Bracket of experimentally measured expansion at two different temperatures (Larive, 1998) (Courtesy of S. Multon)

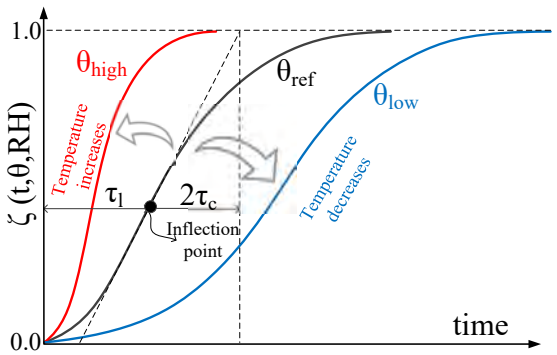

(b) Normalized Expansion Curve ($\xi(t) = \epsilon^{AAR}_{F,Vol}(t)/\epsilon(\infty)$)

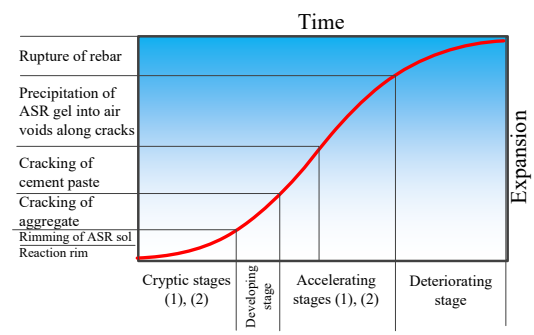

(c) Physical deterioration associated with AAR (Hariri-Ardebili, Saouma, and Merz, 2018)

Figure 2.7: ASR expansion curve

where T is the temperature τ_l and τ_c are the latency and characteristic times, calibrated at T_0. The first corresponds to the inflection point while the second is defined relative to the intersection of the tangent at τ_L with the asymptotic unit value of ξ. Like all chemical reactions, AAR is subject to Arrhenius Law (Arrhenius, 1889), which relates the dependence of the rate constant, k, of a chemical reaction on absolute temperature (T expressed in Kelvin, $TK = 273 + T^oC$) and activation energy, E_a.

$$k = Ae^{-\frac{E_a}{RT}} \tag{2.4}$$

Substituting k with τ_L and τ_C, Ulm et al. (2000) has shown that these values at temperature T can be expressed in terms of the corresponding values at temperature T_0 through:

$$\begin{aligned} \tau_l(T) &= \tau_l(T_0)\exp\left[U_l\left(\frac{1}{T}-\frac{1}{T_0}\right)\right] \\ \tau_c(T) &= \tau_c(T_0)\exp\left[U_c\left(\frac{1}{T}-\frac{1}{T_0}\right)\right] \end{aligned} \tag{2.5}$$

where U_l and U_c are the activation energies required to trigger the reaction for latency and characteristic times, respectively. Activation energies can be easily determined by rewriting Eq. 2.5 in its non-exponential form:

$$\ln k = \ln\left(Ae^{-\frac{E_a}{RT}}\right) = \ln A - \frac{E_a}{RT} \tag{2.6}$$

which is the equation of a straight line with slope $-E_a/RT$ We can thus determine the activation energy from values of k observed at different temperatures by simply plotting k as a function of $1/T$.Activation energies for Eq. 2.5 were determined to be:

$$\begin{aligned} U_l &= 9,400 \pm 500K \\ U_c &= 5,400 \pm 500K \end{aligned} \tag{2.7}$$

To the best of the authors' knowledge, the only other tests for these values were performed by Ben Haha (2006), who obtained values within 20% of Larive's, while dependency on the types of aggregates and alkali content of the cement has not been investigated. In the absence of other tests, these values can thus be reasonably considered as representative.

It should be emphasized that not only are the latency and characteristic times temperature-dependent, but considerable variability can also be present for the same concrete specimen chosen from among others. This point is illustrated in Table 2.2 for four specimens (ϕ13H24 kept at 38^oC) tested by Larive (1998).

Role of temperature on expansion is shown in Figure 2.8(b).

Parameters affecting the kinetics of the ASR can be obtained by accelerated expansion tests. Saouma (2020) has a compilation of numerous such tests, along with other investigative tools for a thorough diagnosis of ASR.

Table 2.2: Variation of $\epsilon(\infty)$, τ_c and τ_l for 4 specimens, (Larive, 1998)

specimen		501	475	287	19	Mean	NSD (%)
$\epsilon(\infty)$	%	0.198	0.195	0.168	0.230	0.198	12.8
τ_c	days	19.9	35.3	25.8	22.0	25.7	26.5
τ_l	days	102.1	83.9	94.8	64.8	86.4	18.8
τ_l/τ_c	-	5.1	2.4	3.7	2.9	3.4	0.7

2.2.3 Volumetric Expansion

The general (uncoupled) equation for the incremental free volumetric AAR strain is given by

$$\dot{\boldsymbol{\varepsilon}}_V^{AAR}(t) = \Gamma_t(f_t'|w_c, \sigma_I|COD_{max})\Gamma_c(\overline{\sigma}, f_c')g(h)\dot{\xi}(t,\theta)\ \varepsilon^{\infty}|_{\theta=\theta_0} \tag{2.8}$$

where COD is the crack opening displacement, $\xi(t,\theta)$ is a sigmoid curve expressing the volumetric expansion in time as a function of temperature and is given by Eq. 2.2, and ε^{∞} is the laboratory determined (or predicted) maximum free volumetric expansion at the reference temperature θ_0, Figure 2.7(b).

The retardation effect of the hydrostatic compressive stress manifests itself through τ_l. Hence, Eq. 2.5 is expanded as follows

$$\tau_l(\theta, \theta_0, I_\sigma, f_c') = f(I_\sigma, f_c')\tau_l(\theta_0)\exp\left[U_l\left(\frac{1}{\theta} - \frac{1}{\theta_0}\right)\right] \tag{2.9}$$

where

$$f(I_\sigma, f_c') = \begin{cases} 1 & \text{if } I_\sigma \geq 0 \\ 1 + \alpha\frac{I_\sigma}{3f_c'} & \text{if } I_\sigma < 0 \end{cases} \tag{2.10}$$

I_σ is the first invariant of the stress tensor and f_c' the compressive strength. Based on a careful analysis of (Multon, 2004), it was determined that $\alpha = 4/3$.

The stress dependency (through I_σ) of the kinetic parameter τ_l makes the model a truly coupled one between the chemical and mechanical phases.

Coupling with the thermal component is a loose one (hence a thermal analysis can be separately run); $0 < g(h) \leq 1$ is a reduction function to account for humidity given by

$$g(h) = h^m \tag{2.11}$$

where h is the relative humidity Capra and Bournazel, 1998. However, one can reasonably assume that (contrary to bridges) inside a dam, $g(h) = 1$ for all temperatures. Figure 2.8(a) highlights the role of RH.

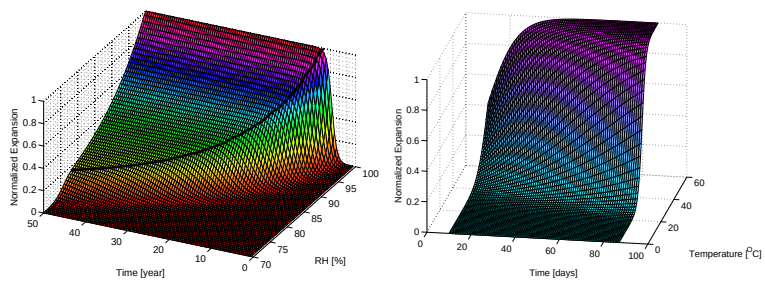

(a) Role of RH (b) Role of Temperature

Figure 2.8: Environmental factors affecting AAR expansion

$\Gamma_t(f'_t|w_c, \sigma_I|COD_{max})$ accounts for AAR reduction due to tensile cracking (in which case gel is absorbed by macro-cracks), Figure 2.9.

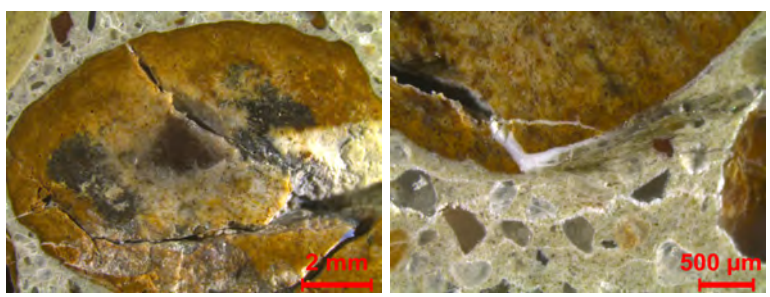

(a) Chert in CA causing AAR (b) Chert with gel close to crack

Figure 2.9: Stress induced cracks with potential gel absorption

A hyperbolic decay with a non-zero residual value is adopted, Figure 2.10:

$$\text{Smeared Crack} \begin{cases} \text{No} \quad \Gamma_t = \begin{cases} 1 & \text{if} \quad \sigma_I \leq \gamma_t f'_t \\ \Gamma_r + (1-\Gamma_r)\gamma_t \frac{f'_t}{\sigma_I} & \text{if} \quad \gamma_t f'_t < \sigma_I \end{cases} \\ \text{Yes} \quad \Gamma_t = \begin{cases} 1 & \text{if} \quad \text{COD}_{max} \leq \gamma_t w_c \\ \Gamma_r + (1-\Gamma_r)\gamma_t \frac{w_c}{\text{COD}_{max}} & \text{if} \quad \gamma_t w_c < \text{COD}_{max} \end{cases} \end{cases} \tag{2.12}$$

γ_t is the fraction of the tensile strength beyond which gel is absorbed by the crack; Γ_r is a residual AAR retention factor for AAR under tension. If an elastic model is used, then f'_t is the the tensile

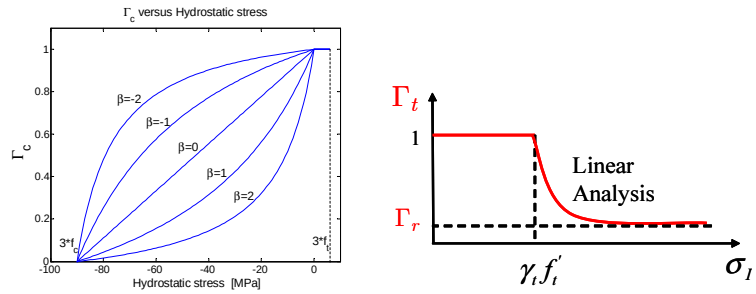

Figure 2.10: Graphical representation of Γ_c and Γ_t

strength and σ_I the maximum principal tensile stress. If a smeared crack model is adopted, then COD_{max} is the maximum crack opening displacement at the current Gauss point, and w_c the maximum crack opening displacement in the tensile softening curve Whitman et al., 1988.

Concrete pores being seldom interconnected and the gel viscosity relatively high, gel absorption by the pores is not explicitly accounted for. Furthermore, gel absorption by the pores is accounted for by the kinetic equation through the latency time which depends on concrete porosity. The higher the porosity, the larger the latency time.

Γ_c in turn accounts for the reduction in AAR volumetric expansion under compressive stresses (in which case gel is absorbed by diffused micro-cracks) Multon, 2004:

$$\Gamma_c = \begin{cases} 1 & \text{if} \quad \overline{\sigma} \leq 0. \quad \text{Tension} \\ 1 - \frac{e^{\beta}\overline{\sigma}}{1+(e^{\beta}-1.)\overline{\sigma}} & \text{if} \quad \overline{\sigma} > 0. \quad \text{Compression} \end{cases} \tag{2.13}$$

$$\overline{\sigma} = \frac{\sigma_I + \sigma_{II} + \sigma_{III}}{3f'_c} \tag{2.14}$$

This expression will also reduce expansion under uniaxial or biaxial confinement, Figure 2.10; these conditions are more directly accounted for below through the assignment of weights.

2.2.4 AAR Strain Redistribution

The third major premise of the model is that the volumetric AAR strain must be redistributed to the three principal directions according to their relative propensity for expansion on the basis of a weight which is a function of the respective stresses.

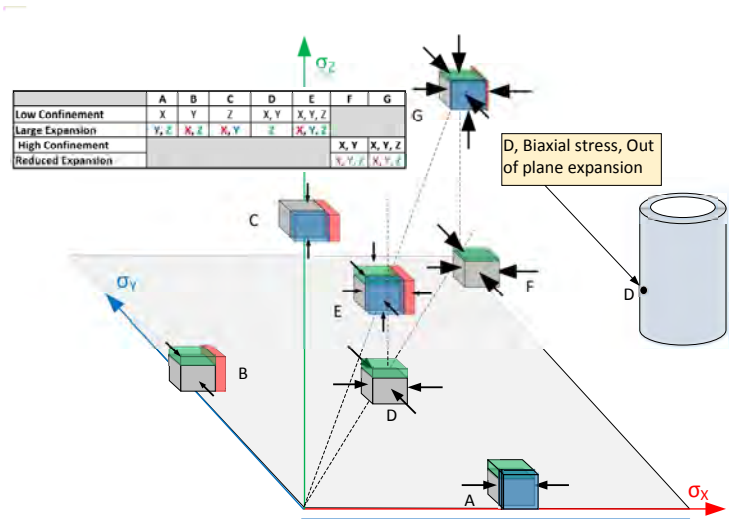

	A	B	C	D	E	F	G
Low Confinement	X	Y	Z	X, Y	X, Y, Z		
Large Expansion	Y, Z	X, Z	X, Y	Z	X, Y, Z		
High Confinement						X, Y	X, Y, Z
Reduced Expansion						X, Y, Z	X, Y, Z

Figure 2.11: Effect of confinement on AAR strain redistribution

The determination of the weight is relatively straightforward for triaxial AAR expansion under uniaxial confinement (for which some experimental data is available), but it is more problematic for biaxially or triaxially confined concrete. Given a principal stress vector defined by $\sigma_k, \sigma_l, \sigma_m$, we need to assign a weight to each of those three principal directions. These weights will control the AAR volumetric expansion distribution. For instance, with reference to Figure 2.12, we consider three scenarios.

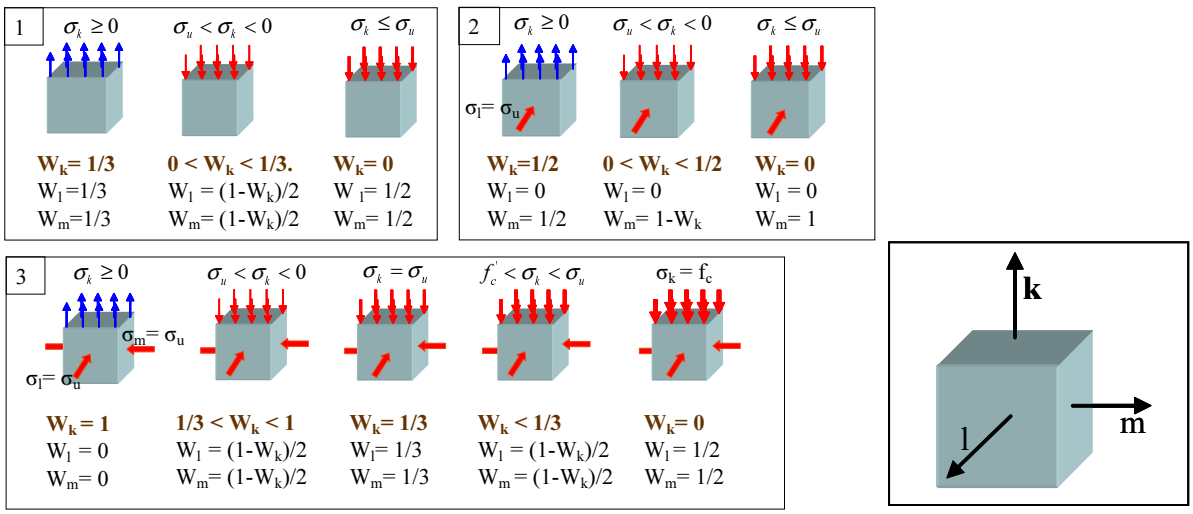

Figure 2.12: Weight of volumetric aar redistribution in selected cases

Uniaxial state of stress, where we distinguish the following three cases:

(1) In the first case, we have uniaxial tension, and hence, the volumetric AAR strain is equally redistributed in all three directions.

(2) Under a compressive stress greater than the limiting one (σ_u), the weight in the corresponding (k) direction should be less than one third. The remaining AAR has to be equally redistributed in the other two directions.

(3) If the compressive stress is lower than σ_u, than AAR expansion in the corresponding direction is prevented (weight equal zero), and thus the other two weights must be equal to one half.

Biaxial state of stress in which we have a compressive stress equal to σ_u in one of the three

principal directions. In this case, the corresponding weight will always be equal to zero. As to the possible three combinations:

(1) Tension in one direction, equal weights of one half.

(2) Compression greater than σ_u in one direction, then the corresponding weight must be less than one half, and the remaining weight is assigned to the third direction.

(3) Compression less than σ_u, then the corresponding weight is again zero, and a unit weight is assigned to the third direction.

Triaxial state of stress in which we have σ_u acting on two of the three principle directions. We identify the following five cases:

(1) Tension along direction k, then all the expansion is along k.

(2) Compressive stress greater than σ_u, then we have a triaxial state of compressive stress, and the corresponding weight will be between one and one third. The remaining complement of the weight is equally distributed in the other two directions.

(3) Compression equal to σ_u, hence we have a perfect triaxial state of compressive stress. In this case we have equal weights of one third. It should be noted that the overall expansion is reduced through Γ_c.

(4) Compression less than σ_u but greater than the compressive strength. In this case, the weight along k should be less than one third, and the remaining equally distributed along the other two directions.

(5) Compression equal to the compressive strength. In this case, the corresponding weight is reduced to zero, and the other two weights are equal to one half each.

Based on the preceding discussion, we generalize this weight allocation scheme along direction k as follows

(1) Given σ_k, identify the quadrant encompassing σ_l and σ_m, Figure 2.13. Weight will be determined through a bilinear interpolation for those four neighboring nodes.

(2) Determine the weights of the neighboring nodes from Table 2.3 through proper linear interpolation of σ_k.

Table 2.3: Triaxial weights

Node			Weights		
No.	σ_l	σ_m	$\sigma_k \geq 0$	$\sigma_k = \sigma_u$	$\sigma_k = f'_c$
1	0.	0.	1/3	0.	0.
2	σ_u	0.	1/2	0.	0.
3	σ_u	σ_u	1.	1/3	0.
4	0.	σ_u	1/2	0.	0.
5	f'_c	0.	1/2	0.	0.
6	f'_c	σ_u	1.	1/2	0.
7	f'_c	f'_c	1.	1.	1/3
8	σ_u	f'_c	1.	1/2	0.
9	0.	f'_c	1/2	0.	0.
10	f'_t	f'_c	1/2	0.	0.
11	f'_t	σ_u	1/2	0.	0.
12	f'_t	0.	1/3	0.	0.
13	f'_t	f'_t	1/3	0.	0.
14	0.	f'_t	1/3	0.	0.
15	σ_u	f'_t	1/2	0.	0.
16	f'_c	f'_t	1/2	0.	0.

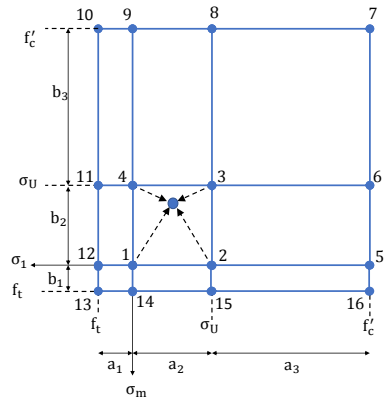

Figure 2.13: Weight regions

(3) Compute the weight from:

$$W_k(\sigma_k, \sigma_l, \sigma_m) = \sum_{i=1}^{4} N_i(\sigma_l, \sigma_m) W_i(\sigma_k) \tag{2.15}$$

where N_i is the usual two bilinear shape function used in finite element and is given by

$$\mathbf{N}(\sigma_l, \sigma_m) = \frac{1}{ab} \lfloor \ (a-\sigma_l)(b-\sigma_m) \quad \sigma_l(b-\sigma_m) \quad \sigma_l\sigma_m \quad (a-\sigma_l)\sigma_m \ \rfloor \tag{2.16}$$

$$\mathbf{W}(k) = \lfloor \ W_1(\sigma_k) \quad W_2(\sigma_k) \quad W_3(\sigma_k) \quad W_4(\sigma_k) \ \rfloor^t \tag{2.17}$$

$$a = (a_1|a_2|a_3) \qquad b = (b_1|b_2|b_3) \tag{2.18}$$

$$\sigma_l = (\sigma_l|f'_c - \sigma_l) \qquad \sigma_m = (\sigma_m|f'_c - \sigma_m) \tag{2.19}$$

The $i-j$ stress space is decomposed into nine distinct regions, Figure 2.13, where σ_u is the upper (signed) compressive stress below which no AAR expansion can occur along the corresponding direction (except in triaxially loaded cases). Hence, a and b are the dimensions of the quadrant inside which σ_i and σ_j reside.

Weights of the individual nodes are in turn interpolated according to the principal stress component in the third direction σ_k, Table 2.3. Those weights are for the most part based on the work of (Larive, 1998) and (Multon, 2004), but in some cases due to lack of sufficient experimental data, based on simple "engineering common sense."

A simple example for weight determination is shown here. Assuming that the principal stresses are given by $\lfloor \ \sigma_l \quad \sigma_m \quad \sigma_k \ \rfloor = \lfloor \ -5.0 \quad -8.0 \quad -5.0 \ \rfloor$ MPa, and that f_c, f'_t, and σ_u are

equal to -30.0, 2.0, and -10.0 MPa respectively, we seek to determine W_k. The stress tensor places us inside the quadrant defined by nodes 1-2-3-4 whose respective weights are equal to: $W_1 = \frac{1}{2}\left(\frac{1}{3}\right) = \frac{1}{6}$, $W_2 = \frac{1}{2}\left(\frac{1}{2}\right) = \frac{1}{4}$, $W_3 = \frac{1}{3} + \frac{1}{2}\left(1.0 - \frac{1}{3}\right) = \frac{2}{3}$, and $W_4 = \frac{1}{2}\left(\frac{1}{2}\right) = \frac{1}{4}$. Also, a and b are both equal to -10 MPa, and the "shape factors" will be $N_1 = \frac{1}{100}\left[(-10+5)(-10+8)\right] = \frac{1}{10}$, $N_2 = \frac{1}{100}\left[-5(-10+8)\right] = \frac{1}{10}$, $N_3 = \frac{1}{100}\left[(-5)(-8)\right] = \frac{4}{10}$, $N_4 = \frac{1}{100}\left[-8(-10+5)\right] = \frac{4}{10}$, and finally $W_k = \frac{1}{10} \times \frac{1}{6} + \frac{1}{10} \times \frac{1}{4} + \frac{4}{10} \times \frac{2}{3} + \frac{4}{10} \times \frac{1}{4} = 0.40833$.

Based on the earlier work of (Struble and Diamond, 1981) in which it was reported that no gel expansion can occur at pressures above 11 MPa, σ_u is taken as -10 MPa. This value was also confirmed by (Larive, 1998). f'_t and f'_c are the concrete tensile and compressive strengths respectively.

Individual strain is given by

$$\dot{\varepsilon}_i^{AAR} = W_i \dot{\varepsilon}_V^{AAR} \tag{2.20}$$

The proposed model will indeed result in an anisotropic AAR expansion. While not explicitly expressed in tensorial form, the anisotropy stems from the different weights assigned to each of the three principal directions.

2.2.5 Degradation

Deterioration being time dependent, the following time dependent non-linear model is considered, Figure 2.14.

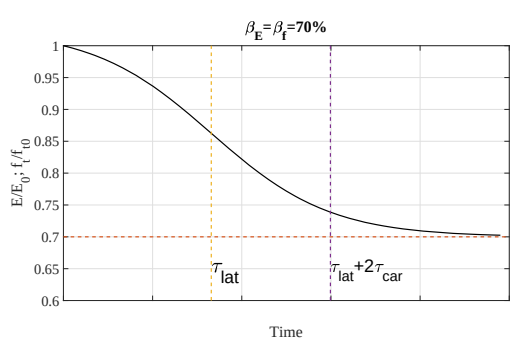

Figure 2.14: Degradation of E and f'_t

$$E(t,\theta) = E_0\left[1-(1-\beta_E)\,\xi(t,\theta)\right] \tag{2.21}$$

$$f'_t(t,\theta) = f'_{t,0}\left[1-(1-\beta_f)\,\xi(t,\theta)\right] \tag{2.22}$$

where E_0 and $f'_{t,0}$ are the original elastic modulus and tensile strength; β_E and β_f are the corresponding residual fractional values when ε_{AAR} tends to $\varepsilon^{\infty}_{AAR}$.

2.2.6 Interaction with Creep

Figure 2.15 shows the inetraction of AAR with creep. As seen in this figure the creep deformation is obliterated by AAR expansion. However, in the current study the effect of creep will not be considered as the AAR in the case study dam truely manifested itself about 40 years after the dam construction.

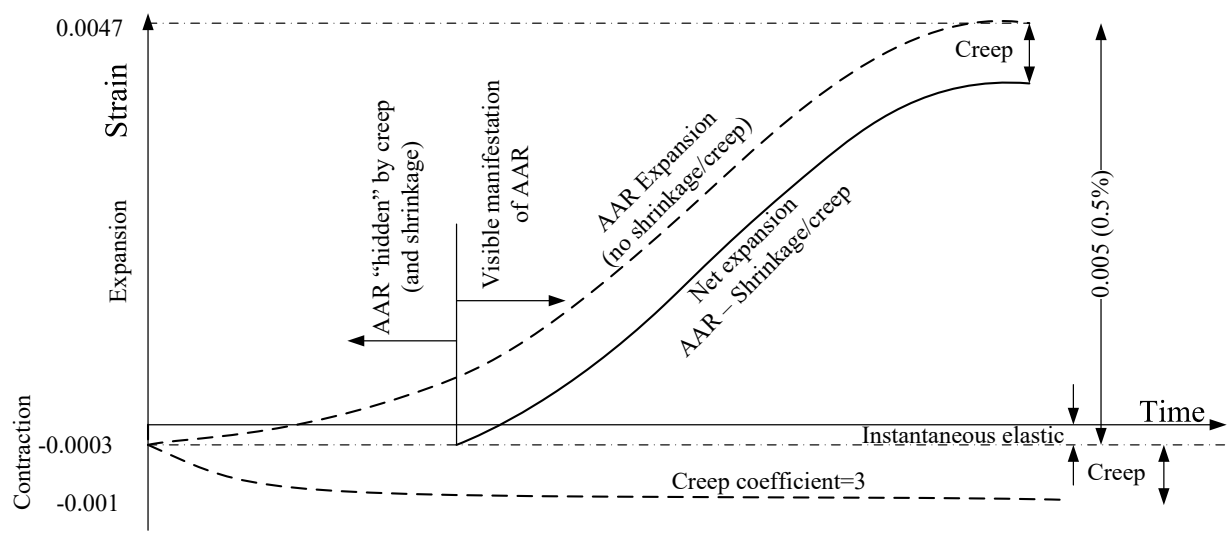

Figure 2.15: Effect of creep (Saouma and Hariri-Ardebili, 2021c)

Chapter 3

Methodology for Thermal Analysis with Solar Radiation

Abstract

This chapter discusses the fundamentals and formulations of solar radiation. More specifically, this chapter contains the methodology on how to calculate the amount of solar radiation on a surface of interest and consequently the amount of temperature increase due to it.

3.1 Preliminaries

3.1.1 Units

Proper attention must be given to the units. In this context, we distinguish between thermal and stress analyses.

For thermal analyses, units are shown in Table 3.1. The time unit is the so-called Analysis tTime Unit(ATU) which is equivalent to one month. In such an analysis, there are no applied forces

For stress analysis, the units are defined in Table 3.2. Note that in the incremental stress analysis, each increment will be one ATU.

3.1.2 Conversions for selected quantities

One has to be particularly attentive to the conversion facotrs for the variables, especially in the thermal analysis. Here are some key conversions.

Table 3.1: Thermal Analysis

Quantity	Dimensions		Units	
	Technical	Base Units	Definition	Used in this report
Length	L	L	m	
Time	t	t	s	
Mass	M	M	Kg	
Temperature	T	T	K	
Mass Density (ρ)	$\mathrm{M.L^{-3}}$	$\mathrm{M.L^{-3}}$		$\mathrm{Kg.m^{-3}}$
Force (F)	F	$\mathrm{M.L.t^{-2}}$	N	$\mathrm{Kg.m.s^{-2}}$
Heat (Q)	F.L	$\mathrm{M.L^2.t^{-2}}$	J	$Kg.m^2.ATU^{-2}$
Power	$\mathrm{J.t^{-1}}$	$\mathrm{M.L^2.t^{-3}}$	W	$Kg.m^2.ATU^{-3}$
Specific heat (c_p)	$\mathrm{J}.T^{-1}.M^{-1}$	$\mathrm{L^2.t^{-2}}.T^{-1}$	$\mathrm{J.M^{-1}}.T^{-1}$	$\mathrm{J.Kg^{-1}.K^{-1}}$
Thermal Conductivity (k)	$\mathrm{W.L^{-1}}.T^{-1}$	$\mathrm{M.L.t^{-3}}.T^{-1}$	$\mathrm{J.t^{-1}.L^{-1}}.T^{-1}$	$\mathrm{J.ATU^{-1}.m^{-1}.\ K^{-1}}$
Thermal diffusivity (μ)	$\mathrm{M^2.T^{-1}}$	$\mathrm{L^2.t^{-1}}$	$\mathrm{L^2.t^{-1}}$	

Thermal Conductivity; SI Converting to month:

$$\begin{aligned}[\mathrm{J\,m^{-1}\,K^{-1}\,mo^{-1}}] &= \frac{\mathrm{J}}{\mathrm{sW}}3,600\frac{\mathrm{s}}{\mathrm{h}}24\frac{\mathrm{h}}{\mathrm{d}}30.438\frac{\mathrm{d}}{\mathrm{mo}}[\mathrm{W\,m^{-1}\,K^{-1}}] \\ &= (2,629,843)[\mathrm{W\,m^{-1}\,K^{-1}}] \end{aligned} \tag{3.1}$$

Thermal Conductivity; Imperial from Engineering Toolbox:

$$[\mathrm{J\,m^{-1}\,K^{-1}\,h^{-1}}] = 6,230[\mathrm{BTU\,ft^{-1}\,h^{-1}\,{}^\circ F^{-1}}] \tag{3.2}$$

$$\begin{aligned}[\mathrm{J\,m^{-1}\,K^{-1}\,mo^{-1}}] &= 6,230[\mathrm{BTU\,ft^{-1}\,h^{-1}\,{}^\circ F^{-1}}]24\frac{\mathrm{h}}{\mathrm{d}}30.438\frac{\mathrm{d}}{\mathrm{mo}} \\ &= 4,551,090[\mathrm{BTU\,ft^{-1}\,h^{-1}\,{}^\circ F^{-1}}] \end{aligned} \tag{3.3}$$

Specific Heat; Imperial From this table:

$$[\mathrm{BTU\,lb^{-1}\,{}^\circ F^{-1}}] = 2.3885^{-4}[\mathrm{J\,kg^{-1}\,K^{-1}}] \tag{3.4}$$

Film Coefficient; SI Converting to month

$$\begin{aligned}[\mathrm{W\,m^{-2}\,K^{-1}}] &= \frac{\mathrm{sW}}{\mathrm{J}}\frac{\mathrm{h}}{3600\mathrm{s}}\frac{\mathrm{d}}{24\mathrm{h}}\frac{\mathrm{mo}}{30.438\mathrm{d}}[\mathrm{J\,m^{-2}\,K^{-1}\,mo^{-1}}] \\ &= (3.8025e-7)[\mathrm{J\,m^{-2}\,K^{-1}\,mo^{-1}}] \end{aligned} \tag{3.5}$$

Table 3.2: Stress Analysis

Quantity	Dimensions Technical	Dimensions Base Units	Units Used in this report
Length	L	L	m
Time	t	t	s
Mass	M	M	Kg
Temperature	T	t	K
Force (F)	F	$\mathrm{M.L.t^{-2}}$	MN
Pressure (p)	$\mathrm{F.L^{-2}}$	$\mathrm{M.L^{-3}.t^{-2}}$	MPa

Film Coefficient; Imperial From here

$$
\begin{aligned}
[\mathrm{W\,m^{-2}\,K^{-1}}] &= 0.1761[\mathrm{BTU\,ft^{-2}\,h^{-1}\,{}^{\circ}F^{-1}}]24\frac{\mathrm{h}}{\mathrm{d}}30.438\frac{\mathrm{d}}{\mathrm{mo}} \\
&= 128.6432[\mathrm{BTU\,ft^{-2}\,mo^{-1}\,{}^{\circ}F^{-1}}] \qquad (3.6)
\end{aligned}
$$

From Equation 3.5 and 3.6 :

$$
\begin{aligned}
[\mathrm{J\,m^{-2}\,K^{-1}\,mo^{-1}}] &= \frac{128.6432}{3.8025e-7}[\mathrm{BTU\,ft^{-2}\,mo^{-1}\,{}^{\circ}F^{-1}}] \\
&= (3.3831e+08)[\mathrm{BTU\,ft^{-2}\,mo^{-1}\,{}^{\circ}F^{-1}}] \qquad (3.7)
\end{aligned}
$$

3.1.3 Concrete Thermal Properties

Concrete thermal properties are taken from (Hatch, 2015)

Mass density $\rho = 155.3$ [lb/ft^3]

$$
\begin{aligned}
\rho &= 155.3\mathrm{lb/ft^3} \\
&= (155.3)(16.02) \\
&= 2487\mathrm{kg/m^3} \qquad (3.8)
\end{aligned}
$$

Specific heat $c_p = 0.2$ [$\mathrm{BTU\,lb^{-1}\,{}^{\circ}F^{-1}}$]

Table 3.3: Concrete thermal properties;
* From (Hatch, 2015)
** From (Malm, Hassanzadeh, and Hellgren, 2017)

Quantity	Symbol	Hatch*	Icold**	units
Mass Density	ρ	2,487	2,300	$\mathrm{kg\,m^{-3}}$
Specific Heat	c_p	837	900	$\mathrm{J\,kg^{-1}\,K^{-1}}$
Conductivity	k	3.44 9,057,000	2	$\mathrm{W\,m^{-1}\,K^{-1}}$ $\mathrm{J\,m^{-1}\,K^{-1}\,mo^{-1}}$
Thermal Diffusivity	μ	0.143 4.35	?? $\mathrm{m^2\,mo^{-1}}$	$\mathrm{m^2\,d^{-1}}$

Using equation 3.4 c_p is converted to $[\mathrm{J\,kg^{-1}\,K^{-1}}]$ units:

$$\begin{aligned} c_p &= 0.2\mathrm{BTU/lb/^\circ F} \\ &= \frac{(0.2)}{(2.3885e-4)} \\ &= 837\mathrm{J/kg/K} \end{aligned} \tag{3.9}$$

Thermal Conductivity $k = 1.99\ [\mathrm{BTU\,ft^{-1}\,h^{-1}\,^\circ F^{-1}}]$

From Equation 3.3.

$$\begin{aligned} k &= 1.99\mathrm{BTU/ft/h/^\circ F} \\ &= (1.99)(4,551,090) \\ &= 9,056,669\mathrm{J/m/K/mo} \end{aligned} \tag{3.10}$$

Also, from Equation 3.1 we can compute:

$$\begin{aligned} k &= 9,056,669\mathrm{J/m/K/mo} \\ &= \frac{(9,056,669)}{(2,629,843)} \\ &= 3.44\mathrm{W/m/K} \end{aligned} \tag{3.11}$$

For the purpose of validating the material properties of the concrete used in this study the values are compared to those taken from (Malm, Hassanzadeh, and Hellgren, 2017) which are as follows and they have the same order of magnitude with those used herein.

3.2 Solar Radiation

Solar Radiation refers to the power (J/m^2) received by the sun in the form of electromagnetic radiation. It is a function of the orientation of the surface with respect to the sun. An exact mathematical model for solar radiation is quite complex, and an approximation by Kreider and Rabl (1994) offered the following linear simplification

$$q_s = \alpha\, I(s,t) \tag{3.12}$$

where I is total solar radiation or global radiation on a surface s at time t and α is the absorptivity of the surface which is defined by the fraction of I absorbed by the surface structure. For concrete, $\alpha = 0.65$.

The global radiation ,I_{glo}, is the sum of the diffuse radiation, I_{diff} (i.e. solar radiation received its direction has been changed by scattering by the atmosphere), and direct radiation, I_{dir} (solar radiation intercepted by a surface with negligible direction change and scattering in the atmosphere). Those radiations are naturally site specifics and can be downloaded from various Typical Meteorological Years (TMY) sites such as (DOE EnergyPlus^{TM} 9.3.0, 2020).

3.2.1 Preliminary Definitions

3.2.1.1 Solar Time

t_{sol} is the time based on apparent angular motion of the sun across the sky with solar noon being the time the sun crosses the meridian of the observer. It is given by

$$t_{sol} = t_{std} + \frac{L_{std} - L_{loc}}{15} + \frac{ET}{60} \tag{3.13}$$

where

L_{std} = longitude of the standard time zone ($degrees$). For example, in the United States, the longitudes of the standard time zones are 75^oW for Eastern, 90^oW for Central, 105^oW for Mountain, and 120^oW for Pacific.

L_{loc} = site longitude (*degrees*) Whereas exact, this equation does not account for the eccentricity of the Earth's orbit and the Earth's axial tilt. Hence, the equation is adjusted by an approximation empirical term ET defined by the following:

$$\begin{aligned} ET &= 9.87 \sin 2\left(360^o \times \frac{n-81}{364}\right) - 7.53 \cos\left(360^o \times \frac{n-81}{364}\right) \\ &\quad -1.5 \sin\left(360^o \times \frac{n-81}{364}\right) \end{aligned} \tag{3.14}$$

and n is day of the year (i.e. $n = 1$ for Jan 1).

3.2.1.2 Solar Angles

δ is the angular position of the sun at solar noon (when the sun is in the local meridian) with respect to the plane of the equator, north positive, and $-23.45° \leq \delta \leq 23.45°$, Figure 3.1. It can be expressed by

$$\sin \delta = -\sin 23.45^o \cos \frac{360^o \times (n+10)}{365.25} \tag{3.15}$$

where n is defined as mentioned before.

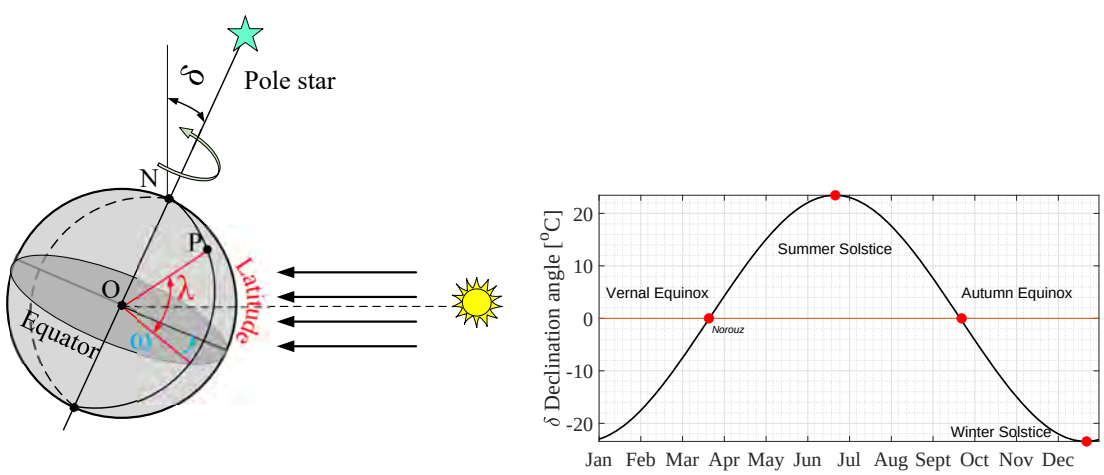

(a) Declination angle (b) Seasonal variation of δ

Figure 3.1: Solar declination

Note that the heat flux, q_s, can only be applied during the hours between sunrise and sunset.

The sunrise (t_{sr}) and sunset times (t_{ss}) can be determined from the following:

$$t_{sr} = 12 - \frac{1}{15}\cos^{-1}(-\tan\lambda\tan\delta) \tag{3.16}$$

$$t_{ss} = 12 + \frac{1}{15}\cos^{-1}(-\tan\lambda\tan\delta) \tag{3.17}$$

in which λ is latitude of the location and δ is solar declination.

3.2.1.3 Zenith Angle

θ_s is the angle between the zenith and the centre of the Sun's disc. as shown in Figure 3.2 is given by

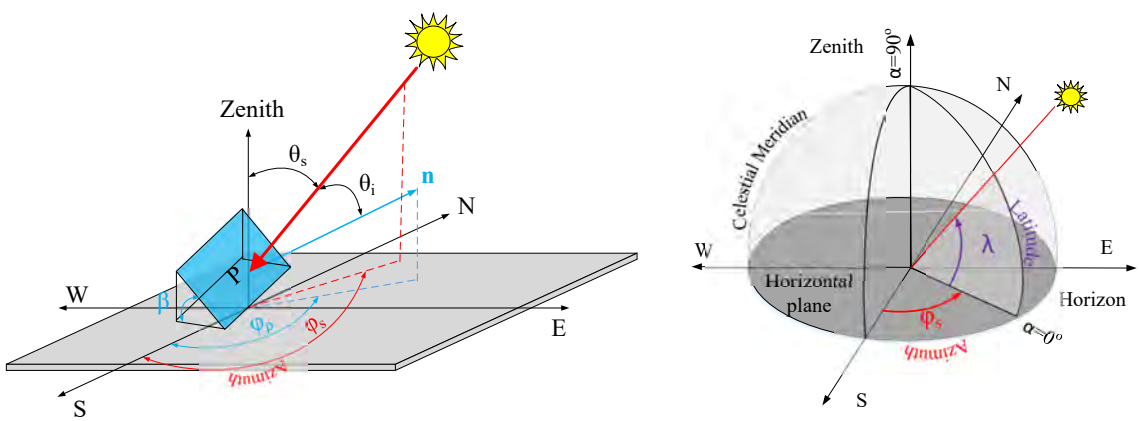

Figure 3.2: Solar characteristic angles

$$\cos\theta_s = \cos\lambda\cos\delta\cos\omega + \sin\lambda\sin\delta \tag{3.18}$$

where λ is the latitude of the location (north is positive), δ the solar declination, and ω is the angular displacement of the sun east or west of the local meridian due to rotation of the earth on its axis at 14° per hour; morning negative, afternoon positive; it is given by

$$\omega = \frac{t_{sol} - 12}{24} \times 360^o \tag{3.19}$$

where t_{sol} is the solar time in $hours$.

3.2.1.4 Incidence Angle

θ_i is the angle between the normal of the surface at point P and the line from point P to the sun, Figure 3.2 given by

$$\cos\theta_i = \cos\theta_s \cos\beta + \sin\theta_s \sin\beta \cos(\phi_s - \phi_p) \tag{3.20}$$

In this equation β is the angle between the surface and horizontal direction.

3.2.1.5 Plane azimuth angle

ϕ_p is the angle, measured on the surface, between the south and the projection of the plane normal $\mathbf{n}$, Figure 3.2.

3.2.1.6 Sun azimuth angle

ϕ_s is the angle of the Sun's position. This horizontal coordinate defines the Sun's relative direction along the local horizon whereas the solar zenith angle (or its complementary angle solar elevation) defines the Sun's apparent altitude, Figure 3.2. It is defined by

$$\sin\phi_s = \frac{\cos\delta \sin\omega}{\sin\theta_s} \tag{3.21}$$

3.2.2 Solar Flux

3.2.2.1 Horizontal Surfaces

The total radiation on the horizontal surface or, in other words, global horizontal radiation is given by

$$I_{glo,hor} = I_{dir} \cos\theta_s + I_{diff} \tag{3.22}$$

where θ_s is the zenith angle of the sun.

Table 3.4: Reflectivity of selected surfaces (Kreider and Rabl, 1994)

Surface	Reflectivity ρ_g
Soils	0.75
Water	0.07
Concrete, new	0.35
Concrete, old	0.25
Earth roads	0.04
Grass, dry	0.20
Grass, green	0.26

3.2.2.2 Inclined Surfaces

Calculation of the total radiation on an inclined surface is far more complex, and is given by

$$I_{global} = I_{dir} \cos\theta_i + I_{diff} \frac{(1 + cos\beta)}{2} + I_{glo,hor} \rho_g \frac{(1 - cos\beta)}{2} \tag{3.23}$$

where θ_i is the incidence angle, Figure 3.2.

ρ_g = Reflectivity of the ground. The values of the reflectivity of some selected surfaces can be tabulated in Table 3.4

3.2.3 Discussion

3.2.3.1 Incidence angle

The role of the incidence angle in attenuating I_{dir} is further clarified by Figure 3.3 which shows the results of average monthly solar radiation calculations of a plane facing various directions in the space ($0^o < \phi_p < 270^o$). Eq. 3.23 suggests that the solar radiation intensity depends on cosine of the incidence angle ($cos(\theta_i)$) and therefore depends on the direction of the sun and also the surface. Figure 3.3(a) is an illustration of the physical meaning of this equation. Based on the assumption behind the equation, the surfaces facing South, West, North, and East would have $\phi_p = 0^o,\ 90^o\ 180^o$ and 270° respectively.

Figure 3.3(b) shows that in February the azimuth angle of the sun (ϕ_s) is about -2°.

On the other hand, Figure 3.3(c) shows that $\cos(\theta_i)$ is maximum and therefore the direct

solar radiation is also maximum facing South and minimum facing East. For other directions, the direct flux would be zero. This is consistent with Figure 3.3(a).

3.2.3.2 Roles of various solar radiation forms

Finally, the preceding equations are best understood through Figure 3.4 associated with location latitude =42.1558°, longitude=-106.908° (site of a dam suffering from AAR), concrete reflectivity ρ_g =0.25, reflectivity α =0.65 in terms of ϕ_p and time. Solar flux are obtained from (DOE EnergyPlus^{TM} 9.3.0, 2020).

These plots call for the following observations:

(1) Direct flux is predominant, Figure 3.4(a), it is minimum at $\phi_p = 270$ (East) and maximum at $\phi_p = 0$ (South) where we have full southern exposure. The cutting (green) plane shows that in February the amount of direct radiation is dominant for southern exposure and diffuse radiation has the greatest participation in global radiation for other directions.

(2) Diffuse and global horizontal intensities are both very small compared to the direct (except for $\phi_p \sim 0$).

(3) Flux is very sensitive to ϕ_p.

(4) Global solar radiation in February is shown for different exposures in Figure 3.4(b); as expected it is maximum for $\phi_p = 0$.

(5) Yearly variation of I_{glo} is shown in Figure 3.4(c). As the azimuth angle of the sun (ϕ_s) varies from $\sim -2^o$ to $\sim 7^o$ (measured from South Figure 3.3(b)), it is expected that surfaces facing South experience higher direct solar radiation; in addition, based on our comments regarding Figure 3.4(a), direct radiation has higher participation in the total solar radiation amount and thus, it is expected that the lower incidence angle θ_i (higher direct radiation) results in generally higher global solar radiation intake. Figure 3.4(c) also shows higher global solar radiation values for South facing plane throughout the year compared to other directions.

(6) Throughout the year, solar zenith angle is out of phase (90°) with the incidence angle,

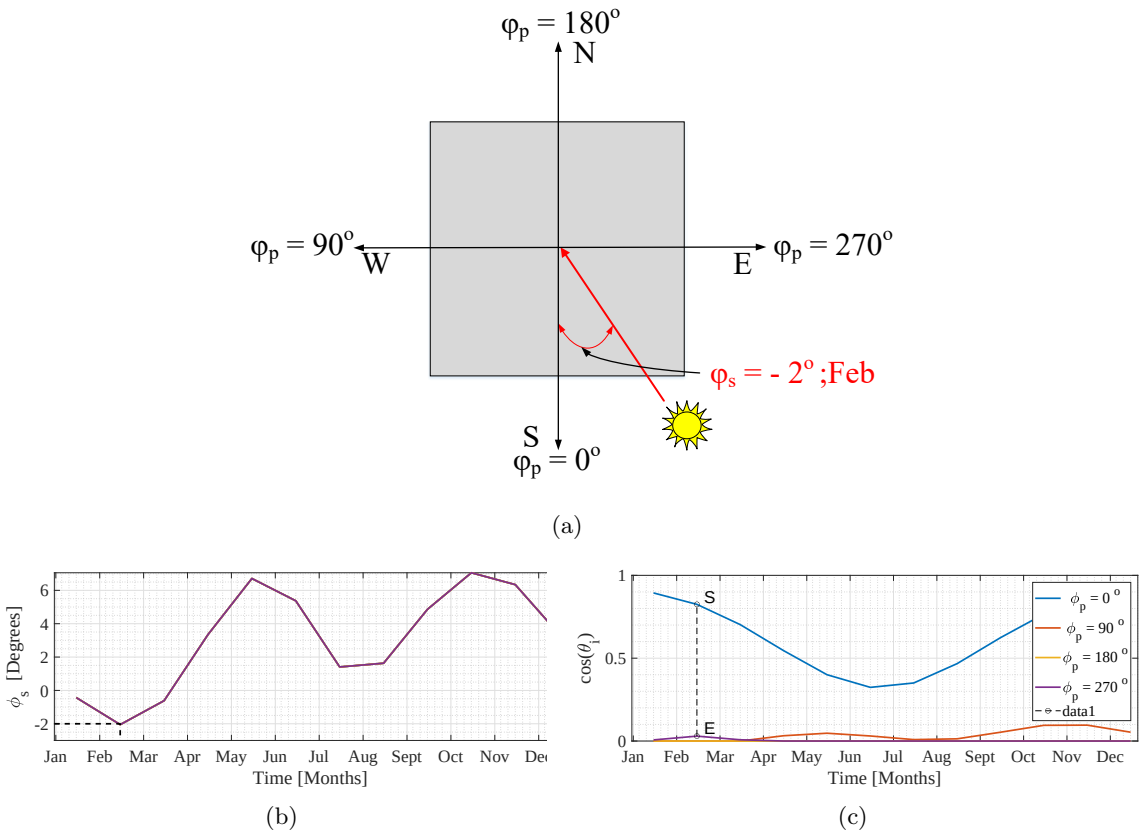

Figure 3.3: Seasonal impact on incidence angle for different plane orientations ϕ_p

Figure 3.4(d). Furthermore, the incidence angle (θ_i) is clearly smallest for South facing plane which explains why solar radiation is largest for southern exposure for the specified location.

It is worth mentioning that the amount of direct solar radiation ($I_{dir}cos(\theta_i)$) received by a surface of interest depends on various factors including the time of the year, the declination and orientation of the surface and the direction of the sun radiation. To illustrate, figure 3.5(a) shows the variation of the three important declination, zenith and incidence angles for a vertical surface facing south. As seen, the zenith angle(θ_s) trend is the reverse of the declination angle (δ) and reaches its minimum value in June. On the other hand, as the surface is vertical, the incidence angle(θ_i) is the complementary angle of the zenith angle and becomes maximum in July. In other words, The sun radiates nearly parallel to the vertical surface in July which is expected to result in receiving less amount of solar radiation in July. However, another important factor is the amount of available direct solar radiation(I_{dir}) itself obtained for the horizontal surface which is then multiplied by $cos(\theta_i)$ to account for the surface declination. Figure 3.5(b) shows the amount of I_{dir} and $I_{dir}cos(\theta_i)$ on the left axis versus the amount of θ_i and $cos(\theta_i)$ on the right axis. It is shown that although the θ_i is maximum in June, the final calculated direct solar radiation $I_{dir}cos(\theta_i)$, is maximum in August since I_{dir} is greater at this time.

3.2.4 Algorithms

3.2.4.1 Solar Flux

The algorithm to determine the solar flux on a surfce is shown in Figure 3.6. The following quantities are site specific, and are assumed to be known: I_{diff}, I_{dir}, ρ_g, λ, ϕ_p, n, t_{loc}, and t_{std}.

(1) Determine the equation of time (ET) using Eq. 3.14 and the solar declination angle (δ) from eq. 3.15

(2) Using Eq. 3.13 calculate the solar time (t_{sol}) and solar hour angle (ω) from Eq. 3.19

(3) Having the latitude of the location(λ) and using (δ) and (ω) from the previous steps, zenith

angle of the sun (θ_s) is then determined using eq. 3.18

(4) The azimuth angle of the sun (ϕ_s) can then be determined using Eq. 3.21

(5) Using values for ϕ_p, ϕ_s and θ_s from steps above, the incidence angle (θ_i) can then be calculated using equation Eq. 3.20 which can take values between 0 and 90 degrees.

(6) Finally Eq. 3.23 determines the solar radiation

3.2.4.2 Finite element determination of ϕ_p

In the thermal (finite element) analysis of a dam, one needs to determine ϕ_p for each element in order to determine the solar flux, Figure 3.7. It is assumed that the element is planar, and node numbering is counterclockwise looking from the outside. The procedure is as follows, Figure 3.8.

(1) Define two (non colinear) vectors along first and last edge: $\mathbf{V}_{12}$ and $\mathbf{V}_{14}$, Figure 3.7

(2) Take the cross product of those two vectors to define the normal

$$\mathbf{n}' = \mathbf{V}_{12} \times \mathbf{V}_{14} \tag{3.24}$$

(3) Determine the projection of $\mathbf{n}'$ into $\mathbf{n}$ on the horizontal plane ($\mathbf{n}'(x, y, z) \rightarrow \mathbf{n}(x, y)$.

(4) Determine ϕ_p

$$\phi_p = \cos^{-1} \frac{\mathbf{S} \cdot \mathbf{n}}{||\mathbf{n}||\ ||\mathbf{S}||} \tag{3.25}$$

where $\mathbf{S}$ is a normalized vector along the south direction.

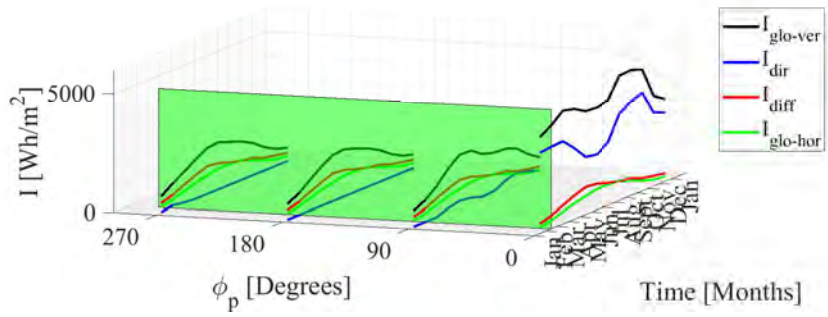

(a) Individual radiation in terms of month and ϕ_p

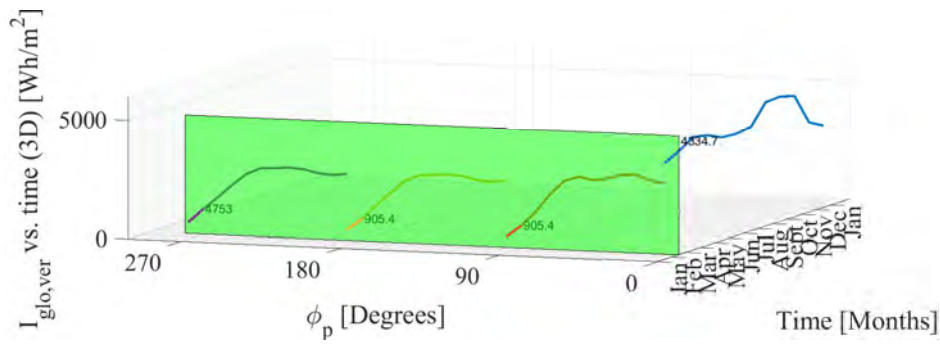

(b) Global solar radiation in February

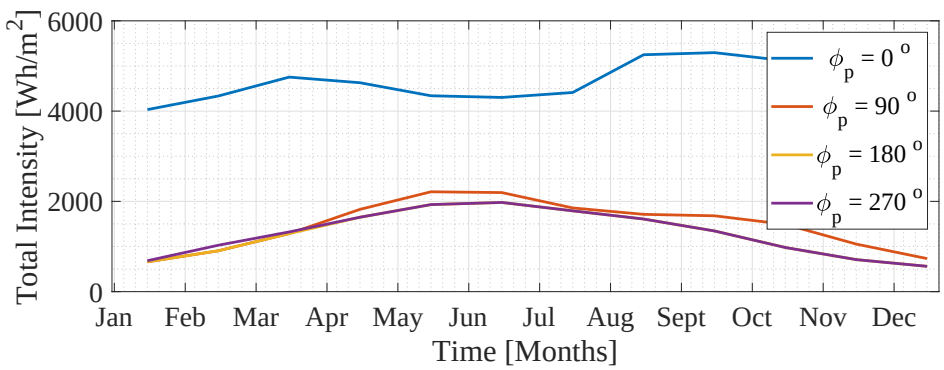

(c) Monthly total intensity

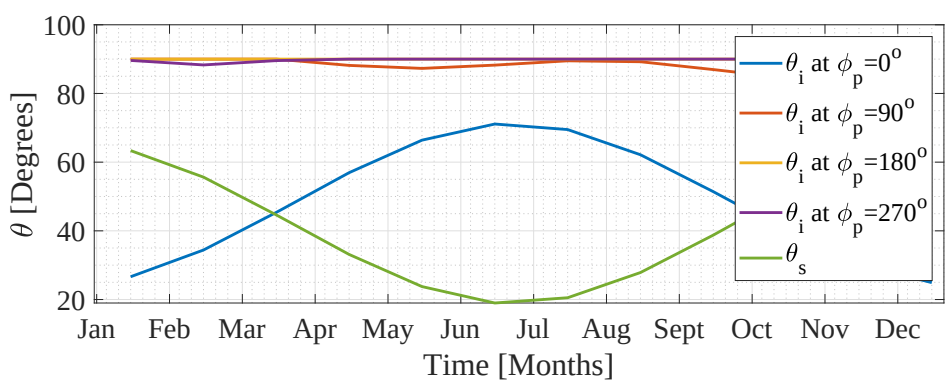

(d) Incidence and surface azimuth angles

Figure 3.4: Solar fluxes at latitude 42.1558° and longitude -106.908°

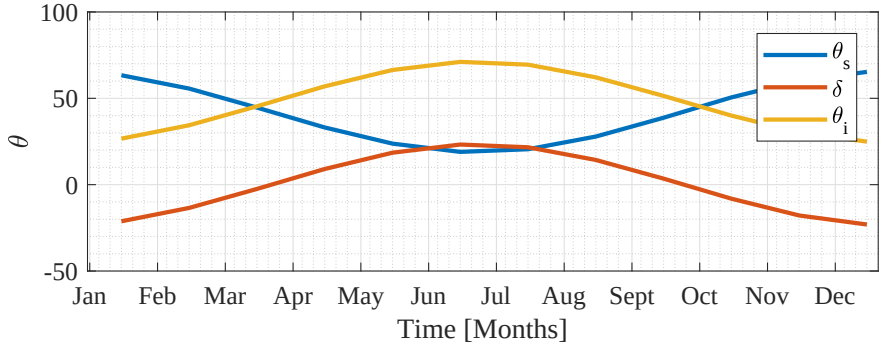

(a) Variation of zenith, declination and incidence angles throughout a year for a vertical surface

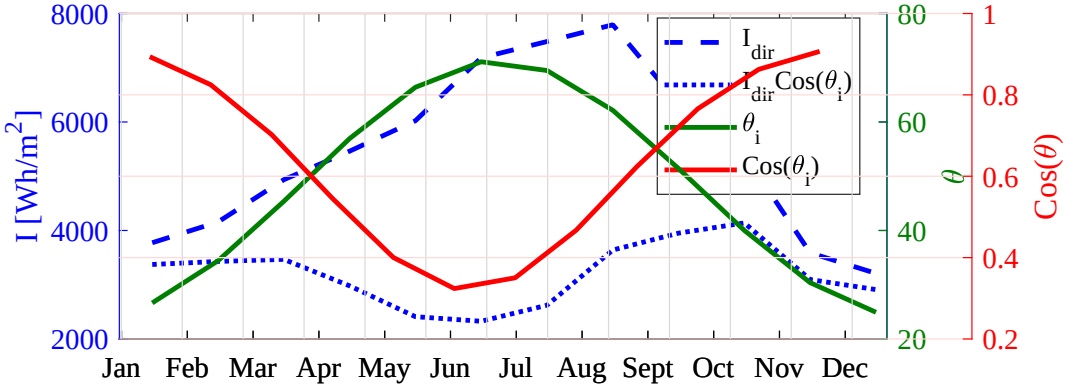

(b) Amount of solar radiation versus incidence angle throughtout a year for a vertical surface

Figure 3.5: Solar radiation and solar angles for a vertical surface at at latitude 42.1558° and longitude -106.908°

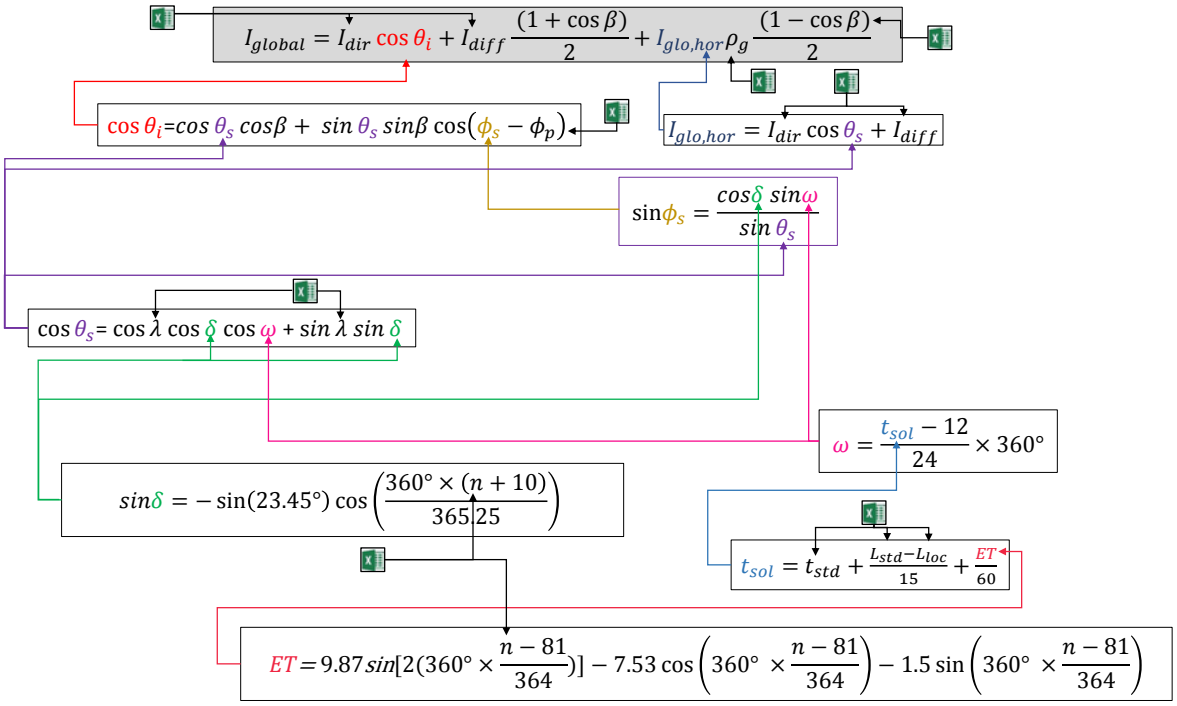

Figure 3.6: Algorithm to determine the solar radiation intensity

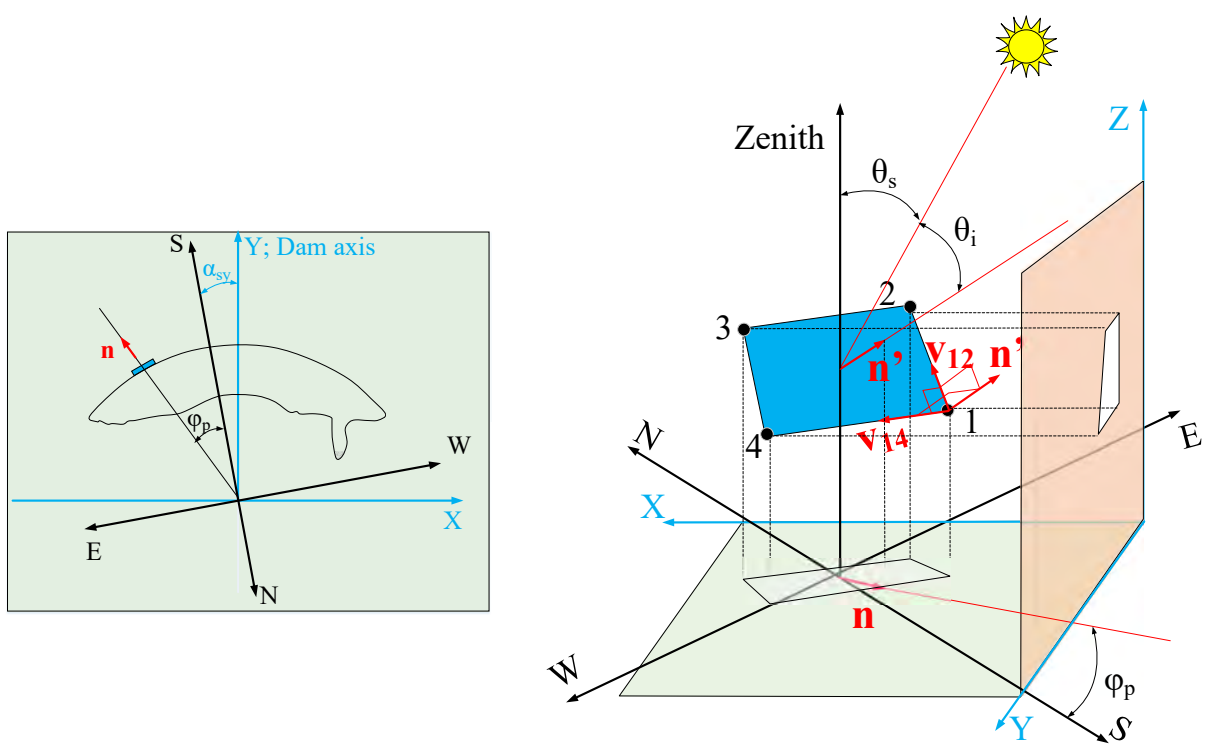

Figure 3.7: Solar radiation on a concrete dam surface

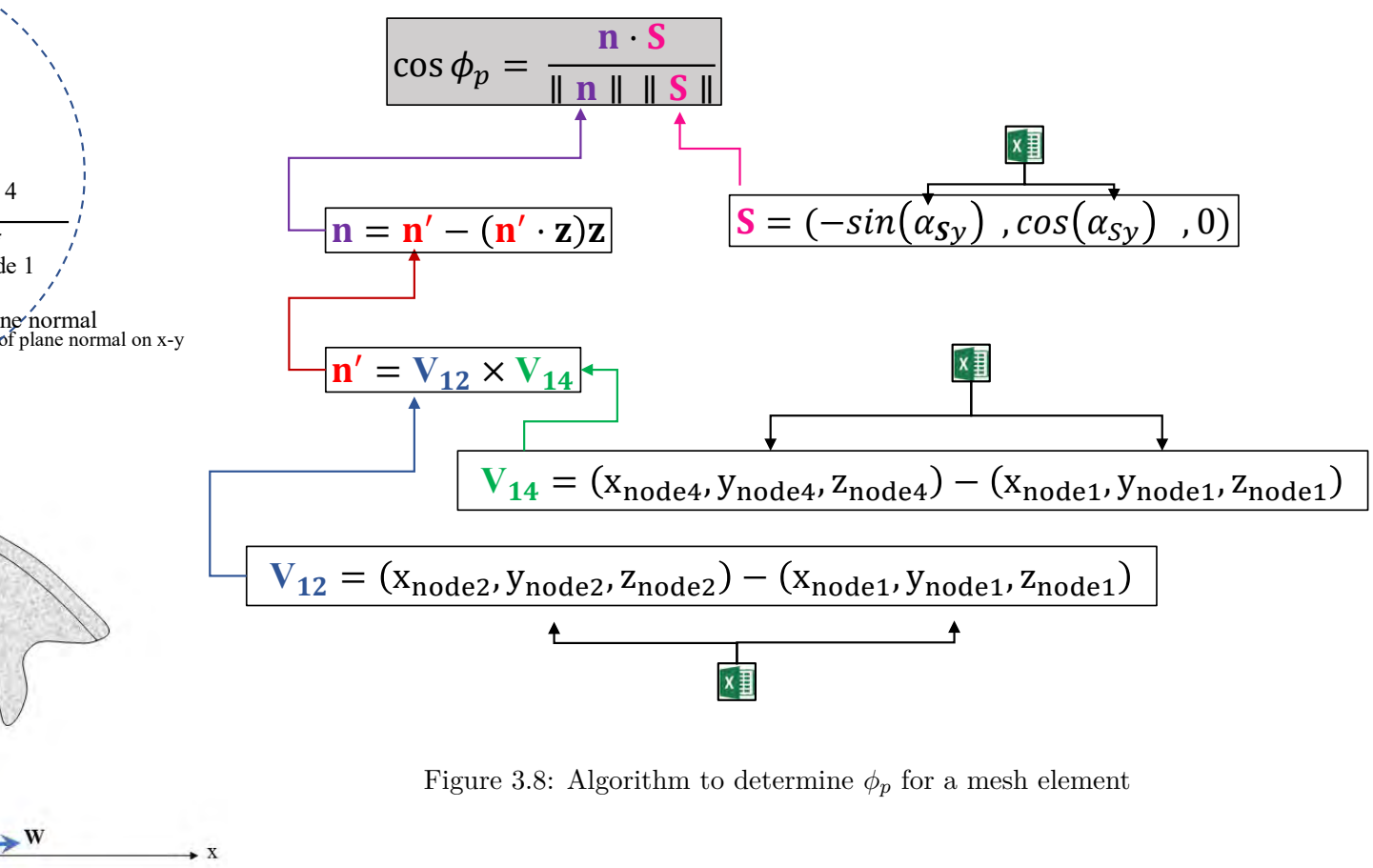

Figure 3.8: Algorithm to determine ϕ_p for a mesh element

3.2.4.3 Temperature Variation Due to Solar Radiation

After the solar flux is calculated using the above-mentioned equations, the next step is to determine the amount of temperature increase caused by the solar radiation using equation 3.26. In this equation q is the solar flux and h is the film coefficient which herein is taken equal to 20 $[\mathrm{W\,m^{-2}\,K^{-1}}]$ for air-concrete interface and was obtained from Hatch (2015).

$$\Delta T = \frac{q}{h} \tag{3.26}$$

Bureau of Reclamation (1981) report provides the temperature increase due to solar radiation at several locations. The reported data are the mean annual temperature variation for tilted surfaces with different inclination and orientations.Figure 3.9 shows the data for latitudes between 40° to 45°. In this study, in order to validate the adopted solar radiation solution, the temperature variation at latitude of 42° is calculated and compared to figure 3.9. Figure 3.10 shows temperature increase resulted from our solution and Bureau of Reclamation (ibid.). As seen, they both follow the same trend as the solar radiation is maximum while the surface angle to the vertical direction increases and the surface faces south (the angle between surface normal and North direction approaches 180); On the other side, the minimum value occurs while the surface is facing the North direction and tilted downward (the angle between the surface and vertical direction is negative). Although the trend is the same for both figures, the two figures are not showing identical minimum temperature values which is due to the fact that there are a set of assumptions made for the calculations which might be different from those from Bureau of Reclamation (ibid.).

Bureau of Reclamation (ibid.) report also provides the average monthly temperature increase due to solar radiation in figure 3.11 for the upstream face of the dam. In figure 3.12 the temperature values from figure 3.11 are re-plotted in centigrade degrees and compared to the results from equation 3.26. The major observations from this figure are that computed temperatures fall within the observed range and the slopes are nearly identical and the dispersion of the numerical case is less than the other one.

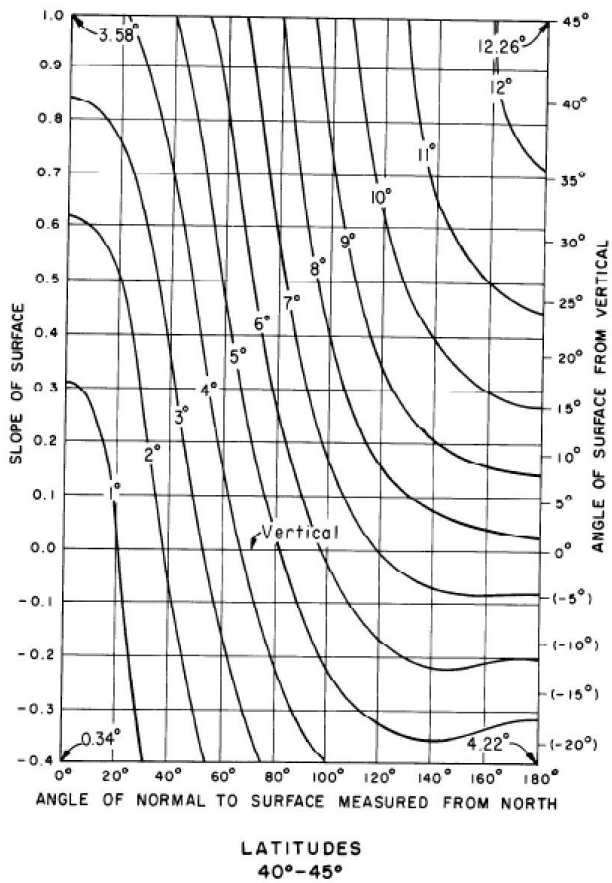

Figure 3.9: Mean annual temperature variation due to solar radiation for surfaces with various orientations and inclinations adopted from Bureau of Reclamation (1981)

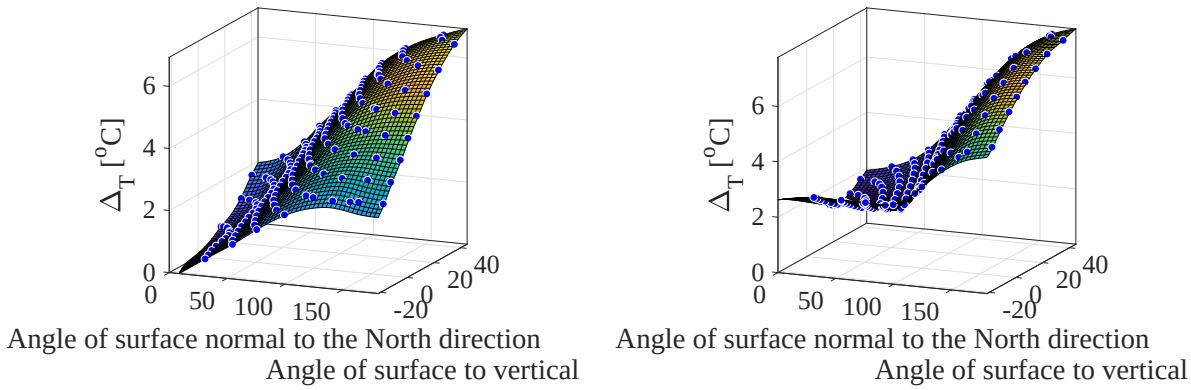

(a) from Bureau of Reclamation (1981)

(b) from equation 3.26

Figure 3.10: Comparison of temperature variation due to solar radiation at latitude 42.1558° and longitude -106.908°

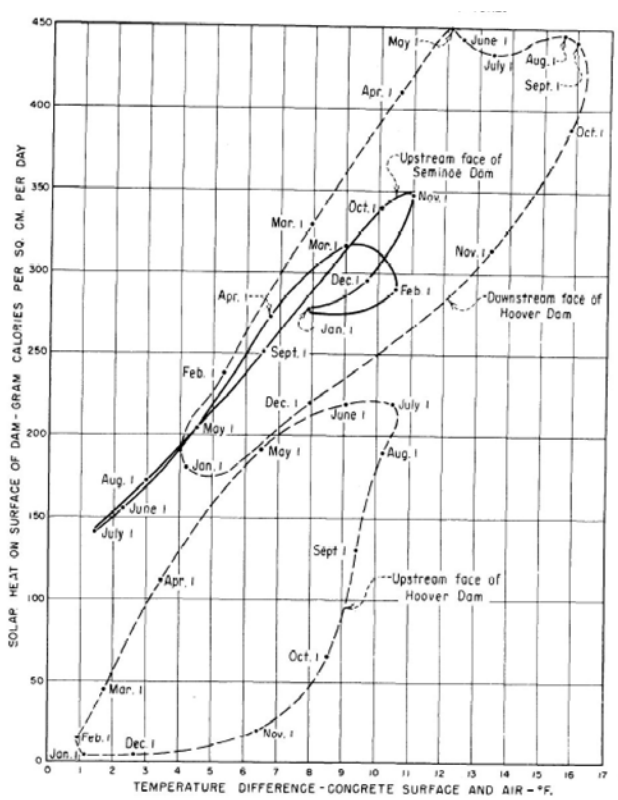

Figure 3.11: Average monthly temperature increase due to solar radiation for upstream face of the dam from Bureau of Reclamation (1981)

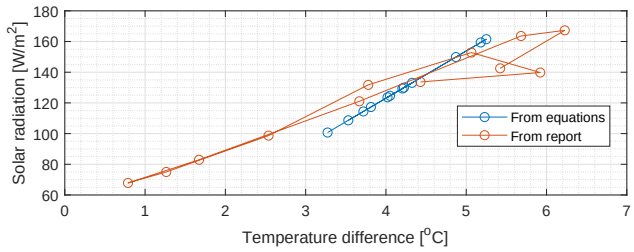

Figure 3.12: Comparison of solar radiation and the resulting temperature increase from Bureau of Reclamation (1981) and equation 3.26

3.3 Conclusion

To summarize, this chapter presented a set of preliminary yet highly important studies to ensure the accuracy of the subsequent complex analysis. In the first section the units and unit conversions are clarified to make all the units consistent within the analysis. In the second part the solar radiation concept is explained and the formulations are discussed; in addition, the procedure of solar radiation calculation was shown in two explaining flowcharts.

Chapter 4

System Identification

A major challenge in the numerical simulation of the temporal concrete expansion (and deterioration) is the ability to use relaible kinetics coefficients, ε^{∞}, τ_l and τ_c introduced in §2.2.2. Whereas those can be obtained through carefully carried laboratory tests (Saouma, 2020), an alternative approach is through system identification.

Mathematically speaking, the problem can be simply formulated as follows. The field-recorded displacements (e.g. crest displacement on a dam) are denoted by $\mathbf{u}(t)$, the target parameters by $\mathbf{x}$ (in our case $x(1) = \tau_c$, $x(2) = \tau_l$ and $(x(3) = \varepsilon(\infty))$, the finite element "operator" by $f(.)$, and computed results by $\mathbf{u}'(t)$. We thus have:

$$f(\mathbf{x}) = \mathbf{u}'(t) \neq \mathbf{u}(t) \tag{4.1}$$

and are seeking to minimize $(\mathbf{u}(t) - \mathbf{u}'(t))^2$, see Figure 9.1.

Such an approach has been often used for dam analysis (Ardito, Maier, and Massalongo, 2008) (Oliveira, Toader, and Vieira, 2012), and is conceptually similar to system identification in nonlinear dynamic systems (Ghanem and Shinozuka, 1995).

4.1 Theory

The parameter identification process seeks to minimize the square of the error between field measurements and those obtained from numerical simulation. Hence, this section will address the underlying theory of least square nonlinear optimization based on trust region algorithm. Optimization algorithms have been widely used to solve various engineering problems. Based on the

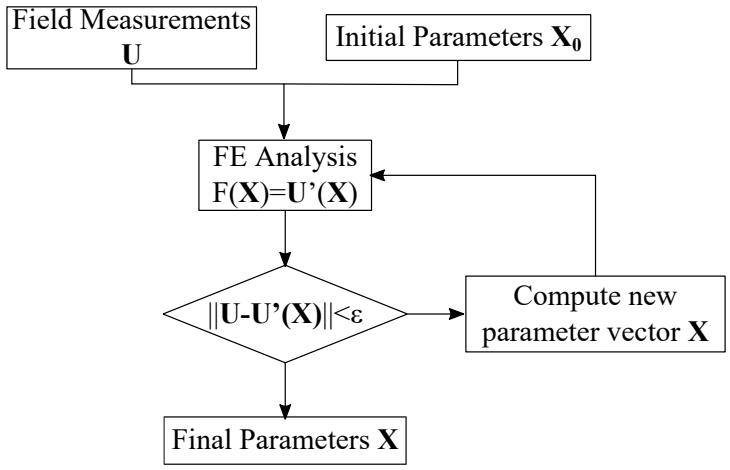

Figure 4.1: Principle of the system identification approach

problem definition, whether the variables are continuous or discrete, constrained or unconstrained. various optimization algorithms should be utilized. In this study we are dealing with a continuous unconstrained problem. Many algorithms for nonlinear optimization problems seek only a local solution, a point at which the objective function is smaller than all other feasible nearby points. They do not always find the global solution,which is the point with lowest function value among all feasible points. Global solutions are needed in some applications,but for many problems they are difficult to recognize and locate. General nonlinear problems, both constrained and unconstrained, may end up finding the local solutions rather than global solutions.

Taylor's Theorem

In order to solve the minimization problems in smooth functions, the Taylor theorem is generally used. Assuming that $f : R^n \to R$ is continuously differentiable and that $p \in R^n$ then we have(Nocedal and Wright, 2006):

$$f(x+p) = f(x) + \nabla f(x+tp)^T p \tag{4.2}$$

for some $t \in (0,1)$. Moreover, if f is twice continuously differentiable, we have:

$$\nabla f(x+p) = \nabla f(x) + \int_0^1 \nabla^2 f(x+tp) p dt \tag{4.3}$$

and that

$$f(x+p) = f(x) + \nabla f(x)^T p + \frac{1}{2} p^T \nabla^2 f(x+tp) p \tag{4.4}$$

for some $t \in (0,1)$. necessary conditions for optimality are derived by assuming that x^* is a local minimizer and then proving facts about $\nabla f(x^*)$ and $\nabla^2 f(x^*)$.

First-Order Necessary Conditions

If x^* is a local minimizer and f is continuously differentiable in and open neighbourhood of x^*, then $\nabla f(x^*) = 0$.

Second-Order Necessary Conditions

If x^* is a local minimizer of f and $\nabla^2 f$ exists and is continuous in an open neighbohood of x^*, then $\nabla f(x^*) = 0$ and $\nabla^2 f(x^*)$ is positive semidefinite.

Second-Order Sufficient Conditions

Suppose that $\nabla^2 f$ is continuous in an open neighborhood of x^* and that $\nabla f(x^*) = 0$ and $\nabla^2 f(x^*)$ is positive definite. Then x^* is a strict local minimizer of f.

4.1.1 Overview of Algorithms

The optimization algorithms usually follow a typical procedure of starting from a first guess point and proceed toward next iterates until it is reached to a solution with acceptable accuracy or there is no further progress. However, the difference of various optimization algorithms is in the strategy of moving from one iterate to the next. Good algorithms should possess the following properties(Nocedal and Wright, 2006):

- Robustness: They should perform well on a wide variety of problems in their class, for all reasonable values of the starting point.
- Efficiency: They should not require excessive computer time or storage.
- Accuracy: They should be able to identify a solution with precision, without being overly sensitive to errors in the data or to the arithmetic rounding errors that occur when the algorithm is implemented on a computer.

There are fundamentally two strategy to find the next iterate in optimization algorithms: 1. Line

Search 2. Trust Region. In line search method basically a direction is determined by the algorithm and the next point is found in that direction such that the function attains a lower value. The trust region strategy uses a region around the current point in which we accept the quadratic approximation of the function. In this study we focus on the later method.

4.1.2 Trust Region

In the trust region strategy, a model function m_k is constructued near the current point x_k which approximates the actual function behavior around that point. However, this function might not be able to approximate the main function at the other points since the search for a minimum value of m_k is restricted to a defined region around x_k. The candidate step p is determined through solving the following equation:

$$\min m_k(x_k + p) \quad s.t. \|p\| \leq \Delta_k \tag{4.5}$$

If the trust region is too large the solution would not result in sufficient reduction of the function and thus the radius of the region should be reduced and the problem should be solve again. Usually, the trust region is a sphere defined by $\|p\|_2 \leq \Delta$, where $\Delta \geq 0$ is the trust-region radius. The model m_k is usually defined as:

$$m_k(x_k + p) = f_k + p^T \nabla f_k + \frac{1}{2} p^T B_k p \tag{4.6}$$

Where f_k and ∇f_k are the function and gradient values calculated at the point x_k. The matrix B_k is either the Hessian$\nabla^2 f_k$ or some approximation to it. if we assume that m_k in each iterate is quadratic based on the taylor series expansion of f we will have:

$$f(x_k + p) = f_k + g_k^T p + \frac{1}{2} p^T \nabla^2 f(x_k + tp) p \tag{4.7}$$

where $f_k = f(x_k)$ and $g_k = \nabla f(x_k)$ and t is some scalar in the interval (0,1). Assuming B_k to be equal to the true Hessian $\nabla^2 f(x_k)$,we will have the trust region Newton method in which we are seeking a solution to subproblem :

$$\min m_k(p) = f_k + g_k^T p + \frac{1}{2} p^T B_k p \quad s.t. \|p\| \leq \Delta_k \tag{4.8}$$

An important step in the trust region method is to determine the trust region radius at each iteration fro this purpose a ratio is defined as:

$$\rho_k = \frac{f(x_k) - f(x_k + p_k)}{m_k(0) - m_k(p_k)} \tag{4.9}$$

If the new function evaluation is greater than the current value, since the denominator is always positive in the above equation, ρ_k is negative, and thus the step did not lead to the increase of the function rather than decreasing it, the step is not acceptable. if ρ_k is close to 1, it shows that the m_k in this step is sufficiently close to the $f(x_k)$ and therefore the region can be expanded in the next iteration. However, if it is close to zero or negative the region radius should be reduced at the next iteration. Figure 4.2 shows 4 iterations of a trust region method with 2 variables, in this figure the blue and red points are indicative of the current point and next iter estimate, respectively. As stated the trust region only expands if the next point guess provide sufficient reduction in the function. For the problem in this study, the corresponding objective function, Jacobian, gradient,

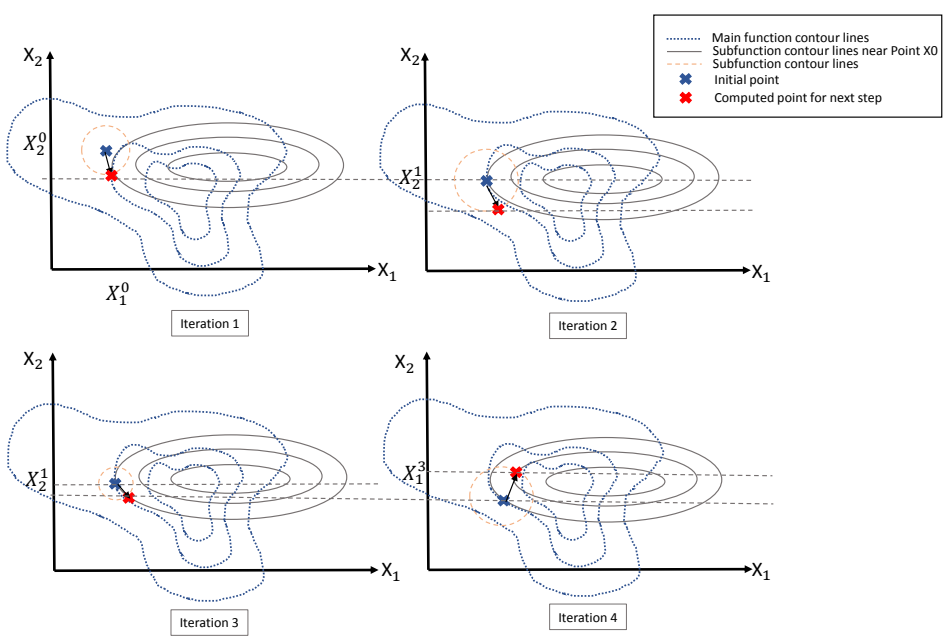

Figure 4.2: Trust region algorithm

and Hessian matrices Dennis and Schnabel, 1983 are then given by:

$$f(\mathbf{x}) = (\mathbf{u}-\mathbf{u}')^T(\mathbf{u}-\mathbf{u}') = \mathbf{r}^T \cdot \mathbf{r} = \sum_{i=1}^{m} (u_i - u_i')^2 \tag{4.10}$$

$$\mathbf{J}(\mathbf{x}) = \frac{\partial \mathbf{r}(\mathbf{x})}{\partial \mathbf{x}^T} = \frac{\partial}{\partial \mathbf{x}^T}\left[(\mathbf{u}-\mathbf{u}')\right] = \frac{\partial \mathbf{u}}{\partial \mathbf{x}^T} - \frac{\partial \mathbf{u}'}{\partial \mathbf{x}^T} = -\frac{\partial \mathbf{u}'}{\partial \mathbf{x}^T} = -\mathbf{L} \tag{4.11}$$

$$\nabla f(\mathbf{x}) = \frac{\partial f(\mathbf{x})}{\partial \mathbf{x}^T} = \frac{\partial}{\partial \mathbf{x}^T}\left[(\mathbf{u}-\mathbf{u}')^T(\mathbf{u}-\mathbf{u}')\right] = 2\mathbf{J}^T\mathbf{r} \tag{4.12}$$

$$\mathbf{H}(\mathbf{x}) = \frac{\partial^2 f}{\partial \mathbf{x}^T \partial \mathbf{x}} = \frac{\partial}{\partial \mathbf{x}}\left(\nabla f\left(\mathbf{x}\right)\right) = \frac{\partial}{\partial \mathbf{x}}\left[2\mathbf{J}^T\mathbf{r}\right] = 2\mathbf{J}^T\mathbf{J} + 2\frac{\partial^2 \mathbf{r}}{\partial \mathbf{x}^T \partial \mathbf{x}}\mathbf{r} \tag{4.13}$$

Near the minimum, $\frac{\partial^2 \mathbf{r}}{\partial \mathbf{x}^T \partial \mathbf{x}}\mathbf{r} \to 0$, we have $\mathbf{H}(\mathbf{x}) \simeq 2\mathbf{J}^T\mathbf{J}$. Use of the Levenberg-Marquardt method ibid. allows solving for $\mathbf{x}_{k+1}$ from:

$$\mathbf{x}_{k+1} = \mathbf{x}_k - \left[\varepsilon_k \mathbf{I} + \mathbf{H}\left(\mathbf{x}_k\right)\right]^{-1} \nabla f\left(\mathbf{x}_k\right) \tag{4.14}$$

where ε_k is such that all eigenvalues of $[\varepsilon_k \mathbf{I} + \mathbf{H}\left(\mathbf{x}_k\right)]$ are positive definite. A development of the Levenberg-Marquardt method, known as the trust region method, can ultimately be introduced. We have indeed sought to minimize the objective function, $m_k(\mathbf{x})$, inside a trust region where the quadratic approximation (as obtained by a Taylor series) is considered reliable:

$$m_k\left(\mathbf{x}, \mathbf{x}_k\right) = f\left(\mathbf{x}_k\right) + \nabla f\left(\mathbf{x}_k\right)^T\left(\mathbf{x} - \mathbf{x}_k\right) + \frac{1}{2}\left(\mathbf{x} - \mathbf{x}_k\right)^T \mathbf{H}\left(\mathbf{x}_k\right)\left(\mathbf{x} - \mathbf{x}_k\right) \tag{4.15}$$

The trust region is defined as follows:

$$\mathbf{\Omega}_k = \left\{\mathbf{x} : \left\|\mathbf{x} - \mathbf{x}_k\right\| \leq \Delta_k\right\}; \Delta_k > 0 \tag{4.16}$$

The optimization problem becomes:

$$\min_{\mathbf{x}} \left\{m_k\left(\mathbf{x}, \mathbf{x}_k\right) : \mathbf{x}_k \in \Omega_k\right\} \tag{4.17}$$

The condition needed to update the region is given by:

$$\rho_k = \frac{f\left(\mathbf{x}_k\right) - f\left(\mathbf{x}_{k+1}\right)}{f\left(\mathbf{x}_k\right) - m_k\left(\mathbf{x}_{k+1}\right)} \tag{4.18}$$

The update of the starting point is the same as that illustrated for the Levenberg-Marquardt method. With this method, we are also able to define the upper and lower bounds for these parameters as:

$$\min_{\mathbf{x}} \left\{m_k\left(\mathbf{x}, \mathbf{x}_k\right) : \mathbf{x}_k \in \Omega_k\right\}; \mathbf{lb} \leq \mathbf{x} \leq \mathbf{ub} \tag{4.19}$$

The starting point of the parameter identification process may be determined from laboratory tests (yielding an initial estimate of $\varepsilon^{\infty}|_{T=T_0}$, $\tau_L(T_0)$ and $\tau_C(T_0)$). Alternatively, curve fitting of the dam crest displacement:

$$u_{irr}^{AAR}(t,\theta) = \frac{1 - e^{-\frac{t}{\tau_C(\theta)}}}{1 + e^{-\frac{(t-\tau_l(\theta))}{\tau_C(\theta)}}} u_{irr}^{AAR,\infty} \tag{4.20}$$

(where u_{irr}^{AAR} and $u_{irr}^{AAR,\infty}$ are the irreversible, time and temperature-dependent displacement and the final displacement due to AAR respectively) provides a conservative estimate for the times but not for $\varepsilon^{\infty}|_{T=T_0}$. The target parameters must be normalized such that all initial values have the same order of magnitude, i.e.: a) the initial variation must be large enough to produce a variation in the computed results (large normalized values can lead to an immediate stop of the identification process); and b) the final variation of parameters must be small enough to allow for a small final adjustment of the identified parameters without large oscillations around the final solution (an overly small normalized parameter may result in a large final oscillation).

A weight function can be introduced to assign importance to the last data field, which typically contains a major absolute value and is thus more representative of the irreversible effect of AAR expansion with respect to the effect of normal loads. Let's note that this system identification does not require a thermal analysis and, from a practical standpoint, entails a simple modification of three variables included in the stress analysis input file.

4.1.2.1 Algorithm

Given $\hat{\Delta} > 0$, $\Delta_0 \in (0, \hat{\Delta})$, and $\eta \in [0, \frac{1}{4})$: ((Nocedal and Wright, 2006))

for $k = 0, 1, 2, ...$

evaluate ρ_k

if $\rho_k < \frac{1}{4}$

$\Delta_{k+1} = \frac{1}{4}\Delta_k$

else

if $\rho_k > \frac{3}{4}$ and $\|p_k\| = \Delta_k$

$$\Delta_{k+1} = \min(2\Delta_k, \hat{\Delta})$$

else

$$\Delta_{k+1} = \Delta_k;$$

if $\rho_k > \eta$

$$x_{k+1} = x_k + p_k$$

else

$$x_{k+1} = x_k;$$

end(for)

4.2 Implementation

4.2.1 Matlab® Formulation

The process is coded in Matlab® through the flowchart shown in Fig. 4.3. The code is essentially built around the function `lsqnonlin` problems which minimizes the square of the Euclidian norm of $\mathbf{f}(\mathbf{x})$

$$\min||\mathbf{f}(\mathbf{x})||_2^2 = \min\left(f_1(\mathbf{x})^2 + f_2(\mathbf{x})^2 + \cdots + f_n(\mathbf{x})^2\right) \tag{4.21}$$

where

$$\mathbf{f}(\mathbf{x}) = \begin{bmatrix} f_1(\mathbf{x}) \\ f_2(\mathbf{x}) \\ \vdots f_n(\mathbf{x}) \end{bmatrix} \tag{4.22}$$

$$||\mathbf{f}(\mathbf{x})||_2 = \sqrt{f_1(\mathbf{x})^2 + f_2(\mathbf{x})^2 \cdots f_n(\mathbf{x})^2} \tag{4.23}$$

$$\text{Residual} \qquad \mathbf{x}(t) = \mathbf{x}_{\text{fea}}(t) - \mathbf{x}_{\text{meas}}(t) \tag{4.24}$$

where $\mathbf{x}_{\text{fea}}(t)$ is the vector of displacement (at a selected point) computed by the finite element analysis, and $\mathbf{x}_{\text{meas}}(t)$ is the corresponding vector of measured values. Both are in terms of time.

It is a pretty simple operation in Matlab®

```
[x,resnorm,residual,exitflag,output] = lsqnonlin(fun,x0,lb,ub,options)
```

where

`fun`	Function to be minimized
`x0`	Initial values vector
`lb`	Lower bound vector
`ub`	Upper bound vector
`options`	Strcuture defining the optimization options
`resnorm`	squared 2-norm of the residual at x: $\sum(fun(\mathbf{x}).^2)$
`residual`	Value of the objective function at solution, usually (fun($\mathbf{x}$).
`exitflag`	Reason for stopping of the solver
`output`	Final information about the optimization process (a structure)

Whereas most of the parameters are relatively straightforward, the most critical set are the `options`. Those used in this project include

`MaxFunEvals`	Maximum number of function evaluation
`MaxIter`	Maximum number of iterations
`TolFun`	Tolerance for the function
`tolx`	Tolerance for the unknowns
`MaxPCGIter`	Maximum number of preconditioned conjugate gradient iterations
`TolPCG`	Termination tolerance on the PCG iteration
`Typicalx`	Array that specifies typical magnitude of array of parameters $\mathbf{x}$ used for scaling finite differences for gradient estimation.
`FiniteDifferenceStepSize`	A vector step size factor for finite differences; this is defined manually to make sure that the exploration is working properly.

The finite difference step size had a pivotal role in the progress of our analysis. If not specified, the default value for this parameter is sqrt(eps) for forward finite differences. However, this default value in our case study led to having too small finite difference steps to call a change and therefore,

the program was unable to capture any difference by variating the input variables and eventually yielded to the initial guess as the optimization response. By defining a vector of finite difference step sizes (v) the program calculates the finite difference δ for each variable x as:

$$\boldsymbol{\delta} = \mathbf{v} \cdot \max(abs(\mathbf{x}), \text{Typical}\mathbf{x}); \tag{4.25}$$

Defining higher values resulted in more tangible differences in variables and thus ensuring a reasonable exploration for the function within the response variable domain.

4.2.2 Matlab® code

The Matlab® code is described in Fig. 4.3 and is relatively simple to follow.

(1) Field measurements are read and adjusted as described in §9.2.2.

(2) The control input file is read, and partitioned in three parts: a central one containing the lines to be modified by the code (associated with the AAR properties), and the two adjacent ones which would remain unchanged. Corresponding separator line numbers are recorded for subsequent use by the minimization function.

(3) User defined variables (Table 9.1) are read from an external Excel file.

(4) Optimization parameters are set

(5) The `lsqnonlin` function, §4.2.1, is then called.

4.2.2.1 Function definition

A critical part of the algorithm is the definition of the function to be minimized.

(1) Write a new input file in terms of $\mathbf{x}$ (first iteration, use the default values of $\mathbf{x} = \mathbf{x}_0$. This is facilitated by the previous partitioning of the control file.

(2) Perform the finite element analysis (using Merlin in this case).

(3) Extract from the output file the computed displacements, $\mathbf{x}_{\text{fea}}(t)$

(4) Compute the residual $\mathbf{x}(t) = \mathbf{x}_{\text{fea}}(t) - \mathbf{x}_{\text{meas}}(t)$.

(5) Compute the norm e of the residuals.

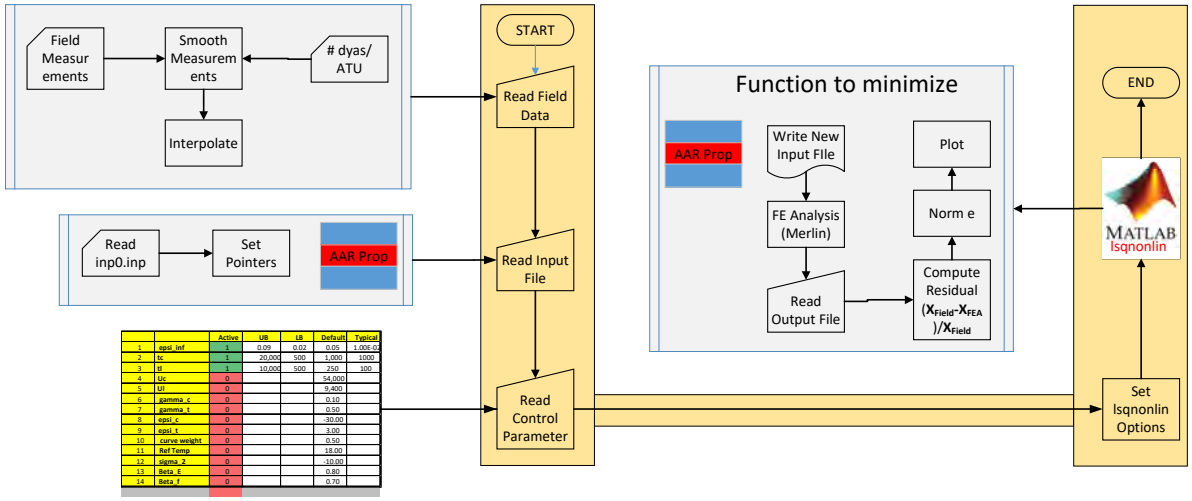

		Active	UB	LB	Default	Typical
1	epsl_inf	1	0.09	0.02	0.05	1.00E-02
2	tc	1	20,000	500	1,000	1000
3	tl	1	10,000	500	250	100
4	Uc	0			54,000	
5	Ul	0			9,400	
6	gamma_c	0			0.10	
7	gamma_t	0			0.50	
8	epsl_c	0			-30.00	
9	epsl_t	0			3.00	
10	curve weight	0			0.50	
11	Ref Temp	0			18.00	
12	sigma_2	0			-10.00	
13	Beta_E	0			0.80	
14	Beta_f	0			0.70	

Figure 4.3: System identification procedure flow chart

(6) Return the norm new vector of displacements.

Completion of the program is governed by `lsqnonlin` on the basis of the norm and options previously selected (§4.2.1). Because there is no direct call to the function to be minimized by the Matlab® code, extra parameters (such as $\mathbf{x}_{\text{meas}}(t)$ are passed through as `global` variables.

4.2.2.2 Real time visualization

Keeping in mind that the nonlinear finite element simulation of the AAR expansion in a dam may take upward from 3 hours each, and that in the context of the parameter identificaiton procedures multiple analyses are needed, this is a very computer intensive process.

Hence, a graphical user interface is used, Figure 4.4. The first quadrant is a plot of the intermediary displacements ($\mathbf{x}_{\text{fea}}(t)$) in comparison with the measured ones ($\mathbf{x}_{\text{meas}}(t)$). The other three quadrants are plots of selected variables to be identified (ε^{∞}, τ_l, and τ_c) in terms of iteration numbers.

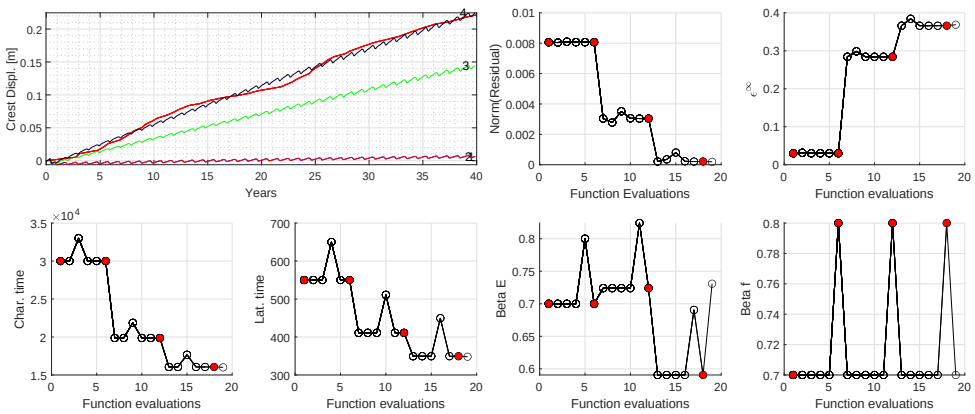

Figure 4.4: Graphical user interface for AAR parameter identification

Chapter 5

Seismic Analysis

Abstract

This chapter discusses the fundamentals of dam seismic analysis. In other words, this chapter contains the methodology on modeling the fluid-structure interaction, soil-structure interaction, and ground motion selection.

5.1 Fluid Structure Interaction; Westergaard's model

In a landmark paper, Westergaard (1933) developed a model to quantify the hydrodynamic forces acting on a dam using an added (or lumped in the context of finite element) mass. This model will be used in the current analysis.

Despite its wide spread adoption, and to the best of the author's knowledge the model has never been described fully. Instead, its final equations are presented, and adopted.

5.1.1 Theoretical Model

Whereas one jump to §5.1.2 to compute the added mass to account for hydrodynamic forces, understanding their derivation is important as it is a most elegant fusion of mathematics, mechanics and engineering.

Hence, this section will review in great details the landmark papeer by (ibid.).

When the water pressures are known, their influence on the stresses may be computed by the

methods applying to static loads. The problem that needs particular attention, therefore, is that of the changes of the water pressures during the earthquake.

Notation

The following notation is adopted:

x, y, z	rectangular co-ordinates x and y as shown in Fig. 5.1 ; the axis of x is along the undisturbed surface of the water, is directed up stream, and is perpendicular to the plane up-stream face of the dam; the axis of y is vertical downward.
t	time.
h	depth of reservoir.
g	acceleration due to gravity. (Eq. 5.8)
w	weight of water per unit of volume, (Eq. 5.8)
k	Bulk modulus of water (pressure divided by reduction of volume per unit of volume). (Eq. 5.8)
ξ and η	displacements of a particle of water in the directions of x and y. respectively.
ξ_0	value of ξ at up-stream face of the dam.
σ	stress in the water due to the dynamie action, positive as tension (to be combined with the hydrostatic pressure existing beforehand).
α	ratio measuring the intensity of the earthquake = maximum horizontal component of the acceleration of the foundation divided by g.
T	period of horizontal vibrations of the foundation.
r, v	amplitude and maximum velocity of horizontal vibrations of the foundation.
v_n	velocity of sound in water.
i	length of waves of expansion in the water when the period is T.
c_n	value defined by Equations , , and (with $n = 1, 3, 5 \ldots$).
p	maximum pressure of the water on the dam at the depth, y, due to the dynamic action.
p_0	value of p at the bottom ($y = h$).

Q	horizontal shear produced in a straight gravity dam at the depth, y, by the pressures, p.
Q_0	value of Q at the bottom ($y = h$).
M	bending moment produced in a straight gravity dam at the depth, y. by the pressures, p.
M_s	value of M at the bottom ($y = h$).
o, K	coeffieients in approximate formulas (Eq. to 5.38).
b, b'	dimensions shown in Fig. 5.3

Equations on Motion of the Water

Since the motions involved are small, relatively simple equations (sound in liquid) may be used. These equations may be interpreted in terms of the theory of elasticity of solids as equations of elasticity without shearing stresses. The forces acting on an element of volume, $dxdydz$, are expressed in terms of the stress, σ, which must be superimposed on the hydrostatic pressure existing before the disturbance.

Using D'Alembert's principle for the dynamic equilibrium for a Newtonian fluid (ie. incompressible) (Eq. G.1) we have

$$\frac{\partial \sigma}{\partial x} = \frac{w}{g}\frac{\partial^2 \xi}{\partial t^2} \tag{5.1}$$

$$\frac{\partial \sigma}{\partial y} = \frac{w}{g}\frac{\partial^2 \eta}{\partial t^2} \tag{5.2}$$

This is the equation of motion in the direction of x and y. We do not consider motion in the z (vertical) direction since the motion is parallel to the xy-plane. The strain is given by

$$\varepsilon = \frac{\partial \xi}{\partial x} + \frac{\partial \eta}{\partial y}$$

For the water

$$p = \frac{1}{2}\sigma_{ii} = k\varepsilon_{ii}$$

Hence, the stress can be rewritten as

$$\sigma = k\left(\frac{\partial \xi}{\partial x} + \frac{\partial \eta}{\partial y}\right) \tag{5.3}$$

The motion is thus governed by Equations 5.1, 5.2 and 5.3. A comparison with the general equations of hydrodynamics for compressible fluids shows that those equations apply only when ξ and η are small, and when, in addition, the ratios of the products, $\frac{\partial \xi}{\partial t}\frac{\partial \sigma}{\partial x}$ and $\frac{\partial \eta}{\partial t}\frac{\partial \sigma}{\partial y}$ to $\frac{\partial \sigma}{\partial t}$, are negligible.

In the solutions given in Equations 5.13, 5.14, and 5.18, these ratios will be found to be of the order of the amplitude of the motions divided by the depth of the reservoir.

Preliminary Study, Assuming Horizontal Motion Only

Though the water acting on the dam may have a vertical displacement, this preliminary study will ignore this vertical motion. It will nevertheless shed some light on the problem. With $\eta = 0$, Eq. 5.1 and 5.3 will give:

$$k\frac{\partial^2 \xi}{\partial x^2} = \frac{w}{g}\frac{\partial^2 \xi}{\partial t^2} \tag{5.4}$$

This is the wave equation (Eq. G.2) which general solution is of the form

$$G(x,t) = f\left(t - \frac{x}{v_s}\right) + g\left(t + \frac{x}{v_s}\right)$$

As a simplifying assumption, we consider that during the earthquake the dam moves in a simple harmonic motion with period, T, and a maximum acceleration, αg, occurring when $t = 0, T, 2T$, etc. The motion will thus be given by

$$\xi_0 = -\frac{\alpha g T^2}{4\pi^4}\cos\frac{2\pi t}{T} \tag{5.5}$$

With $\xi_{\mathrm{x}=0} = \xi_0$, Equation 5.4 will be satisfied by

$$\xi = -\frac{\alpha g T^2}{4\pi^2}\left[\beta\cos\frac{2\pi}{T}\left(t - \frac{x}{v_2}\right) + (1-\beta)\cos\frac{2\pi}{T}\left(t + \frac{x}{v_s}\right)\right] \tag{5.6}$$

where β is a constant, and,

$$v_s = \sqrt{\frac{gk}{w}} \tag{5.7}$$

v_s, is the wave velocity in the water; that is, the sound velocity (on account of the low frequency, these waves, of course, would not be audible as sound). Using

$$\begin{aligned} k &= 300,000 \text{ lbs/in}^2 = 21,600\text{ton/ft}^2 \\ g &= 32.2 \text{ ft/sec}^2 \\ w &= 0.03125 \text{ ton/ft\^{}3} \end{aligned} \tag{5.8}$$

give $v_s = 4,718$ ft/sec.

The term in Equation 5.6 containing the factor, β, in front of the cosine represents waves moving away from the dam, while the one containing the factor, $1-\beta$, represents waves moving toward the dam.

Equations 5.6 and 5.3 give for $x = 0$ (that is, at the up-stream face of the dam):

$$\sigma = (1-2\beta)\frac{\alpha T}{2\pi}\sqrt{gkw}\sin\frac{2\pi t}{T} \tag{5.9}$$

When $\beta > 1/2$, the waves moving away (from the dam) predominate over those moving toward it.

Equation 5.9 shows that the maximum pressure on the dam, that is, $(-\sigma)_{max}$ occurs at times $t = \frac{T}{4}, \frac{5T}{4}, \frac{9T}{4}, \ldots\ldots$, and is equal to,

$$p = (2\beta-1)\frac{\alpha T}{2\pi}\sqrt{gkw} \tag{5.10}$$

It should be noted that the largest acceleration of the dam, and, consequently, the greatest inertia forces due to the moving mass of the dam, occur when $t = 0, T, 2T, \ldots$ The stresses in the dam due to the pressures, p, and the inertia forces, therefore, would have to be combined in the manner of two alternating currents with a difference of phase of one-quarter of the period.

From Equation 5.5, the maximum velocity of the dam is,

$$v = \frac{\alpha g T}{2\pi} \tag{5.11}$$

Thus, substituting Equation 5.7 5.11into 5.10 we obtain the value of the pressure

$$p = (2\beta-1)\frac{v}{v_s}k \tag{5.12}$$

With $\beta = 1$, that is, when the waves move away from the dam only, Equation 5.10 (or, alternatively Equation 5.12), with the numerical constants given in Equations 5.8, and with $\alpha = 0.1$ and $T = \frac{4}{3}$ sec., gives $p = 3.13$ tons/ft^2. But since the water can "escape" vertically the pressures are actually much less, and are not distributed uniformly through the depth of the reservoir. A correct solution should yield zero pressures in the water at the top.

Solution Considering Horizontal and Vertical Motions of the Water

If we allow water to also move vertically, we would still have to satisfy Equations 5.1 5.2 and 5.3 but subjected to the following boundary conditions:

(1) $\sigma = 0$, at $y = 0$;

(2) $\eta = 0$, at $y = h$;

(3) $\xi = -\frac{\alpha g T^2}{4\pi^2} \cos \frac{2\pi t}{T}$, at $x = 0$;

(4) σ converges toward 0 when x becomes large.

From the first condition, for small values of η it makes no appreciable difference whether one specifies $\sigma = 0$ at the undisturbed or the disturbed surface.

A solution that satisfies the three equations and the boundary condition is one based on the Fourier series

$$\xi = -\frac{\alpha g T^2}{\pi^3} \cos \frac{2\pi t}{T} \sum_{1,3,5,\ldots}^{n} \frac{1}{n} e^{-q_n} \sin \frac{n\pi y}{2h} \tag{5.13}$$

$$\eta = \frac{\alpha g T^2}{\pi^3} \cos \frac{2\pi t}{T} \sum_{1,3,5..}^{n} \frac{1}{n c_n} e^{-q_n} \cos \frac{n\pi y}{2h} \tag{5.14}$$

where

$$c_n = \sqrt{1 - \frac{16 w h^2}{n^2 g k T^2}} \tag{5.15}$$

and

$$q_n = \frac{n\pi c_n x}{2h} \tag{5.16}$$

Equation 5.15 gives,

$$\frac{1}{c_{\mathrm{n}}} - c_{\mathrm{n}} = \frac{16 w h^2}{n^2 c_n g k T^2} \tag{5.17}$$

Then Equations 5.3, 5.13, 5.14, and 5.17 will give

$$\sigma = -\frac{8\alpha w h}{\pi^2} \cos \frac{2\pi t}{T} \sum_{1,3,5,\ldots}^{n} \frac{1}{n^2 c_n} e^{-q_n} \sin \frac{n\pi y}{2h} \tag{5.18}$$

One can easily verify that Equations 5.13, 5.14, and 5.18 satisfy Equations 5.1 and 5.2 at all points by differentiating with respect to t, x, and y. Equation 5.3 is satisfied because it was used in deriving Equation 5.18 from Equations 5.13 and 5.14. Furthermore, inspection of the expressions

for η and σ readily show that conditions 1, 2, and 4 are satisfied. To verify that condition 3, for $x = 0$, is satisfied, one has to compare Equation 5.13 for $x = 0$ with the expression for $\frac{\pi}{4}$, in terms of a Fourier series when $0 < u < \pi$,

$$\frac{\pi}{4} = \sin u + \frac{1}{3}\sin 3u + \frac{1}{5}\sin 5u + \dots \tag{5.19}$$

In the present application, $u = \frac{\pi y}{2h}$.

Thus, all the specified conditions are satisfied. The applicability of the equations depends, however, on an additional condition: the displacements defined by the solution, as well as their derivatives with respect to x and y must be small. One must thus consider the possibilities of large displacements. One possibility is identified with resonance in the water; another will be investigated by determining the shape of the wave formed by the surface of the water and the vertical motions along the up-stream face of the dam.

Pressures on the Dam

From Equation 5.18, the maximum water pressure ($p = -\sigma$ for $x = 0$), occurs when $t = 0, T, 2T, \dots$. Thus,

$$p = \frac{8\alpha wh}{\pi^2} \sum_{1,3,5,\dots}^{n} \frac{1}{n^2 c_n} \sin \frac{n\pi y}{2h} \tag{5.20}$$

where, as before, according to Equation 5.18, and with the numerical constants given in Equations 5.8:

$$c_n = \sqrt{1 - \frac{16wh^2}{n^2 gkT^2}} = \sqrt{1 - \frac{0.71889}{n^2}\left(\frac{h \text{ sec.}}{1000 \text{ T ft}}\right)^2}. \tag{5.21}$$

The largest value of the pressure, p, occurs at the bottom of the reservoir ($y = h$), and is,

$$p_0 = \frac{8\alpha wh}{\pi^2} \sum_{1,3,5,\dots}^{n} \frac{(-1)^{\frac{n-1}{2}}}{n^2 c_n} \tag{5.22}$$

Fig. 5.1 shows the pressure p distribution profile. From Equation 5.22, the derivative, $\frac{dp}{dy}$ is infinite when $y = 0$, and zero when $y = h$; that is, the curve for p has a horizontal tangent at the top and a vertical tangent at the bottom.

Items 1 and 2 of Table 5.1 contain numerical values of the ratio, $\frac{p_0}{\alpha h}$, and of p_0, computed from Equations 5.21 and 5.22. The ratio, $\frac{p_0}{\alpha h}$, varies only slowly with h. For $h = 600$ ft, $T = \frac{4}{3}$ sec.

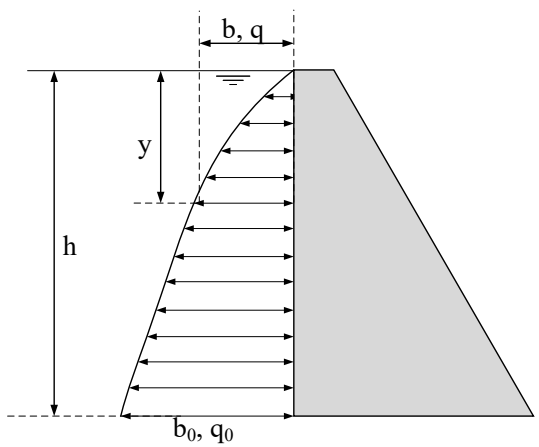

Figure 5.1: Pressures on the dam due to dynamic action of the water (Westergaard, 1933)

(and for $h = 200$ ft, $T = \frac{4}{9}$ sec.), the pressure at the depth, $y = \frac{h}{2}$, was found to be $p = 0.814p_0$.

Shear and Moments

It can be particularly useful to express the horizontal shearing forces and the bending moments produced by the loads, p, in various horizontal sections of the dam acts as a cantilever (gravity dam). The shears are stated as force per unit of width of the cantilever, for example, in tons per foot, and the moments are stated as moment per unit of width, for example, in foot-tons per foot (or simply in tons). The shears, Q, at the depth, y, and Q_0 at the depth, h, and the moments, M, at the depth, y, and M_0, at depth, h, are obtained from p in Eq. 5.20 by the integration

$$Q = \int_0^y p dy; \quad Q_0 = \int_0^h p dy; \quad M = \int_0^y Q dy; \quad M_0 = \int_0^h Q dy \tag{5.23}$$

Defining

$$q = \sum_{1,3,5,\ldots}^{n} \frac{1}{n^2 c_n} \tag{5.24}$$

we obtain:

$$Q = \frac{16\alpha wh}{\pi^3}\left(q - \sum_{1,3,5,\ldots}^{n} \frac{1}{n^2 c_n} \cos\frac{n\pi y}{2h}\right) \tag{5.25}$$

$$Q_0 = \frac{16}{\pi^3}\alpha v h^2 q \tag{5.26}$$

$$M = \alpha w h^3 \left(\frac{16q}{\pi^2}\frac{y}{h} - \frac{32}{\pi^4}\sum_{1,3,5,\ldots}^{n} \frac{1}{n^4 c_n} \sin\frac{n\pi y}{2h}\right) \tag{5.27}$$

$$M_0 = \alpha w h^3 \left(\frac{16q}{\pi^2} - \frac{32}{\pi^4}\sum_{1,3,5,\ldots}^{n} \frac{(-1)^{\frac{n-1}{3}}}{n^4 c_n}\right) \tag{5.28}$$

$$\tag{5.29}$$

Numerical values of the ratios, $\frac{Q_0}{\alpha h^2}$ and $\frac{M_0}{\alpha h^3}$, and of Q_0 and M_{00} computed from Equations 5.24, 5.26, and 5.28, are also given in Table 5.1 (Items, 3, 4, 5 , and 6).

Derivation of Approximate Formulas

Computations can be simplified by replacing the diagram of pressures in Fig. 5.1 by a quadrant of an ellipse (see Equation 5.41 derived below); the ellipse becomes a circle when drawn to some particular scale for p. A more satisfactory approximate representation is obtained, however, by

Table 5.1: Numerical Results Corresponding to the Period, $T = \frac{4}{3}$ second

Item	Depth of reservoir, h	Ft.	Small	200	600	800
1	Coefficient of pressure, $\frac{p_0}{sh}$	ton/ft^3	0.023202	0.023407	0.025254	0,027257
2	Pressure at bottom, p_0, when $a = 0, 1$	ton/ft^2	$\cdots$	0.468	1.515	2.181
3	Coefficient of shear,	ton/ft^3	0.016961	0.017094	0.018286	0.019576
4	Shear at bottom, Q_0, when $\alpha = 0.1$	ton/ft	$\ldots$	68.4	658.3	1253
5	Coefficient of moment, $\frac{M_0}{\alpha h^3}$	ton/ft^3	0.0068089	0.0068576	0.0072947	0.0077666
6	Moment at bottom, M_0, wben $a = 0, 1$	ft.-ton/ft	$\ldots$	5486	157600	397600
7	$C = \frac{15M_0}{4\alpha m^2}$	ton/ft^3	0.025533	0.025716	0.027355	0.029125
8	$K = C\sqrt{1 - 0.72\left(\frac{h \text{ sec.}}{1000\text{T ft.}}\right)^2}$	ton/ft^3	0.025533	0.025507	0.025282	0.025068
	Approximate coefficients from Eq. 5.30, 5.31, 5.32, 5.38, and 5.1.2					
9	$\frac{p_0}{a^h}$	$\frac{\text{ton}}{ft^3}$	0.0255	0.0257	0.0276	0.0296
10	$\frac{Q_0}{ah^2}$	$\frac{\text{ton}}{ft^3}$	0.0170	0.0171	0.0184	0.0198
11	$\frac{M_0}{ah^3}$	$\frac{\text{ton}}{f^3}$	0.00680	0.00686	0.00736	0.00790

The maximum horizontal acceleration equals αg. When T is varied, the coefficients stated remain constant if h is changed by the same ratio; for example, the coefficients stated for $h = 800$ft., $T = \frac{4}{3}$ sec., apply to the cases, $h = 600$ft., $T = 1$ sec., and $h = 200$ft., $T = \frac{1}{3}$ sec.; the coefficients stated for $h = 200$ft, $T = \frac{4}{3}$ sec., apply to the case, $h = 600\text{ft}, T = 4\text{sec}$.

replacing the curve in Fig. 5.1 by a parabola with vertical axis, as shown in Fig. 5.2, even if this parabola has a sloping tangent at the bottom. The parabola leads to the following simple formulas,

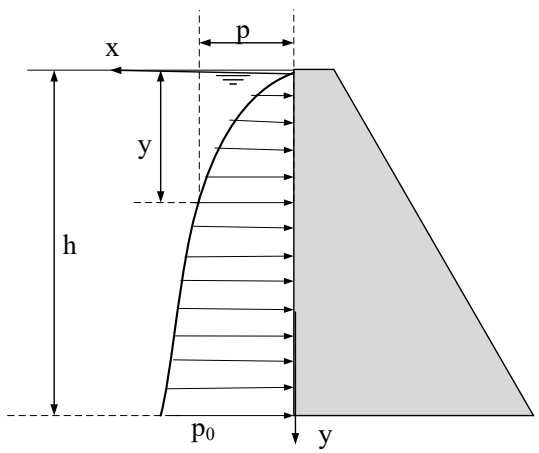

Figure 5.2: Approximate distribution of pressures (Westergaard, 1933)

in which, C is a coefficient depending on the ratio of h to T:

$$p = C\alpha\sqrt{hy}; \qquad p_0 = C\alpha h \tag{5.30}$$

$$Q = \frac{2}{3}C\alpha y\sqrt{hy}; \qquad Q_0 = \frac{2}{3}C\alpha h^2 \tag{5.31}$$

$$M = \frac{4}{15}C_{\alpha y^2}\sqrt{hy}; \qquad M_0 = \frac{4}{15}C_\alpha h^2 \tag{5.32}$$

The coefficient, C, might be determined so that p_0 will have the value computed from Equation 5.22, but one obtains a better representation of the diagram of pressures as a whole, by determining C so that the moment, M_0, will have the value computed from Equation 5.28. In terms of a known M_0, one finds then,

$$C = \frac{15M_0}{4\alpha h^2} \tag{5.33}$$

Table 5.1 (Item 7) shows some numerical values of C. It is noted that the dimension of C is force per unit of volume; C multiplied by ah gives the pressure as force per unit of area.

The coefficient, C, varies slowly within the range considered. For quick estimates one may

very well assume some constant value of C; for example, with $T \geq \frac{4}{3}$ sec:

$$h < 310 \text{ ft} \qquad C = 0.026 \frac{\text{ton}}{\text{ft}^3} \tag{5.34}$$

$$310 \text{ ft} < h < 540 \text{ ft} \qquad C = 0.027 \frac{\text{ton}}{\text{ft}^3} \tag{5.35}$$

$$540 \text{ ft} < h < 680 \text{ ft} \qquad C = 0.028 \frac{\text{ton}}{\text{ft}^3} \tag{5.36}$$

Those are discrete values of C. It would be better to have a continuous function to express C which will apply approximately within the entire range. The main source of variation of C is the constant, c_n, defined by Equation 5.21 with $n = 1$; c_1 appears in the denominator of the first term of each of the sums in Equations 5.24 and 5.28. It is reasonable, therefore, to try out an approximate formula of the type, $C = \frac{K}{c_1}$, in which, K is a constant. The formula would be

$$C = \frac{K}{\sqrt{1 - 0.72\left(\frac{h}{1000T}\right)^2}} \tag{5.37}$$

The values of K shown in Table 2 (Item 8) were computed from this formula by using the values of C in Item 7. Inspection of these results shows that one may adopt the value, $K = 0.0255$ ton-ft^{-3}. It is concluded that the coefficient, C, in Equations 5.30, 5.31, and 5.32, is satisfactorily given by the formula

$$C = \frac{0.0255 \text{ ton-ft}^{-3}}{\sqrt{1 - 0.72\left(\frac{h}{1000\mathrm{T}}\right)^2}} \tag{5.38}$$

Resulting Approximate formula for the Water Pressures

The following approximate formula for the maximum water pressures, to be added to the hydrostatio pressures existing before the earthquake, represents the main conclusion from this study; it is obtained directly from Equations 5.30 and 5.38:

$$p = C\alpha\sqrt{hy} \tag{5.39}$$

$$= \frac{0.0255 \text{ ton-ft}^{-3}}{\sqrt{1 - 0.72\left(\frac{h}{1000T}\right)^2}}\alpha\sqrt{hy} \tag{5.40}$$

For quick computations, however, Equations 5.30, 5.34, 5.35, and 5.36 may be used. Values of the coefficients, $\frac{p_0}{\alpha h}$, $\frac{Q_0}{\alpha h^2}$, and $\frac{M_0}{\alpha h^2}$, obtained by use of Equation 5.1.2, are stated as Items 9, 10, and 11

in Table 2. A comparison with Items 1,3 , and 5, respectively, shows that the approximation is satisfactory.

Using a quadrant of an ellipse (as suggested above) instead of the parabola to represent the pressures, one obtains the following approximate formula by a process similar to that leading to Equation 5.1.2:

$$p = \frac{0.0204 \text{ ton ft}^{-3} \alpha \sqrt{y(2h-y)}}{\sqrt{1 - 0.72\left(\frac{h}{1000T}\right)^2}} \tag{5.41}$$

This formula gives exactly the same values of M_0 as Equation 5.1.2, but gives too small values of p_0 and of the total force, Q_0. Equation 5.1.2 gives slightly too large values of p_0 and Q_0, and is preferable.

It is noted that the pressures, p, occur when $t = 0, T, 2T$, etc., that is, (see Condition (3)), when the dam (during the vibration) is in the extreme position down stream. The stresses due to these water pressures, therefore, must be added to the maximum stresses due to the accelerations of the mass of the dam iself.

When, during the vibration, the dam is in the extreme position up stream, the pressures, p, are reversed and become tensions. These tensions, like the pressures in the extreme position down stream, are to be combined with the hydrostatic pressures existing beforehand. Inspection of the numerical values in Table 2 shows that when the pressure of the atmosphere is included, there is no prospect of the resultant stress in the water becoming either a tension or a very small compression.

Applicability of formulas to cases other than those assumed

The formulas were derived under the assumption that there is no overflow. In case of overflow over a spillway it is suggested that Equation 5.1.2 be used with the depths, h and y, measured from the plane surface of the reservoir at some distance behind the dam. The parabolic diagram of pressures is then used as before, only the top is cut off.

While the formulas were derived under the assumption that the up-stream face is a vertical plane, they will furnish an indication of the pressures which may be expected in other cases, for example, in the ease of arch dams.

5.1.2 Added Mass

To visualize the dynamic action of the water on the dam, one may think of a certain body of water as moving with the dam while the remainder of the reservoir remains inactive. For this purpose the body of water moving with the dam may be imagined as frozen into horizontal layers of added mass (ice in (Westergaard, 1933)), while the remainder of the reservoir is emptied.

Simply put, we are replacing hydrodynamic forces by inertial forces caused by added mass.

The shape of the body of water or added mass thus considered to move with the dam must be determined so that the inertia forces become equal to the pressures actually exerted by the water due to the dynamic action.

The added mass can be applied in either one of two ways

Increase width b as originally formulated by Westergaard (ibid.). Here b is the transverse dimension of the added mass in the direction of x at the depth, y. Then, the corresponding mass per unit of area of the up-stream face of the dam becomes $\frac{bw}{g}$, and the corresponding inertia force when the acceleration is αg becomes $\frac{bw}{g} \times \alpha g = \alpha w b$, which must be equal to p, or

$$b = \frac{p}{\alpha w} \tag{5.42}$$

The shape of this added mass (or ice) is the same as that of the diagram for p when the pressures are laid off to a proper scale.

It will be sufficient for the present purpose to determine b by one of the approximate expressions for p; for example (compare Equations 5.30, 5.34, 5.35, and 5.36),

$$p = 0.02734 \text{ ton-ft}^{-3} \alpha \sqrt{hy} \tag{5.43}$$

which gives, with $w = 0.03125$ ton-ft^{-3},

$$b = \frac{7}{8}\sqrt{hy} \tag{5.44}$$

Fig. 5.3 shows the body of water or ice defined by Equation 5.44. Instead of the body of water, one may prefer to consider an equivalent body of concrete, having the same mass.

If the concrete weighs 144 lb/ft^3, the dimension corresponding to b becomes,

$$b' = 0.38\sqrt{hy} \tag{5.45}$$

The dotted curve in Fig. 5.3 indicates this body of concrete.

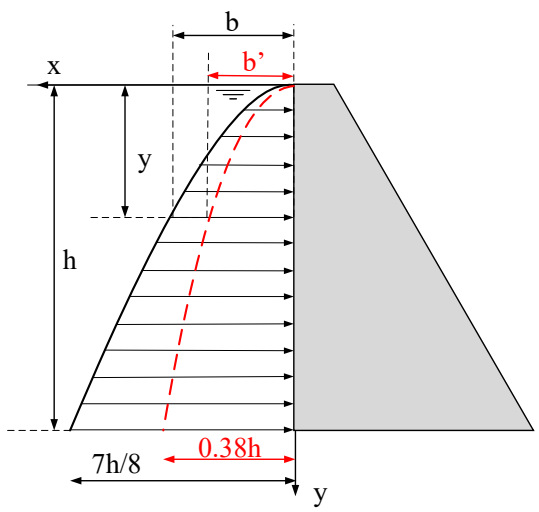

Figure 5.3: Body of water which may be considered to move with dam. (Westergaard, 1933)

Added Mass is a more convenient approach in the context of a finite element analysis. This will entail adding a mass per unit area of the upstream face of the dam

$$\gamma_{lump}(y) = \frac{p(y)}{\alpha g} \tag{5.46}$$

The hydrodynamic pressure is again given by Equation

$$p(y) = C\alpha\sqrt{hy} \tag{5.47}$$

where C was determined in Eq. 5.38, and can be rewritten (From Eq. 5.21) as

$$C = \frac{K}{\sqrt{1 - \frac{16\rho_w H_w^2}{gkT^2}}} \tag{5.48}$$

Combining Equations 5.46-5.48 the final relation to determine the lumped mass per unit area of the upstream dam face due to dynamic action of the water on the dam will be

$$\gamma_{lump}(y) = \frac{K\sqrt{hy}}{g\sqrt{1 - \frac{16\rho_w h^2}{gkT^2}}} \tag{5.49}$$

It should be noted that in his original paper, Westergaard did go through an additional simplification of the preceding equation (removing the dependency on T) yielding:

$$\gamma_{lump}(y) = \frac{7}{8}\rho_w\sqrt{hy} \tag{5.50}$$

which is most often referenced in the literature, yet it is less exact than Equation 5.49. Figure 5.4 shows the differences between the approximate and exact solutions based on the aforementioned equations for a hypothetical dam model in which the water level, h, is 100 m.

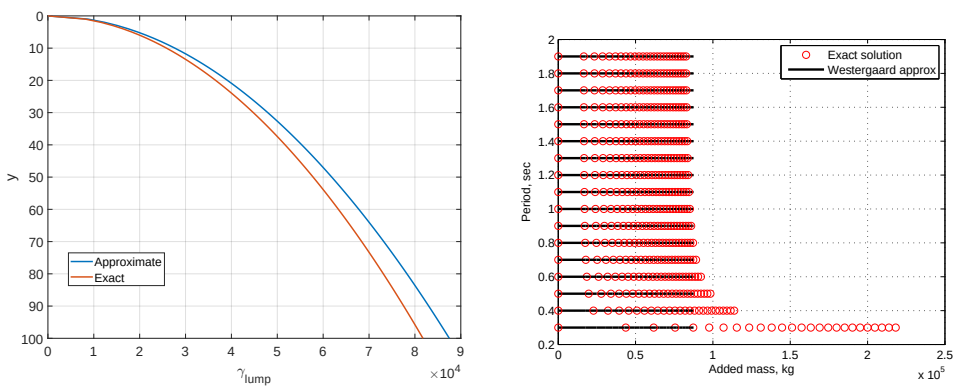

(a) Lumped mass per unit area versus the height

(b) Added mass versus the vibration period

Figure 5.4: Comparison of the approximate and exact solutions for a hypothetical dam; Adapted from Saouma and Hariri-Ardebili (2021c)

5.2 Dynamic Soil Structure Interaction

All operating plants in the United States must quantify the margin for beyond design basis events and take necessary actions to improve the margin if required. This effort is mostly completed by performing Seismic Probabilistic Risk Assessment (SPRA) requiring Soil-Structure Interaction (SSI) analysis as part of the overall analysis. Given the site profile data and the structural model developed as part of the Final Safety Analysis Report (FSAR) are generated many years ago, it is necessary to evaluate the SSI effects for structures founded on rock sites which were considered as fixed base condition during the original analysis.

It is often assumed that dynamic analysis for existing plants that are rock-founded (i.e. with shear wave velocity > 3500 fps) may be completed without consideration of soil structure interaction (SSI) effects (Hashemi, 2012).

5.2.1 Lysmer Model

Lysmer and Kuhlemeyer (1969) were the first to investigate this problem. Their solution is simple, elegant and quite effective. It is based on the premises that one can surround the rock boundary by *viscous boundaries* (through energy absorbent dashpots) with

$$t_n = \rho V_P \dot{u}; \quad t_{s1} = \rho V_S \dot{v}; \quad t_{s2} = \rho V_S \dot{w}; \tag{5.51}$$

where t_n and t_s are the normal and shear tractions respectively; $\dot{u}$, $\dot{v}$ and $\dot{w}$ the normal and two tangential particle velocities at the boundary; ρ is the mass density; V_S and V_P are the shear and pressure waves velocities respectively given by

$$V_S = \sqrt{\frac{\mu}{\rho}} \quad \text{and} \quad V_P = \frac{1}{s} V_S \quad \text{where} \quad s^2 = \frac{1-2\nu}{2(1-\nu)} \tag{5.52}$$

where μ and ν are the shear modulus and the Poisson ratio respectively.

Lysmer determined the ratio of the reflected energy to incident energy (of the P waves per unit time per unit area) as

$$\frac{E_r}{E_i} = A^2 + s\frac{\sin\beta}{\sin\alpha}B^2 \tag{5.53}$$

where a unit ratio corresponds to a perfect reflection (undesired), while a zero ratio corresponds to complete absorption (desired). A similar equation was determined for S waves. In both cases, it was found that a viscous boundary defined by $a = b = 1$ is: a) 95% effective in absorbing S waves; and b) absorbs nearly all waves for $\alpha > 30^o$ (some reflection occurs at smaller angles), Figure 5.5.

One must thus enforce the so-called Sommerfeld boundary condition (Zienkiewicz, Kelly, and Bettess, 1979) which is more casually referred to as Lysmer-Kuhlemeyer boundary condition. It is an exact solution if the P and S waves impinge at a right angle the artificial boundary. However they are only approximate solutions for inclined body waves where the reflected energy is only a

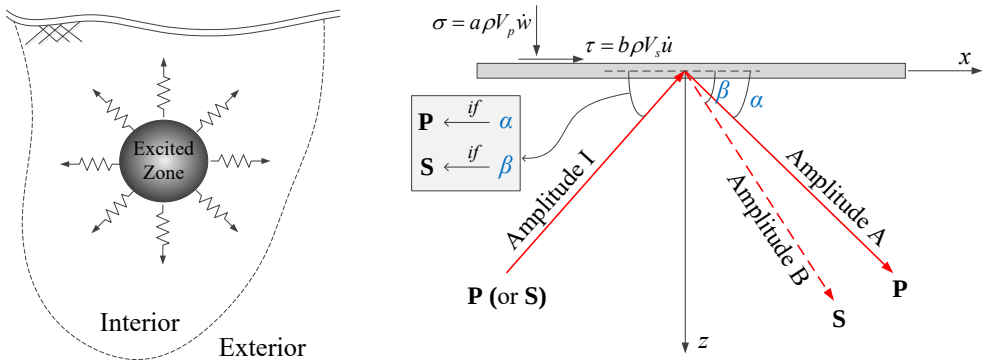

(a) Typical infinite system

(b) Incident P- and S-waves at viscous boundary

Figure 5.5: Elastic waves in an infinite medium

small part of the total energy. In many cases, the farther one chooses the artificial boundary to be from a source which radiates waves, the more the angle of incidence with respect to the artificial boundary will approach 90°, and, thus, the better the viscous dampers will perform, (Wolf, 1988).

A major limitation of this approach is that the required damping coefficients are frequency dependent and consequently they can (strictly speaking) only be used in frequency domain calculations, though they are also often used in time domain analyses such as in (Zhang et al., 2003).

From a practical point of view, in the context of a finite element simulation, Fig. 5.6 illustrates the dashpot distribution for a mesh subjected to only lateral excitation. Should there be a vertical component, then the vertical support at the base of the dashpots should also be removed (which would raise some problems in the presence of body forces). This model has been implemented in the SHAKE program for the frequency-domain analysis for shear-wave propagation in layered soils (Schnabel, Lysmer, and Seed, 1972).

Whereas the viscous boundary model eliminated wave reflections, it did not necessarily account for the proper boundary conditions. This was addressed by Lysmer and Drake (1972) in an *energy transmitting boundary* model. This model assumed a linear variation of shear strain, and those in turn are transformed into equivalent nodal forces to be applied on the numerical one. This model was implemented in (frequency domain) program FLUSH, (Lysmer, Udaka, and Seed, 1975).

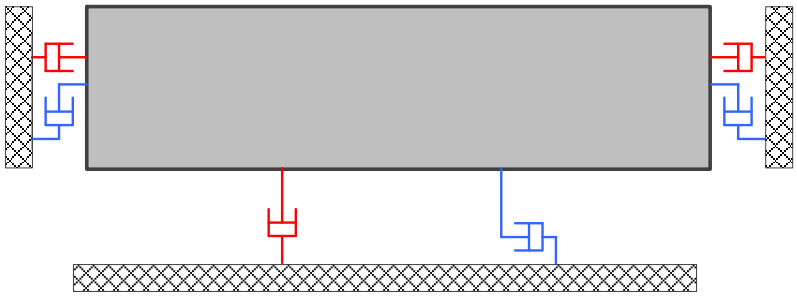

Figure 5.6: Lysmer Modeling for Lateral Excitation

Finally,Lysmer boundary conditions can modeled in Merlin using either one of two models, figure 5.7: lumped or distributed.

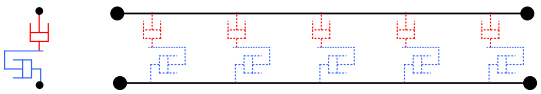

(a) Lumped viscous element

(b) Distributed viscous element

Figure 5.7: Viscous elements (dash-pots)

5.2.2 Other SSI Models

A *Superimposing boundaries* approach was proposed by Smith (1974) who showed that the reflection from the boundary of a model can be completely eliminated by simply adding the solutions of the Dirichlet and Neumann problems (corresponding to free and fixed boundaries respectively). Hence two separate analyses are performed with different boundary conditions. The first with fixed in normal and free in the tangential, the second free in normal and fixed in tangential directions. Furthermore, if n boundary faces are required to be nonreflecting, than 2^n solutions will be necessary for a full solution. Cundall et al. (1979) refined this method by summing incrementally the Dirichlet and Neumann solutions at the boundaries of the finite element (or finite difference). This

had the advantage of eliminating the reflections as soon as they occur, and thus multiple reflections (encountered by Smith) are voided and only one solution must be performed. However, the fixed-free boundary conditions of Smith are replaced by constant velocity, constant stress ones. In a two dimensional analysis, this corresponds to a) constant velocity in the x and constant stress in the y; and b) constant stress in the x and constant velocity in the y. Again, rather than performing the same calculation twice with different boundary conditions (as suggested by Smith), two overlapping grids are employed (modeling the free field) with each of the two boundary conditions used separately for each grid. Boundary being represented by four elements, all variables of the two grids are added every three or four time-steps. Hence, the Lysmer-Kuhlemeyer model with absorbing dashpots on the side and bottom is now enriched with a simultaneous free-field calculation that imposes stress conditions on the side boundaries. This model was implemented in the time-history program NEESI, (Cundall et al., 1980). Analysis of a dam using analogous boundary conditions was performed by Lemos (1999) (albeit with a discrete element system) in which one-dimensional calculations representing the left and right free-field conditions are performed in parallel with the main model. The free field is represented by a one-dimensional finite-difference mesh.

Bielak and Christiano (1984) introduced an effective seismic input model model in which the soil-structure interaction problem is transformed into one in which the source is exclusively inside the computation domain, thus eliminating the need to explicitly transmit seismic excitation through the boundary (which has to simply absorb the outgoing waves).

These two step approaches are analogous to the one of Bielak et al. (2001) where heterogeneity and scale are accounted for through a two tier approach. The first at the macro scale represents the "far-field" in great details and simulates the earthquake source and propagation path effects with a detailed model. The second models local site effects and presumably includes the structure of interest. Those two analyses are coupled through continuity of displacements and transfer of forces from the first subdomain to the other.

A most recent and noteworthy development, which alleviates the restriction placed on the orientation of the incoming wave, is the Perfectly Matched Layer (PML) (originally developed for

electromagnetic wave propagation). When this layer is placed adjacent to a truncated model of an unbounded domain, waves of all frequencies and all angles of incidence are absorbed into without any reflection from the interface: the PML is thus "perfectly matched" to the truncated domain, (Basu and Chopra, 2004) and (Basu, 2009).

It should be noted that the implementation of both the effective seismic input and the perfectly matched layer require substantial modification of the computer code. This is not the case in the proposed model.

Despite the numerous innovative models in SSI, even applications continue to use the Lysmer-Kuhlmeyer model as is the case in Zhang et al. (2003).

5.2.3 Miura-Saouma (MS) Model

5.2.3.1 Disclaimer

The model of Saouma et al. (2011) will be described in great details in this section. The model is conceptually simple to understand, but complex to implement.

A major contribution of this thesis is the development of a library of matlab codes to automate the procedure for ssi using any arbitrary finite element program (Saouma, Červenka, and Reich (2010) in this case). This required a thorough review of the original paper (where a few mistakes were uncovered), the implementation of the model, its verification and finally its use with an actual dam (not previously done).

Because of the extensive number of equations, and complex figures, the author acknowledge to have adapted this section from Saouma and Hariri-Ardebili (2021b) (to rewrite the section in her own words, and to redraw the figures, would have consumed the better of two-three months of effort). Instead effort was focused on the numerical tasks.

5.2.3.2 Introduction

In an earlier publication (in Japanese) Miura and Toki (1987) and (Japan Society of Civil Engineers, 2000) considered both viscous boundary and energy transmitting boundaries. Those are

divided into a) absorption of scattering wave energy on the sides and the bottom; and b) energy inflow from outer free fields.

The model was investigate by Saouma through his contract with the Tokyo Electric Power Service Company (TEPSCO) which required its implementation in Merlin. The model was deemed to be incomplete, and lacking proper traceable derivations by the first author. More specifically, there is no derivation of the matrices, how the method is to be actually implemented in a finite element analysis, and is limited to 2D homogeneous models. A closer examination of the Japanese version of the model, (Miura and Okinaka, 1989), indicates that the free field is analysed in parallel with the main body, and the principle of virtual work is invoked in the derivation. Regretfully, the derivation is again limited to 2D problems, and many critical steps are omitted. Finally, a 2D implementation of this model is reported to be in (Kenkyusho, 1995).

Hence, the authors have revisited the original model of Miura, systematically rederived all the equations, extended it to three dimensional non-homogeneous problems and provided the reader with all necessary analytical expressions for the finite element implementation (Saouma et al., 2011).

It will be shown that implementation of this method does not require internal modification of a finite element code, however extensive data transfer between separate analyses would have to be performed. Lebon, Saouma, and Uchita (2010) reports on the results of a parametric investigation contrasting Lysmer's model, Miura's model, and the lack of absorbing boundary conditions in the context of transient analysis of a concrete dam.

The model seeks to concurrently account for 1) absorption of the outgoing scattered wave motion (or radiation damping); and 2) input of the free field ground motion into the numerical model.

The former will be addressed by the classical Lysmer-Kuhlemeyer model. On the other hand, the input from the free field will be addressed through separate analysis, and resulting displacements and velocities will be transferred as discrete forces to the model.

A key advantage of this method, is the simplicity of the model, and the fact that it is purely

a pre or post processing operation which (contrarily to some prevailing methods) does not require modification of the source code. All relevant equations (including 3D) are given, thus greatly facilitating implementation of the model with existing finite element codes. It is worth noting that, the same concept has been used with a different implementation approach by Løkke and Chopra (2019).

5.2.3.3 Model Description

The interaction between the free field and the foundation is examined first, Fig. 5.8. We

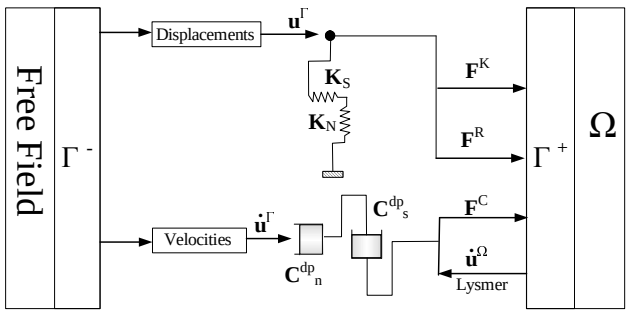

Figure 5.8: Conceptual Model

identify four distinct parts: 1) The free field itself (F) without its contact surface Γ^-; 2) The contact surface of the free field Γ^-; 3) the contact surface of the model Γ^+; and 4) the model Ω without its contact surface Γ^+. Hence, mass, damping, and stiffness matrices can each be decomposed into four parts as

$$\left[\begin{array}{cc|cc} FF & F\Gamma^- & F\Gamma^+ & F\Omega \\ \Gamma^- F & \Gamma^-\Gamma^- & \Gamma^-\Gamma^+ & \Gamma^-\Omega \\ \hline \Gamma^+ F & \Gamma^+\Gamma^- & \Gamma^+\Gamma^+ & \Gamma^+\Omega \\ \Omega F & \Omega\Gamma^- & \Omega\Gamma^+ & \Omega\Omega \end{array}\right] \tag{5.54}$$

where each term XY infers the effect of Y on X. This is clearly a tightly coupled problem, however if we neglect the influence of the model on the free field response, this reduces to

$$\left[\begin{array}{cc|cc} FF & F\Gamma^- & 0 & 0 \\ \Gamma^- F & \Gamma^-\Gamma^- & 0 & 0 \\ \hline 0 & 0 & \Gamma^+\Gamma^+ & \Gamma^+\Omega \\ 0 & 0 & \Omega\Gamma^+ & \Omega\Omega \end{array}\right] \rightarrow \left[\begin{array}{c|c} F & 0 \\ \hline 0 & \Omega^* \end{array}\right] \tag{5.55}$$

then $\Gamma^-\Gamma^+$ becomes zero we now have a loosely coupled system through $\Gamma^+\Gamma^-$. Hence we can consider the equation of motion for the free field by itself, and will account for the interaction in the equation of motion in Ω by adding forces, stemming from $\Gamma^+\Gamma^-$, on the right hand side. We next write the first equation of motion for the free field:

$$\mathbf{M}^F\ddot{\mathbf{u}}^F + \mathbf{C}^F\dot{\mathbf{u}}^F + \mathbf{K}^F\mathbf{u}^F = \mathbf{t}^F \tag{5.56}$$

solving this equation, we determine the displacements and velocities along Γ^-, and then solve for the equation of motion in the model:

$$\mathbf{M}^\Omega\ddot{\mathbf{u}}^\Omega + \mathbf{C}^\Omega\dot{\mathbf{u}}^\Omega + \mathbf{K}^\Omega\mathbf{u}^\Omega = \mathbf{t}^\Omega_{\text{bot}} - \underbrace{\left(\mathbf{C}^R_{\text{lft}}\dot{\mathbf{u}}^{\Gamma^-}_{\text{lft}} + \mathbf{K}_{\text{lft}}\mathbf{u}^{\Gamma^-}_{\text{lft}}\right)}_{\text{Left Virtual Interface}} - \underbrace{\left(\mathbf{C}^R_{\text{rgt}}\dot{\mathbf{u}}^{\Gamma^-}_{\text{rgt}} + \mathbf{K}_{\text{rgt}}\mathbf{u}^{\Gamma^-}_{\text{rgt}}\right)}_{\text{Right Virtual Interface}} \tag{5.57}$$

where $\mathbf{M}$, $\mathbf{C}$, and $\mathbf{K}$ are the usual mass, damping and stiffness matrices respectively; the subscripts $_{\text{lft}}$, $_{\text{rgt}}$, and $_{\text{bot}}$ correspond to left, right, and bottom; the superscript R corresponds to Rayleigh damping.

So far, we have not accounted for one of the premises of the model, that is absorbtion of the outgoing scattered wave, this is simply added through the inclusion of the dashpots in accordance with the Lysmer-Kuhlmeyer model. We note that the viscous forces should be expressed in terms of the relative displacements between Γ^+ and Γ^-.

$$\begin{aligned}\mathbf{M}^\Omega\ddot{\mathbf{u}}^\Omega + \mathbf{C}^\Omega\dot{\mathbf{u}}^\Omega + \mathbf{K}^\Omega\mathbf{u}^\Omega + \mathbf{C}^{dp}_{\text{lft}}\left(\dot{\mathbf{u}}^{\Gamma^+}_{\text{lft}} - \dot{\mathbf{u}}^{\Gamma^-}_{\text{lft}}\right) + \mathbf{C}^{dp}_{\text{rgt}}\left(\dot{\mathbf{u}}^{\Gamma^+}_{\text{rgt}} - \dot{\mathbf{u}}^{\Gamma^-}_{\text{rgt}}\right) + \mathbf{C}^{dp}_{\text{bot}}\dot{\mathbf{u}}^\Omega_{\text{bot}} \\ = \mathbf{t}^\Omega_{\text{bot}} - \left(\mathbf{C}^R_{\text{lft}}\dot{\mathbf{u}}^{\Gamma^-}_{\text{lft}} + \mathbf{K}_{\text{lft}}\mathbf{u}^{\Gamma^-}_{\text{lft}}\right) - \left(\mathbf{C}^R_{\text{rgt}}\dot{\mathbf{u}}^{\Gamma^-}_{\text{rgt}} + \mathbf{K}_{\text{rgt}}\mathbf{u}^{\Gamma^-}_{\text{rgt}}\right)\end{aligned} \tag{5.58}$$

This equation can be rewritten by separating known and unknown quantities, and : substituting the effects of the free field displacements and velocities by their corresponding nodal equivalent

forces

$$\left[\mathbf{M}^{\Omega}\ddot{\mathbf{u}}^{\Omega}+\mathbf{C}^{\Omega}\dot{\mathbf{u}}^{\Omega}+\mathbf{K}^{\Omega}\mathbf{u}^{\Omega}\right]+\left[\mathbf{C}^{dp}_{\text{lft}}\dot{\mathbf{u}}^{\Omega}_{\text{lft}}+\mathbf{C}^{dp}_{\text{rgt}}\dot{\mathbf{u}}^{\Omega}_{\text{rgt}}+\mathbf{C}^{dp}_{\text{bot}}\dot{\mathbf{u}}^{\Omega}_{B}\right]$$
$$=\mathbf{t}^{\Omega}_{\text{bot}}+\left[\mathbf{F}^{C}_{\text{lft}}+\mathbf{F}^{K}_{\text{lft}}+\mathbf{F}^{R}_{\text{lft}}\right]+\left[\mathbf{F}^{C}_{\text{rgt}}+\mathbf{F}^{K}_{\text{rgt}}+\mathbf{F}^{R}_{\text{rgt}}\right] \tag{5.59}$$

Where $\mathbf{F}^{C}$, $\mathbf{F}^{K}$, and $\mathbf{F}^{R}$ are the vectors of nodal equivalent forces caused by the free field velocities, stiffness and damping respectively. They will be separately derived later. The corresponding three dimensional equation would be

$$\left[\mathbf{M}^{\Omega}\ddot{\mathbf{u}}^{\Omega}+\mathbf{C}^{\Omega}\dot{\mathbf{u}}^{\Omega}+\mathbf{K}^{\Omega}\mathbf{u}^{\Omega}\right]+\left[\mathbf{C}^{dp}_{\text{lft}}\dot{\mathbf{u}}^{\Omega}_{\text{lft}}+\mathbf{C}^{dp}_{\text{rgt}}\dot{\mathbf{u}}^{\Omega}_{\text{rgt}}+\mathbf{C}^{dp}_{\text{bck}}\dot{\mathbf{u}}^{\Omega}_{\text{bck}}+\mathbf{C}^{dp}_{\text{fro}}\dot{\mathbf{u}}^{\Omega}_{\text{fro}}+\mathbf{C}^{dp}_{\text{bot}}\dot{\mathbf{u}}^{\Omega}_{B}\right]$$
$$=\mathbf{t}^{\Omega}_{\text{bot}}+\left[\mathbf{F}^{C}_{\text{lft}}+\mathbf{F}^{K}_{\text{lft}}+\mathbf{F}^{R}_{\text{lft}}\right]+\left[\mathbf{F}^{C}_{\text{rgt}}+\mathbf{F}^{K}_{\text{rgt}}+\mathbf{F}^{R}_{\text{rgt}}\right]+\left[\mathbf{F}^{C}_{\text{bck}}+\mathbf{F}^{K}_{\text{bck}}+\mathbf{F}^{R}_{\text{bck}}\right]+\left[\mathbf{F}^{C}_{\text{fro}}+\mathbf{F}^{K}_{\text{fro}}+\mathbf{F}^{R}_{\text{fro}}\right] \tag{5.60}$$

where $_{\text{bck}}$ and $_{\text{fro}}$ correspond to the back and front sides respectively.

To derive the expressions of the forces in the right hand side of Eq. 5.60 we apply the principle of virtual work to the *system*

$$\int_{\Omega}\delta\mathbf{u}.\left[\rho\ddot{\mathbf{u}}+\eta\dot{\mathbf{u}}+\mathbf{F}\right]\mathrm{d}\Omega=\int_{\Gamma}\delta\mathbf{u}.\left(\mathbf{t}^{\text{bot}}+\mathbf{t}^{\Gamma^{-}}\right)\mathrm{d}\Gamma \tag{5.61}$$

where ρ is the mass density, η the viscosity parameter, $\mathbf{F}$ the internal force, $\mathbf{u}$ the displacement vector, $\mathbf{t}^{\text{bot}}$ and $\mathbf{t}^{\Gamma^{-}}$ are the surface traction on the boundary Γ (base and free field). It can be readily shown that the left and right hand sides of Eq. 5.61 corresponds to the integral form of the left and right hand sides of Eq. 5.60 respectively.

Internal Virtual Work

Discretizing the continuum through shape function, (Zienkiewicz, Taylor, and Zhu, 2005), it can be readily shown that the left hand side and the first right hand side term of Eq. 5.61 correspond to the classical form of the equation of motion

$$\mathbf{M}^{\Omega}\ddot{\mathbf{u}}^{\Omega}+\mathbf{C}^{\Omega}\dot{\mathbf{u}}^{\Omega}+\mathbf{K}\mathbf{u}^{\Omega}$$

In the context of the present analysis, this can be generalized to the right hand side of Eq. 5.60.

External Virtual Work

Focusing on the remaining term of the external virtual force can be expressed as

$$\int_{\Gamma} \delta \mathbf{u}.\mathbf{t}^{\Gamma^-} \mathrm{d}\Gamma = \int_0^{t_y} \int_0^{t_z} \left[\delta u t_n + \delta v t_{s1} + \delta w t_{s2}\right] \mathrm{d}z\mathrm{d}y \tag{5.62}$$

In the next sections we will separately determine the tractions caused by presence of dashpots or the free field displacements.

Forces Caused by Velocity

Due to the presence of the dashpots around the bounded model, we substitute Eq. 5.52 into Eq. 5.62. It should be noted that in the model, the velocities will actually correspond to difference in velocities between the free field and the bounded model: $\dot{\mathbf{u}}^{\Omega}_{\text{lft}} - \dot{\mathbf{u}}^{\Gamma^-}_{\text{lft}}$ as in Eq. 5.58. The nodal displacements along the surface boundary can be expressed in terms of the known nodal ones through the shape functions (assuming a linear variation). Considering the x-plane the finite element discretization yields

$$\begin{cases} u = \mathbf{N}_u \overline{\mathbf{u}}; \quad \delta u = \mathbf{N}_u \delta \overline{\mathbf{u}}; \quad V_p \dot{u} = V_p \mathbf{N}_u \dot{\overline{\mathbf{u}}} \\ v = \mathbf{N}_v \overline{\mathbf{u}}; \quad \delta v = \mathbf{N}_v \delta \overline{\mathbf{u}}; \quad V_s \dot{v} = V_s \mathbf{N}_v \dot{\overline{\mathbf{u}}} \\ w = \mathbf{N}_w \overline{\mathbf{u}}; \quad \delta w = \mathbf{N}_w \delta \overline{\mathbf{u}}; \quad V_s \dot{w} = V_s \mathbf{N}_w \dot{\overline{\mathbf{u}}} \end{cases} \tag{5.63}$$

where the shape functions, for the bilinear element shown in Fig. 5.9, are given by

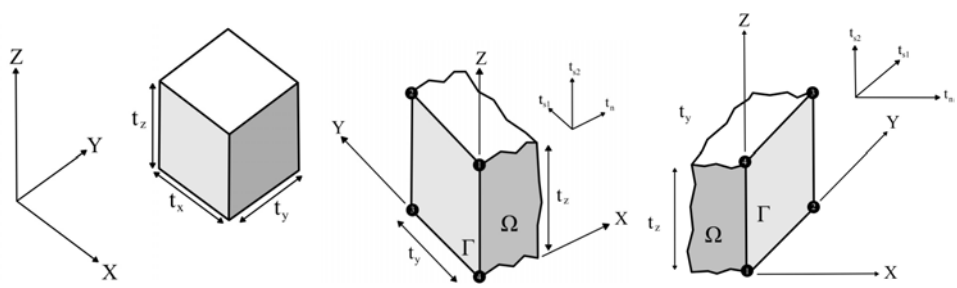

Figure 5.9: 2D Idealization and Γ_x Plane

$$
\begin{aligned}
\mathbf{N}_u &= \tfrac{1}{t_y t_z}\lfloor\ (t_y-y)(t_z-z) \quad 0 \quad 0 \quad (t_z-z)y \quad 0 \quad 0 \quad zy \quad 0 \quad 0 \quad z(t_y-y) \quad 0 \quad 0\ \rfloor^T \\
\mathbf{N}_v &= \tfrac{1}{t_y t_z}\lfloor\ 0 \quad (t_y-y)(t_z-z) \quad 0 \quad 0 \quad (t_z-z)y \quad 0 \quad 0 \quad zy \quad 0 \quad 0 \quad z(t_y-y) \quad 0\ \rfloor^T \\
\mathbf{N}_w &= \tfrac{1}{t_y t_z}\lfloor\ 0 \quad 0 \quad (t_y-y)(t_z-z) \quad 0 \quad 0 \quad (t_z-z)y \quad 0 \quad 0 \quad zy \quad 0 \quad 0 \quad z(t_y-y)\ \rfloor^T
\end{aligned}
\tag{5.64}
$$

and

$$
\overline{\mathbf{u}} = \lfloor\ \overline{u}_1 \quad \overline{v}_1 \quad \overline{w}_1 \quad \overline{u}_2 \quad \overline{v}_2 \quad \overline{w}_2 \quad \overline{u}_3 \quad \overline{v}_3 \quad \overline{w}_3 \quad \overline{u}_4 \quad \overline{v}_4 \quad \overline{w}_4\ \rfloor^T \tag{5.65}
$$

Substituting[1] in Eq. 5.62,

$$
\int_\Gamma \delta\mathbf{u}.\mathbf{t}\mathrm{d}\Gamma = \rho\int_0^{t_z}\int_0^{t_y} V_p\mathbf{N}_u.\mathbf{N}_u^T + V_s\left(\mathbf{N}_v.\mathbf{N}_v^T + \mathbf{N}_w.\mathbf{N}_w^T\right)\mathrm{d}y\mathrm{d}z \tag{5.66}
$$

or $\mathbf{F}^C = \mathbf{C}_x^{dp}\dot{\mathbf{u}}$ where

$$
\mathbf{C}_x^L = \frac{\rho t_y t_z}{36}\begin{bmatrix}
4V_p & 0 & 0 & 2V_p & 0 & 0 & V_p & 0 & 0 & 2V_p & 0 & 0 \\
0 & 4V_s & 0 & 0 & 2V_s & 0 & 0 & V_s & 0 & 0 & 2V_s & 0 \\
0 & 0 & 4V_s & 0 & 0 & 2V_s & 0 & 0 & V_s & 0 & 0 & 2V_s \\
2V_p & 0 & 0 & 4V_p & 0 & 0 & 2V_p & 0 & 0 & V_p & 0 & 0 \\
0 & 2V_s & 0 & 0 & 4V_s & 0 & 0 & 2V_s & 0 & 0 & V_s & 0 \\
0 & 0 & 2V_s & 0 & 0 & 4V_s & 0 & 0 & 2V_s & 0 & 0 & V_s \\
V_p & 0 & 0 & 2V_p & 0 & 0 & 4V_p & 0 & 0 & 2V_p & 0 & 0 \\
0 & V_s & 0 & 0 & 2V_s & 0 & 0 & 4V_s & 0 & 0 & 2V_s & 0 \\
0 & 0 & V_s & 0 & 0 & 2V_s & 0 & 0 & 4V_s & 0 & 0 & 2V_s \\
2V_p & 0 & 0 & V_p & 0 & 0 & 2V_p & 0 & 0 & 4V_p & 0 & 0 \\
0 & 2V_s & 0 & 0 & V_s & 0 & 0 & 2V_s & 0 & 0 & 4V_s & 0 \\
0 & 0 & 2V_s & 0 & 0 & V_s & 0 & 0 & 2V_s & 0 & 0 & 4V_s
\end{bmatrix}
\tag{5.67}
$$

The same expression applies on the positive and negative faces.

The two dimensional equivalent matrix is obtained by simply adding rows and columns 1-4,

[1] All operations performed by *Mathematica*.

3-6, 7-10, 9-12 (while dropping rows and columns 2, 5, 8 and 11) in Eq. 5.67. This reduces to

$$\mathbf{F}^C = \frac{\rho t_z}{6}\begin{bmatrix} 2V_p & 0 & V_p & 0 \\ 0 & 2V_s & 0 & V_s \\ V_p & 0 & 2V_p & 0 \\ 0 & V_s & 0 & 2V_s \end{bmatrix}\begin{Bmatrix} \dot{u}_1 \\ \dot{v}_1 \\ \dot{u}_2 \\ \dot{v}_2 \end{Bmatrix} \tag{5.68}$$

It should be noted that both the left and right sides will be subjected to the same $\mathbf{C}_x^L$ matrix.

Forces Caused by Displacements

The lateral forces exerted on the bounded domain by the free field displacements are determined next. The free field will be modeled as a shear beam (where $\frac{\partial u}{\partial x} = 0$) and in the most general case, Fig. 5.9, there will be displacements along the three axis x, y and z. Hence, unsymmetric and non-homogeneous boundaries could be accounted for. The traction terms to be substituted in Eq. 5.62 are thus

$$\begin{cases} t_n = \sigma_{xx} = \lambda\left(\varepsilon_{xx} + \varepsilon_{yy} + \varepsilon_{zz}\right) + 2\mu\varepsilon_{xx} = \lambda\left(\frac{\partial v}{\partial y} + \frac{\partial w}{\partial z}\right) \\ t_{s1} = \tau_{xy} = \mu\gamma_{xy} = \mu\frac{\partial u}{\partial y} \\ t_{s2} = \tau_{xz} = \mu\gamma_{xz} = \mu\frac{\partial u}{\partial z} \end{cases} \tag{5.69}$$

where λ and μ are the classical Lame's parameters,

$$\lambda = \frac{\nu E}{(1+\nu)(1-2\nu)}; \qquad \mu = \frac{E}{2(1+\nu)} \tag{5.70}$$

The internal displacements can be expressed in terms of the known nodal ones through the shape functions, Eq. 5.64. Substituting into Eq. 5.62, we obtain:

$$\delta W_{ext} = \delta\overline{\mathbf{u}}\int_0^{t_z}\int_0^{t_y}\left[\mathbf{N}_u.\left[\lambda\left(\frac{\partial \mathbf{N}_v}{\partial y} + \frac{\partial \mathbf{N}_w}{\partial z}\right)\right] + \mathbf{N}_v.\left(\mu\frac{\partial \mathbf{N}_u}{\partial y}\right) + \mathbf{N}_w.\left(\mu\frac{\partial \mathbf{N}_u}{\partial z}\right)\right]\mathrm{d}y\mathrm{d}z\overline{\mathbf{u}} \tag{5.71}$$

Or

$$\mathbf{F}^K = \mathbf{K}_x^+\overline{\mathbf{u}} \tag{5.72}$$

where

$$\mathbf{F}^K = \lfloor\ F_{1,u} \quad F_{1,v} \quad F_{1,w} \quad F_{2,u} \quad F_{2,v} \quad F_{2,w} \quad F_{3,u} \quad F_{3,v} \quad F_{3,w} \quad F_{4,u} \quad F_{4,v} \quad F_{4,w}\ \rfloor^T \tag{5.73}$$

and the corresponding stiffness matrix is given by

$$\mathbf{K}_x^+ = \frac{1}{12}\begin{bmatrix} 0 & -2t_z\lambda & -2t_y\lambda & 0 & 2t_z\lambda & -t_y\lambda & 0 & t_z\lambda & t_y\lambda & 0 & -t_z\lambda & 2t_y\lambda \\ -2t_z\mu & 0 & 0 & 2t_z\mu & 0 & 0 & t_z\mu & 0 & 0 & -t_z\mu & 0 & 0 \\ -2t_y\mu & 0 & 0 & -t_y\mu & 0 & 0 & t_y\mu & 0 & 0 & 2t_y\mu & 0 & 0 \\ 0 & -2t_z\lambda & -t_y\lambda & 0 & 2t_z\lambda & -2t_y\lambda & 0 & t_z\lambda & 2t_y\lambda & 0 & -t_z\lambda & t_y\lambda \\ -2t_z\mu & 0 & 0 & 2t_z\mu & 0 & 0 & t_z\mu & 0 & 0 & -t_z\mu & 0 & 0 \\ -t_y\mu & 0 & 0 & -2t_y\mu & 0 & 0 & 2t_y\mu & 0 & 0 & t_y\mu & 0 & 0 \\ 0 & -t_z\lambda & -t_y\lambda & 0 & t_z\lambda & -2t_y\lambda & 0 & 2t_z\lambda & 2t_y\lambda & 0 & -2t_z\lambda & t_y\lambda \\ -t_z\mu & 0 & 0 & t_z\mu & 0 & 0 & 2t_z\mu & 0 & 0 & -2t_z\mu & 0 & 0 \\ -t_y\mu & 0 & 0 & -2t_y\mu & 0 & 0 & 2t_y\mu & 0 & 0 & t_y\mu & 0 & 0 \\ 0 & -t_z\lambda & -2t_y\lambda & 0 & t_z\lambda & -t_y\lambda & 0 & 2t_z\lambda & t_y\lambda & 0 & -2t_z\lambda & 2t_y\lambda \\ -t_z\mu & 0 & 0 & t_z\mu & 0 & 0 & 2t_z\mu & 0 & 0 & -2t_z\mu & 0 & 0 \\ -2t_y\mu & 0 & 0 & -t_y\mu & 0 & 0 & t_y\mu & 0 & 0 & 2t_y\mu & 0 & 0 \end{bmatrix} \tag{5.74}$$

Rayleigh Damping

$$\left[\mathbf{F}^R\right] = \frac{\zeta}{\pi f}\left[\mathbf{K}\right] \tag{5.75}$$

where ζ is the damping factor at frequency f. We note that this is stiffness proportional only since we are dealing with a massless element.

Again, the two dimensional equivalent matrix is obtained by simply adding rows and columns 1-4, 3-6, 7-10, 9-12 (while dropping rows and columns 2, 5, 8 and 11). This reduces to If we were to limit ourselves to the two dimensional case, then on the lateral boundary

$$\delta W_{ext} = \delta\mathbf{u}.\mathbf{t} = t\int_0^h \left[\delta u t_n + \delta w t_s\right] \mathrm{d}z \tag{5.76}$$

and

$$\begin{cases} t_n = \sigma_{xx} = \lambda\left(\varepsilon_{xx} + \varepsilon_{zz}\right) + 2\mu\varepsilon_{xx} = \lambda\frac{\partial w}{\partial z} \\ t_s = \tau_{xz} = \mu\varepsilon_{xz} = \mu\frac{\partial u}{\partial z} \end{cases} \tag{5.77}$$

The internal displacements can be expressed in terms of the known nodal ones through the linear shape functions. Substituting into equation 5.76, we obtain:

$$\delta W = t\delta\overline{\mathbf{u}}\int_0^h \left[\underbrace{\mathbf{N}_u.\lambda\frac{\partial\mathbf{N}_w}{\partial z}}_{K_n} + \underbrace{\mathbf{N}_w.\mu\frac{\partial\mathbf{N}_u}{\partial z}}_{K_s}\right]\overline{\mathbf{u}}\mathrm{d}z \tag{5.78}$$

or $\mathbf{F}^K = \mathbf{K}\overline{\mathbf{u}}$ where

$$\mathbf{F}^K = \lfloor\ F_{1,u} \quad F_{1,v} \quad F_{2,u} \quad F_{2,v}\ \rfloor^T \tag{5.79}$$

These equations are similar to the one of Miura in the Super flush manual (Kenkyusho, 1995).

$$\mathbf{K}_x^+ = \frac{1}{2}\begin{bmatrix} 0 & -\lambda & 0 & \lambda \\ -\mu & 0 & \mu & 0 \\ 0 & -\lambda & 0 & \lambda \\ -\mu & 0 & \mu & 0 \end{bmatrix} \tag{5.80}$$

5.2.3.4 Finite Element Formulation

Recognizing that in practice we do not have a rigid support for the foundation but rather a flexible one, we need to account for this added variability, Figure 5.10.

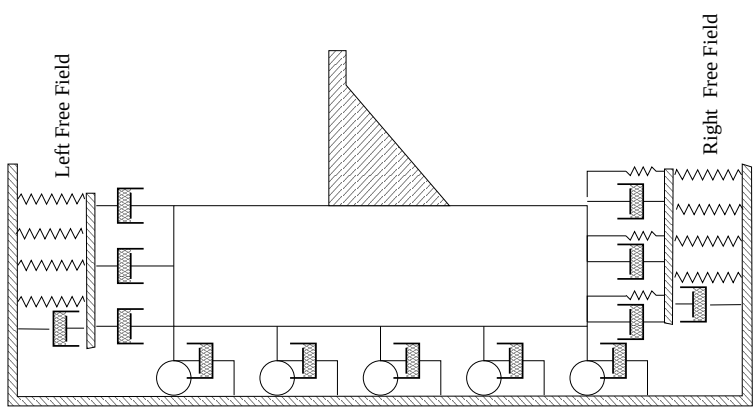

Figure 5.10: Foundation boundary conditions for radiating flexible foundation

The methodology adopted here is based on the work of Miura and Toki, 1987. The governing

equation for a dam foundation system in an infinite flexible medium is given by

$$
\begin{aligned}
&[\mathbf{M}]\{\ddot{\mathbf{x}}\} + ([\mathbf{C}] + [\mathbf{C}_B] + [\mathbf{C}_L] + [\mathbf{C}_R])\{\dot{\mathbf{x}}\} + [\mathbf{K}]\{\mathbf{x}\} \\
&= \{\mathbf{f}\} + [\mathbf{C}_L]\{\dot{\mathbf{x}}_L\} + [\mathbf{C}_R]\{\dot{\mathbf{x}}_R\} + [\mathbf{G}_{CL}]\{\dot{\mathbf{x}}_L\} \\
&+ [\mathbf{G}_{CR}]\{\dot{\mathbf{x}}_R\} + [\mathbf{G}_L]\{\mathbf{x}_L\} + [\mathbf{G}_R]\{\mathbf{x}_R\}
\end{aligned}
\tag{5.81}
$$

This equation can be rewritten as

$$
\begin{aligned}
&\left[\begin{array}{cc|c|c}
\mathbf{M}_{II} & \mathbf{M}_{IB} & \mathbf{M}_{IL} & \mathbf{M}_{IR} \\
\mathbf{M}_{BI} & \mathbf{M}_{BB} & \mathbf{M}_{BL} & \mathbf{M}_{BR} \\
\hline
\mathbf{M}_{LI} & \mathbf{M}_{LB} & \mathbf{M}_{LL} & 0 \\
\hline
\mathbf{M}_{RI} & \mathbf{M}_{RB} & 0 & \mathbf{M}_{RR}
\end{array}\right]
\left\{\begin{array}{c}
\ddot{\mathbf{x}} \\ \ddot{\mathbf{x}}_B \\ \ddot{\mathbf{x}}_L \\ \ddot{\mathbf{x}}_R
\end{array}\right\}
+
\left[\begin{array}{cc|c|c}
\mathbf{C}_{II} & \mathbf{C}_{IB} & \mathbf{C}_{IL} & \mathbf{C}_{IR} \\
\mathbf{C}_{BI} & \mathbf{C}_{BB} & \mathbf{C}_{BL} & \mathbf{C}_{BR} \\
\hline
\mathbf{C}_{LI} & \mathbf{C}_{LB} & \mathbf{C}_{LL} & 0 \\
\hline
\mathbf{C}_{RI} & \mathbf{C}_{RB} & 0 & \mathbf{C}_{RR}
\end{array}\right]
\left\{\begin{array}{c}
\dot{\mathbf{x}} \\ \dot{\mathbf{x}}_B \\ \dot{\mathbf{x}}_L \\ \dot{\mathbf{x}}_R
\end{array}\right\} \\
&+
\left[\begin{array}{cc|c|c}
\mathbf{K}_{II} & \mathbf{K}_{IB} & \mathbf{K}_{IL} & \mathbf{K}_{IR} \\
\mathbf{K}_{BI} & \mathbf{K}_{BB} & \mathbf{K}_{BL} & \mathbf{K}_{BR} \\
\hline
\mathbf{K}_{LI} & \mathbf{K}_{LB} & \mathbf{K}_{LL} & 0 \\
\hline
\mathbf{K}_{RI} & \mathbf{K}_{RB} & 0 & \mathbf{K}_{RR}
\end{array}\right]
\left\{\begin{array}{c}
\mathbf{x} \\ \mathbf{x}_B \\ \mathbf{x}_L \\ \mathbf{x}_R
\end{array}\right\}
=
\left\{\begin{array}{c}
\mathbf{f} \\ \mathbf{f}_B \\ \mathbf{f}_L \\ \mathbf{f}_R
\end{array}\right\} \\
&+
\left[\begin{array}{cc|c|c}
0 & & & \\
 & 0 & & \\
\hline
 & & \mathbf{C}_{LL} + \mathbf{G}_{CL} & \\
\hline
 & & & \mathbf{C}_{RR} + \mathbf{G}_{CR}
\end{array}\right]
\left\{\begin{array}{c}
\dot{\mathbf{x}}_I \\ \dot{\mathbf{x}}_B \\ \dot{\mathbf{x}}_L \\ \dot{\mathbf{x}}_R
\end{array}\right\} \\
&+
\left[\begin{array}{cc|c|c}
0 & & & \\
 & 0 & & \\
\hline
 & & \mathbf{G}_L & \\
\hline
 & & & \mathbf{G}_R
\end{array}\right]
\left\{\begin{array}{c}
\mathbf{x} \\ \mathbf{x}_B \\ \mathbf{x}_L \\ \mathbf{x}_R
\end{array}\right\}
\end{aligned}
\tag{5.82}
$$

where $[\mathbf{M}]$ is the mass matrix, $[\mathbf{C}]$ damping matrix, $[\mathbf{K}]$ stiffness matrix and subscripts I, B, L, R refer to interior, bottom, left, and right nodes; $\{\mathbf{x}\}$, $\{\dot{\mathbf{x}}\}$, $\{\ddot{\mathbf{x}}\}$ are the nodal displacements, velocities, and accelerations.

$[\mathbf{C}_B]$ is Lysmer (dashpot) viscous boundary conditions at the bottom (tuned to shear wave for lateral excitation and to pressure waves for vertical excitation).

$$[\mathbf{C}_B] = \frac{\rho L}{2}\begin{bmatrix} V_H & 0 & 0 & 0 \\ 0 & V_V & 0 & 0 \\ 0 & 0 & V_H & 0 \\ 0 & 0 & 0 & V_V \end{bmatrix}, \quad \begin{cases} V_H = V_S\cos\theta + V_P\sin\theta \\ V_V = V_P\cos\theta + V_S\sin\theta \end{cases} \tag{5.83}$$

$[\mathbf{C}_L], [\mathbf{C}_R]$ are Lysmer (dashpot) left and right boundary conditions tuned to pressure wave for lateral excitation and shear waves for vertical excitation. $[\mathbf{G}_L], [\mathbf{G}_R]$ are the boundary stiffness matrices associated with the displacement of the free field.

$$[\mathbf{G}] = \frac{1}{2}\begin{bmatrix} 0 & -\lambda & 0 & \lambda \\ -\mu & 0 & \mu & 0 \\ 0 & -\lambda & 0 & \lambda \\ -\mu & 0 & \mu 0 & \end{bmatrix} \tag{5.84}$$

where λ and μ are the Lame parameters, $\lambda = \frac{\nu E}{(1-2\nu)(1+\nu)} = K - \frac{2}{3}G$ and $\mu = \frac{E}{2(1+\nu)} = G$. For a symmetric foundation ($\mathbf{x}_L = -\mathbf{x}_R$) we can ignore this term. $[\mathbf{G}_{CL}], [\mathbf{G}_{CR}]$ are the boundary damping matrices associated with the free field. Their effects also cancel out for symmetric cases.

Hence, for symmetric boundary conditions, we can ignore $[\mathbf{G}_R], [\mathbf{G}_L], [\mathbf{G}_{CR}], [\mathbf{G}_{CL}], \mathbf{x}_R, \mathbf{x}_L$, and the resulting governing partial differential equation to be solved is reduced to:

$$\begin{aligned} &[\mathbf{M}]\{\ddot{\mathbf{x}}\} + ([\mathbf{C}] + [\mathbf{C}_b] + [\mathbf{C}_L] + [\mathbf{C}_R])\{\dot{\mathbf{x}}\} + [\mathbf{K}]\{\mathbf{x}\} \\ &\quad = \{\mathbf{f}\} + [\mathbf{C}_L]\{\dot{\mathbf{x}}_L\} + [\mathbf{C}_R]\{\dot{\mathbf{x}}_R\} \end{aligned} \tag{5.85}$$

or

$$
\begin{bmatrix}
\mathbf{M}_{II} & \mathbf{M}_{IB} & \mathbf{M}_{IL} & \mathbf{M}_{IR} \\
\mathbf{M}_{BI} & \mathbf{M}_{BB} & \mathbf{M}_{BL} & \mathbf{M}_{BR} \\
\mathbf{M}_{LI} & \mathbf{M}_{LB} & \mathbf{M}_{LL} & 0 \\
\mathbf{M}_{RI} & \mathbf{M}_{RB} & 0 & \mathbf{M}_{RR}
\end{bmatrix}
\begin{Bmatrix} \ddot{\mathbf{x}} \\ \ddot{\mathbf{x}}_B \\ \ddot{\mathbf{x}}_L \\ \ddot{\mathbf{x}}_R \end{Bmatrix}
+
\begin{bmatrix}
\mathbf{C}_{II} & \mathbf{C}_{IB} & \mathbf{C}_{IL} & \mathbf{C}_{IR} \\
\mathbf{C}_{BI} & \mathbf{C}_{BB} & \mathbf{C}_{BL} & \mathbf{C}_{BR} \\
\mathbf{C}_{LI} & \mathbf{C}_{LB} & \mathbf{C}_{LL} & 0 \\
\mathbf{C}_{RI} & \mathbf{C}_{RB} & 0 & \mathbf{C}_{RR}
\end{bmatrix}
\begin{Bmatrix} \dot{\mathbf{x}} \\ \dot{\mathbf{x}}_B \\ \dot{\mathbf{x}}_L \\ \dot{\mathbf{x}}_R \end{Bmatrix}
$$

$$
+
\begin{bmatrix}
\mathbf{K}_{II} & \mathbf{K}_{IB} & \mathbf{K}_{IL} & \mathbf{K}_{IR} \\
\mathbf{K}_{BI} & \mathbf{K}_{BB} & \mathbf{K}_{BL} & \mathbf{K}_{BR} \\
\mathbf{K}_{LI} & \mathbf{K}_{LB} & \mathbf{K}_{LL} & 0 \\
\mathbf{K}_{RI} & \mathbf{K}_{RB} & 0 & \mathbf{K}_{RR}
\end{bmatrix}
\begin{Bmatrix} \mathbf{x} \\ \mathbf{x}_B \\ \mathbf{x}_L \\ \mathbf{x}_R \end{Bmatrix}
\tag{5.86}
$$

$$
=
\begin{Bmatrix} \mathbf{f} \\ \mathbf{f}_B \\ \mathbf{f}_L \\ \mathbf{f}_R \end{Bmatrix}
+
\begin{bmatrix}
0 & & & \\
& 0 & & \\
& & \mathbf{C}_{LL} & \\
& & & \mathbf{C}_{RR}
\end{bmatrix}
\begin{Bmatrix} \dot{\mathbf{x}}_I \\ \dot{\mathbf{x}}_B \\ \dot{\mathbf{x}}_L \\ \dot{\mathbf{x}}_R \end{Bmatrix}
$$

In order to solve this equation, we still need some quantities on the right hand side of the equation, namely $\dot{\mathbf{x}}_L$ and $\dot{\mathbf{x}}_R$. These can be obtained from two separate (one if we take advantage of symmetry) analyses of the free field which can be discretized as shown in Figure 5.11. We note the vertical

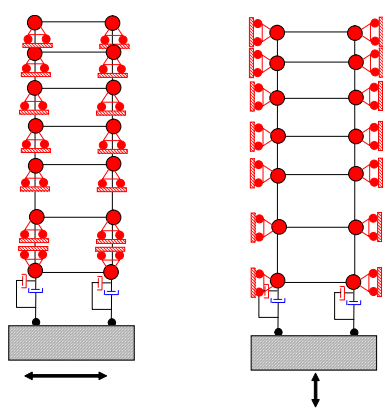

Figure 5.11: Finite element discretization of the free field

restraint for lateral excitation and the lateral restraint for vertical excitation in order to respect

the far field boundary conditions. Thus the governing differential equations for these analyses are

$$[\mathbf{M}_L]\left\{\ddot{\mathbf{x}}_L^?\right\} + [\mathbf{C}_L]\left\{\dot{\mathbf{x}}_L^?\right\} + [\mathbf{K}_L]\left\{\mathbf{x}_L^?\right\} = \left\{\mathbf{f}_L^\surd\right\} \tag{5.87}$$

$$[\mathbf{M}_R]\left\{\ddot{\mathbf{x}}_R^?\right\} + [\mathbf{C}_R]\left\{\dot{\mathbf{x}}_R^?\right\} + [\mathbf{K}_R]\left\{\mathbf{x}_R^?\right\} = \left\{\mathbf{f}_R^\surd\right\} \tag{5.88}$$

from which we solve for $\dot{\mathbf{x}}_L$ and $\dot{\mathbf{x}}_R$.

Once the free field velocities have been obtained, they can in turn be used in the full 2D analysis of the dam/foundation discretization shown in Figure 5.12.

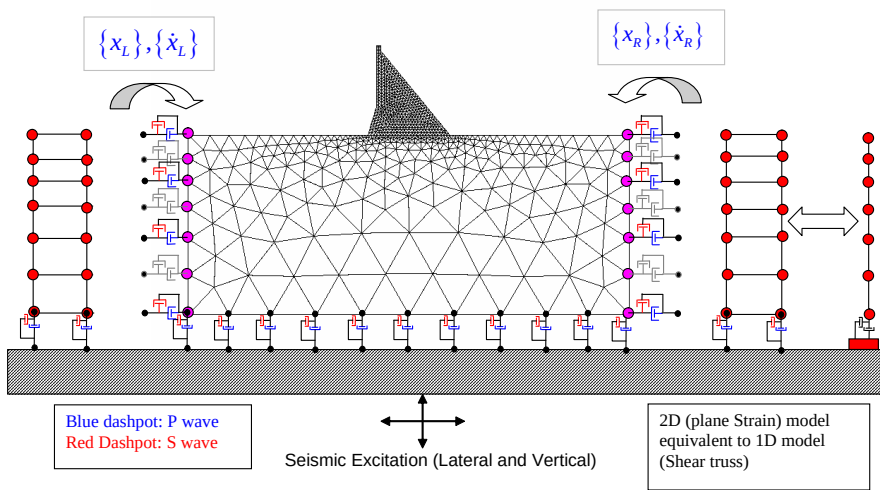

Figure 5.12: Discretization of 2D dam foundation with free field velocities

$$\begin{bmatrix} \mathbf{M}_{II} & \mathbf{M}_{IB} & \mathbf{M}_{IL} & \mathbf{M}_{IR} \\ \mathbf{M}_{BI} & \mathbf{M}_{BB} & \mathbf{M}_{BL} & \mathbf{M}_{BR} \\ \mathbf{M}_{LI} & \mathbf{M}_{LB} & \mathbf{M}_{LL} & 0 \\ \mathbf{M}_{RI} & \mathbf{M}_{RB} & 0 & \mathbf{M}_{RR} \end{bmatrix} \begin{Bmatrix} \ddot{\mathbf{x}}^? \\ \ddot{\mathbf{x}}_B^? \\ \ddot{\mathbf{x}}_L^? \\ \ddot{\mathbf{x}}_R^? \end{Bmatrix} + \begin{bmatrix} \mathbf{C}_{II} & \mathbf{C}_{IB} & \mathbf{C}_{IL} & \mathbf{C}_{IR} \\ \mathbf{C}_{BI} & \mathbf{C}_{BB} & \mathbf{C}_{BL} & \mathbf{C}_{BR} \\ \mathbf{C}_{LI} & \mathbf{C}_{LB} & \mathbf{C}_{LL} & 0 \\ \mathbf{C}_{RI} & \mathbf{C}_{RB} & 0 & \mathbf{C}_{RR} \end{bmatrix} \begin{Bmatrix} \dot{\mathbf{x}}^? \\ \dot{\mathbf{x}}_B^? \\ \dot{\mathbf{x}}_L^? \\ \dot{\mathbf{x}}_R^? \end{Bmatrix}$$
$$+ \begin{bmatrix} \mathbf{K}_{II} & \mathbf{K}_{IB} & \mathbf{K}_{IL} & \mathbf{K}_{IR} \\ \mathbf{K}_{BI} & \mathbf{K}_{BB} & \mathbf{K}_{BL} & \mathbf{K}_{BR} \\ \mathbf{K}_{LI} & \mathbf{K}_{LB} & \mathbf{K}_{LL} & 0 \\ \mathbf{K}_{RI} & \mathbf{K}_{RB} & 0 & \mathbf{K}_{RR} \end{bmatrix} \begin{Bmatrix} \mathbf{x}^? \\ \mathbf{x}_B^? \\ \mathbf{x}_L^? \\ \mathbf{x}_R^? \end{Bmatrix} = \begin{Bmatrix} \mathbf{f}^\surd \\ \mathbf{f}_B^\surd \\ \mathbf{f}_L^\surd \\ \mathbf{f}_R^\surd \end{Bmatrix} + \begin{bmatrix} 0 & & & \\ & 0 & & \\ & & \mathbf{C}_{LL} & \\ & & & \mathbf{C}_{RR} \end{bmatrix} \begin{Bmatrix} \dot{\mathbf{x}}_I \\ \dot{\mathbf{x}}_B^? \\ \dot{\mathbf{x}}_L^\surd \\ \dot{\mathbf{x}}_R^\surd \end{Bmatrix} \tag{5.89}$$

5.2.3.5 Finite Element Implementation

All the components of Equation 5.60 having been defined, the analysis could then proceed as follows (for the 2D case), Figure 5.13:

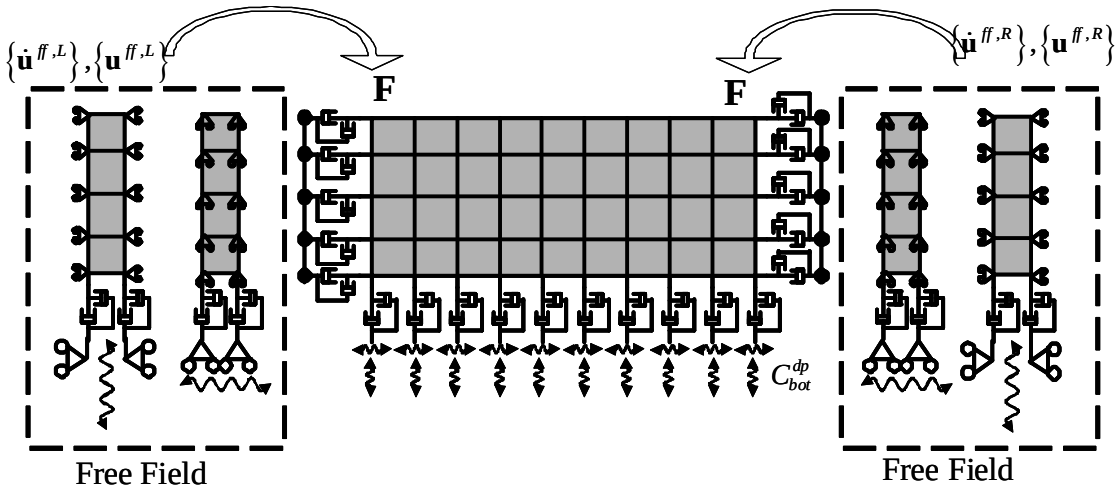

Figure 5.13: 2D Finite Element Modeling

(1) Discretize the free field with an arbitrary mesh which is topologically consistent with the adjacent one in the bounded domain (that is, to each boundary node of the foundation mesh corresponds a node in the free field mesh). Place dashpots at the base of the mesh.

(2) Constrain the vertical displacements of all the nodes (thus allowing only shear deformation), apply an horizontal excitation and analyze.

(3) If the seismic record includes a vertical component, repeat the analysis by constraining all the horizontal displacements (thus allowing only axial deformation), apply the vertical component of the excitation and analyze.

(4) Determine the nodal equivalent forces $\mathbf{F}^C$, $\mathbf{F}^K$, and $\mathbf{F}^R$ from Eqs. 5.68, 5.72, and 5.75, respectively.

(5) Apply these as external (time dependent) boundary forces to the bounded domain (as in Equation 5.59) and analyze.

In 3D, the model becomes more complex, Figure 5.14.

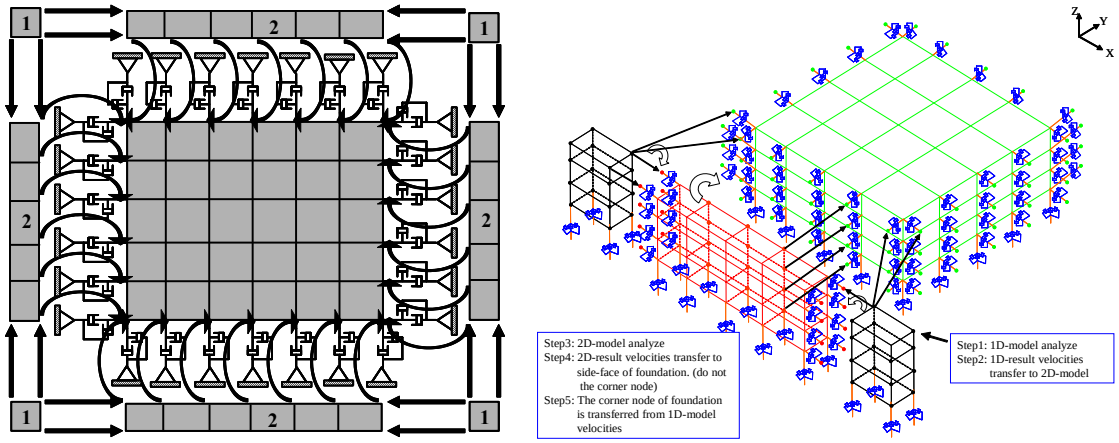

Figure 5.14: 3D extension; procedure outline

We would have to perform three analyses (assuming that the earthquake record has x, y, and z components) of each of the corner blocks then transfer the nodal equivalent forces to the four side blocks using the procedure outlined above. Those in turn will be analyzed three times each, and finally nodal equivalent forces would again be transferred to the bounded domain. Thus, potentially twenty four analyses would have to be performed before the foundation can be analyzed. It should be noted that each one of those free field analyses is not computationally intensive, the major difficulty is "book-keeping" to properly determine the nodal forces and transfer them, at each time increment, to the correct corresponding node.

A major advantage of this method is that there is no need to modify existing finite element programs (as is the case in (Bielak and Christiano, 1984) and (Basu, 2009)). The entire operation is the result of clever post- and pre-processing of analysis which can be performed on most existing finite element codes (only requirement: support dashpot elements).

Figure 5.17 is showing the model created for the case study dam along with the free field meshes compatible for each side of the dam. Figure 5.16 shows different steps required for a free

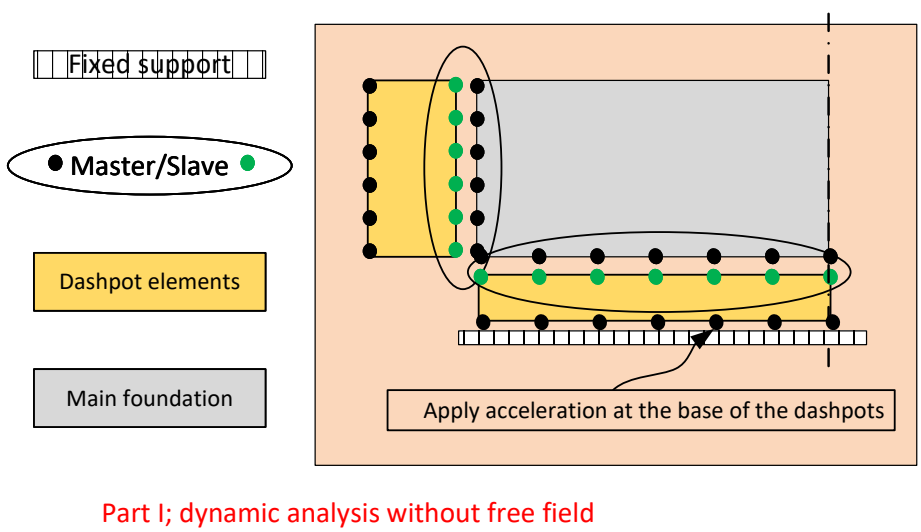

Figure 5.15: Boundary conditions for free field modeling

field analysis. Each free field analysis entails performing 9 different dynamic analysis (i.e. there

are 4 corner meshes, 4 side meshes and 1 main mesh). As shown in figure 5.16 these analyses has to be performed in a sequential manner. A matlab code is developed to automate this process.

(1) Storing Initial Information: In order to facilitate the book keeping for free field analysis, the first step is to store all of the required node and element numbers in an organized manner in an excel file. In this phase the node numbers for all 9 meshes need to be stored in the same order as their correspondents from adjacent mesh where the responses will be transferred. Once the node numbers where stored in the excel file, starting from step 2 and onward a Matlab code will take care of the writing input files, running input files and reading the outputs.

(2) Level one analyses: In this first set of Matlab codes the node numbers from C meshes (C stands for corner) are read and responses are recorded.

(3) Level two analyses: In this set of Matlab codes the node numbers from S meshes (S stands for Side) are read and the responses of the nodes on P4 are recorded.The nodes corresponding to P1 will be used to apply the excitation at the base and responses from C meshes are transferred to their corresponding nodes from P2 and P3 on the S meshes.

(4) Level three analysis: Finally the node numbers associated with the base of the main mesh are selected to apply the acceleration while the responses from side P4 patches are transferred to P2 through P5 patches of main mesh.

Figure 5.18 provides a better representation of the required meshes and required dashpots as boundary conditions (shown as red surfaces) for a set of free field analysis. As seen the free field meshes need to be compatible with the boundaries of the main mesh. Finally for a single seismic excitation one would need to perform 9 different seismic analyses in other words, 4 on the corner meshes, 4 on the side meshes and 1 for the main dam mesh.

5.2.4 Validation Problems

To assess the effectiveness of the method in dissipating elastic waves an extensive parametric study is performed. We consider a soft foundation with E, ρ and ν equal to 1.563×10^3 MN/m^2,

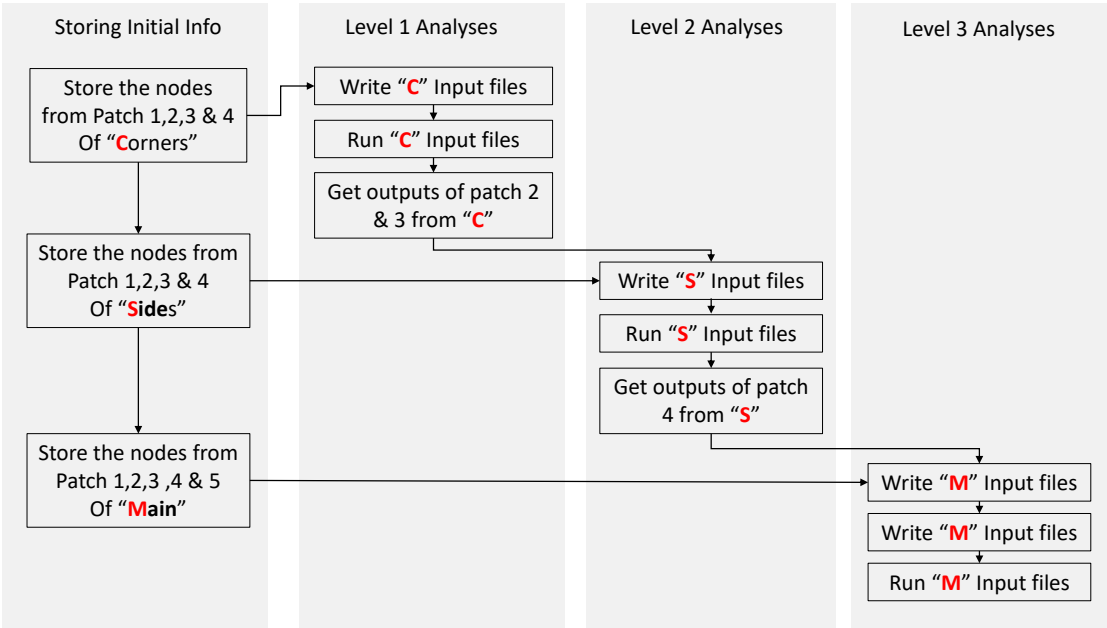

Figure 5.16: Free field analysis flowchart

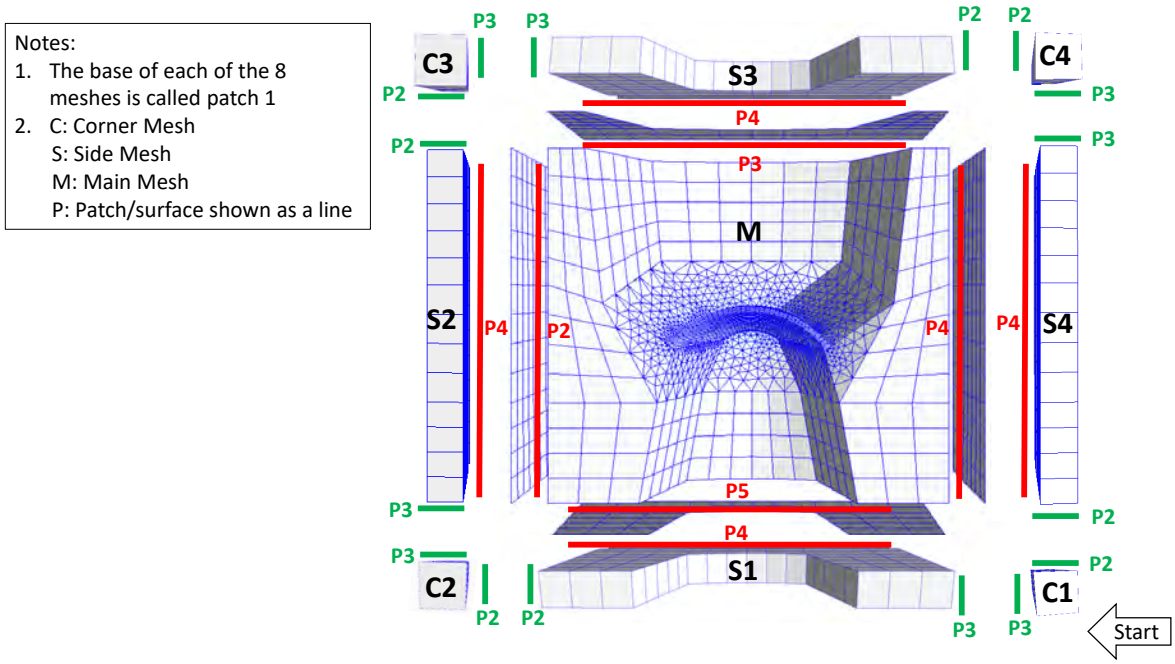

Figure 5.17: Free field modeling

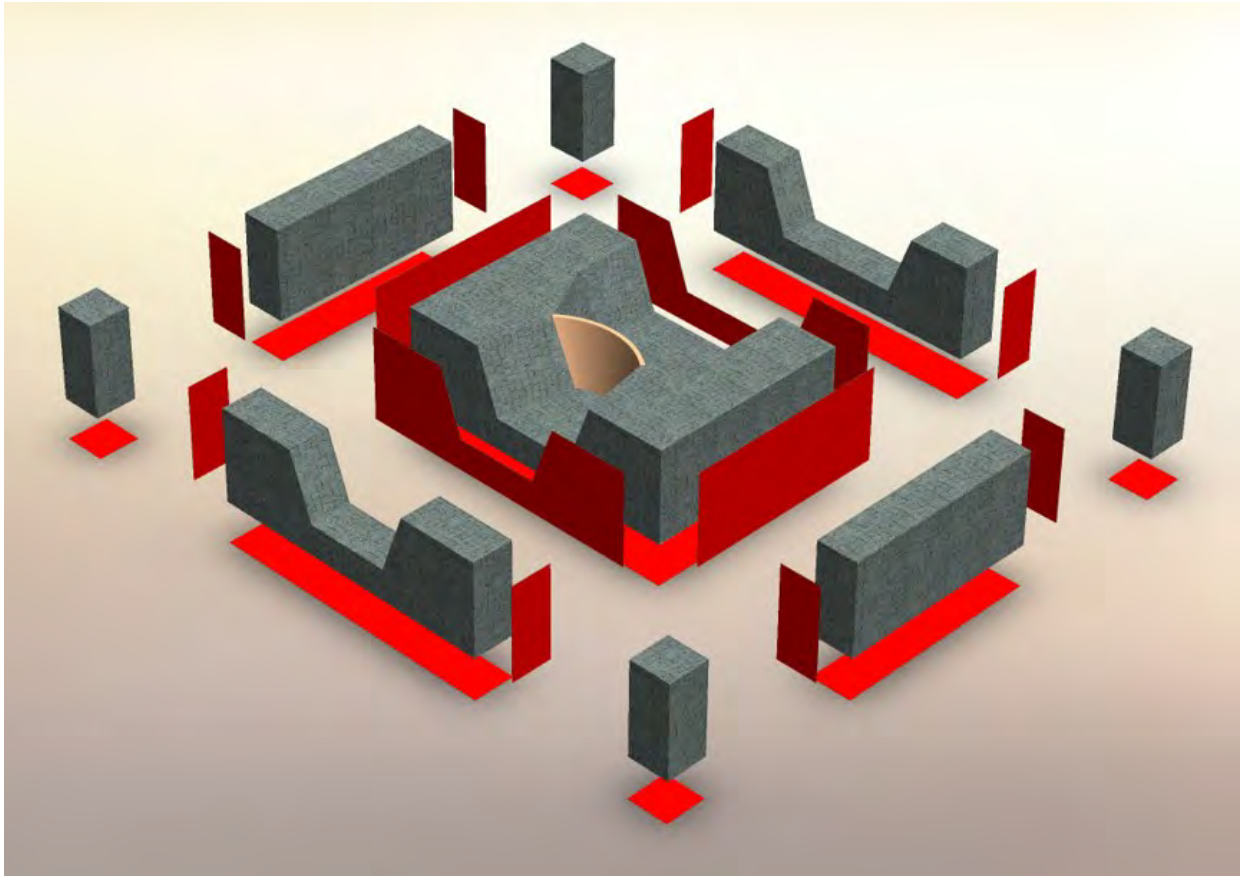

Figure 5.18: Free field boundaries and meshes

2,500 kg/m^3 and 0.25 respectively. This corresponds to a shear wave velocity (V_S from Eq. 5.52) of 500 m/sec. Hence by exciting the base with a harmonic excitation with period of 0.4 sec, a full wave length develops over 200 m which is the height of the model. Length is set to 800 m, and the 3D model in turn is 200 by 800 by 800 m. Since the base excitation has a magnitude of 1 m/sec.^{2}, ideally we should have a similar (though with a phase lag) response at the top of the bounded domain. In both cases element size was 25 m (except for a fine 2D mesh with half this size). Results are assessed by examining the acceleration at the top, distribution of accelerations at $h/8$ increments, deformed shapes and velocity or acceleration contour lines. From this investigation we conclude that:

(1) When the boundaries are left bare (for both 2D and 3D analyses), results are totally unacceptable, Fig. 5.19.

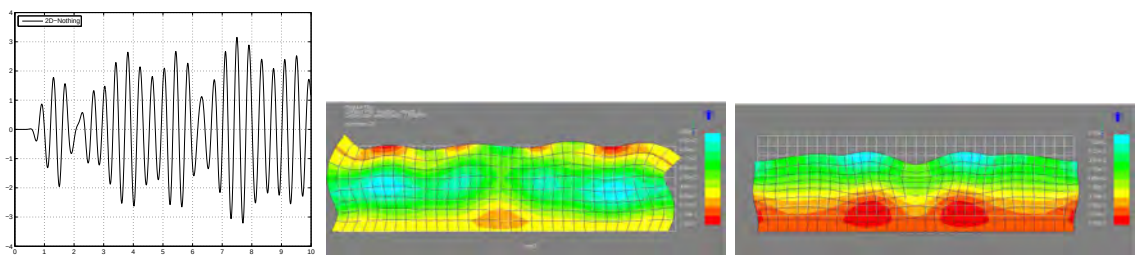

Figure 5.19: Selected results for 2D analyses with free boundaries; Crest accelerations, deformed shapes with contour lines of V_X and V_Y

(2) 2D Lysmer yields nearly perfect (0.9) acceleration at h, nearly zero accelerations at the knots ($h/4$ and $3h/4$) barely acceptable displacements for horizontal excitation, and very bad ones for a vertical excitation. Top accelerations due to vertical excitation were slightly better than when a horizontal was applied, Fig. 5.20.

(3) 2D Present model gave excellent top acceleration ($\sim$ 1.0), nearly zero ones at the knots (have as large as those predicted by Lysmer), and a deformation which indeed is consistent with a shear beam. It should be noted that best results are achieved when both terms where included (C and K). Similarly, excellent results were obtained for vertical excitation (the importance of including both terms was more accentuated than for the horizontal

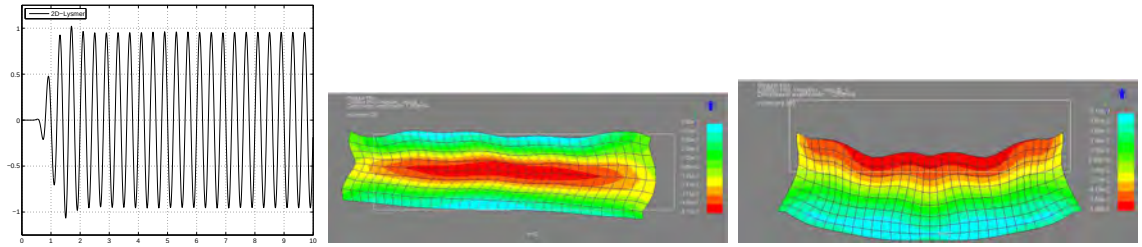

Figure 5.20: Selected results for 2D Lysmer analyses; Crest accelerations, deformed shapes with contour lines of V_X and V_Y

acceleration), Fig. 5.21.

(4) The 3D analysis based on Lysmer's model yields top acceleration slightly higher than 1.0,, a good deformation, and not quite a homogeneous velocity distribution, Fig. 5.22.

(5) the 3D analysis based on the present model yielded a nearly perfect acceleration distribution from bottom to top, a very smooth deformation, and internal velocity distribution, Fig. 5.23.

In summary, Lysmer's model performs better in 3D than in 2D, whereas the Miura-Saouma model yields excellent results in all analyses.

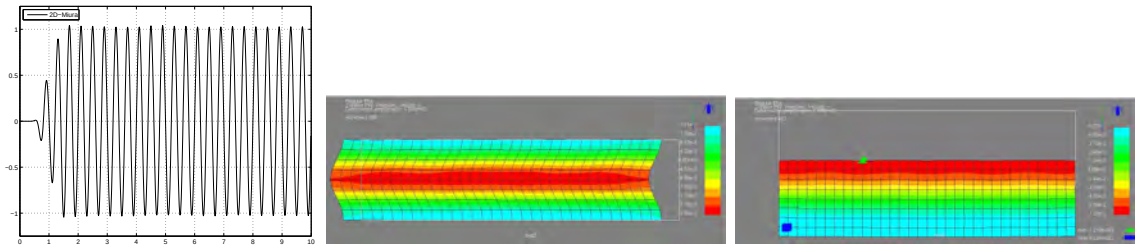

Figure 5.21: Selected results for 2D Miura-Saouma analyses; Crest accelerations, deformed shapes with contour lines of V_X and V_Y

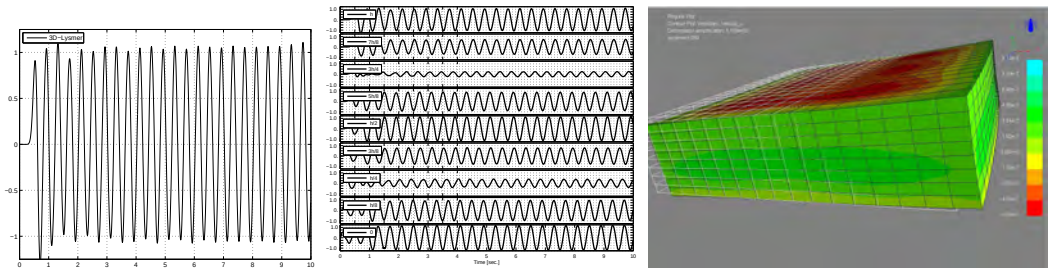

Figure 5.22: Selected results for 3D Lysmer analyses; Crest accelerations, accelerations at $h = 0$, h/8, h/4, 3h/8, h/2, 5h/8, 3h/4, 7h/8 and h; deformed shapes with contour lines of V_X

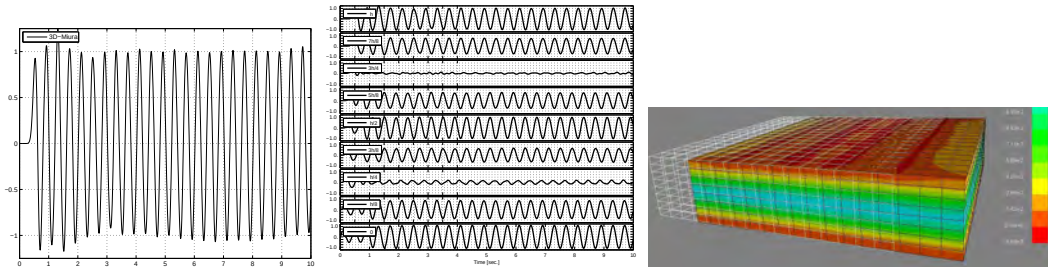

Figure 5.23: Selected results for 3D Miura-Saouma analyses; Crest accelerations, accelerations at $h = 0$, h/8, h/4, 3h/8, h/2, 5h/8, 3h/4, 7h/8 and h; deformed shapes with contour lines of V_X

When modeling the wave motion in a spatial domain, it is essential to introduce artificial boundaries to limit the bounded domain to a reasonable size. The simple Dirichlet boundary condition, in which displacements are fixed, is unsuitable as substantial reflection (through Snell's law) will occur at the boundary and reflected waves will degrade the solution. A solution to this problem could be to enlarge the numerical mesh, thus delaying the side reflections. Obviously this solution considerably increases the expense of computation and is not viable unless artificial damping can be introduced in the material near the far field (Hudson, Idriss, and Beikae, 1994).

Thus, a numerical model (finite element in our case) should absorb the incoming waves just as they would be absorbed by the free field physically.

5.3 Nonlinear Analysis Methods

In order to investigate the response of the structure and in particular our case study dam, there is a need to employ a nonlinear analysis methods so to determine the performance of the structure under certain circumstances. For the current case study we are after finding the performance of the AAR affected dam when subjected to seismic loads. There are several nonlinear analysis methods such as Incremental dynamic analysis (IDA), Multiple strip analysis (MSA) and Cloud analysis (CLA) (figure 5.24).

In IDA method a set of ground motions are selected and each individual ground motion is scaled to multiple IM levels and the structure is analyzed subject to the set of scaled ground motions; the maximum engineering demand parameter (EDP) from each individual analysis is then recorded. Connecting all the points on and IM-EDP plot an IDA curve is generated (Vamvatsikos and Cornell, 2004). While IDA has been widely used among researchers for the dynamic analysis of most of the structures, the relatively large number of required analysis has made this method computationally expensive besides the fact that the scaling of the ground motion can lead to applying unrealistic ground motion scenarios to the structure. On the other hand, the MSA method uses a suite of ground motions at different intensity levels which provide responses as discrete intensity levels. Due to the above-mentioned limitations associated with IDA and MSA methods, In this thesis the

cloud analysis is preferred over the others.

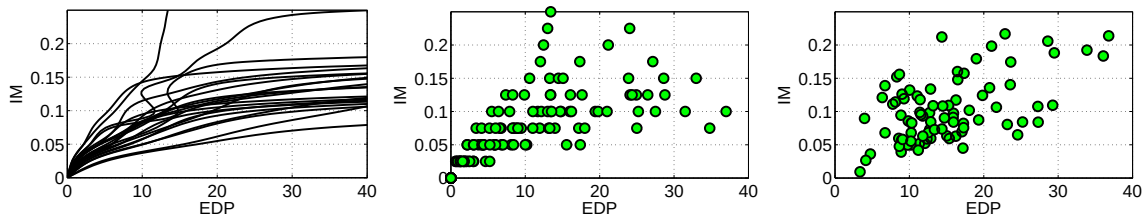

(a) IDA (b) MSA (c) CLA

Figure 5.24: Comparison of various analysis methods (Saouma and Hariri-Ardebili, 2021c)

5.3.1 Cloud Analysis (CLA)

CLA procedure consists of selecting a relatively large set of un-scaled ground motions and analyzing the structure subject to those ground motions. The EDP's recorded from the ground motions are ploted versus the IMs forming the cloud response (5.25). It is a well-accepted assumption that the discrete data points resulted from CLA have a linear trend in the logarithmic scale implying a power form in the arithmetic scale:

$$\eta_{EDP|IM} = a.IM^b$$

where a and b are the regression constants and $\eta_{EDP|IM}$ is the median value of EDP given IM. Also, the logarithmic standard deviation is:

$$\beta_{EDP|IM} \cong \sqrt{\frac{\sum(ln(edp_i) - ln(a.IM^b))^2}{n-2}}$$

where n is the number of nonlinear transient analyses.

5.3.2 Endurance Time Analysis (ETA); Fundamentals

ETA is a dynamic pushover procedure used to estimate the seismic performance of structures when subjected to pre-designed intensifying excitation (Estekanchi, Vafai, and Sadeghazar, 2004). The purpose of the simulated acceleration functions is to transition the structure through different levels of excitation in a single time history analysis. This process starts with a low excitation level,

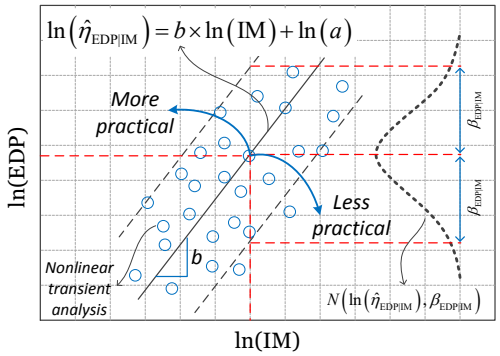

Figure 5.25: Cloud Based Analysis(Hariri-Ardebili and Saouma (2016))

keeping the structural response within the elastic range. It then progresses to a moderate excitation level, introducing some nonlinearity in the structure's response. Finally, it culminates in a high excitation level that leads to structural failure.

The challenging part of this method is in generating the endurance time acceleration functions (ETAF). Different versions of ETAFs have been generated by Nozari and Estekanchi (2011) and further optimized by Mashayekhi and Estekanchi (2013). The major steps for producing ETAFs are(Hariri-Ardebili et al. (2016)):

- Generate a stationary random acceleration function, $Z(t)$ (using $\delta t = 0.01$, $N_{pnt} = 2^{11}$ node, and PGA= 1.0 g). Note that N_{pnt} is optional.
- Transfer this function to the frequency domain, $Z(i\omega) = \mathcal{F}(Z(t))$, where i is an imaginary unit and ω is frequency.
- Apply an appropriate filter function in order to resemble real ground motions (Clough, R.W. and Penzien, J., 1993):

$$A(i\omega) = \frac{1 + 2i\xi_1 \frac{\omega}{\omega_1}}{1 - \left(\frac{\omega}{\omega_1}\right)^2 + 2i\xi_1 \frac{\omega}{\omega_1}} \frac{\left(\frac{\omega}{\omega_2}\right)^2}{1 - \left(\frac{\omega}{\omega_2}\right)^2 + 2i\xi_2 \frac{\omega}{\omega_2}} Z(i\omega) \tag{5.90}$$

  where the first and second terms are low-pass and high-pass filter functions, respectively; ω_1 and ξ_1 are frequency and damping coefficients for the low-pass filter function, and ω_2 and ξ_2 are frequency and damping coefficients for the high-pass filter function.
- Use several cycles of stepwise modifications on frequency content of the filtered acceleration

functions, $A(i\omega)$, in order to make the resulting response spectrum compatible with the target.

$$A^{new}(i\omega) = A^{old}(i\omega)\,\frac{S_a^{\text{trg}}(\omega)}{S_a^{\text{gen}}(\omega)} \tag{5.91}$$

where $A^{new}(i\omega)$ is the modified frequency content being replaced with the previous content in each modification cycle. $S_a^{\text{trg}}(\omega)$ is the target spectrum (code-based spectrum or from a probabilistic seismic hazard analysis), and $S_a^{\text{gen}}(\omega)$ is the generated response spectrum.

- Modify the acceleration time history by a linear profile function, $l(t) = t/t_{trg}$, that makes the resulting one intensifying at various time intervals. Note that t_{trg} is optional, though it is usually considered to be 10 seconds.
- Modify both the acceleration and displacement response spectra by applying a linear profile function. An unconstrained optimization technique in the time domain may be used, such as:

$$\underset{\ddot{u}_g}{min} F(\ddot{u}_g) = \int_0^{T_{max}} \int_0^{t_{max}} \left\{ \left[S_a(T,t) - \frac{t}{t_{\text{trg}}} S_a^{\text{trg}}(T) \right]^2 + \chi_0 \left[S_d(T,t) - \frac{t}{t_{\text{trg}}} \left(\frac{T}{2\pi}\right)^2 S_a^{\text{trg}}(T) \right]^2 \right\} \tag{5.92}$$

where a_g is the ETAF being sought, χ_0 a weight parameter, t_{max} and T_{max} are the maximum time and period in the optimization process, respectively. Figure 5.26(a) shows a sample ETAF.

In order to retrieve a capacity function in the form of Figure 5.26(c), the "ETA curve" should first be derived, see Figure 5.26(b). This curve is a diagram, whose vertical axis refers to the maximum absolute values of EDP during the time interval from 0 to t (see Equation 5.93) and whose horizontal axis is time.

$$\Omega\left(\text{EDP}(t)\right) \equiv \max\left\{\text{Abs}\left(\text{EDP}(\tau) : \tau \in [0,t]\right)\right\} \tag{5.93}$$

Finally, the "time" parameter is converted to IM (this can be easily performed due to the direct relation between time and acceleration, Figure 5.26(a)), and the EDP-IM coordinate is changed to IM-EDP. The resulting stepwise capacity function can be smoothed later, Figure 5.26(c). Note that although this procedure is applicable only with a single ETAF, in order to reduce the

uncertainty (due to its random nature) of ETAFs, the mean of three is typically used (Hariri-Ardebili and Mirzabozorg, 2014) (Hariri-Ardebili and Saouma, 2015).

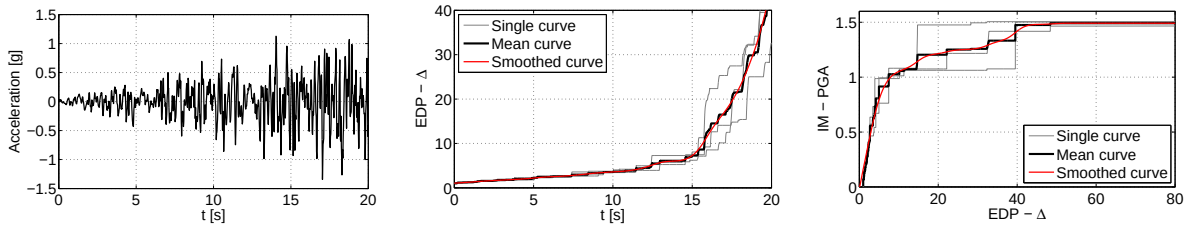

(a) Sample ETAF (b) ETA curve (c) Capacity function

Figure 5.26: ETA-based capacity function generation (Hariri-Ardebili and Saouma, 2017)

5.3.3 Intensifying Artificial Accelerations; Advances

The IAA is an artificially designed sequence of acceleration data, where one or more of its intensity measures (IMs), such as response spectra, follow a predefined time-dependent pattern (i.e., optimization constraint). In its most general form, an IAA can be represented as follows:

$$F_{IAA}(\ddot{u}_g) = \sum_{i=1}^{n} \left(\int_{\mu=1}^{\mu_{max}} \int_{T=0}^{T_{max}} \int_{t=0}^{t_{max}} \gamma_i \left[\Gamma_i(t,T,\mu) - \Gamma_i^*(t,T,\mu) \right]^{\beta_i} \, \mathrm{d}t \, \mathrm{d}T \, \mathrm{d}\mu \right) \tag{5.94}$$

where $\ddot{u}_g(t)$ is the acceleration time series of the IAA, $\Gamma_i(t,T,\mu)$ is a desired intensity measure parameter to be used to optimize the IAA, and it can be a function of time, t, period ,T , ductility ratio μ, or any other variable. γ_i is the weighting scale factor (i.e., optimization coefficient) that denotes the contribution of each term in the overall optimization process. β_i is the power coefficient that typically takes values of one or two, depending on the objective function. Finally, n is the total number of IM parameters to be included in the optimization process.

During a series of computationally intensive non-constraint optimization processes, the IM parameters, $\Gamma_i(t,T,\mu)$, are forced to follow the general trend of the target function, $\Gamma_i^*(t,T,\mu)$. The profile may take a simple linear form, for example, for acceleration response spectrum, or a nonlinear (i.e., ground motion-dependent format) for some other IMs such as nonlinear displacement, and the hysteretic energy.

Several studies have investigated the generation of intensifying acceleration time series. The pioneering work belongs to Nozari and Estekanchi (2011), who generated IAAs compatible with a smoothed acceleration and displacement response spectra. Additionally, Mashayekhi et al. (2018) introduced the hysteretic energy concept, as well as cumulative absolute velocity, in IAA generation. Furthermore, Zhang et al. (2021) proposed a modification for the IAA by using a time-domain spectral matching method.

While it is possible to generate new series of IAAs for any type of structural system and seismic hazard scenario, this process is often time-consuming and requires specific skills in optimizing time-series data. Additionally, it contradicts the essence of the ETA method, which was originally developed to be a rapid technique for seismic performance evaluation with minimal complexities in ground motion selection and generation. Therefore, the focus of this thesis is on publicly available IAAs for the assessment of the dam under study.

The IAA functions have lengths of equal to 20 seconds and belong to five different generations, as discussed in (Estekanchi et al., 2020; Saouma and Hariri-Ardebili, 2021c). Figure 5.27 illustrates the target acceleration response spectra used for each of five IAA generations. As seen, they are different in shape and magnitude which implies different IAAs in terms of intensity and spectral acceleration. The major features of these five generations are as follows((Hariri-Ardebili and Sattar, 2023)):

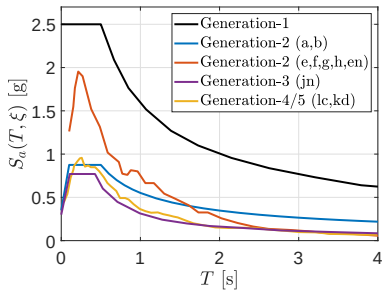

Figure 5.27: Target acceleration response spectra used in different IAA generations(Adapted from Hariri-Ardebili and Sattar (2023)).

- **First generation** was developed based on the theory of random vibration without any

specific constraint in the response spectrum.

- **Second generation** was developed using time-domain optimization techniques and a linear response spectrum assumption in the objective function. Acceleration and displacement response spectra were used as constraints, . Series "a" and "b" (each with three samples) are not recommended for nonlinear analysis and are solely useful for optimization benchmarking. A generic design response spectrum was used in their generation. Series "e" and "f" (each with three samples) cover longer periods, making them suitable for nonlinear simulations. Their generation used the average response spectra from seven records given by FEMA 440 for soil type C (i.e., stiff soil) as the target spectrum. Series "g" and "h" (each with three samples) are an extended version of "e" and "f", with a shaking duration of 40 seconds.
- **Third generation** was developed by including nonlinear displacement responses in the optimization process. Series "en" (three samples) is similar to "e" but incorporates nonlinear optimization, resulting in up to 20% improvement in response prediction. Series "in" (nine samples overall) is similar to "en" but includes three-component functions, making it suitable for multi-component analysis. Series "jn" (three sample) is based on ASCE-7 design spectrum with a nonlinear optimization objective.
- **Fourth generation** was developed by incorporating ground motion duration via cumulative absolute velocity (CAV) in the optimization process. Series "lc" (three samples) was developed based on the average response spectrum of 22 far-field records in FEMA P695. Acceleration, displacement, and CAV (equivalent to duration) were used in the nonlinear optimization.
- **Fifth generation** was developed by incorporating damage (i.e., hysteretic energy compatibility) consistency in the nonlinear optimization process. Series "kd" is based on the same average response spectrum as series "lc" and includes five samples.

Figure 5.28 compares the time-period-spectral acceleration for all 32 IAAs in five generations. The color contour illustrates $S_a(T, t)$. As seen, at the same time, t, there are considerable differences

among the IAA realizations.

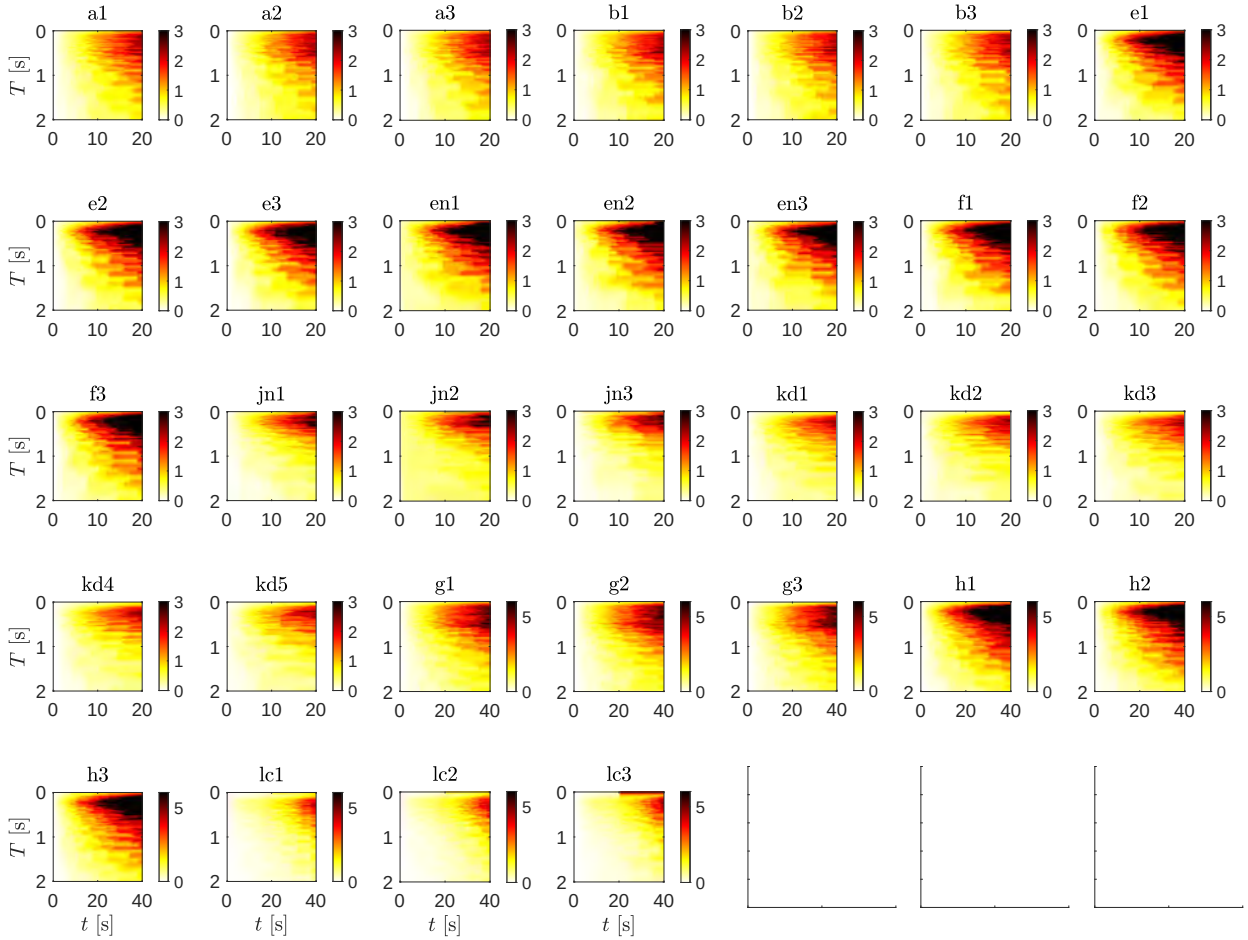

Figure 5.28: Variation of time- and period-dependent acceleration response spectra in IAAs. The horizontal axis represents time, and the vertical axis represents vibration period. The contour lines and colorbar represent the $S_a(T, t)$ in g. A 2.5% damping ratio is considered for all cases.(adapted from Hariri-Ardebili and Sattar (2023))

5.3.4 Generation of Intensifying Artificial Acceleration (IAA); Implementation

In this method an intensifying acceleration is applied to the structure and performance of the structure is evaluated by recording the time interval that takes until the structure reaches a certain performance level of interest. This method has numerous advantages over other methods of analysis in terms of reducing the computational time and effort. While other methods such as IDA, MSA and cloud analysis require a large number of analysis, the ETA method can provide a

good estimate of the model performance through a single dynamic analysis.

As mentioned earlier, the key part of the ETA method is the generation of intensifying accelerations. In this section the process of developing a MATLAB code to generate a basic form of IAA is described. An optimization process is utilized to generate the intensifying acceleration such that the corresponding response spectra at each time interval matches the defined target response spectra. The objective function for the above mentioned optimization can be a function of each of the acceleration, velocity and/or displacement response spectra or a combination of them. The optimization procedure initially implemented by Estenkanchi et al. in MATLAB is modified to add more features by the author. This code uses the MATLAB "lsqnonlin" function to optimize the intensifying acceleration.

In this method it is first assumed that the target spectra, defined by the user, corresponds to a certain time interval at the intensifying acceleration time history. Then using linear interpolation (equation 5.95) various spectra are generated for the other time intervals figure 5.29.

$$S_{aT}(T,t) = (\frac{t}{t_{Target}})S_{aC}(T,t) \tag{5.95}$$

The current code has been modified to include two input target spectra for each response instead of one. The added feature to the code allows user to define a combination of the three response spectra with different factors into the objective function. The objective function in the optimization process consists of a matrix of squared error of the spectra which may include the displacement and velocity spectra in addition to the acceleration and different weights can be assigned to each of the spectra. If acceleration is the only response spectra considered in the objective function then the matrix will write:

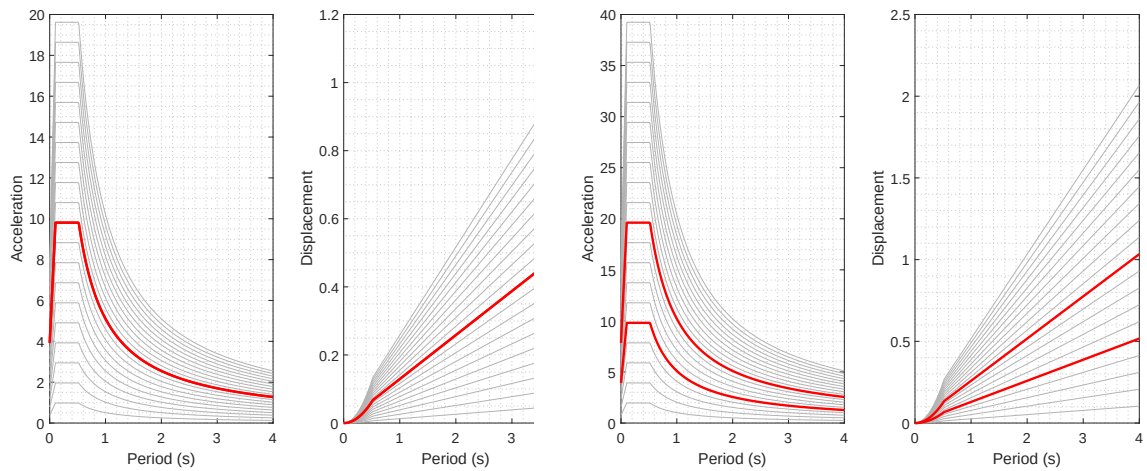

(a) Single input spectra (b) Double input spectra

Figure 5.29: Generation of target response spectra for different time intervals using linear interpolation

$$
\begin{array}{c}
 \\ T_1 \\ T_2 \\ \vdots \\ T_n
\end{array}
\begin{array}{c}
\begin{array}{cccc} t_1 & t_2 & \cdots & t_m \end{array} \\
\begin{bmatrix}
M_{1,1} & M_{1,2} & \dots & M_{1,m} \\
M_{2,1} & M_{2,2} & \dots & M_{2,m} \\
\dots & \dots & M_{i,j} & \dots \\
M_{n,1} & M_{n,2} & \dots & M_{n,m}
\end{bmatrix}
\end{array}
\tag{5.96}
$$

In which the columns correspond to the difference of the target and calculated response spectra at each time interval t_i. It is worth noting that the modified code is capable of selecting the periods not only by linear steps but also by logarithmic steps more weighted on either short or long periods. Furthermore, if another response spectra such as the displacement is also used in the optimization process the 2 matrices are appended as:

$$
\begin{array}{c}
 \\ T_1 \\ T_2 \\ \vdots \\ T_n
\end{array}
\begin{array}{c}
\begin{array}{cccc|cccc} t_1 & t_2 & \cdots & t_m & t_1 & t_2 & \cdots & tm \end{array} \\
\left[\begin{array}{cccc|cccc}
M_{1,1} & M_{1,2} & \dots & M_{1,m} & M'_{1,1} & M'_{1,2} & \dots & M'_{1,m} \\
M_{2,1} & M_{2,2} & \dots & M_{2,m} & M'_{1,1} & M'_{1,2} & \dots & M'_{1,m} \\
\dots & \dots & M_{i,j} & \dots & \dots & \dots & M'_{i,j} & \dots \\
M_{n,1} & M_{n,2} & \dots & M_{n,m} & M'_{1,1} & M'_{1,2} & \dots & M'_{1,m}
\end{array}\right]
\end{array}
\tag{5.97}
$$

Figure 5.30 is showing the intensifying acceleration generated by the code assuming the single input response spectra, and optimizing the acceleration and displacement response spectra simultaneously based on the input acceleration as the initial point of optimization process. Figure 5.31 shows the target versus calculated response spectra at the start and end of the optimization process. While the initial spectra does not fit well with the targets the optimization process was able to successfully match the calculated and target spectra for various times as shown in the figure. It is noteworthy that only the spectra at 10 different time intervals are demonstrated and compared in this plot for the sake of space.

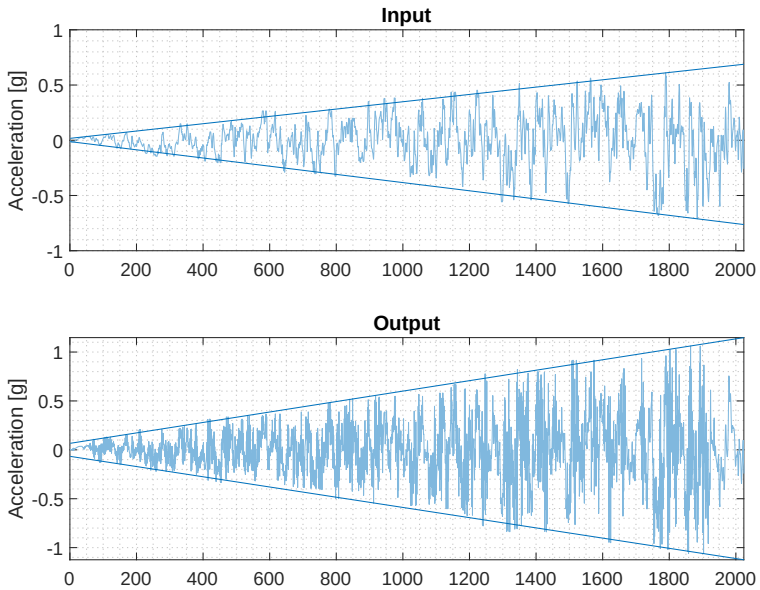

Figure 5.30: Input and output intensifying acceleration acceleration

5.4 Damage Index

Damage index is a term defined to quantify the state of the damage. While one can look into the local damage indices in an arch dam, such as material local cracking and yielding, there are multiple global damages that can express the extent of damage to the structure, such as foundation sliding, leakage and even the crest displacements. The damage indices in an arch dam can be summarized as:

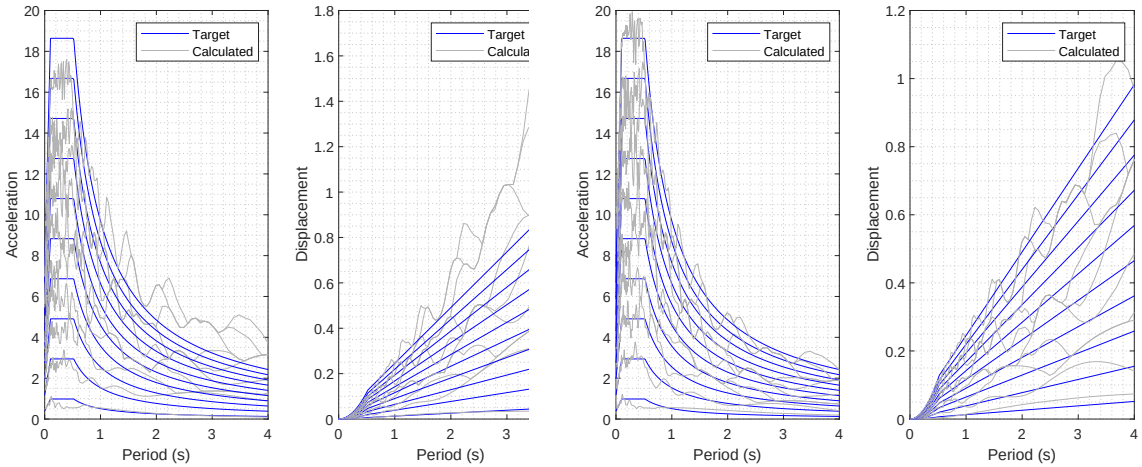

(a) Initial Spectra (b) Final Spectra

Figure 5.31: Calculated vs target response spectra before and after optimization

- Local
  - Concrete yielding: Mohr-coulomb failure criterion
  - Cracking: Drucker-Prager failure criterion
  - Overstressing
- Global
  - Sliding
  - Crack opening under the dam
  - Crest displacements
  - Leakage
  - Lose of arch effect

The detailed interpretation of various arch dam failure modes can be found in literature and has been specifically discussed in Brand and Nuss (2021).

5.4.1 Probability of Exceedance

In order to determine the probability of exceedance from a certain limit state, the 2 methods have been selected to determine the fitting function using(Baker, 2015):

- Maximum likelihood Estimation: In this method the parameters are determined such that a certain distribution is most likely to produce the observed data. In the current study, the maximum likelihood estimation is used to fit a log-normal cumulative distribution function to the stress ratios in time (figure 10.17). In other words, the objective is to find the probability of the principal stresses exceeding the tensile strength at different time steps. For each specific point on the dam, at each time step t_j, a number of analysis out of total (200 analyses in this study) would result in the stress to exceed the threshold(tensile strength). Assuming 2 possible event: 1. exceed the threshold and 2. Not to exceed the threshold, the probability of observing z_j exceedance out of n_j analyses at each x_j can be determined by the binomial distribution:

$$P(z_j \text{exceedance in } n_j \text{ analyses}) \equiv \begin{pmatrix} n_j \\ z_j \end{pmatrix} p_j^{z_j} (1-p_j)^{n_j - z_j} \tag{5.98}$$

where p_j is the probability that an analysis at time t_j will exceed the threshold. In order to find the likelihood of the whole data, the probabilities at all time steps are multiplied:

$$\text{Likelihood} \equiv \prod_{j=1}^{m} \begin{pmatrix} n_j \\ z_j \end{pmatrix} p_j^{z_j} (1-p_j)^{n_j - z_j} \tag{5.99}$$

where m is the number of time steps. substituting the equation for log-normal CDF into the equation above We then have:

$$\text{Likelihood} \equiv \prod_{j=1}^{m} \begin{pmatrix} n_j \\ z_j \end{pmatrix} \Phi\left(\frac{\ln(x_j/\theta)}{\beta}\right)^{z_j} \left[1 - \Phi\left(\frac{\ln(x_j/\theta)}{\beta}\right)\right]^{n_j - z_j} \tag{5.100}$$

As mentioned above the goal is to find the parameters so that the the distribution has the highest likelihood of representing the data. Thus the next step is to find the parameters that maximize the logarithm of the likelihood funtion, since it is easier, therefore we have:

$$\begin{aligned} \left\{\hat{\theta}, \hat{\beta}\right\} \quad \equiv \quad & \underset{\theta,\beta}{\operatorname{argmax}} \sum_{j=1}^{m} \left\{ \ln \begin{pmatrix} n_i \\ z_j \end{pmatrix} + z_j \ln \Phi\left(\frac{\ln(x_j/\theta)}{\beta}\right) \right. \\ & \left. + (n_j - z_j) \ln \left[1 - \Phi\left(\frac{\ln(x_j/\theta)}{\beta}\right)\right] \right\} \end{aligned} \tag{5.101}$$

All these procedure is followed using the code by (Baker, 2015).

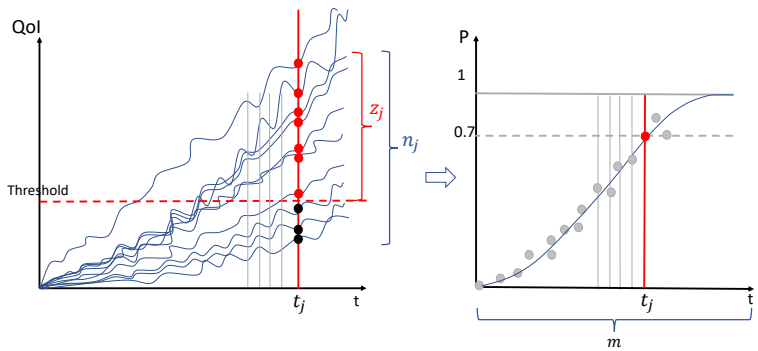

Figure 5.32: Schematic curve fitting procedure

- Sum of squared errors: This method is based on minimizing the sum of squared errors (SSE) between the observed data and predicted ones.

$$\left\{\hat{\theta}, \hat{\beta}\right\} \equiv \underset{\theta,\beta}{\operatorname{argmin}} \sum_{j=1}^{m} \left[\frac{z_j}{n_j} - \Phi\left(\frac{\ln(x_j/\theta)}{\beta}\right)\right]^2 \tag{5.102}$$

Part II

APPLICATION

Chapter 6

Physical Properties

Abstract

The complexity of the analysis involving a 3D nonlinear analysis of an arch-gravity dam subjected to AAR commands great care in proper preparation of all relevant input parameters.

This will be covered in this chapter extracting key and relevant parameters that have been summarized in Appendix 7.

6.1 Properties

6.1.1 Thermal Analysis

The input data for the thermal analysis of the dam including concrete material properties and film coefficients are described in this section.

6.1.1.1 Concrete Material Properties

The material properties of the dam concrete used during the thermal analysis is presented in table 6.1. It is worth mentioning that the units provided in this table are exactly adopted in the thermal analysis.

Table 6.1: Concrete material Properties used in thermal analysis
* From (Hatch, 2015)

Quantity	Symbol	Value*	units
Mass Density	ρ	2,487	$\mathrm{kg\,m^{-3}}$
Specific Heat	c_p	837	$\mathrm{J\,kg^{-1}\,K^{-1}}$
Conductivity	k	9,057,000	$\mathrm{J\,m^{-1}\,K^{-1}\,mo^{-1}}$
Thermal Diffusivity	μ	4.35	$\mathrm{m^2\,mo^{-1}}$

6.1.1.2 Film Coefficient

In thermal analysis the surrounding fluid temperature are applied through a film to the structure. For this purpose the film coefficient of water and air are used as shown in table 6.2 which are adopted from Hatch (2015). It is important to note that the film coefficient units should be converted to be consistent with the analysis time step unit.

6.1.1.3 Air Temperature

The dam is exposed to the air at its downstream, crest and a part of upstream above the water level. The air temperature data is available from USBR. For the purpose of conducting a thermal analysis, a sine curve is fitted to the available data to represent the temperature variation throughout the year figure 6.1. The resulting sinusoidal equation used for the application of air temperature is presented below. In this equation t denotes the analysis time in days.

$$T(t)_{DS,Air} = 12.7 + 13.4sin(0.0175t - 1.95) \tag{6.1}$$

Table 6.2: Air and water film coefficients

	Film Coefficient	units
Air	20	$\mathrm{W\,m^{-2}\,K^{-1}}$
	$5.26 * 10^7$	$\mathrm{J\,m^{-2}\,K^{-1}\,mo^{-1}}$
Water	60	$\mathrm{W\,m^{-2}\,K^{-1}}$
	$1.6 * 10^8$	$\mathrm{J\,m^{-2}\,K^{-1}\,mo^{-1}}$

$$T(t)_{US,Air} = 12.8 + 12.98sin(0.0175t - 1.96) \tag{6.2}$$

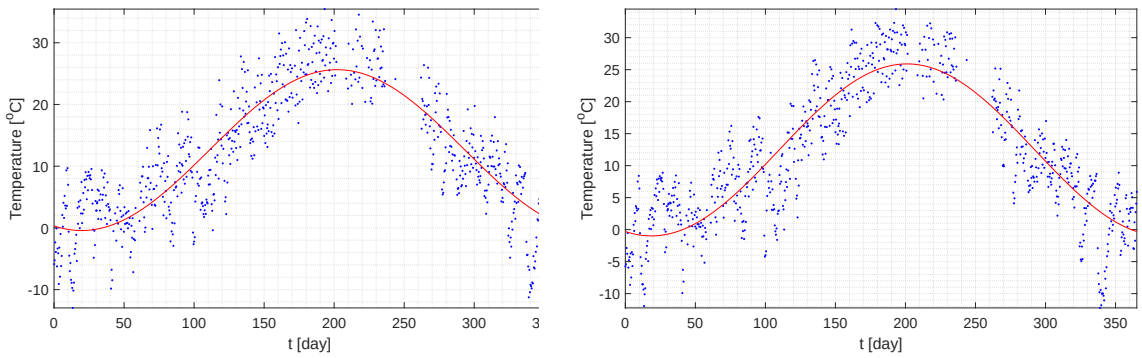

(a) Upstream (b) Downstream

Figure 6.1: The dam air temperature

6.1.1.4 Solar Radiation

In addition to the surrounding air, the surface temperature of the dam is affected by the amount of solar energy radiating during the daylight hours which should be taken into account during the thermal analysis. Because dam upstream is facing the south direction with an angle of about $3^o3'30"$, and as a matter of fact, the solar direct radiation is maximum at the south direction, the dam upstream which is facing south receives the maximum amount of solar radiation while the downstream is facing back to the sun. Therefore, the effect of solar radiation is applied at the exposed part of the upstream face of the dam. It is worth mentioning that the temperature increase due to solar radiation for the dam crest is computed using the solar flux for horizontal surfaces obtained from (DOE EnergyPlus^{TM} 9.3.0, 2020).

6.1.1.5 Water Temperature

Approximation of the monthly variation of the water temperature at different depths is an important task in the lack of sufficient field data during thermal analysis. For the case study dam, the water temperature during various months at 10 different depths from surface down to 100 ft

is available. However, the equations suggested for the water temperature approximation in dams, require that at least some data from the bottom of the reservoir be available. In this case the available reservoir temperatures are used to fit a sin curve to represent the surface temperature and a constant temperature equal to 4^oC is taken as the bottom temperature based on the statement in Tatin et al. (2018) that the water temperature cannot become less than this value. The Ardito, Maier, and Massalongo (2008) equation A.5 parameter ϕ is then obtained by fitting the data to equation A.5 using those two defined top and bottom temperatures. The ϕ value was determined to be equal to -0.02 for the case study dam.

$$T_w(y_w, t) = T_{bot}(t).\frac{1 - e^{-\phi y_w}}{1 - e^{-\phi H}} + T_{top}(t).\frac{e^{-\phi y_w} - e^{-\phi H}}{1 - e^{-\phi H}} \tag{6.3}$$

where T_{bot} is the time sequence of temperature measurements at $y_w = H$ (reservoir bottom); T_{top} is the time sequence of temperature measurements at $y_w = 0$ (reservoir top), and most importantly ϕ is an empirical parameter that must be properly determined for the specific dam. The resulted equation is presented below. It should be noted that the R-squared goodness of fit is about 0.6.

$$\begin{aligned} T_{Bottom} &= 4 \\ T_{Top} &= 10.3 - 5.3sin(\frac{2\pi}{12}t - 0.11) \\ T(t, y_w, H)_{Reservoir} &= (T_{Bottom}).\frac{1 - e^{-(-0.02)y_w}}{1 - e^{-(-0.02)H}} + (T_{Top}).\frac{e^{-(-0.02)y_w} - e^{-(-0.02)H}}{1 - e^{-(-0.02)H}} \end{aligned} \tag{6.4}$$

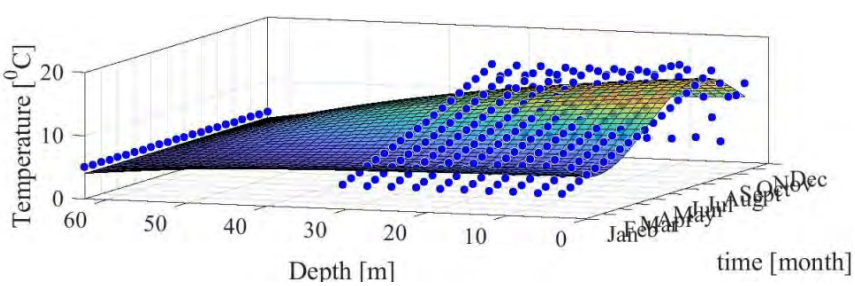

Figure 6.2: Dam reservoir temperature

6.1.1.6 Water Elevation

As discussed previously, the water elevation does not maintain the similar values for a particular day within several years. Yet as shown in figure 6.3 here the mean value of the whole available data of about 63$[m]$ and a variation of 2.2$[m]$ is considered for the water level elevation variation.

$$T(t, y_w, H)_{Reservoir} = 63 + 2.2sin(0.0172t + 220/63) \tag{6.5}$$

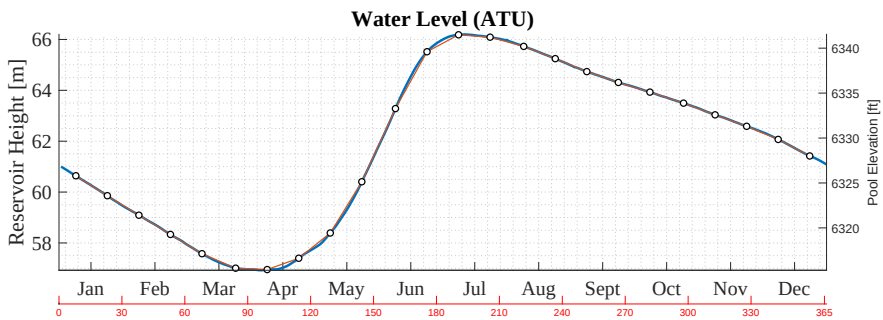

Figure 6.3: Pool Elevations

6.1.2 AAR Analysis

6.1.2.1 Concrete and AAR Properties

The concrete, and (initial, as some values will be determined later from the parameter identification process, Chapter 9) AAR properties used for the AAR analysis are summarized in tables 6.3 and 6.4. It should be noted that the modulus of elasticity is considered variable through the height of the dam considering lower values at the top portion of the dam. Since the AAR model automatically accounts for the reduction of the concrete elastic modulus and tensile strength as expansion occurs, the initial values for the elastic modulus was considered according to the reported values at 1980 which is the starting year of the AAR analysis and based on the later test results no more than 20% reduction is assumed for that. As for the concrete tensile strength, based on the available core test results in 2009 and 2013, the initial value in 1980 is considered to be equal to 1.5 MPa with a reduction factor of 0.33.

Also, the rock properties are briefly tabulated in 6.5.

Table 6.3: Concrete Material Properties

Concrete				
No.	**Description**	**Symbol**	**Unit (SI)**	**Mean**
1	Thickness	t	m	1
2	Mass density	ρ	Gg/m^3	0.00225
3	Thermal expansion coefficient	α	1/°C	9.90E-06
4	Poisson's ratio	ν		0.2

No.	Description	Symbol	Unit (SI)	Mean elevation(m)	Mean
5	Modulus of elasticity	E1	Mpa	1929.5	16217.3
		E2	Mpa	1,912.6	24,515.3
		E3	Mpa	1,897.4	30,083.2
		E4	Mpa	1,882.2	30,083.2
		E5	Mpa	1,870.7	30,083.2

6.1.2.2 Joint Properties

The Properties of the modeled contraction and peripheral joints used in the finite element analysis is shown in table 6.6. It should be noted that the concrete rock joint specified in this table only refers to the dam-abutment interface and a full concrete-rock bound is considered below the dam.

6.2 Analysis Procedures

6.2.1 Procedure for Thermal Analysis

Since AAR is a temperature dependent reaction, a thermal analysis is a prerequisite for conducting an AAR analysis. The detailed procedure for the input data preparation required for thermal analysis is summarized in the flowchart of figure 6.4.

Table 6.4: Initial AAR Properties

Initial AAR Properties (Concrete)				
No.	**Description**	**Symbol**	**Unit (SI)**	**Mean**
1	material group ID	MatID #		1
	Expansion characteristics			
	1 ATU			
2	Maximum volumetric strain at temperature T0test	ε^{∞}		4.80E-02
3	Characteristic time at temperature $\theta_0^{test} = 273 + T_0^{test}$	τ_c	ATU	999.00
4	Latency time at temperature $\theta_0^{test} = 273 + T_0^{test}$	τ_l	ATU	210.0
	Thermodynamic properties			
5	Activation energy associated with τ_c	U_c	$\circ K$	5,400
6	Activation energy associated with τ_l	U_l	$\circ K$	9,400
12	Reference temperature (oC) of tests for τ_l and τ_c	T_0	$\circ C$	18
	Strength			
10	Tensile strength	$f_t^{'}$	MPa	1.5
9	Compressive strength (must be negative)	$f_c^{'}$	MPa	-30.0
	Γ_t			
7	Residual reduction factor for Γ_t	Γ_r		0.1
8	Fraction of ft prior to reduction of AAR expansion due to macro cracking	γ_t		0.5
13	Upper compressive stress beyond which there is no more AAR expansion; must be negative	σ_U	MPa	-10
	Γ_c			
11	Shape parameter (0. for straight line)	β		0.5
	Degradation Body			
14	Reduction fraction for Young's Modulus when AAR reaction ends	β_E		0.8
15	Reduction faction for tensile strength when AAR reaction ends	β_f		0.33

Table 6.5: Rock Material Properties

Rock	Weight Density	0.00247	Gg/m^3
	Elastic Modulus	20,684.3	MPa
	Thermal expansion coefficient	0.00	$1/^{\circ}C$

Table 6.6: Joint Properties

The case study dam				
Joint Properties		**Joint location**		**Units**
		7: Conc-Conc	**8:Conc-Rock**	
Thickness	h	1.00	1.00	m
Mass density	ρ	0.00	0.00	Gg/m3
Coefficient of thermal expansion	α	0.00	0.00	
Static Young's modulus	E_s	3.2610E+01	3.26E+01	MPa
Tangential stiffness	K_{ts}	3.2610E+03	3.26E+03	MPa
Normal stiffness	K_{ns}	3.2610E+03	3.26E+03	MPa
Tensile strength	f_{ts}	1.00	1.00	MPa
Cohesion	C_s	0.74	0.74	MPa
Friction angle	F_{fs}	35.00	35.00	degree
Dilatancy angle	F_{Ds}	10.00	10.00	degree
Fracture energy Mode I	$GIFs$	8.00E-05	8.00E-05	MN/m
Fracture energy Mode II	$GIIFs$	8.00E-04	8.00E-04	MN/m
Relative value of irreversible deformation	γ_s	0.30	0.30	
Maximal displacement for dilatancy	u_{Dmaxs}	0.01	0.01	m
Tensile stress at the break-point	s_{1s}	0.00	0.00	MPa
Crack opening displacement at the break- point	sw_{1s}	0.00	0.00	m
Cohesion at the break-point	c_{1s}	0.00	0.00	MPa
Crack sliding displacement at the break-point	cw_{1s}	0.00	0.00	m

As described in this figure, the first step is on the mesh preparation, as well as extraction and classification of elements to which the thermal loads are being applied. In other words, one needs to determine the nodes and elements at the upstream and downstream sides at which the water and air temperature will be applied; in addition the nodes at which the adiabatic boundary conditions are defined has to be separately specified.

The second step for performing a thermal transient analysis is to gather the data corresponding to the thermal loads:

- Air Temperature: The recordings of air temperature at the location of the dam can help to have a good estimate of the temporal variation of the air temperature for the considered analysis time step.
- Solar radiation: The temperature increase due to the effect of solar radiation has to be determined based on the location of the dam and the orientation and inclination of different parts of the dam with respect to the sun. This temperature increase will be added to the air temperature.
- Water temperature: In the absence of sufficient recordings of water temperatures through the whole depth of the reservoir, one can utilize the empirical relations available in the literature to estimate the reservoir temperature.
- Water elevation

Furthermore, the concrete material properties needs to be determined along with air and water film coefficients. Finally, having all the above mentioned information in hand, the thermal loads can be applied to the finite element model, and a thermal transient analysis can be performed.

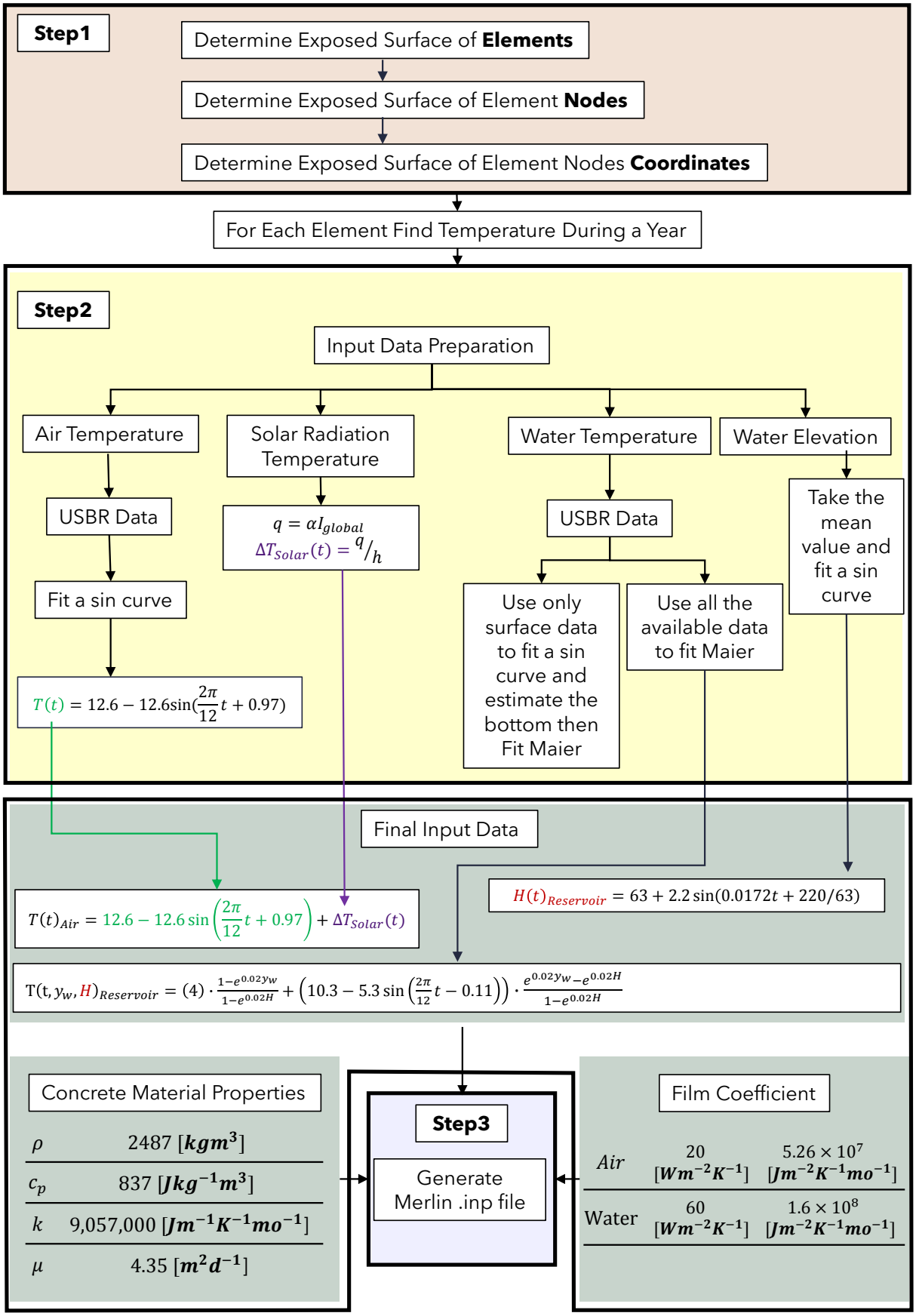

Figure 6.4: Flowchart describing the thermal analysis input data preparation procedure

6.2.2 Procedure for Uncertainty Quantification and Stress Analysis

The AAR analysis requires calibration of the AAR model parameters such that the resulting displacements match the recorded ones. To this purpose, a system identification procedure can be used to determine the parameters associated with the AAR model. When determined, those values will be used as the mean of those random variables for the uncertainty quantification of the stress analysis. As shown in figure 10.10 the procedure of performing the uncertainty quantification(UQ) consists of 2 main parts:

- Thermal Analysis
- Stress Analysis

In a uncertainty quantification procedure there are uncertainties associated with the air and water temperature which in turn translates into the concrete internal temperature. As such, each stress analysis has to be paired with a thermal analysis which determines the concrete internal temperatures.

As seen in the flowchart of figure 10.10 the very first step for every uncertainty quantification is to determine the sources of uncertainty in the analysis and define them as the random variables. It is worth noting that in this study a zero correlation is considered between the variables. Then, the next step would be to determine a distribution which can best describe each random variable as well as the correlations between them. Next is to utilize a sampling technique such as the Latin Hypercube Sampling (LHS) to extract samples from the random variables. Combining these variables, finite element models can be generated and analyzed.

Starting from the thermal analysis, a number of models has to be created and analyzed. As seen in the flowchart, the concrete temperatures obtained from thermal analysis are then gathered and used as the inputs of the AAR analysis in the next stage.

The same sampling procedure as discussed above has to be repeated for the AAR analysis to incorporate the uncertainty associated with the AAR and other concrete properties. Last but not least is to gather and interpret the results from all analyses.

It should be noted that in order to interpret the results, one has to decide about what has to be the outcome of the analysis and what are the useful information which need to be recorded prior to launching the uncertainty quantification(UQ) procedure.

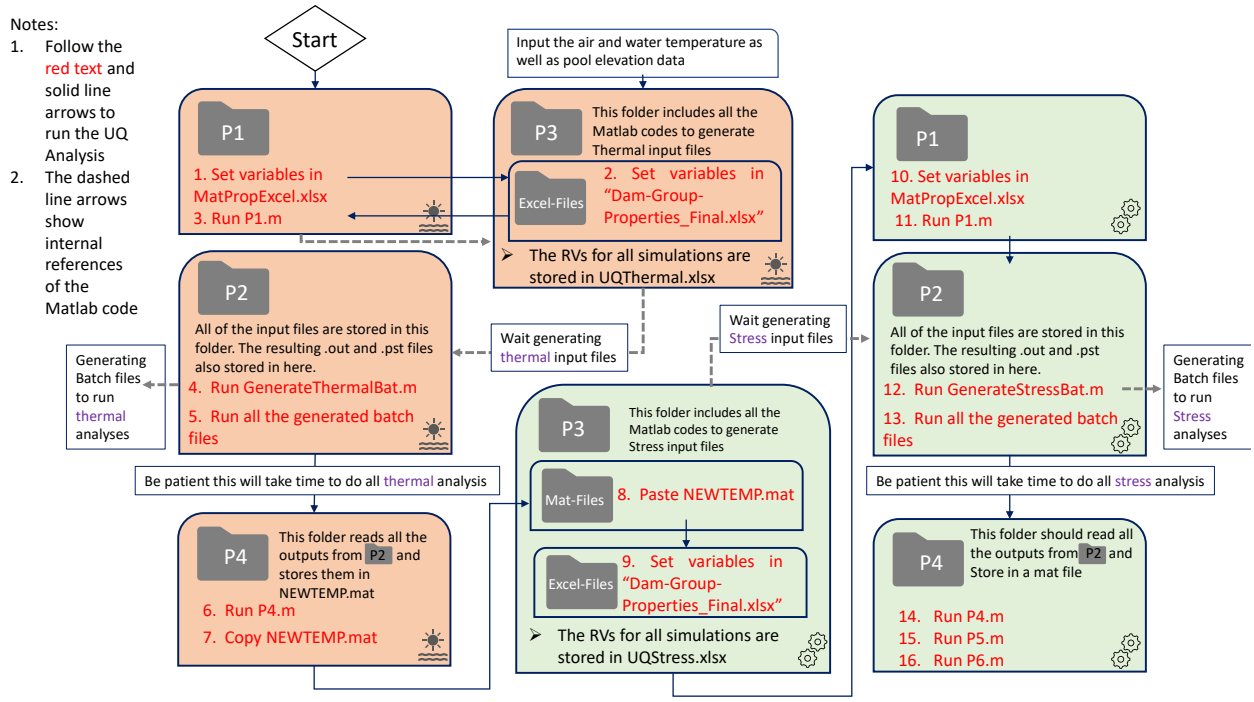

Figure 6.5: Flowchart of UQ Procedure

Chapter 7

Physical Modeling

Abstract

Whereas the preceding chapter has focused on the physical parameters associated with the analysis, this one will address modeling issues.

First, the dam will be described (to the extent possible). Then the "crafting" of a reasonable and representative finite element mesh will be described.

This will be followed by the modeling of stage construction and will highlight its importance.

Then, recognizing that the application of the full hydrostatic load in one load increment may cause convergence errors, it will be shown that that adoping three increments will suffice to avoide this error.

Finally, it will be shown that computational time can be substantially cut if a reduced (yet accurate) foundation model is adopted.

7.1 Physical Model

The dam is a concrete arch dam located on [redacted]. The dam was completed in [redacted] with a structural height of [redacted], a hydraulic height of [redacted], a crest length of [redacted], and a total concrete volume of [redacted] cu yd. The reservoir provides water storage for irrigation, hydroelectric power generation and recreation.

The arch dam has a crest width of [redacted]m, a maximum base width of [redacted] m, a [redacted] m radius for the vertical upstream face, a variable radius for the sloping downstream face, and 1m high concrete parapet walls to el [redacted].

The dam was constructed in one construction season. Construction started on [redacted], and it was completed on [redacted].

The dam is experiencing concrete expansion, cracking and deterioration due to alkali-silica reaction (ASR) and freeze-thaw damage.

7.2 Geometry Model

The geometry model of the dam is prepared based on maps provided by USBR. The geometry model includes the joints (not used in thermal analysis), and multiple regions (blocks) which facilitate implementation of variable temperature.

The geometry of the dam as well as its orientation with respect to the north direction can be obtained from figure 7.1.

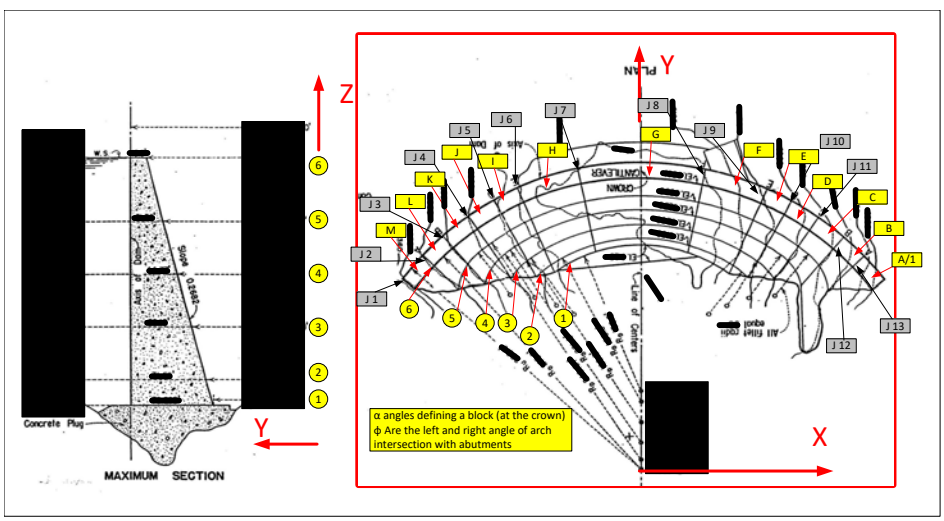

Figure 7.1: Geometry of the Dam; Redacted dimensions

Regretfully, at the sponsor's request dimensions had been redacted.

On the other hand, more insight can be found in Fig. 7.2 which is taken from Salamon,

Dressel, and Liechty (2021).

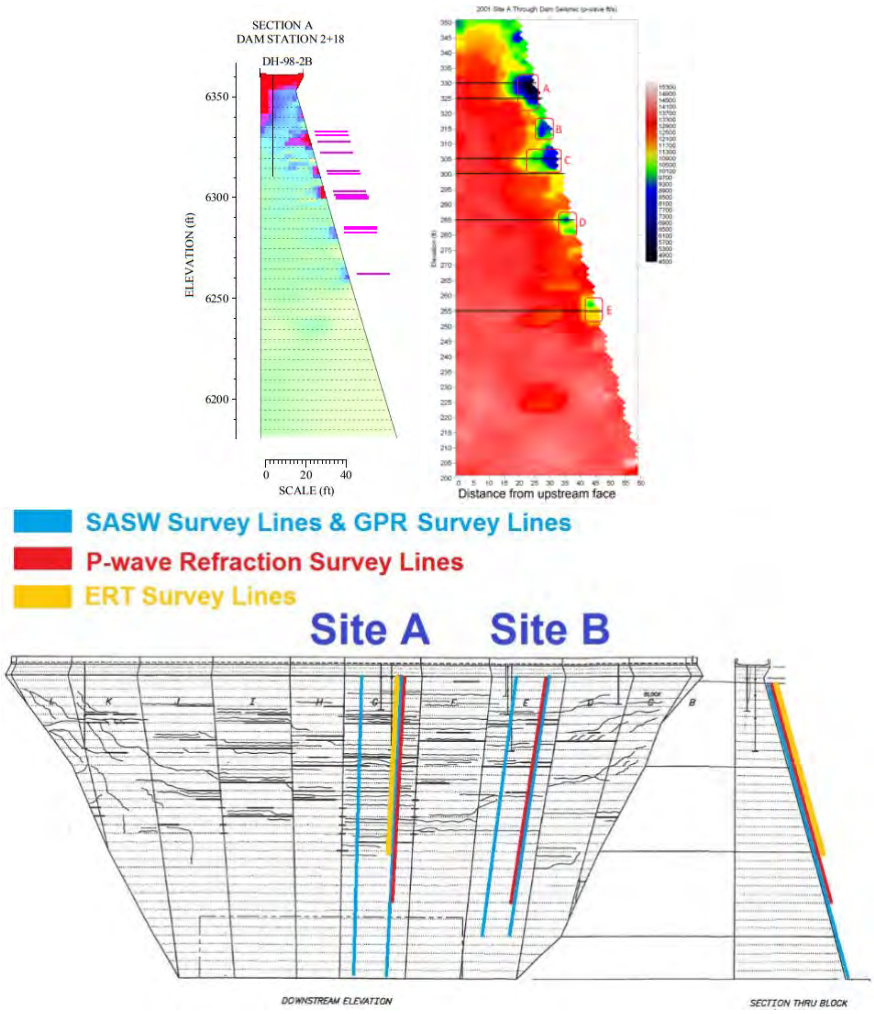

Figure 7.2: Additional description of the dam (Salamon, Dressel, and Liechty, 2021)

In order to develop a precise mathematical model (finite element mesh) of the dam, the geometry of different parts are accurately drawn as shown in figure 7.3 and then using Matlab® a model is developed, Fig. 7.4. The geometry model of the dam is prepared based on maps provided by USBR. The geometry model includes the joints (not used in thermal analysis), and multiple regions (blocks) which facilitate implementation of variable temperature.

Then a Matlab® code is written to display the contour of the dam, Fig. 7.4.

The Matlab® model enabled us to define a "boundary file" of the mesh, which in turn was processed by T3D Rypl, 2021 to generate meshes.

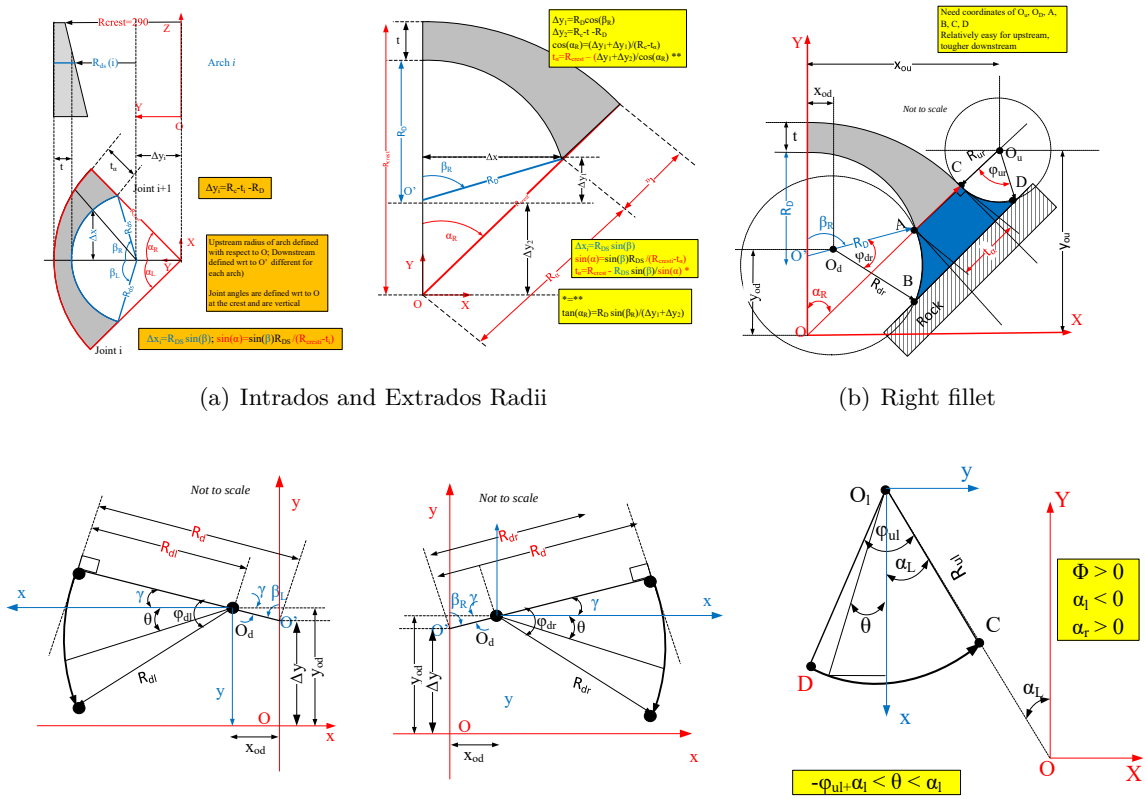

(a) Intrados and Extrados Radii

(b) Right fillet

(c) Left and right fillet downstream

(d) Right fillet upstream

Figure 7.3: Mathematical Modeling of the Dam

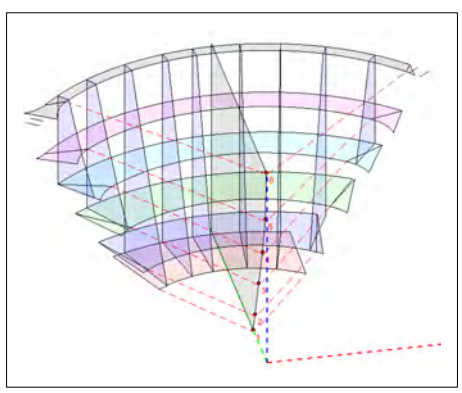

Figure 7.4: Matlab® based final model

The geometry model includes the joints (not used in thermal analysis), and multiple regions (blocks), Fig. 7.5, to facilitate implementation of the stage construction.

Three meshes were generated:

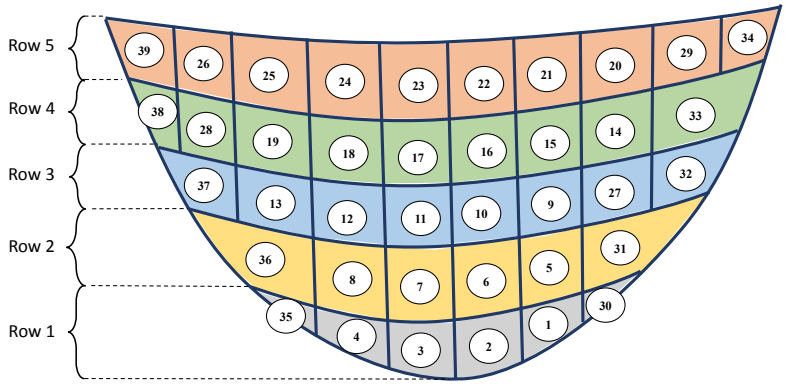

Figure 7.5: Staged construction modeling plan the dam upstream

Thermal: where no joints were inserted between the monoliths or under the concrete dams.

Full: mesh with joints inserted between all the monoliths, and another set "wrapped around" the dam to model the concrete rock-interface. The foundation was extended below the dam. To adequately simulate stage construction and various distribution of AAR expansion, the dam body was subdivided into 39 groups, Fig. 7.5.

Reduced: Identical to the previous one, however rock was modeled by a single layer of elements to reduce computational time while maintaining fidelity.

It should be noted that the lift joints were not modeled.

7.3 Stage Construction

In the stress analysis of an arch dam, it is important to properly simulate the self weight of the structure and the resulting stresses during the construction. In most cases the construction stages is simulated through activating the elements in a sequential manner such that it can represent the construction procedure and capture the induced appropriate stresses by the self-weight of the structure. As a matter of fact, the sequence of activating elements depends on the real construction procedure and therefore it might consist of several stages. It has been widely accepted that applying the self weight of an arch dam with the assumption of being a single monolith results in inaccurately estimating the stresses in the structure. As presented in Malm, Hassanzadeh, and Hellgren (2017) the self weight of the structure is applied sequentially as a part of the static and seismic analysis of an arch dam. This procedure was followed in other studies as well, such as Hariri-Ardebili, Mirzabozorg, and Kianoush (2013) and Alembagheri (2019). Figure 7.7 further clarifies the effect of staged construction on the development of stresses and the importance of considering this in the finite element model. Figure 7.7a, b and c shows the case where a dam is considered to have been built as a single monolith. In this case the only reaction forces that act against the body weight of the structure comes from the rock interface, which also varies based on the shape of the valley. Therefore the wight of the structure will result in development of hanging tensile stresses. On the other hand, looking at figure 7.7d through h building one layer at a time results in the lower layers

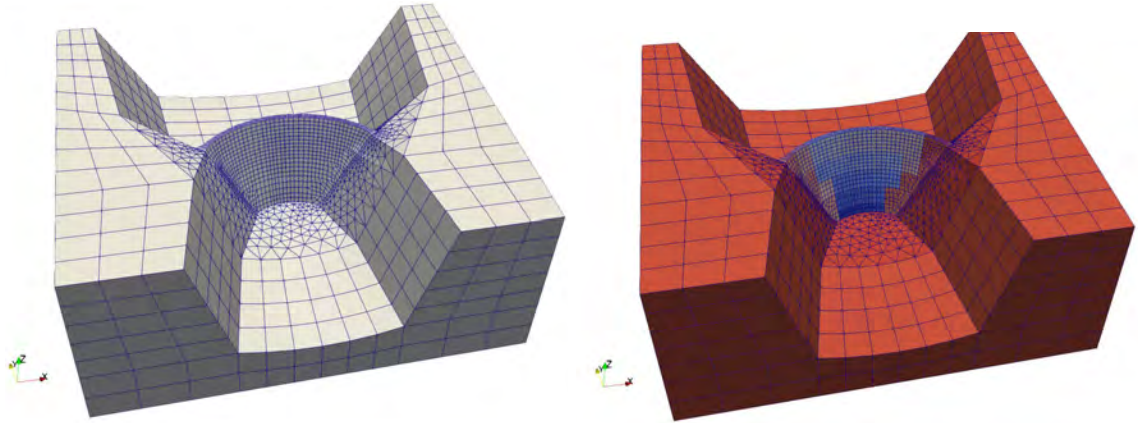

(a) Full mesh

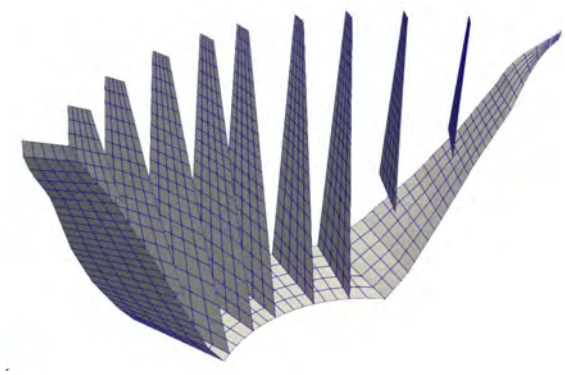

(b) Joints in stress analysis meshes

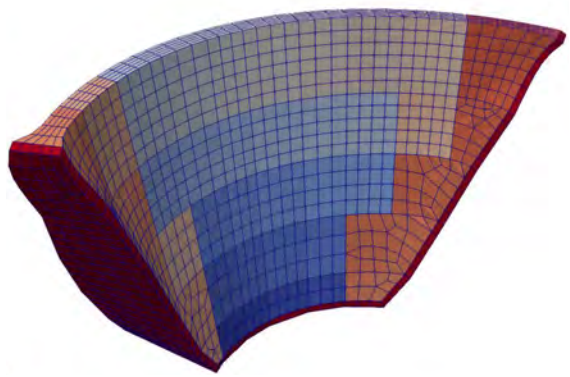

(c) Material groups

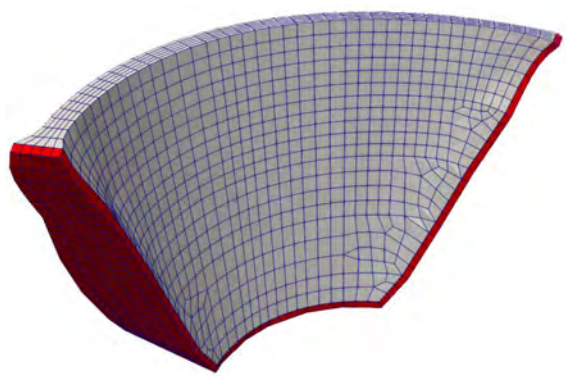

(d) Reduced foundation; Foundation shown in red

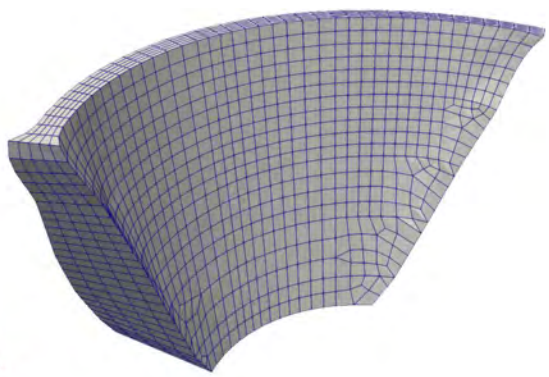

(e) Thermal analysis

Figure 7.6: Finite element mesh

providing an additional support for the weight of the upper layer and thus preventing the stresses shown in figure 7.7c.

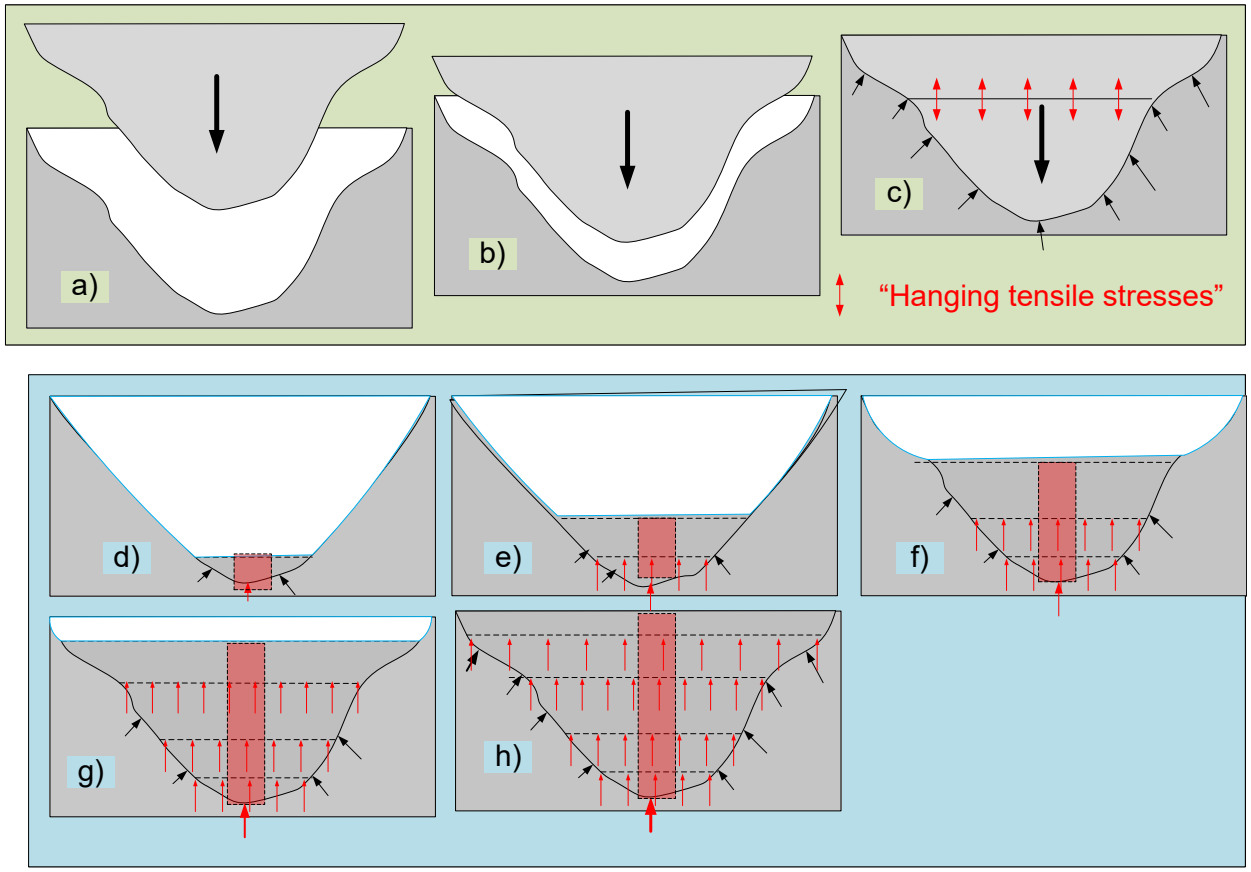

Figure 7.7: Development of Stresses through construction stages

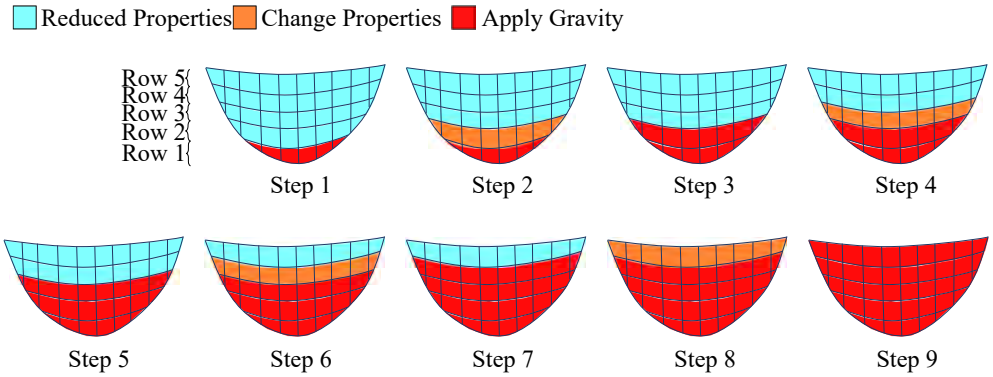

Figure 7.8: Modeling of stage construction

7.3.1 Proposed methodology

Ideally, a computer program should be able to handle so-called "ghost elements" that can be activated or deactivated to model staged construction or excavation respectively.

When this is not possible in a finite element code, one which allows modification of the elastic properties within a load increment (as is the case with Merlin), then an alternative approach is possible.

With reference to Fig. 7.8 A necessary condition is for the used finite element code be capable of modifying material properties (specific weight in particular) within a load increment. This feature may not be present in some programs. the approach is as follows:

(1) Break the dam into multiple blocks/layers which best represents the construction stages

(2) Define the real material properties for the layer that was first constructed and specify reduced properties for Modulus of elasticity(E), Poisson's ratio (ν) and mass density (ρ) for all other layers

(3) Apply gravity load only to the first layer

(4) Tag the next group to have its properties updated one property at a time (this is necessary in Merlin, but not necessarily in other codes)

(5) Apply gravity to the first and second layer

(6) Repeat the previous steps for all layers until all material properties are updated to the real

values and gravity load is applied to the whole dam body

(7) It is necessary to set the displacements to zero after the staged construction in order to only account for the dam long term post-construction deformations.

7.3.2 Verification Study

In order to investigate the effect of modeling staged construction in the dam, the finite element model is analyzed assuming 2 different cases. In the first case, the body force is applied directly to the whole structure at once and in the second attempt the body force is applied gradually through 5 stages to the whole dam body; as shown in figure 7.5 each construction stages are differentiated through various colors. In other words, it is assumed that the dam was constructed such that at first the blocks at the first level in gray are built, then the second level was put on top of that and so on. Therefore, we have activated the body forces assuming this sequence in our finite element analysis to account for the effect of the staged construction. The results of the 2 above mentioned cases are shown and compared in figures 7.11 through 7.10 for upstream, downstream and a vertical cut at the middle of the dam. It is shown in figure 7.9 that in stage one only a portion of the bottom of the dam is experiencing stresses due to the body force which is shown in light red color. In the second stage the light red color climbs up and the stress at the bottom of the dam increases accordingly. As seen this trend continues until the 5th stage in which again the stress distribution is an indicative of the gradual application of the body force to the body of the dam.

7.3.3 Verification

In order to better compare the results of staged construction a segment of the dam is isolated, as shown in figure 7.15, and the vertical stresses integrated at 0, 25, 50 and 75% of the height and the resultant force is compared with the weight of the concrete "column" above the section using the simple formula:

$$W = \rho g V \tag{7.1}$$

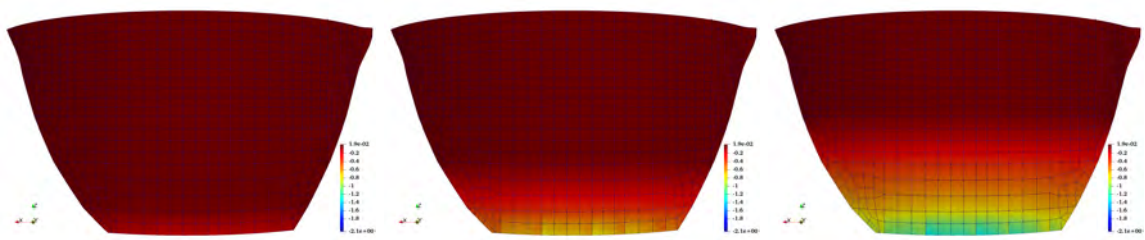

(a) σ_{zz}, Stage 1 (b) σ_{zz}, Stage 2 (c) σ_{zz}, Stage 3

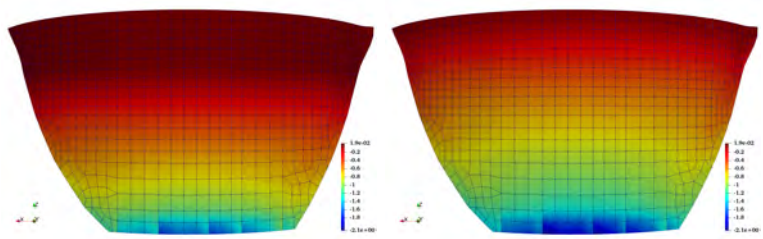

(d) σ_{zz}, Stage 4 (e) σ_{zz}, Stage 5

Figure 7.9: Effect of modeling staged construction the dam Upstream; different stages

where W is the total weight (kN), V is the concrete volume (m^3), ρ the mass density of concrete ($2,500Kg/m3$), g the acceleration of gravity ($9.81m/s2$). Then the error is computed using staged construction and without using staged construction. At all four elevations, the error is much smaller using staged construction as shown in figure 7.16. Interestingly, the error with staged construction (well within 5% at all elevations) increases with height. This may be reflective of local stress redistribution/bridging occurring with height.

7.4 Hydrostatic Load

The next step to the stress analysis, is to apply the hydrostatic load behind the dam. In order to ensure the convergence rather than applying the total amount of water at once, the loading was started from a very low depth and increased in 3 steps. 7.17 shows the increment steps of hydrostatic load application. It can be seen through the figure that the principal stresses are increasing as the reservoir level elevates.

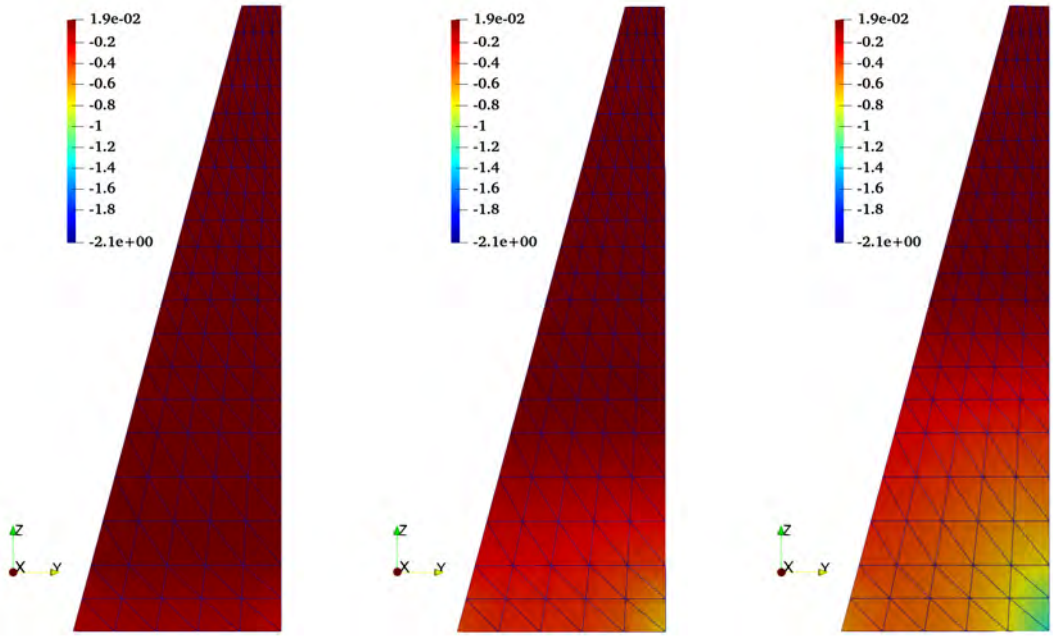

(a) σ_{zz}, Stage 1

(b) σ_{zz}, Stage 2

(c) σ_{zz}, Stage 3

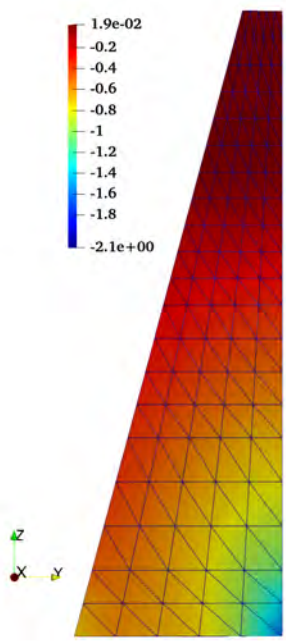

(d) σ_{zz}, Stage 4

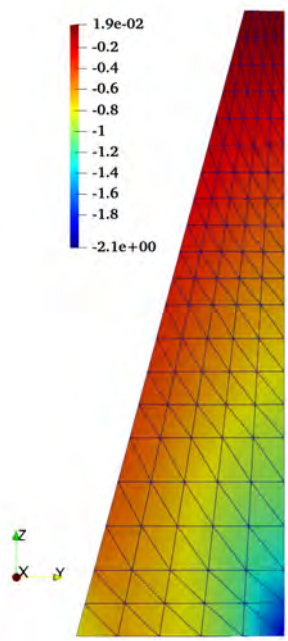

(e) σ_{zz}, Stage 5

Figure 7.10: Effect of modeling staged construction vertical cut from middle of the dam; different stages

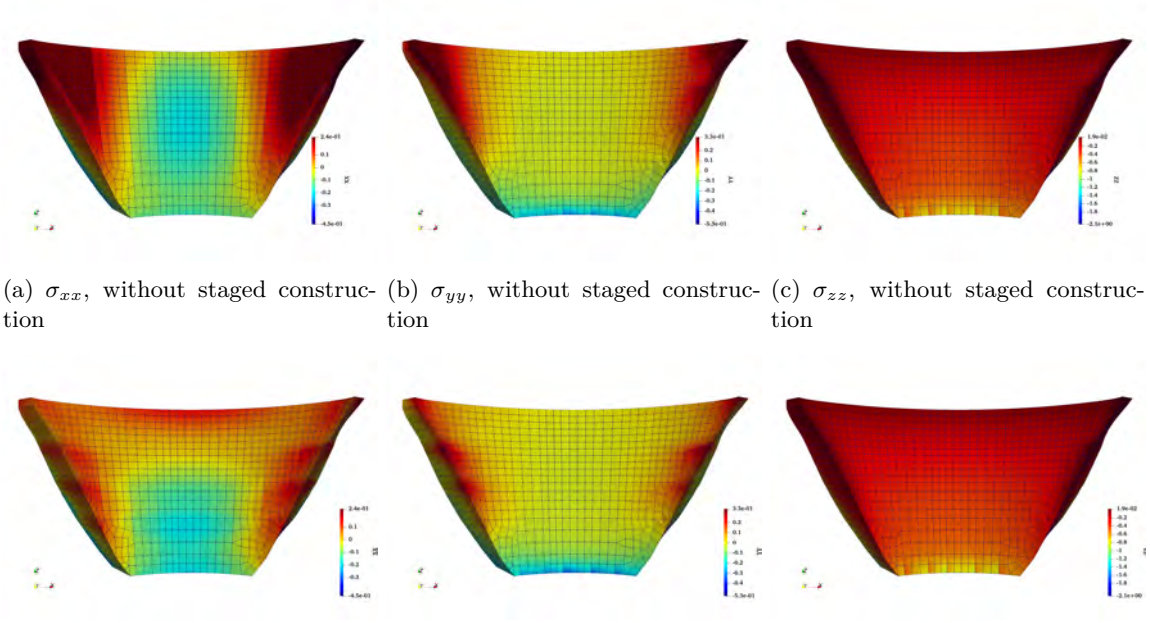

(a) σ_{xx}, without staged construction (b) σ_{yy}, without staged construction (c) σ_{zz}, without staged construction

(d) σ_{xx}, staged construction (e) σ_{yy}, staged construction (f) σ_{zz}, staged construction

Figure 7.11: Effect of modeling staged construction the dam Downstream

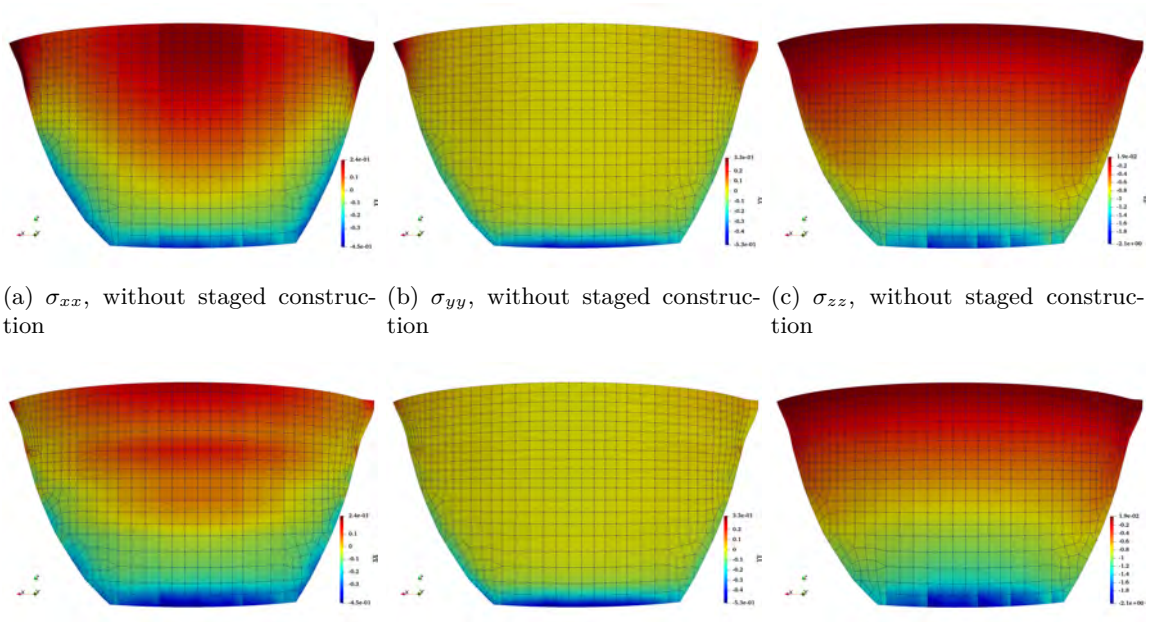

(a) σ_{xx}, without staged construction (b) σ_{yy}, without staged construction (c) σ_{zz}, without staged construction

(d) σ_{xx}, staged construction (e) σ_{yy}, staged construction (f) σ_{zz}, staged construction

Figure 7.12: Stress distribution; with vs. without Staged construction

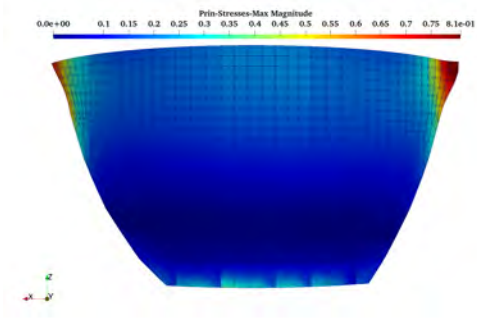

(a) σ_1, without staged construction

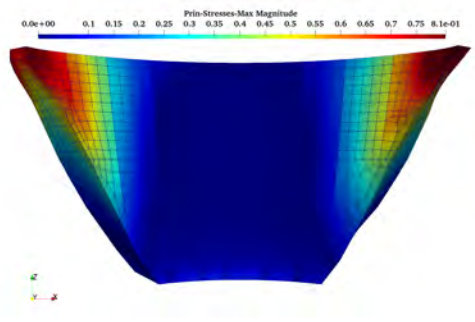

(b) σ_1, without staged construction

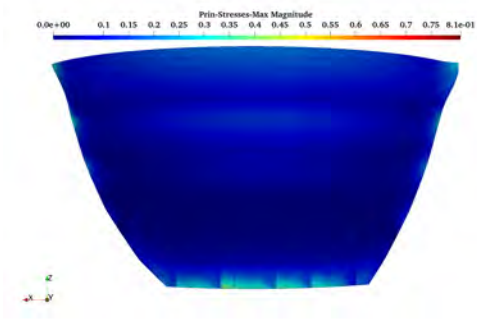

(c) σ_1, staged construction

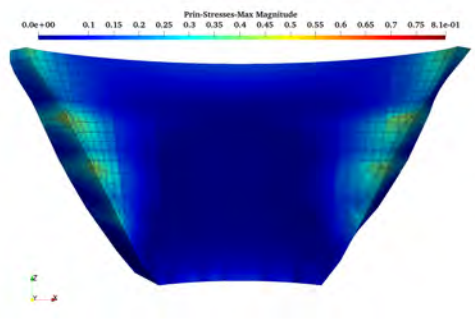

(d) σ_1, staged construction

Figure 7.13: Principal Stresses; With vs. without Staged construction

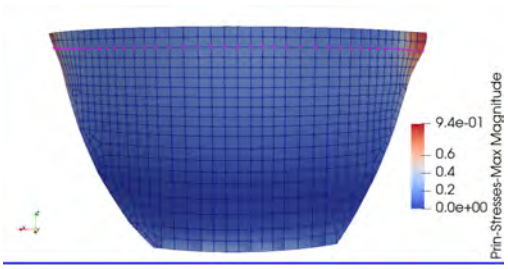

(a) Section cut

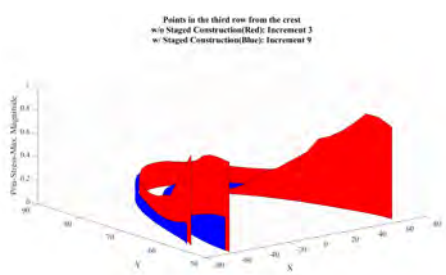

(b) σ_1

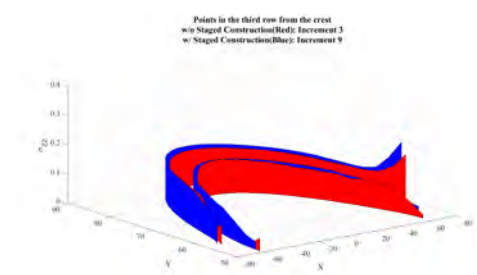

(c) σ_{zz}

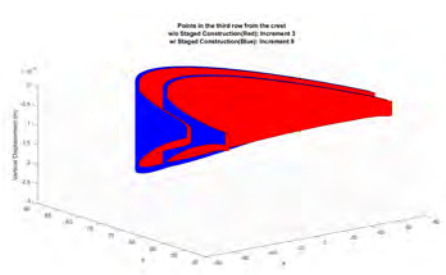

(d) vertical displacement

Figure 7.14: Stresse and displacements near Crest; With vs. without Staged construction

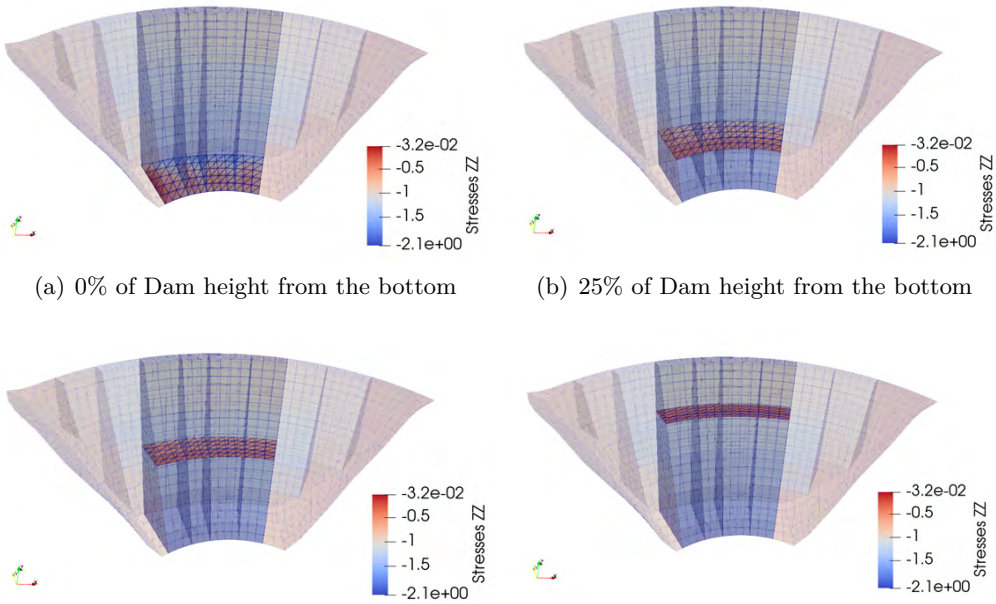

(a) 0% of Dam height from the bottom (b) 25% of Dam height from the bottom

(c) 50% of Dam height from the bottom (d) 70% of Dam height from the bottom

Figure 7.15: Four sections considered for stress integration and comparison with the self-weight

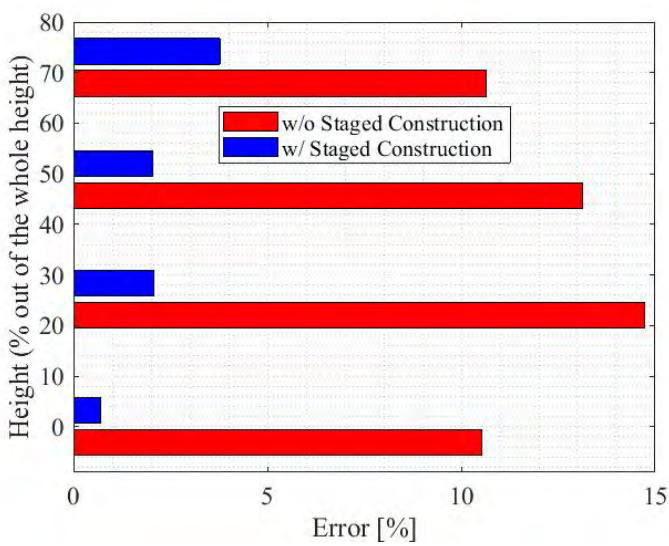

Figure 7.16: Error comparison between the two self-weight analyses

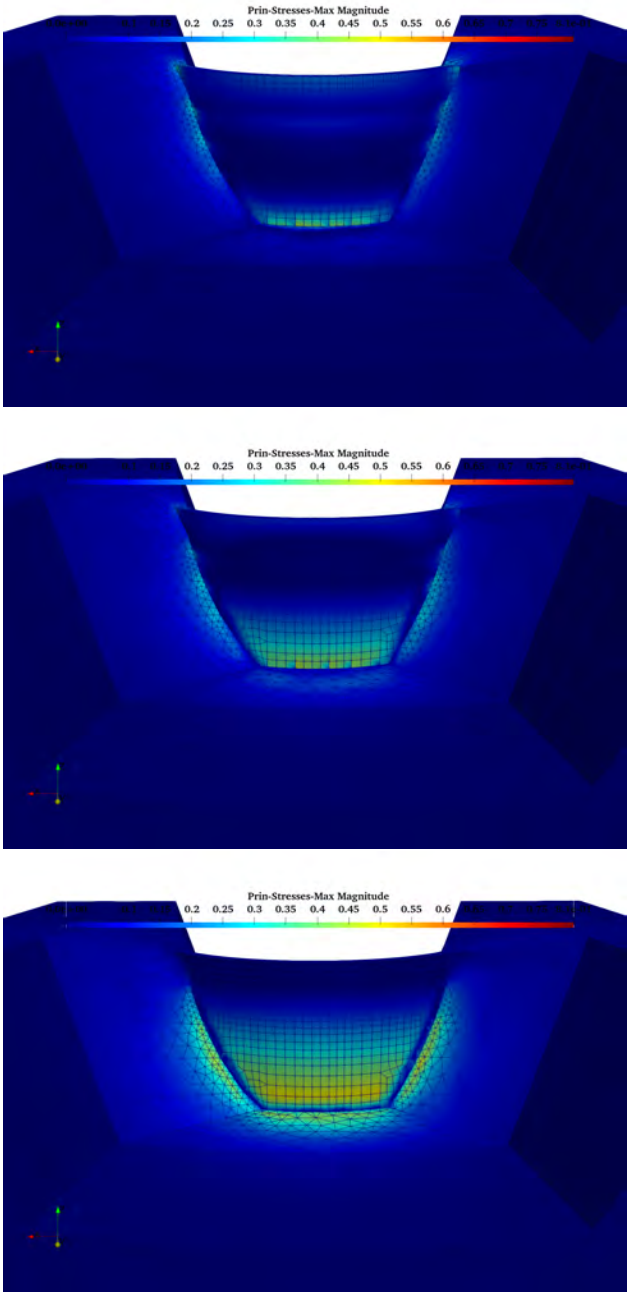

Figure 7.17: Gradual application of hydrostatic load in 3 steps

7.5 Foundation Modeling

The AAR Analysis was conducted based on the calibration of the data on the recorded crest displacements to the AAR model described in chapter 1. The contour plots of the crest displacement in z direction are shown in figure 7.18 after 20 and 40 years of AAR analysis. For clarity, we show only the dam without the foundations. The contour plots for the maximum principal stress is also shown in figure 7.19 which also features the joint openings and the deformed shape of the dm after 40 years of AAR analysis. Since each analysis takes about 7 hours to complete, and both

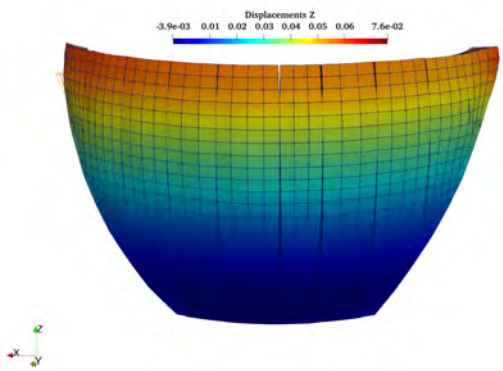

(a) Upstream, time=20 yrs

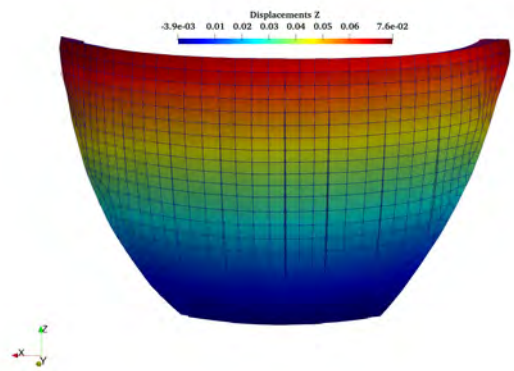

(b) Upstream, time=40 yrs

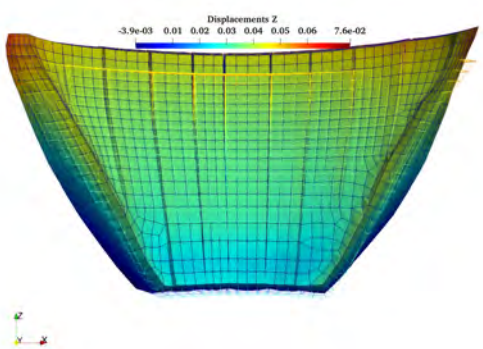

(c) Downstream, time=20 yrs

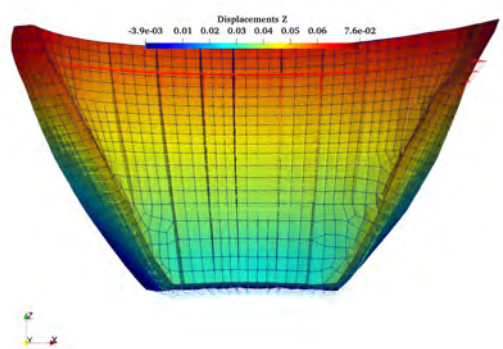

(d) Downstream, time=40 yrs

Figure 7.18: Z direction Displacement contour plots

the system identification procedure, and especially the probabilistic analysis will require multiple

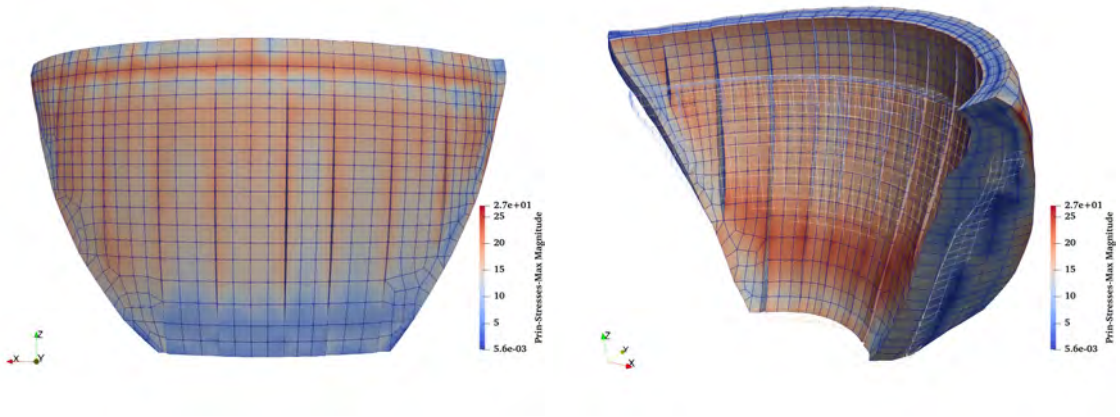

(a) Upstream (b) Downstream

Figure 7.19: Maximum principal stresses after 40 years

executions (100), we have modified the mesh by reducing the rock foundation to its simplest form (wrapped around the dam)(figure 7.20). Execution time was cut by about one third.

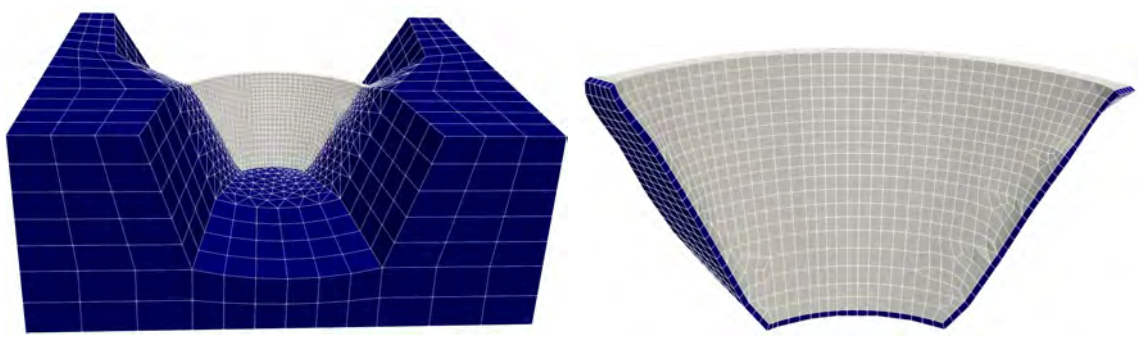

(a) Old Mesh, 12461 nodes (b) New Mesh, 8682 nodes

Figure 7.20: The old versus New mesh where the foundation is shown in blue

To assess the reliability of the new mesh, identical analyses were performed with the mesh with full foundation and the one with reduced, following is a comparison of the results. Figure 7.22 shows the difference of the displacements from the 2 meshes.

Table 7.1: The comparison of the execution time for the full and reduced mesh

	Number of Nodes	Execution time [hours:mins:seconds]
Full Foundation	12461	7:44:32
Reduced Foundation	8682	01:16.1

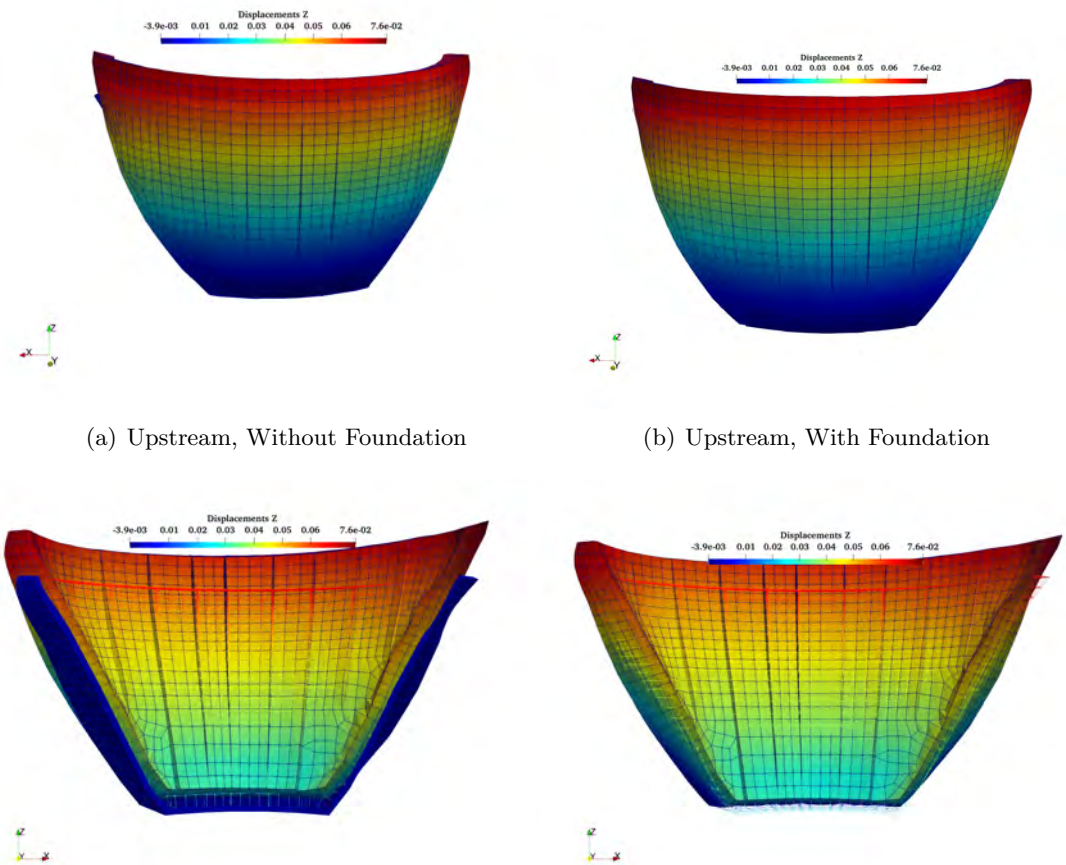

(a) Upstream, Without Foundation

(b) Upstream, With Foundation

(c) Downstream, Without Foundation

(d) Downstream, With Foundation

Figure 7.21: Z direction Displacement contour plots, comparison of models with full and reduced foundation

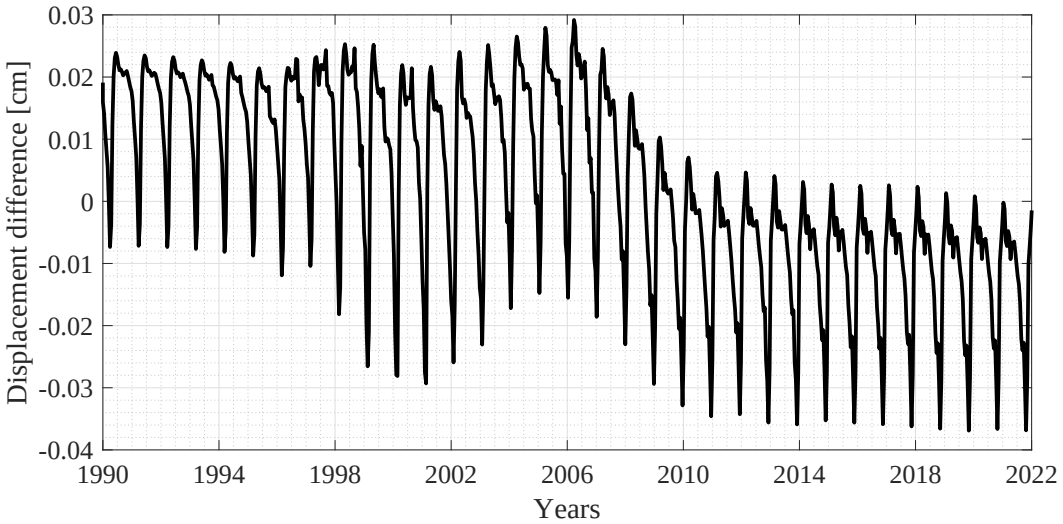

Figure 7.22: Difference of the crest displacement for the 2 meshes with full and reduced foundation

Chapter 8

Deterministic Thermal Analysis

Abstract

This chapter will detail the deterministic thermal analysis. First, results will be compared both with those obtained by Hatch, and the recorded field measurements. Impacts of time steps, solar radiations, and comparison between convection and conduction studies will be reported.

Finally, the spatial and temporal temperature distribution will be shown.

8.1 Analysis Procedure

The input temperature and elevation data have been presented in chapter 6 and will be now used to conduct the thermal analysis assuming the analysis time step equal to 15 days per each increment. Air temperature is applied at the downstream and crest as well as a portion of the upstream face which is exposed to air. Furthermore, the temperature increase due to solar radiation is applied at the upstream and crest elements. The reservoir temperature is applied to the elements beneath the water level taking into account the water level variation in different months.

8.2 Comparison with Hatch (2015)

Using film coefficients for air and water the temperatures are applied at the surface elements and the thermal analysis results for 3 nodes inside the concrete are compared with the measurements from DH03-01 instruments recorded at 3 different elevations of 6360 [ft], 6351 [ft] and 6288 [ft]. It

should be noted that the nodes were chosen to be closest to the location of DH03-01 instruments The results specially, for the 2 upper nodes, show a good match between the measured and computed temperatures besides showing stability within the first few years which vouches for the accuracy of the analysis (figure 8.1). Also, in this figure the results from Hatch, 2015 are presented for each of the measured elevations. Based on the figures, our results show closer match with the measured data.

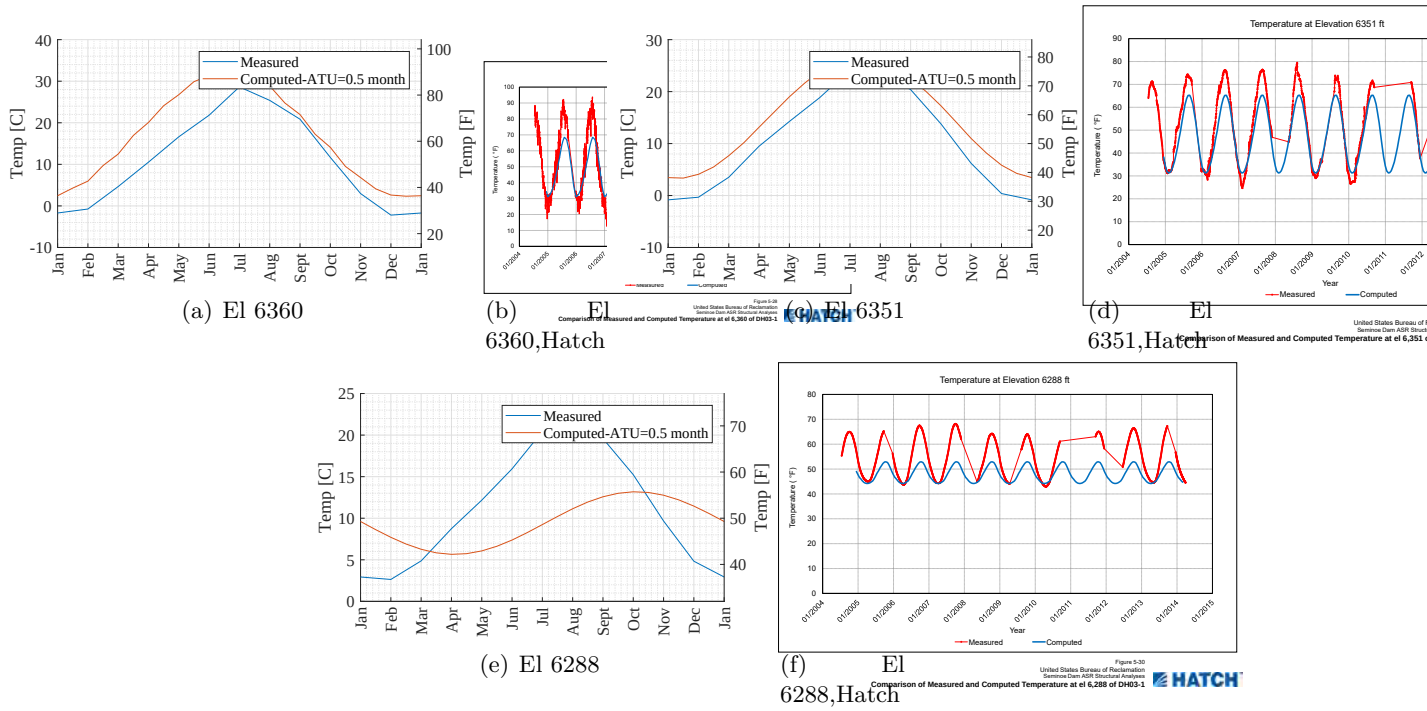

(a) El 6360 (b) El 6360,Hatch (c) El 6351 (d) El 6351,Hatch

(e) El 6288 (f) El 6288,Hatch

Figure 8.1: Comparison of thermal analysis results with measured values

8.3 Impact of Time Step

Figure 8.2 compares the thermal analysis results for 3 different time steps of approximately 7.5 days (about every week), 15 days (every two weeks) and 30 days(every month). Accordingly, the 15 days time step provides the closest values for temperatures to the measured data. In addition, decreasing time step to half, 7.5 days, does not have significant effect on the results and therefore is not worth adding the computational effort.

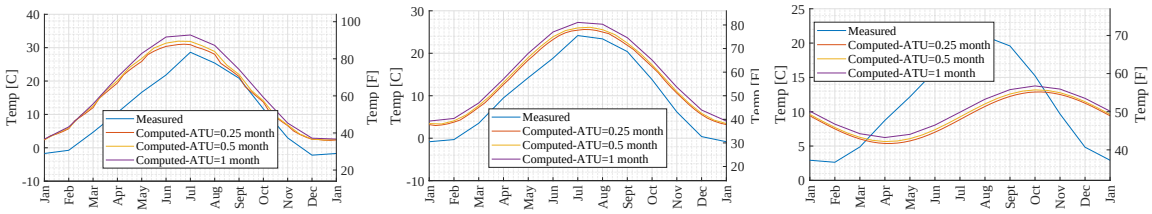

(a) Eleveation 6360 (b) Eleveation 6351 (c) Eleveation 6288

Figure 8.2: Comparison of thermal analysis results with measured values assuming 3 different time steps

8.4 Impact of Solar Radiation

Figure 8.3 is to show the importance of applying temperature difference due to solar radiation. It is shown that the solar radiation results in higher internal temperatures which would affect the further analysis results by increasing the stresses caused by higher temperatures.

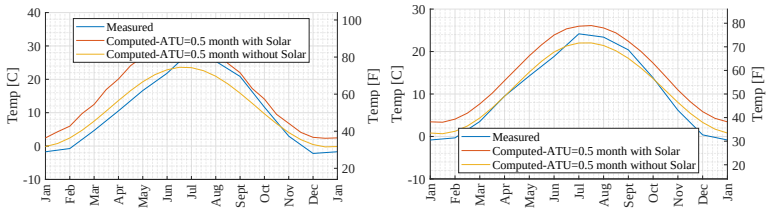

(a) Eleveation 6360 (b) Eleveation 6351

Figure 8.3: Comparison of thermal analysis results with measured values with and without solar radiation

8.5 Comparison of Convection and Conduction

The results presented so far, were obtained through modeling of convection. In other words the heat transfer was assumed to take place through the movement of the surrounding liquid. However, for the sake of comparison the thermal analysis is repeated for conduction in which the heat transfer occurs through direct contact . Figure 8.4 illustrates the difference of the above mentioned cases . As expected, the heat transfer through conduction results in higher internal temperatures compared to convection which gives closer results to the real measured data.

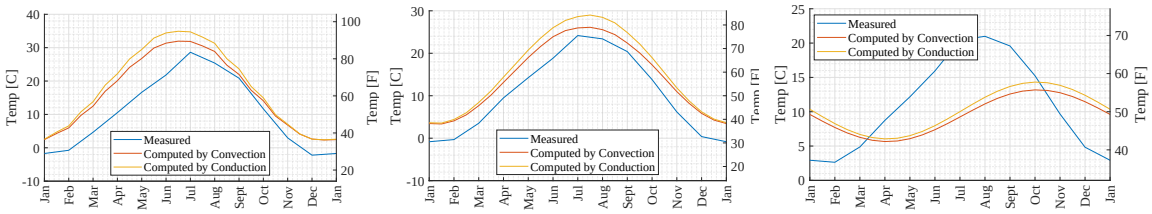

(a) Eleveation 6360 (b) Eleveation 6351 (c) Eleveation 6288

Figure 8.4: Comparison of thermal analysis results with measured values assuming high values for film coefficients

8.6 Internal Temperatures

The concrete internal temperatures obtained from thermal analysis are shown at 3 different cuts throughout the dam. First a cantilever cut through the height of the dam located at the middle of the arch dam (figure 8.5). Second, a horizontal section showing a complete arch of the dam cut from below the water level (Elevation 6243 [ft]) figure 8.6. Third, is the same as second cut except that the section is at an elevation above the water level (Elevation 6348 [ft]) in order to show the temperatures for the portion of the dam which is exposed to the air 8.7. Furthermore, the upstream face of the dam is shown in figure 8.8 in which the water level can be distinguished through the sudden temperature change observed at the top of the dam which is due to the exposure of the area to the solar radiation as well as air temperature. Finally figure 8.9 shows the temperature contour plots throughout one year at the downstream face. From the figures above it is observed that starting January the concrete internal temperature starts gradually decreasing until may, then with the rise of temperature in May through September the concrete internal temperature also increases and the heat propagates to the whole dam structure. The contour plot in november shows that there is just a corner at the bottom of the dam at the upstream side that almost always maintains its low temperature. As shown, the effect of temperature increase inside the dam starts vanishing as approaching the colder months of the year and the procedure is followed by the first month of the following year. Furthermore, it is shown that the temperatures are highest during June through August. Also, The highest temperatures occur at the crest and on upstream face above

the water level. These observations can be verified with the other cuts in the following figures. Due to the fact that figure 8.6 is a section from mid height of the dam. The upstream side is showing the water temperature which is lower than the air temperature observed at the downstream side. Similar to the observations from previous figures, these figures also show the temperature increase starts in May and continues through September and subsequently starts disappearing in October through December followed by the first 3 months of the next year. In figure 8.7, similar to 8.6, the section is horizontal but at a high elevation close to the crest. This figure is provided to show the internal temperatures above the water level. This figure also supports our previous observations throught out the year. Another, key observation drawn from this figure is that the temperature increase is almost uniform throughout the whole arch from East side to the west.

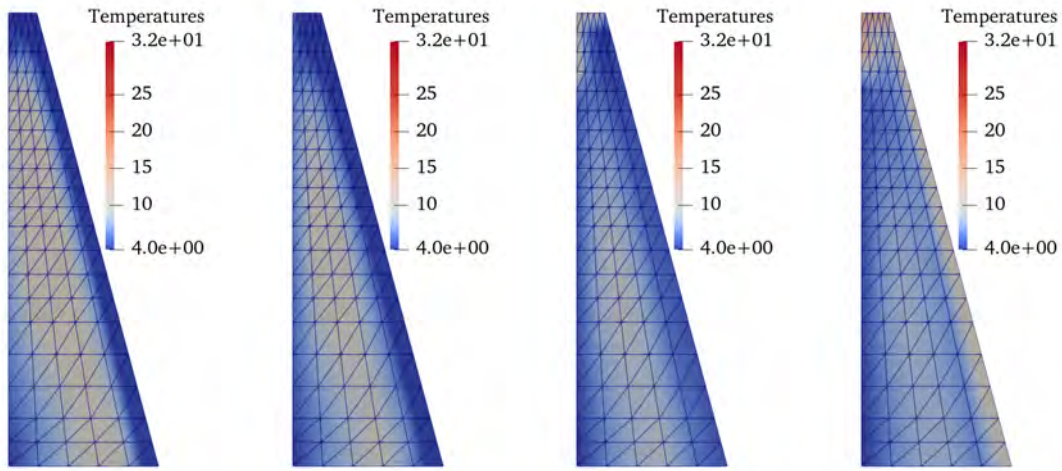

(a) January

(b) February

(c) March

(d) April

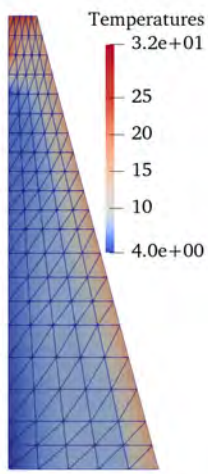

(e) May

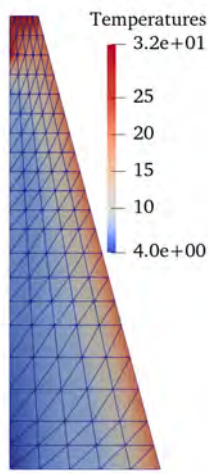

(f) June

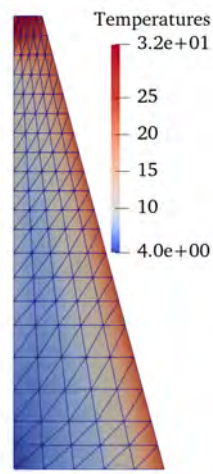

(g) July

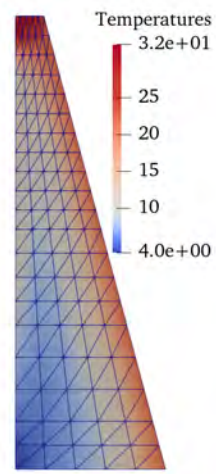

(h) August

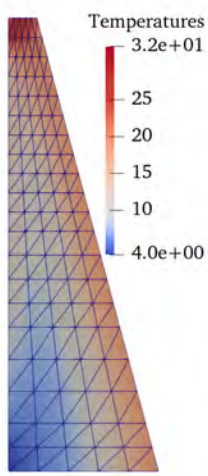

(i) September

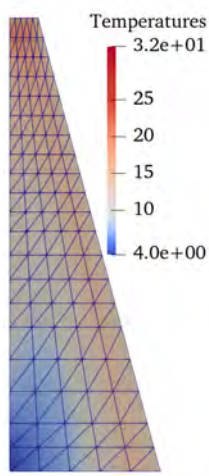

(j) October

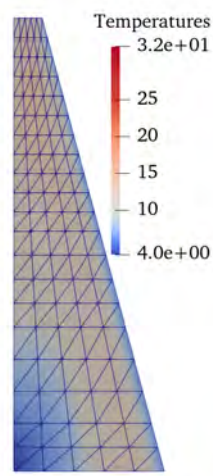

(k) November

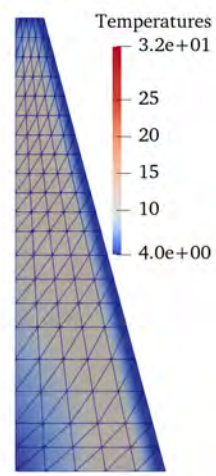

(l) December

Figure 8.5: Temperature contour plots of various months throughout one year at a vertical section cut from the middle of the arch dam

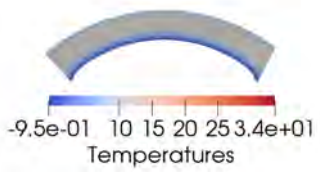

(a) January

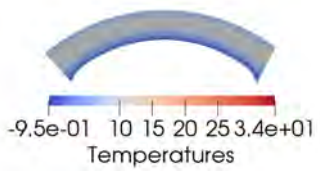

(b) February

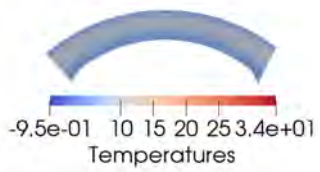

(c) March

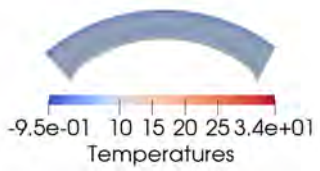

(d) April

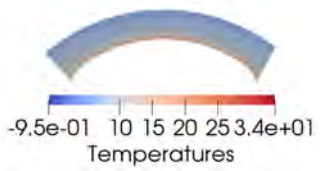

(e) May

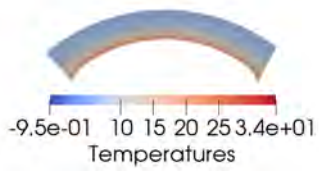

(f) June

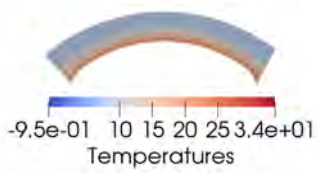

(g) July

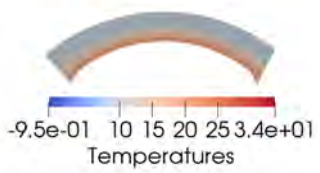

(h) August

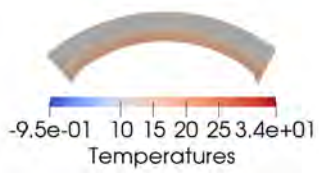

(i) September

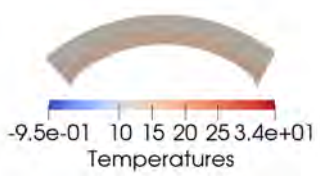

(j) October

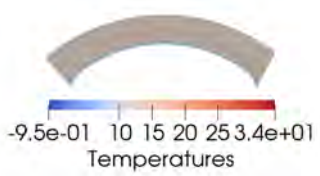

(k) November

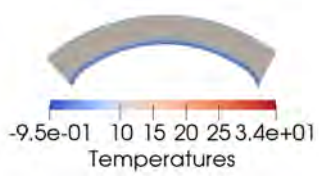

(l) December

Figure 8.6: Temperature contour plots of various months throughout one year at a horizontal section cut from below the water level (Elevation 6243 [ft])

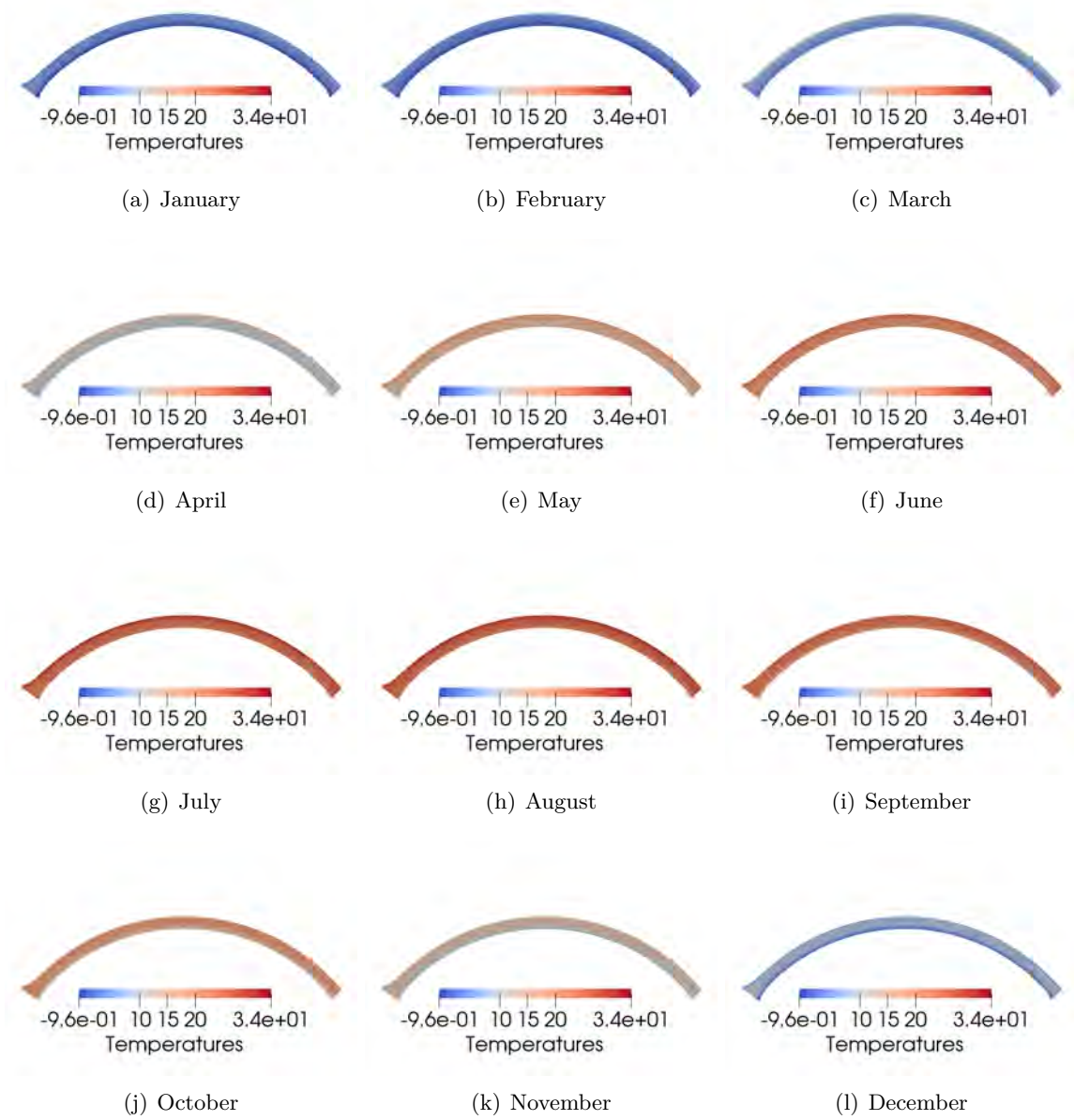

(a) January (b) February (c) March

(d) April (e) May (f) June

(g) July (h) August (i) September

(j) October (k) November (l) December

Figure 8.7: Temperature contour plots of various months throughout one year at a horizontal section cut from above the water level (Elevation 6348 [ft])

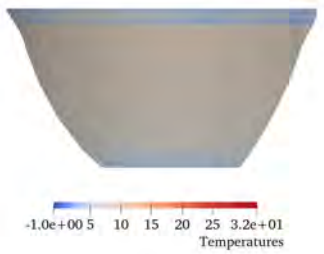

(a) January

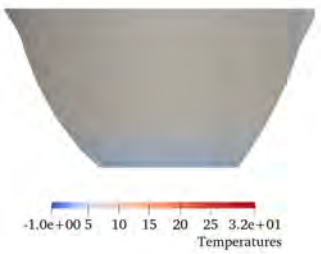

(b) February

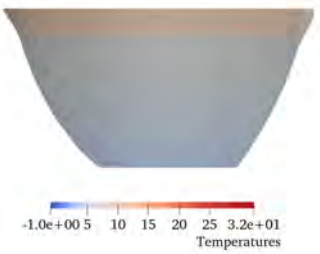

(c) March

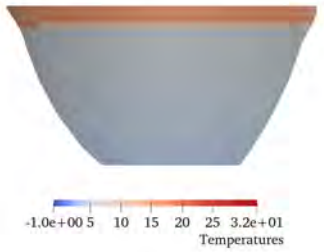

(d) April

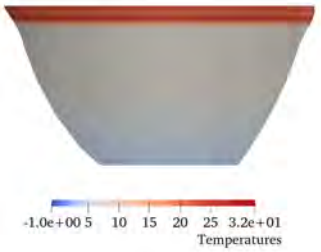

(e) May

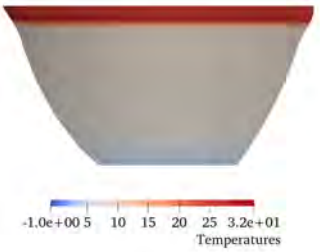

(f) June

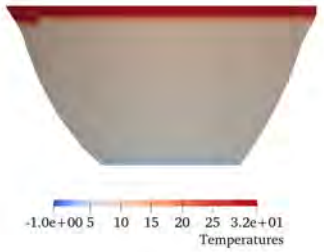

(g) July

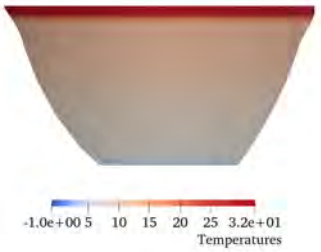

(h) August

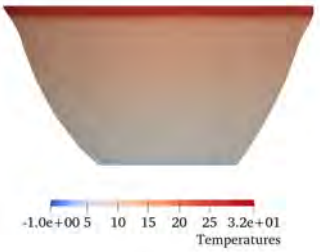

(i) September

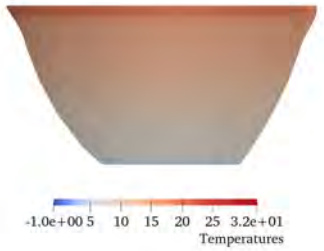

(j) October

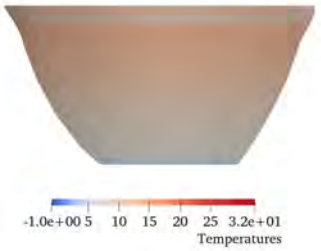

(k) November

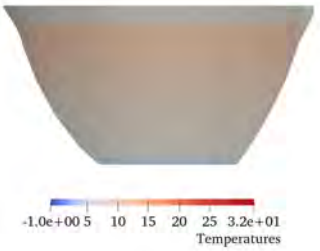

(l) December

Figure 8.8: Temperature contour plots of various months throughout one year at the upstream face of the dam

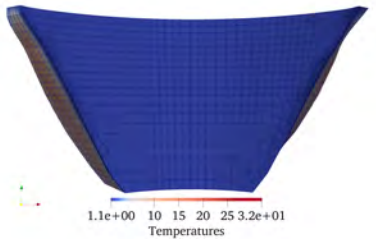

(a) January

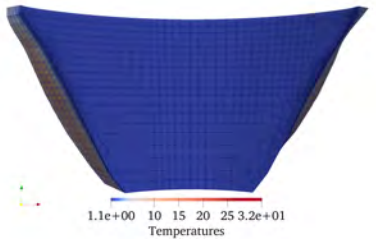

(b) February

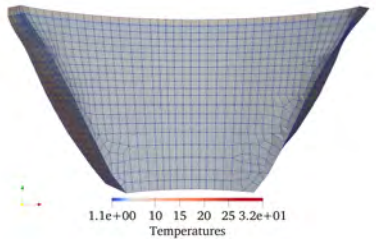

(c) March

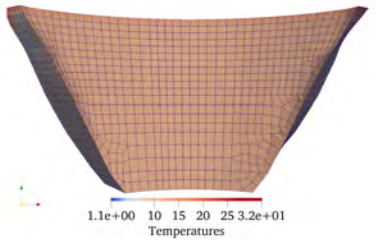

(d) April

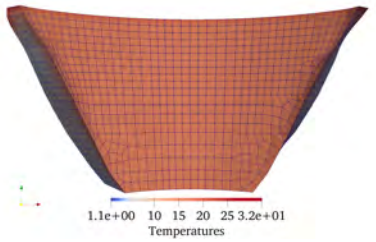

(e) May

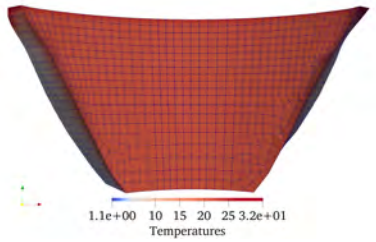

(f) June

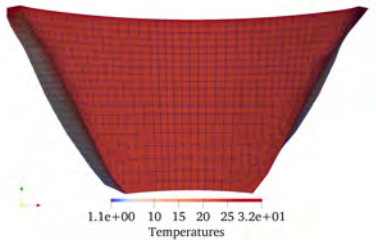

(g) July

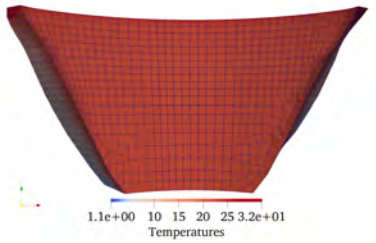

(h) August

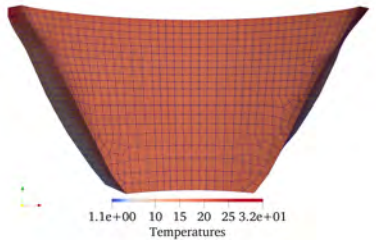

(i) September

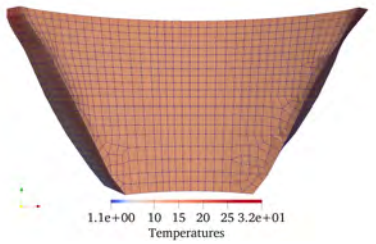

(j) October

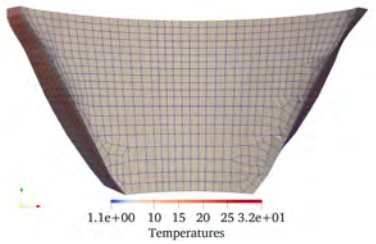

(k) November

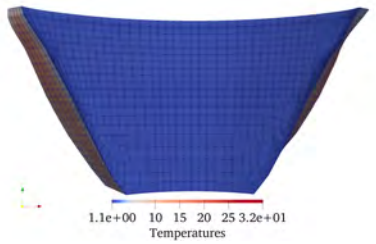

(l) December

Figure 8.9: Temperature contour plots of various months throughout one year at the downstream face of the dam

Chapter 9

Deterministic Stress Analyses Results

Abstract

Parameter identification procedure will now be used to identify the equivalent set of AAR parameters (ε^{∞}, τ_L and τ_C) that would yield the "best" numerical (displacement) prediction in comparison to the recorded ones. Note that in this study set, only the nonlinearity of the joint is modeled (so as to maintain reasonable computational time).

Subsequently, the same set of parameters will be used for a full nonlinear analysis of the dam (including not only joints, but also concrete).

9.1 Parameter Identification Procedure

A major challenge in the numerical simulation of the temporal concrete expansion (and deterioration) is the ability to use reliable kinetics coefficients, ε^{∞}, τ_l and τ_c introduced in §2.2.2. Whereas those can be obtained through carefully carried laboratory tests (Saouma, 2020), an alternative approach is through system identification.

Mathematically speaking, the problem can be simply formulated as follows. The field-recorded displacements (e.g. crest displacement on a dam) are denoted by $\mathbf{u}(t)$, the target parameters by $\mathbf{x}$ (in our case $x(1) = \tau_c$, $x(2) = \tau_l$ and $(x(3) = \varepsilon(\infty))$, the finite element "operator"

by $f(.)$, and computed results by $\mathbf{u}'(t)$. We thus have:

$$f(\mathbf{x}) = \mathbf{u}'(t) \neq \mathbf{u}(t) \tag{9.1}$$

and are seeking to minimize $(\mathbf{u}(t) - \mathbf{u}'(t))^2$, see Figure 9.1.

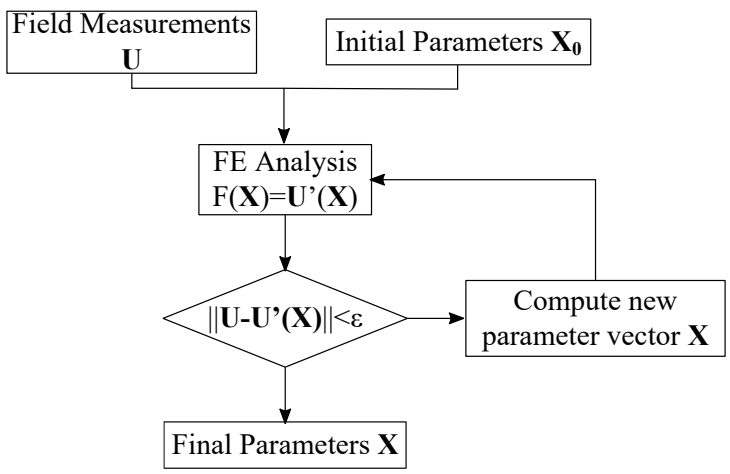

Figure 9.1: Principle of the system identification approach

Such an approach has been often used for dam analysis (Ardito, Maier, and Massalongo, 2008) (Oliveira, Toader, and Vieira, 2012), and is conceptually similar to system identification in nonlinear dynamic systems (Ghanem and Shinozuka, 1995).

9.2 Parameter Identification for Linear Concrete Model

Prior to undertaking the process of parameter identification, the user should first identify the control parameters, and then identify the field measurements which are to be captured through the parameter identification process.

9.2.1 Control Parameters

Control parameters corresponding to the AAR model of Saouma and Perotti (2006a) must first be defined.

This is done through an excel file, Table 9.1, that includes: lower and upper bound values for each of the active parameters (identified by 1), the initial starting point, and a `typical` value which provides the algorithm with an order of magnitude of the variable.

Table 9.1: Data preparation for parameter identification

			Actual Values					
		Active	**UB**	**LB**	**Default**	**Typical**	**factor**	**Finite Dif**
1	ε^{∞}	1	0.20	0.00	0.060	1.00	0.0010	0.05
2	τ_C	1	50,000	500	20,000	1.00	1,000	0.10
3	τ_L	1	100,000	500	40,000	1.00	1,000	0.10
4	U_C	0						
5	U_L	0						
6	γ_c	0						
7	γ_t	0						
8	ε_c	0						
9	ε_t	0						
10	W	0						
11	Ref Temp	0						
12	σ_2	0						
13	β_E	0						
14	β_f	0						

9.2.2 Measured displacements

In the case of this dam, measurements were taken at two locations shown in Fig. 9.2.

As we will need to correlate measured displacements with computed ones, the corresponding nodal coordinates, Fig. 9.2, are given in Table 9.2. As we will need to correlate measured displacements with computed ones, the corresponding nodal coordinates, are given in Table 9.2.

The measured displacements **U** are shown in Table 9.3. Prior to their use in the parameter identification process, a four step pre-processing is needed:

(1) The raw data are first plotted, Fig. 9.3(a) and 9.4(a). We note that when the horizontal displacements were first recorded, the initial reading was not zero. Furthermore, it was not until 10 years later that the vertical displacements were recorded.

(2) In the next step, Fig. 9.3(b) and 9.4(b) we "zero" the crest displacements. The horizontal

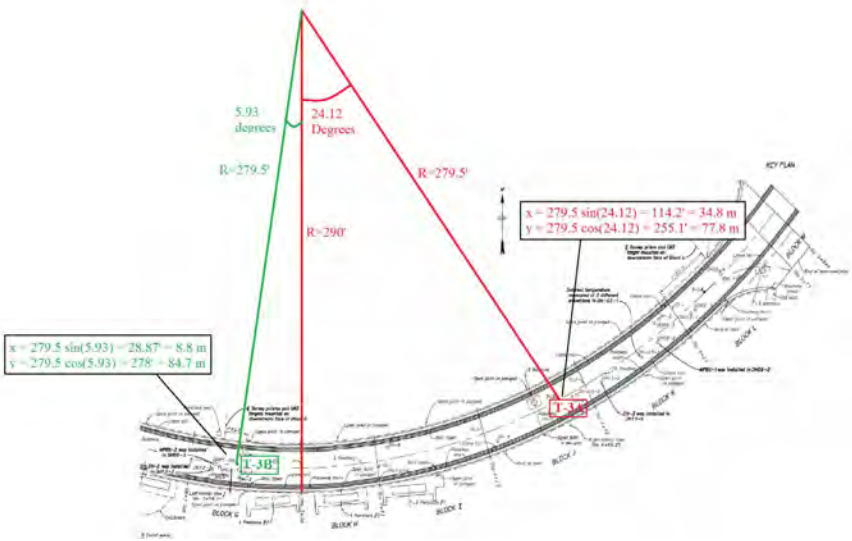

Figure 9.2: Instrumentation locations

one is shifted down to zero, and the vertical one is shifted up by an *arbitrary* amount to reflect that with respect to the first horizontal recording, a vertical one did occur. Yet, we do not know its magnitude, at best this can be numerically estimated later.

(3) Focusing on the horizontal displacement, it is evident that there is certain "ruggedness" which may be caused either by measurement errors, or variable temperature/pool elevation at the time of measurement. Hence it would be reasonable to "smooth" the data using the Matlab® function `smoothdata` with the option `loess` (*Local regression using weighted linear least squares and a 2nd degree polynomial model.*), Fig. 9.3(c)-9.3(d) and 9.4(c)-9.4(d) for vertical-horizontal readings, T3B and T3A respectively.

(4) The smoothed curve has now as many data points as were recorded. However, we would need to have `Nincrement` data points (corresponding to the number of increments in the finite element analysis). Hence the Matlab® `interpolate` function is used to determine those points. Fig. 9.3(e)-9.3(f) and 9.4(e)-9.4(f) for vertical-horizontal dat, T3B and T3A respectively. Recorded values are shown as black filled circles, and interpolated ones as red filled circles.

We note that readings (and thus interpolated values) did not start exactly on January 1 at

Table 9.2: Displacement instrumentation coordinates

Device	Coordinates [m] X	Y	Z	Closest Node ID	Coordinates [m] X	Y	Z
T3A	-34.8	77.8	71.9	3651	-34.3	78.4	71.9
T3B	8.8	84.7	71.9	1394	8.8	84.3	71.9

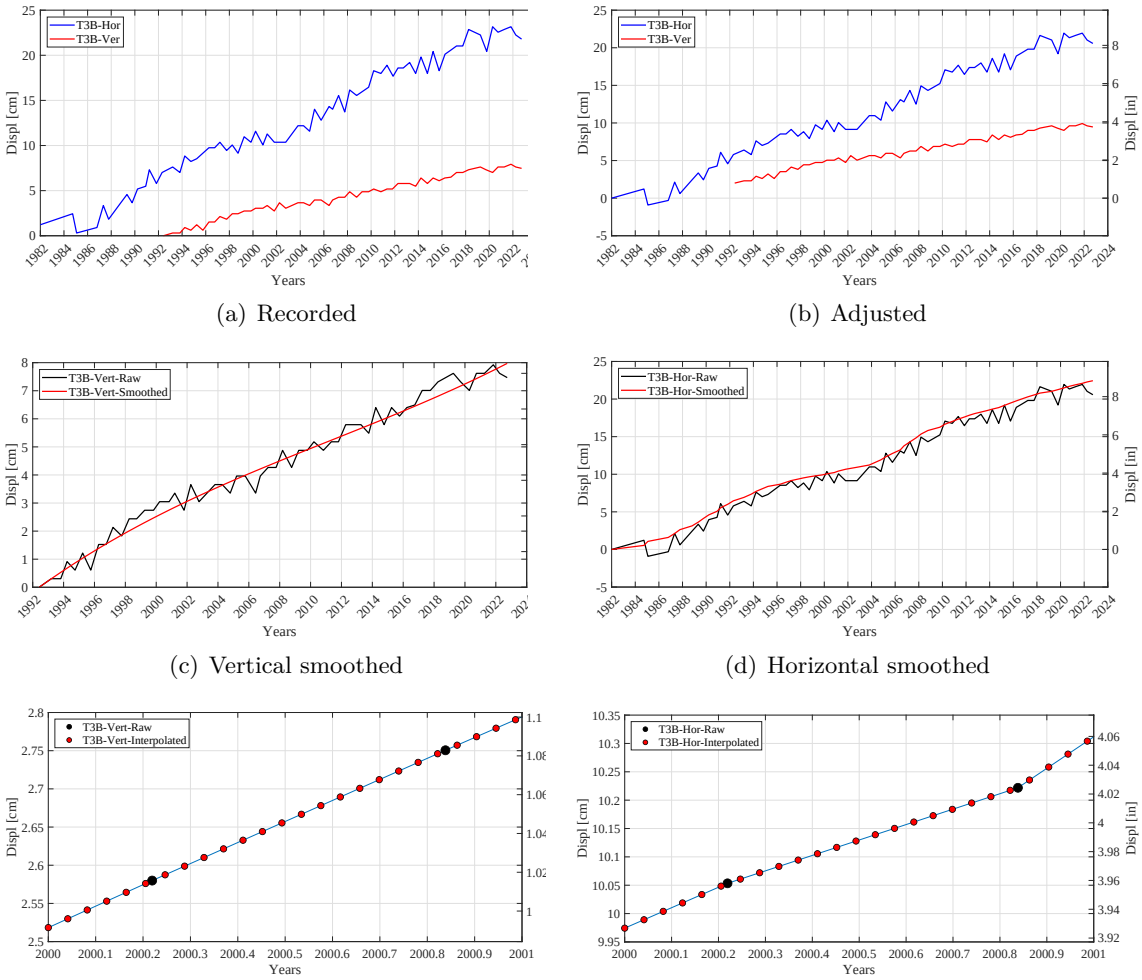

(a) Recorded (b) Adjusted

(c) Vertical smoothed (d) Horizontal smoothed

(e) Vertical interpolated (f) Horizontal interpolated

Figure 9.3: T3B Measurements and adjustments

year zero for the vertical reading (1992), and at nearly January 1 for the horizontal reading (1982). Nevertheless, we shall use these smoothed data for parameter identification. We also note that the seasonal temperature is nearly obliterated by the smoothing process. This should not be an

Table 9.3: T_3B Measurements (Dressel, 2011)

Date	Deflection	Settlement	Date	Deflection	Settlement
Date	(cm)	(cm)	Date	(cm)	(cm)
3/17/2020	21.8	-7.5	9/10/2002	14.0	-4.0
9/19/2019	22.3	-7.6	4/12/2002	11.6	-3.4
4/24/2019	23.2	-7.9	10/6/2001	12.2	-3.7
9/27/2018	22.9	-7.6	4/17/2001	12.2	-3.7
3/20/2018	22.6	-7.6	4/4/2000	10.4	-3.0
10/4/2017	23.2	-7.0	9/23/1999	-	-3.7
4/5/2017	20.4	-	4/16/1999	10.4	-2.7
3/13/2017	-	-7.3	9/9/1998	11.3	-3.4
9/21/2016	22.3	-7.6	4/29/1998	10.1	-3.0
9/24/2015	22.9	-	9/15/1997	11.6	-3.0
9/23/2015	-	-7.3	4/25/1997	10.4	-2.7
3/27/2015	21.0	-7.0	9/27/1996	11.0	-2.7
9/15/2014	21.0	-7.0	3/22/1996	9.1	-2.4
3/24/2014	20.6	-6.5	9/26/1995	10.1	-2.4
9/24/2013	20.1	-	4/4/1995	9.4	-1.8
9/17/2013	-	-6.4	9/9/1994	10.4	-2.1
3/27/2013	18.3	-6.1	4/1/1994	9.8	-1.5
9/21/2012	20.4	-6.4	10/5/1993	9.8	-1.5
3/29/2012	18.0	-5.8	4/2/1993	-	-0.6
9/13/2011	19.8	-6.4	9/22/1992	8.5	-1.2
4/1/2011	18.0	-5.5	3/26/1992	8.2	-0.6
9/28/2010	19.2	-5.8	9/19/1991	8.8	-0.9
3/15/2010	18.6	-5.8	4/23/1991	7.0	-0.3
10/2/2009	18.6	-5.8	9/11/1990	7.6	-0.3
5/4/2009	17.7	-	11/28/1989	-	-
4/14/2009	-	-5.2	10/19/1989	7.0	-
10/27/2008	18.9	-5.2	4/26/1989	5.8	-
4/23/2008	18.0	-4.9	9/19/1988	7.3	-
9/12/2007	18.3	-5.2	6/1/1988	5.5	-
4/9/2007	16.5	-4.9	9/21/1987	5.2	-
9/18/2006	-	-4.9	4/7/1987	3.7	-
4/3/2006	15.5	-4.3	10/30/1986	4.6	-
9/1/2005	16.2	-4.9	4/22/1986	3.7	-
4/1/2005	13.7	-4.3	4/11/1985	1.8	-
9/23/2004	15.5	-4.3	10/30/1984	3.4	-
3/23/2004	14.0	-4.0	4/16/1984	0.9	-
12/4/2003	14.3	-3.4	7/27/1982	0.3	-
4/2/2003	12.8	-4.0	3/26/1982	2.4	-
			7/2/1979	1.2	-

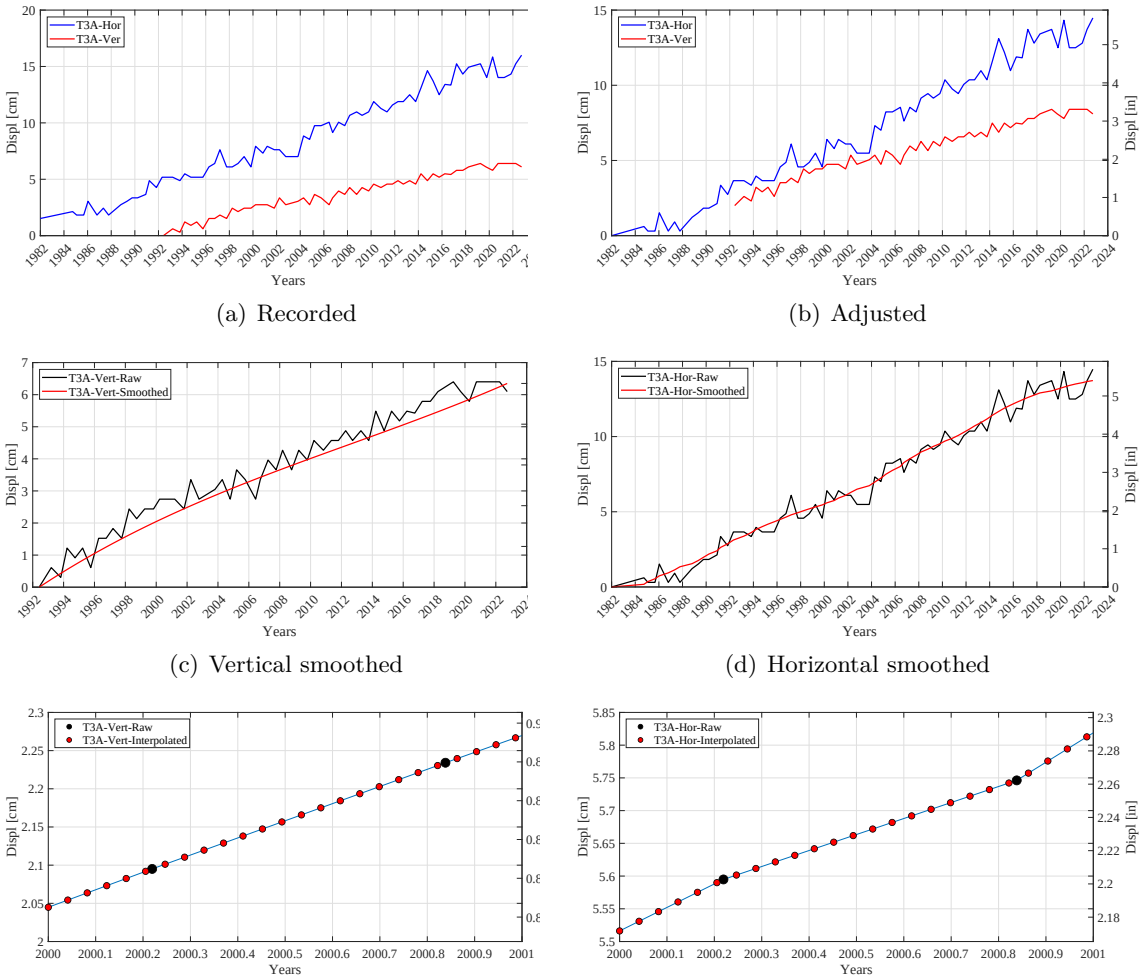

(a) Recorded (b) Adjusted

(c) Vertical smoothed (d) Horizontal smoothed

(e) Vertical interpolated (f) Horizontal interpolated

Figure 9.4: T3A Measurements and adjustments

issue in the context of parameter identification as we attempt globally to approach the target curve without the distraction of small oscillations.

9.2.3 Results

Figure 9.5 is a plot of the system identification user interface which shows the iterative procedure in which the variables are altered one at a time until the termination condition is satisfied; in other words the computed displacement curve becomes as close as possible to the recorded data.

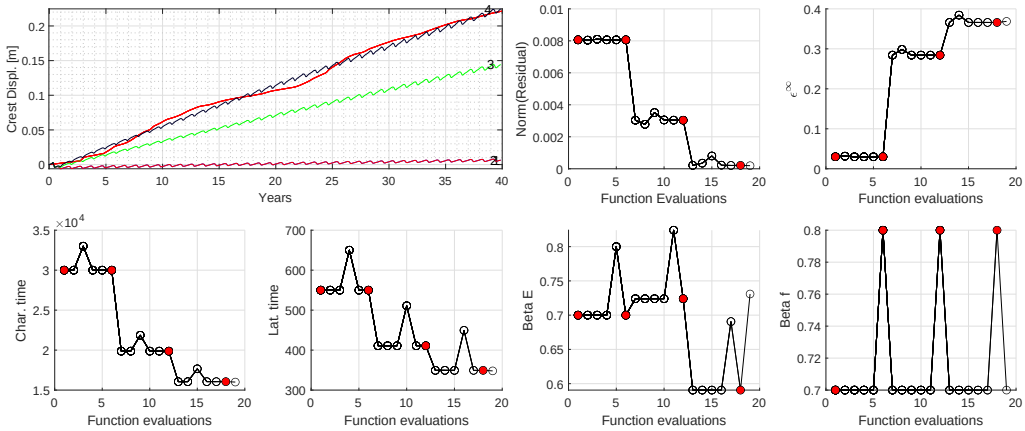

Figure 9.5: System Identification user interface

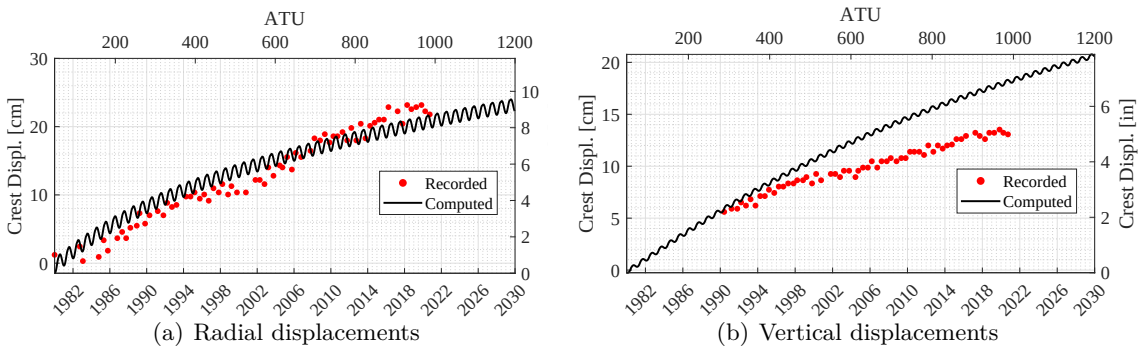

(a) Radial displacements (b) Vertical displacements

Figure 9.6: Displacement comparison following system identification for T3B

In figure 9.6 and 9.7 the displacements obtained from the optimal analysis suggested by the system identification process is plotted with the recorded data. Since the horizontal displacement of the T3B instrument is the most reliable measurement, the system identification objective function was set to optimize the corresponding displacement and as seen in figure 9.6 the resulting curve matches well with the recorded data for the displacement of interest.

As such, the parameters suggested by the system identification will be used as the mean values for the uncertainty quantification of the stress analysis.

9.3 Deterministic Analysis with Nonlinear Concrete Model

In this section the results of the AAR analysis of the dam considering nonlinear material properties is demonstrated and discussed. The concrete model is the one of the computer program ATENA, and described in Cervenka and Papanikolaou (2008). It should be noted that this can be a particularly challenging problem, as there are two sources of nonlinearities, concrete material, and joints.

9.3.1 Displacements

The resulting displacements of the nonlinear analysis at the locations corresponding to T3B and T3A instruments are plotted and compared to that of the linear analysis (Fig. 9.8 and 9.9). As seen, the nonlinear analysis suggests linearly increasing displacement while the displacements ob-

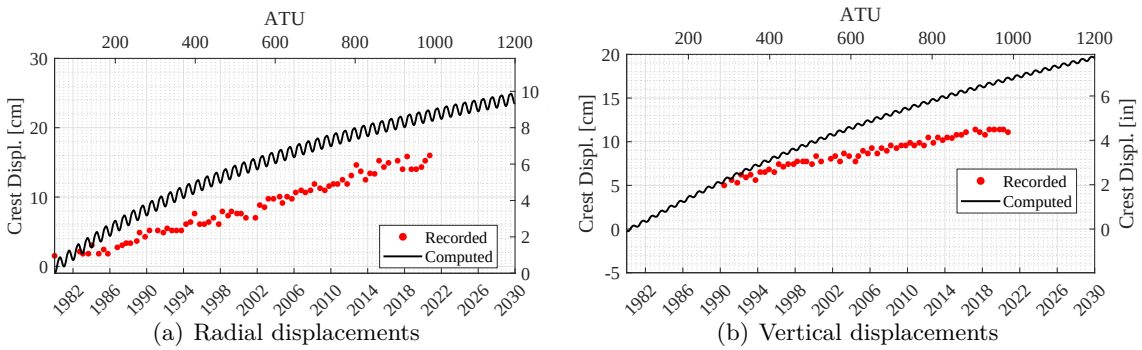

Figure 9.7: Displacement comparison following system identification for T3A

tained from the linear analysis is gradually reaching a plateau; however, both analyses demonstrate good match with the measured displacements of interest. Fig. 9.10 shows the dam displacements

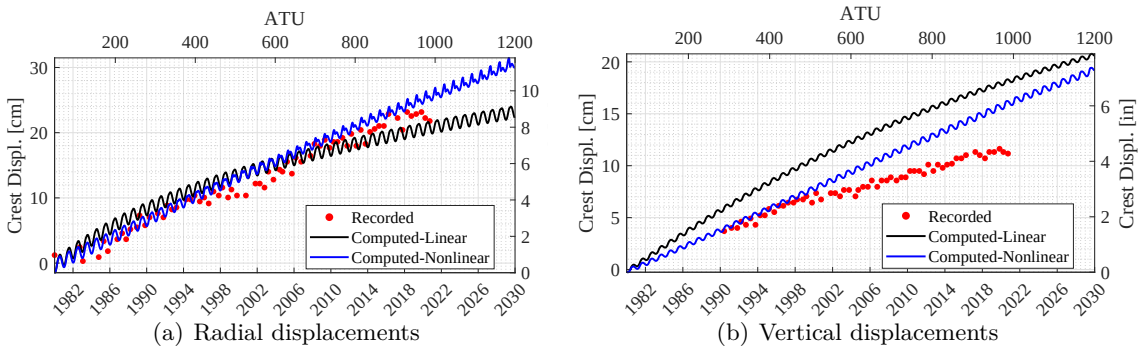

Figure 9.8: Displacement comparison from linear and nonlinear analysis for T3B

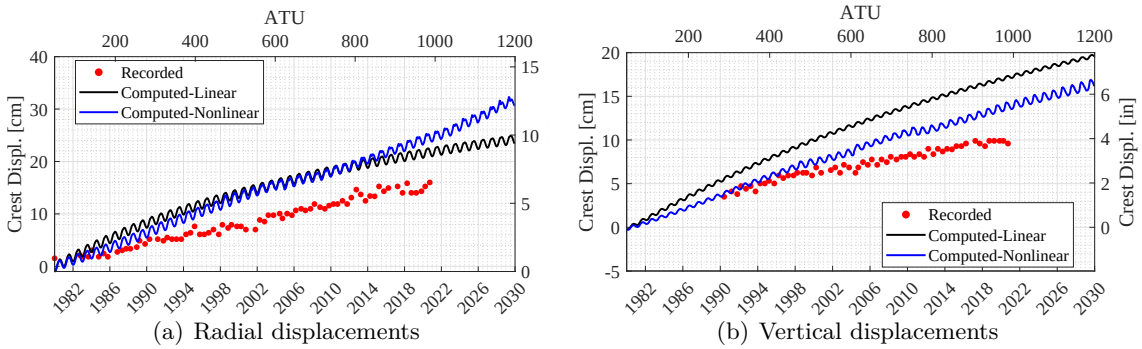

Figure 9.9: Displacement comparison from linear and nonlinear analysis for T3A

in the 3 directions after 50 years of nonlinear analysis. The displacements for the half of the dam

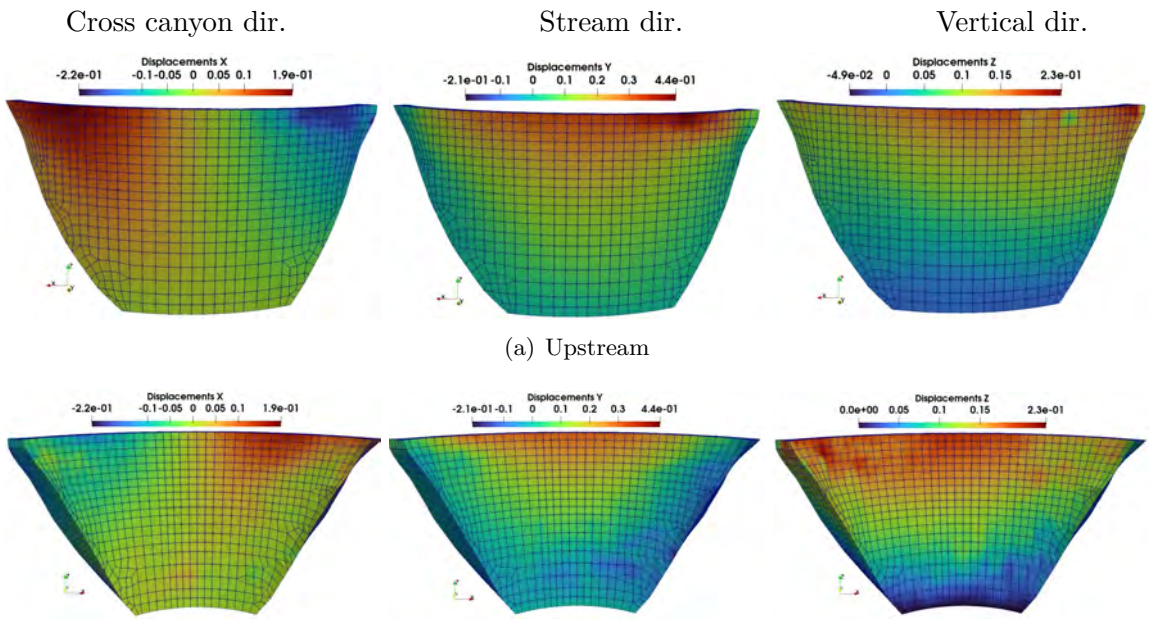

(a) Upstream

(b) Downstream

Figure 9.10: Displacement plots after 50 years of Nonlinear analysis

over time is shown in figure 9.11. As seen while the radial displacement has increased with time, the maximum displacement has always occurred at the crest of crown cantilever observing the dams inclination towards the upstream. Finally, the deformed shape is shown in Fig. 9.12.

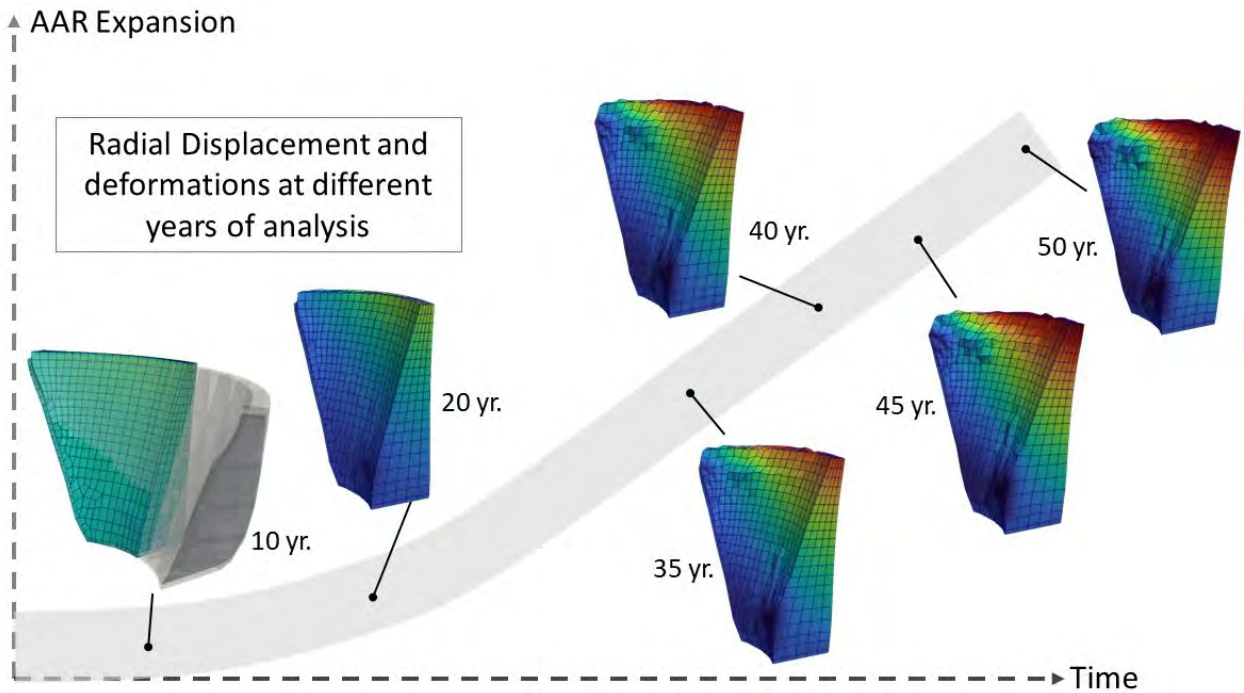

Figure 9.11: Radial displacement and deformations over time(side view)

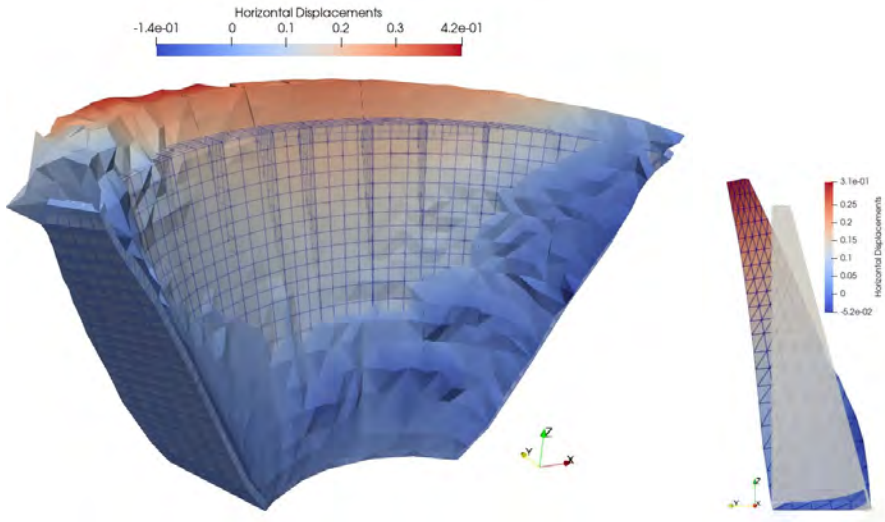

Figure 9.12: Dam deformed shape after 50 years of analysis; Nonlinear analysis

9.3.2 Stress Distribution

9.3.2.1 Stress and Strains

Although the dam does not have a complete symmetrical geometry, the results of the displacements as well as the stress and strain distributions seen in Fig. 9.13 are almost symmetric.

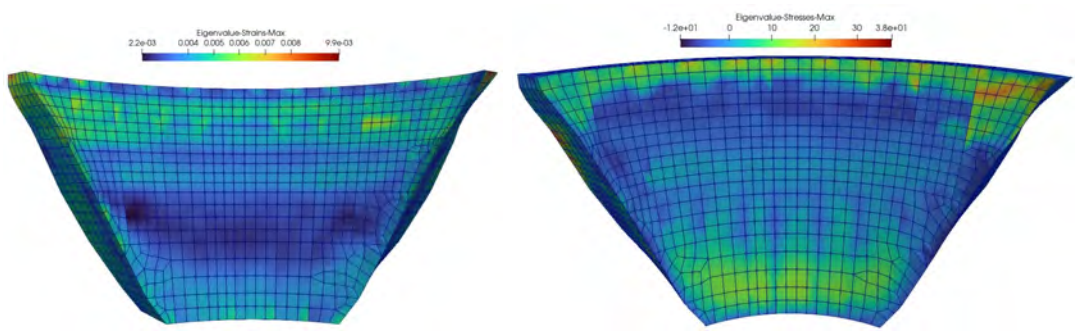

(a) Strain (b) Stress

Figure 9.13: Principal Stress and strain distributions after 50 years of Linear analysis

Therefore it can be concluded that the material and other properties have been assigned symmetrically.

9.3.2.2 Crack Pattern

After 50 years

The cracking pattern shown in Fig. 9.14 is demonstrating an asymmetric formation of the cracks mostly on one side. It is noted that even the smallest asymmetry in the geometry of the dam can result in significant differences between the crack development on the 2 sides of the dam. Thus formation a weak point on a side results in the cracks initiation and propagation from there.

As seen, the cracks are mostly developed at the bottom and inside the dam which can be due to the fact that the higher confinement prevents the concrete from expanding in the vertical direction and thus the expansion is occurred mostly in the 2 horizontal directions as the orientation of the disks also suggest. The detailed explanation of the AAR strain redistribution is also discussed in Chapter 2 and demonstrated in Fig. 2.12.

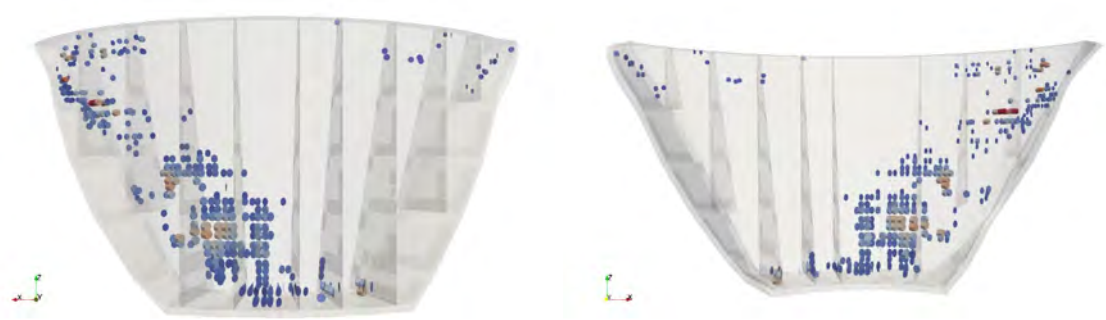

(a) Upstream (b) Downstream

Figure 9.14: Smeared crack profile after 50 years of analysis

9.3.2.3 Simulation Results

The computed downstream stresses are discussed.

In Fig. 9.15 the development of the cracks over the time is shown along with the corresponding maximum principal stresses.

The results show that the cracking initiated in 1998 after 18 years of analysis and they are

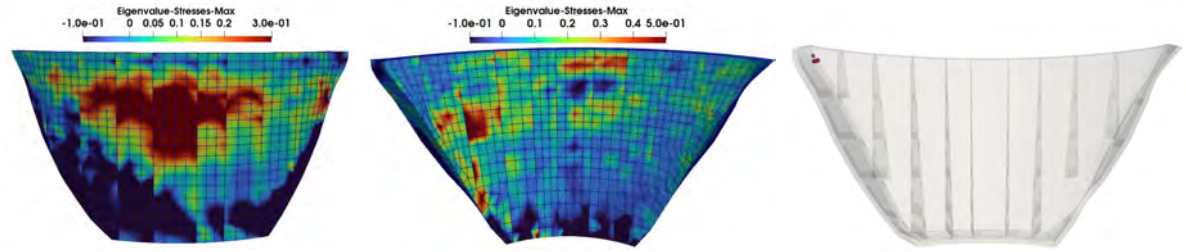

(a) 1998

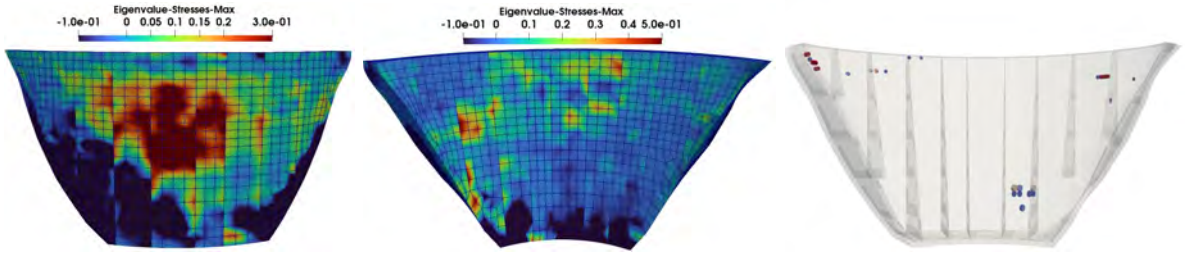

(b) 2005

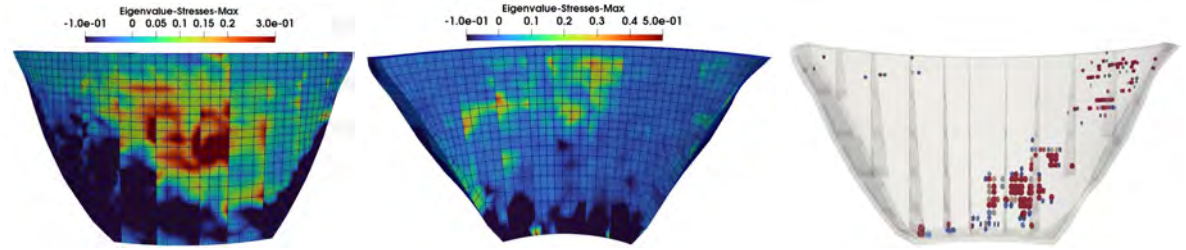

(c) 2020

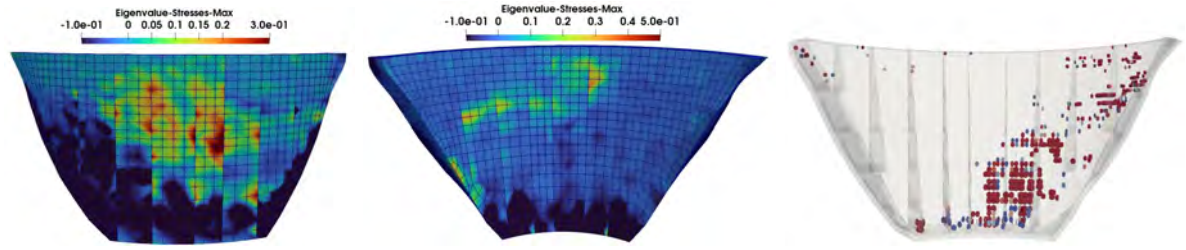

(d) 2030

Figure 9.15: Smeared crack profile over the time compared to the maximum principal stresses

mostly inside the dam. The primary objective of the investigation was to capture the time history of the crest displacement at two locations. This was achieved. However the downstream anticipated crack pattern from a nonlinear model for the concrete failed to fully match the observations.

Regretfully, only one "snapshot" of the crack is available (figure 9.23). This is further dis-

cussed in §9.3.3.1.

The development of maximum principal stress on the upstream over time, demonstrated in figure 9.16, is showing a decrease in the stresses at 50 years compared to the 40 years of analysis which is due to the joint openings and crackings that allow for stress redistribution in the concrete.

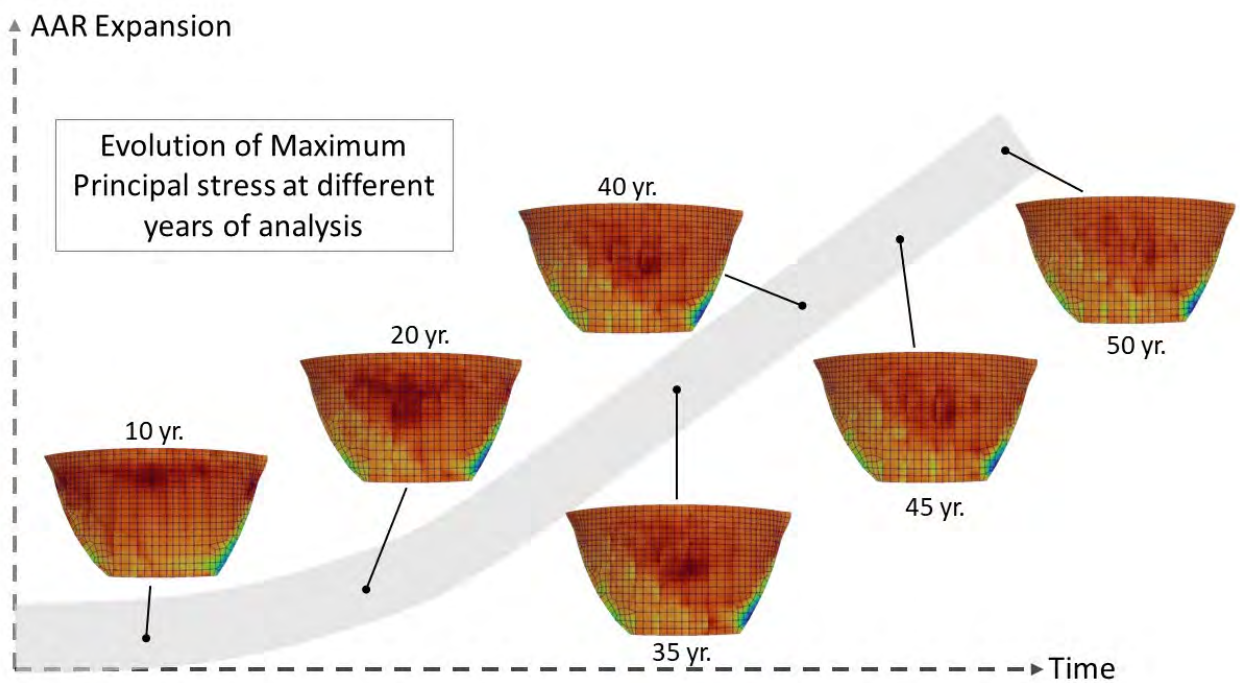

Figure 9.16: Development of Maximum principal stresses over time on the upstream

9.3.2.4 Sectional Cuts of Principal Stresses Over Time

In order to better visualize the results a vertical section cut is selected and the maximum principal stress and strain distributions are plotted in Fig. 9.17.

As seen the majority of the lower portion of the dam and upstream is in compression while the top of the dam and mostly on the downstream side is in tension which can be indicative of possible cracking in that portion.

Winter Summer Principal Stresses Over Time

The maximum principal stresses over time for both summer and winter are shown in Fig. 9.18.

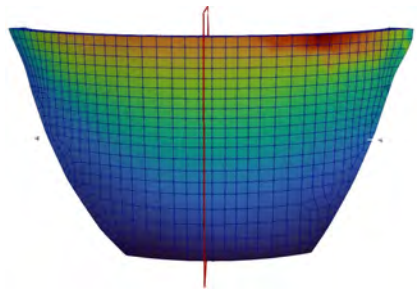

(a) Section cut location

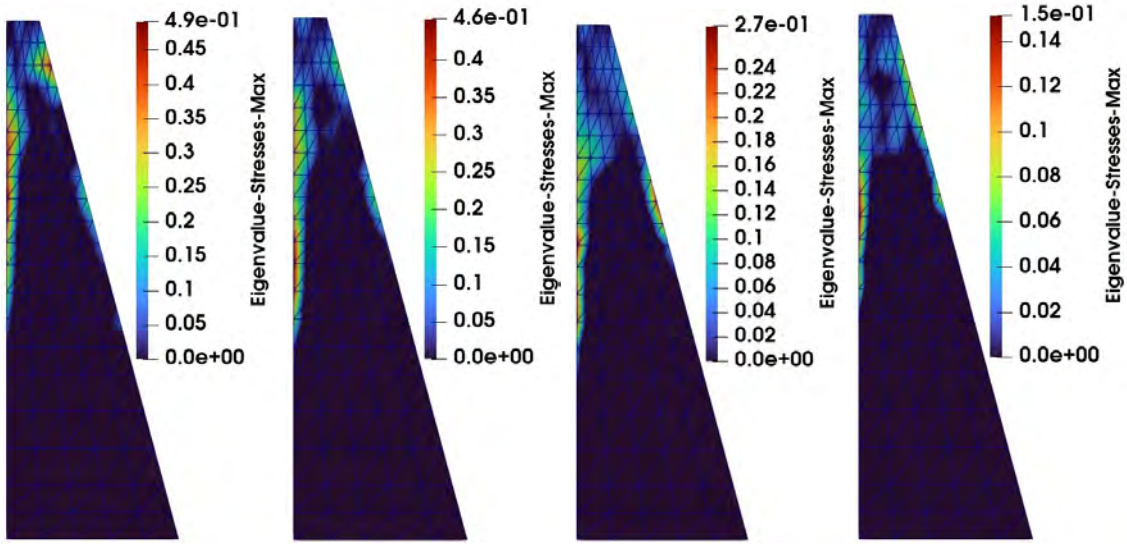

(b) 1998 (c) 2005 (d) 2020 (e) 2030

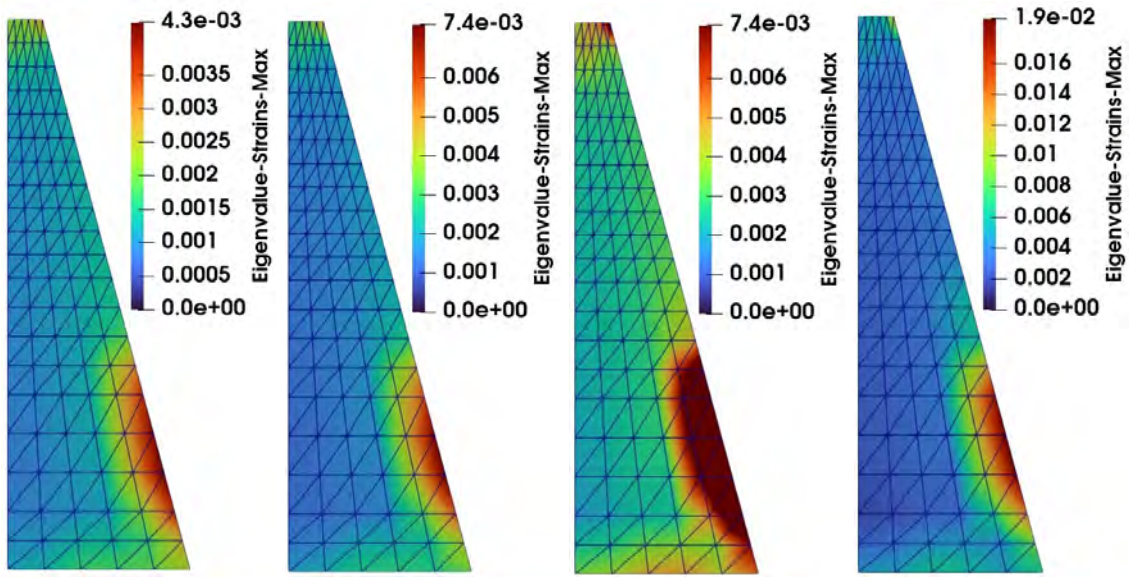

(f) 1998 (g) 2005 (h) 2020 (i) 2030

Figure 9.17: Maximum principal stresses at a section cut over time

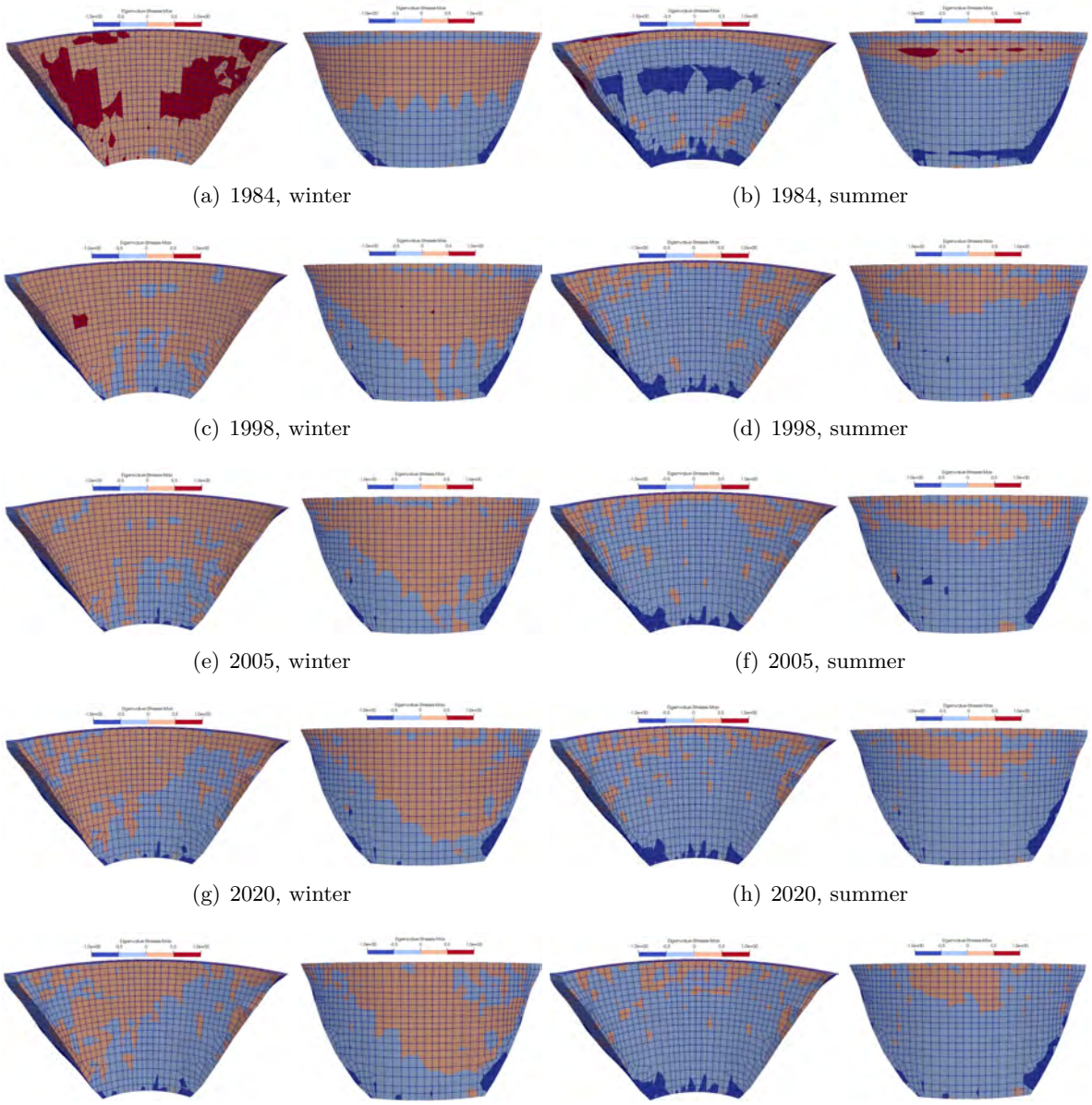

(a) 1984, winter (b) 1984, summer

(c) 1998, winter (d) 1998, summer

(e) 2005, winter (f) 2005, summer

(g) 2020, winter (h) 2020, summer

(i) 2030, winter (j) 2030, summer

Figure 9.18: Maximum principal stresses over summer and winter

Whereas Fig. 9.19 shows the maximum principal stresses at different vertical sections in 2020.

Evolution of Principal AAR Strains over Time

To show the development of AAR, the maximum principal AAR strain profiles are presented in Fig. 9.20. It is seen that there is higher AAR at the crest on the upstream side and on the mid

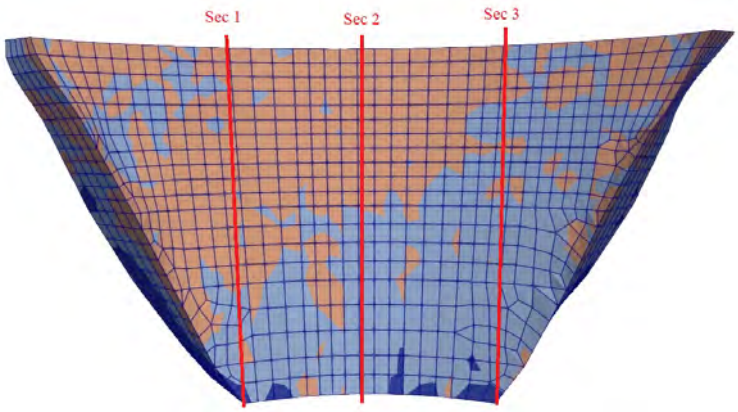

(a) Section cut locations

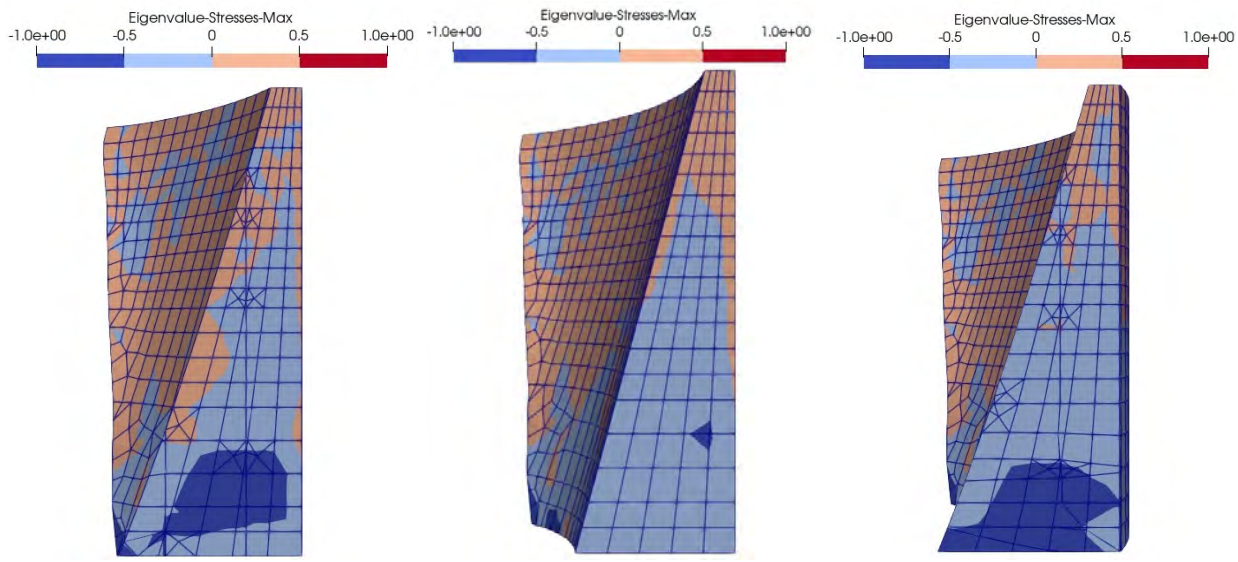

(b) Section 1 (c) Section 2 (d) Section 3

Figure 9.19: Maximum principal stresses at different vertical sections in 2020

to lower height on the downstream side of the dam. Figure 9.21 is showing the development of the AAR volumetric strain over time.

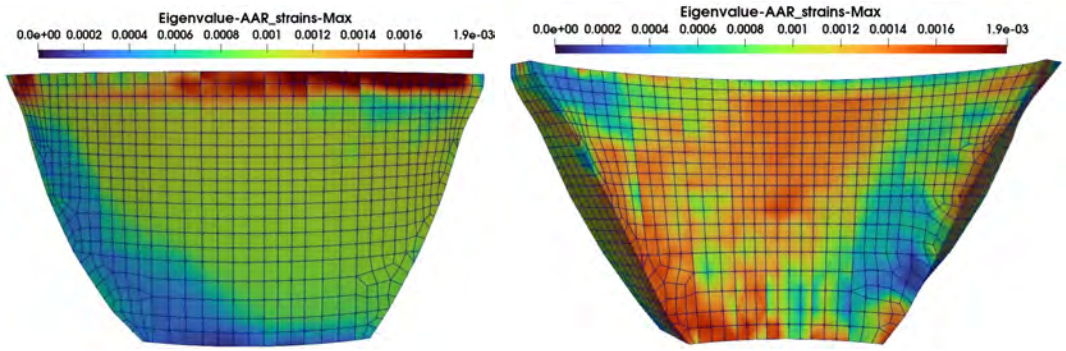

(a) 1998

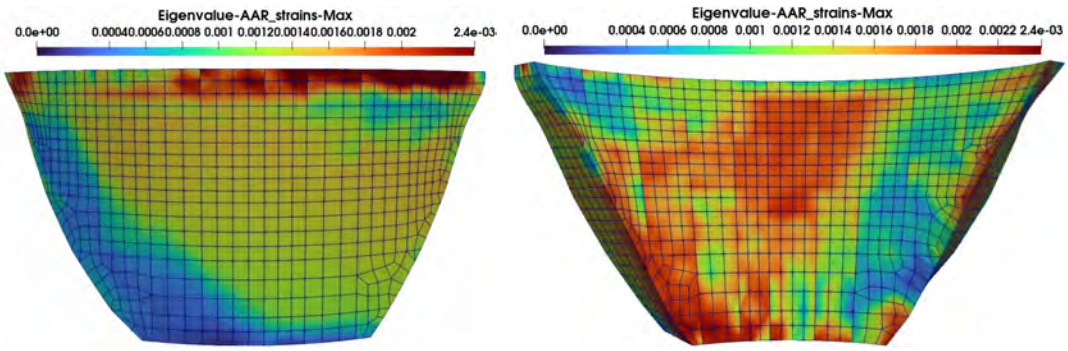

(b) 2005

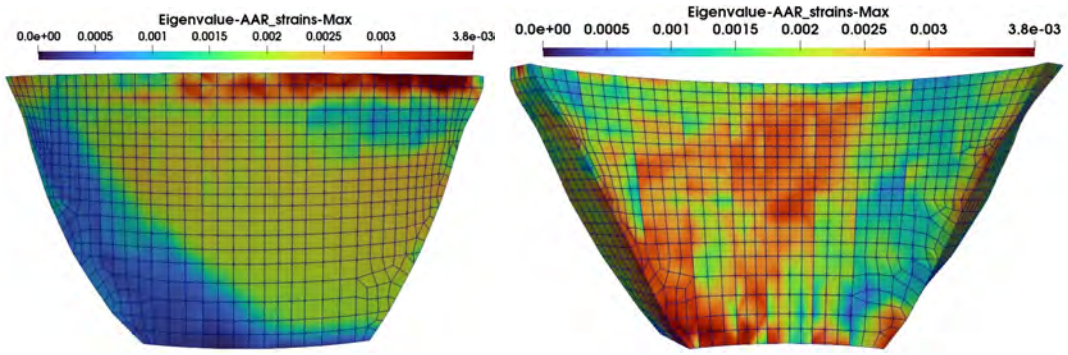

(c) 2020

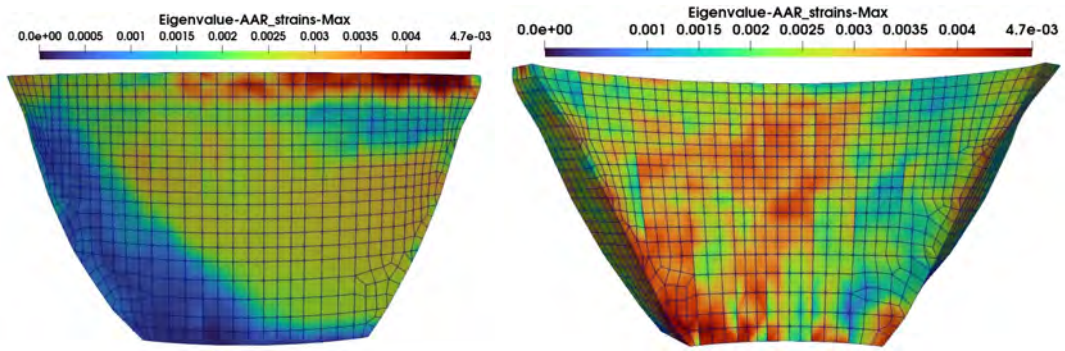

(d) 2030

Figure 9.20: AAR development over the time

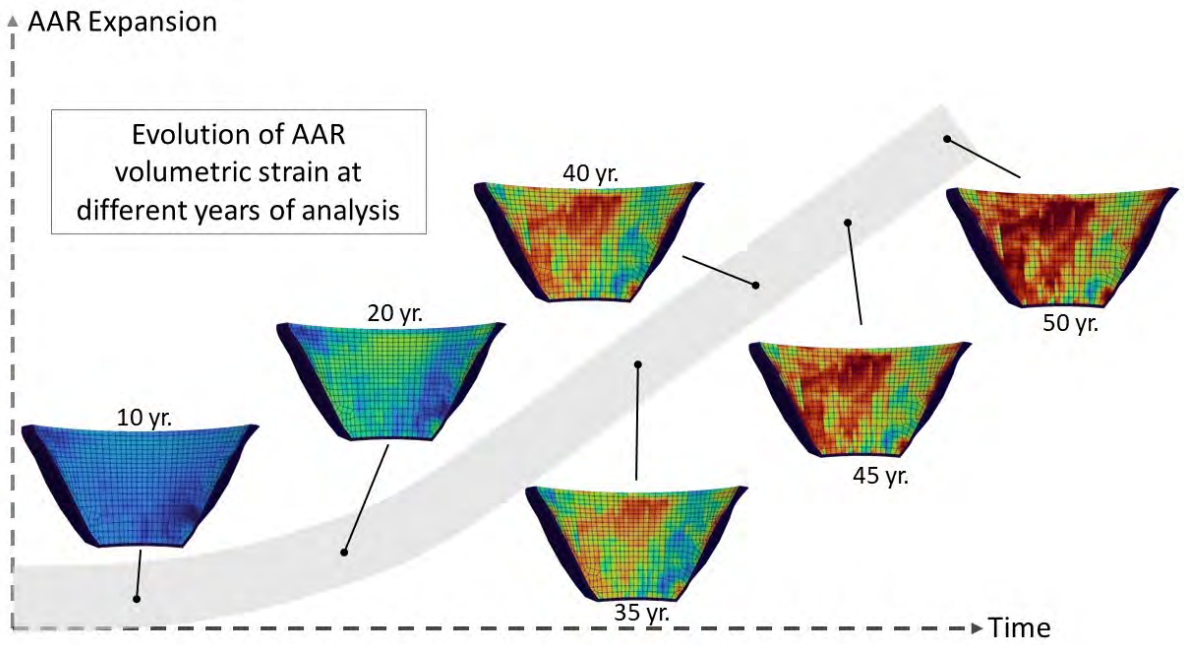

Figure 9.21: Development of AAR volumetric strain over time on the downstream

80 Years Analysis

In order to further investigate the development of cracks the analysis was extended for 30 more years and yet no cracks on the upper portion of the downstream side were detected even after 80 years of AAR. Fig. 9.22 shows the maximum principal stress along with the vertical stress distributions for the end of the 80-year analysis.

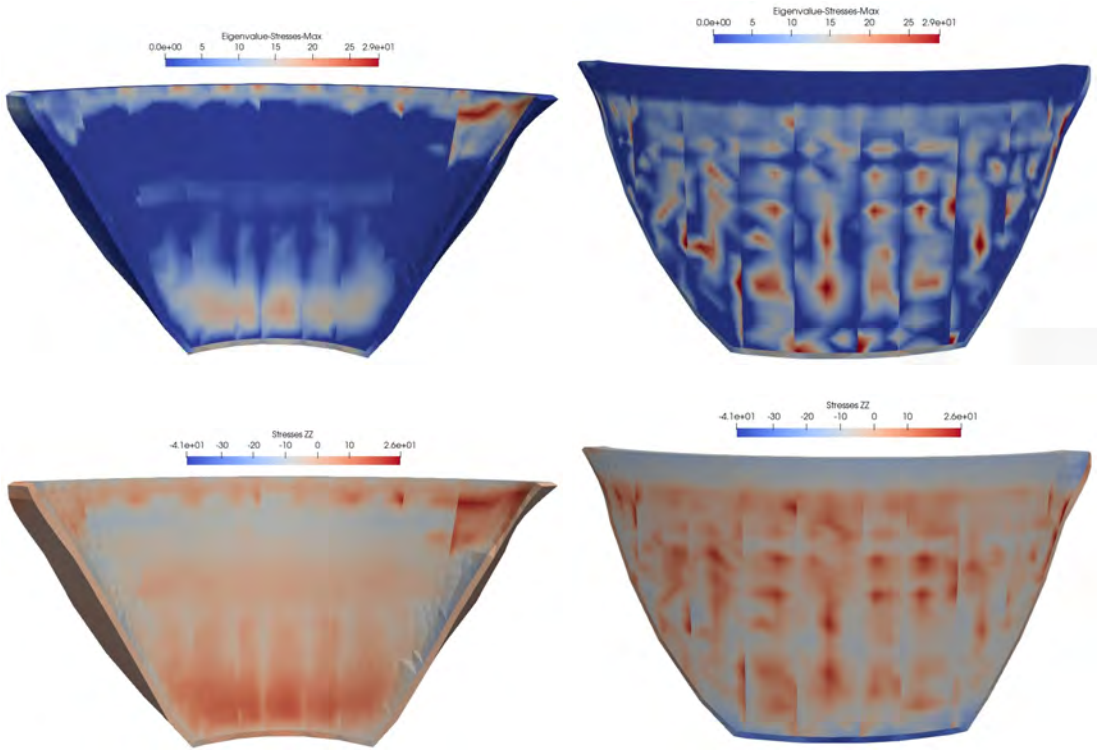

Figure 9.22: Maximum principal stress and vertical stress distribution after 80 years of analysis; Nonlinear analysis

However, it is note worthy that the analysis time started in 1980 and the considered material properties were those corresponding to the same time, which means that the assumed concrete properties at the initial time of the analysis had already experienced some amount of AAR and probably cracking by then.

9.3.3 Downstream Observations

In agreement with the sponsor, the primary objective of the study was to compare numerical results of the finite element simulation with quantifiable measurements on the dam. Since the only reliable (quantitative) measurements were the crest displacements, the study focused on capturing those two responses. Indeed, as shown in Fig. 9.6 those were properly captured thanks to the parameter identification process.

Next is an attempt to compare results of the finite element studies with qualitative observations made on the downstream face and briefly described in Salamon, Dressel, and Liechty (2021). From this public document, we identified a set of two such measurements: photogrammetry and LIDAR (laser imaging, detection, and ranging) which is a method for determining ranges by targeting an object or a surface with a laser and measuring the time for the reflected light to return to the receiver.

The primary outcome of the former is a crack mapping for the first, Fig. 9.23, and "map" of surface deformation, Fig. 9.25 for the second.

As stated by the authors:

> Both methods required relatively similar amounts of time for data collection and processing. The error in the photogrammetry processing was approximately 1mm. The georeferencing error for fitting the photogrammetry to the ground control was approximately 9.5mm. The published accuracy of the Leica ScanStation P40 LIDAR scanner utilized was 9mm + 10 parts per million, and the registration and georeferencing error was reported as approximately 8.5mm.
>
> Currently, the accuracy of the photogrammetric and LIDAR may not be satisfactory for deformation measurements of dams affected by ASR; however, with the continued evolution of the technology, both methods are beneficial for understanding dam behavior over an extended period of time and can be used as an evaluation tool to compare the measurement data with other surveying techniques.
>
> ...
>
> While the UAS photogrammetry is not yet accurate enough to detect short-term ASR deformations, the accuracy of the method is sufficient to capture the majority of cracks and determine the overall cracking patterns and changes over time.
>
> "Monitoring of Dams Suffering from ASR at the Bureau of Reclamation"
> ibid.

(Author's highlight)

It should be noted that only a single image is provided for either technique, and there is no indication of the age of the dam at that time. Hence, in the absence of a historical record, it is impossible to make a qualitative (let alone quantitative) correlation with the AAR expansion.

9.3.3.1 Crack Mapping

At *prima facie* one would be inclined to say that the cracks in Fig. 9.23 are caused by AAR. However, there is no indication of a field inspection (by climbers) to determine: a) the depth of the crack, the magnitude of the crack openings; and most importantly c) the cause of the cracks (which may be caused by shrinkage and solar exposure, lift or cold joints, as opposed to AAR).

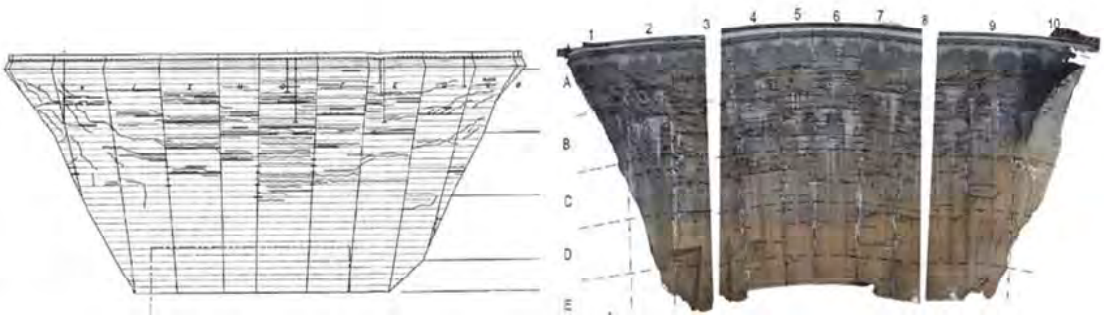

Figure 9.23: Downstream crack pattern observation (Salamon, Dressel, and Liechty, 2021)

To examine this hypothesis, we need to examine the deformation of the dam, Fig. 9.24.

What emerges is that the crown arch is indeed: a) restraining the vertical expansion of the cantilevers, and b) there is less expansion on the abutments that in the center.

The first finding, results in compression on the cantilevers, and will thus "pre-stress" the dam from tension. The flexural induced tension in this case is minimal.

Related to the second observation, one would assume that there will be more cracks above the tall cantilevers than on the shorter ones in the side if indeed cracking was caused by AAR. Evidently, this is not the case in Fig. 9.23.

Hence, one can reasonably assume that the observed crack pattern is not AAR related.

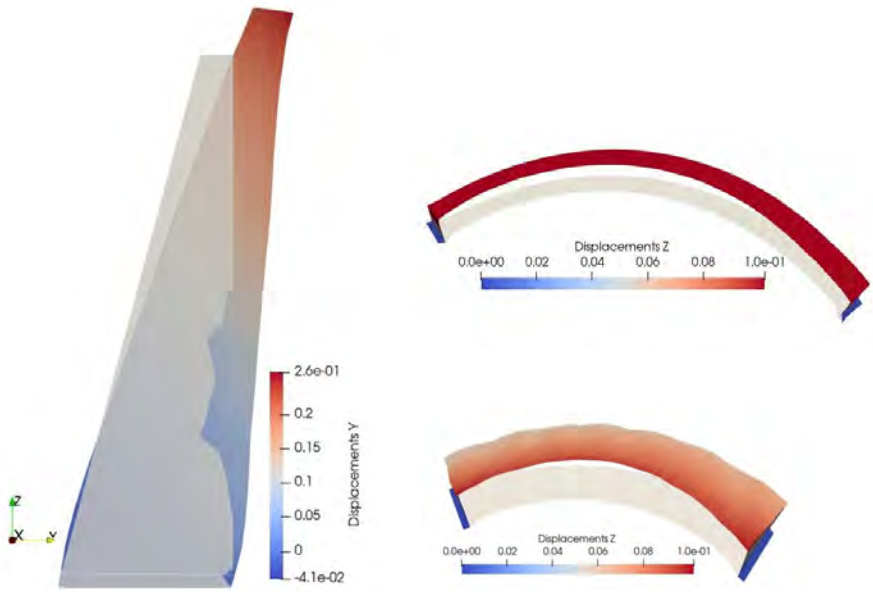

Figure 9.24: Selected views of the deformed shape

Should one have a time history record of cracking, than indeed we could have modified our parameter identification procedure to not only capture crest displacements but also tensile stresses at key locations. This would have been possible with adjustment of our Matlab® function. However, we are not yet fully convinced that these ar AAR induced.

9.3.3.2 LIDAR observations

The upstream/downstream displacements, the anticipated internal cracking (from a non linear analysis), and the reported LIDAR image are shown in Fig. 9.25(a), 9.25(b) and 9.25(c) resectively. Of course, no rational comparison can be made (yet), as: a) we do not what exactly the LIDAR is supposed to reprsent (damage, displacements,strains?), and b) more importantly we do not know the time interval which is captured by this image[1]

Thus we observe that:

(1) The LIDAR image, Fig. 9.25(c), is not compatible with the image of the downstream

[1] To construct a LIDAR image one needs an initial iamge at time t_0 and a subsequent one at time t_1, hence the LIDAR would capture the evolution of a quatitty during the time interval $\Delta t = t_1 - t_0$.

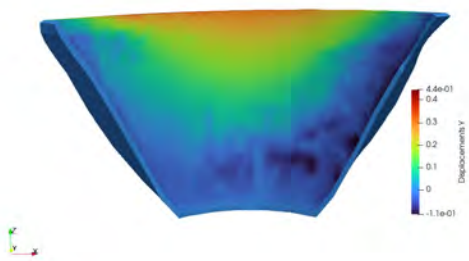

(a) Y (US/DS) displacements

(b) Downstream cracking

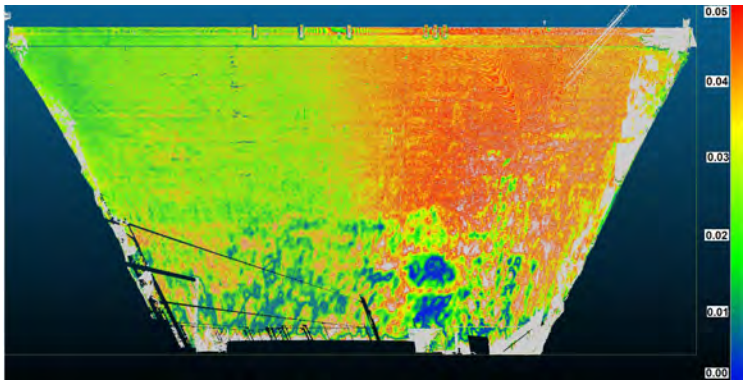

(c) LIDAR Measurements

Figure 9.25: Comparison of computed results with LIDAR point clouds

cracks, Fig. 9.23.

(2) The image appear to match the determined cracking, Fig. 9.25(b), with a small level of confidence.

Hence, we conclude that there are encouraging signs for correlation, but certainly not definite. More LIDAR readings would be needed, and more related information would be necessary for a more comprehensive correlation with the finite element simulation.

Chapter 10

Uncertainty Quantification

Abstract

In so far, all analyses were deterministic. In this final chapter, we will perform an uncertainty quantification (a.k.a. "Monte Carlo" simulation) study for both thermal and stress analysis.

In the stress analysis the only source of non-linearity will be the presence of the joints (this is justified by Fig. 9.8).

Probabilities of exceedance of critical threeshold values will be analytically developed, along with the importance of the sample sizes (three were used: 50, 100 and 200).

10.1 Thermal Analysis

Since thermal analysis is a prerequisite to the stress analysis, the uncertainty quantification of thermal parameters is also required prior to conducting any uncertainty assessment of stress analysis. Therefore, this section is to discuss the effect of parameter uncertainties used in thermal analysis of the case study dam on the resulting concrete internal temperatures. To this purpose, among all (figure 10.1), the thermal parameters which were believed to have some extent of uncertainty were taken as random variables. These parameters are as follows:

- Specific heat
- Conductivity
- Air temperature amplitude

- Water surface temperature amplitude
- Water bottom temperature amplitude

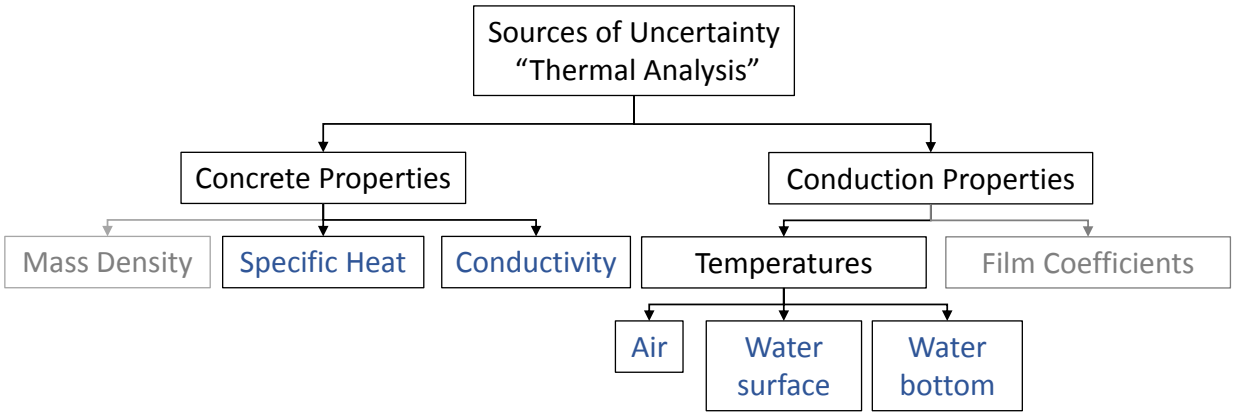

Figure 10.1: Sources of uncertainty in thermal analysis

The particular point of interest (POI) for nodal temperature has the recorded values shown in Fig. 10.2.

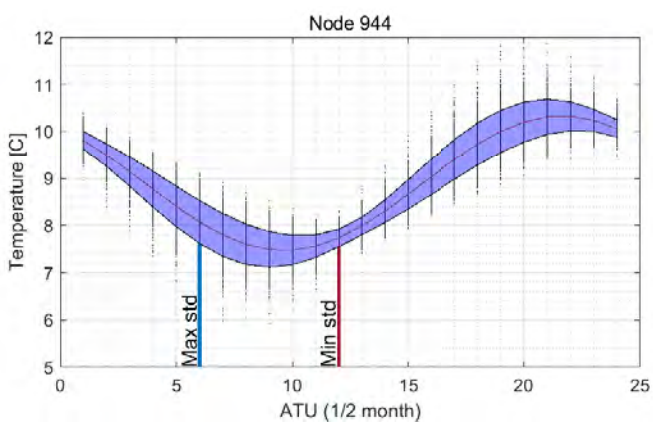

Figure 10.2: Monthly temperatures at PoI (Node 944), with mean and standard deviation

It should be noted that other thermal parameters, such as film coefficients were assumed to be deterministic variables as there are certain values available for them in the literature and there is no need to treat them as uncertain variables. Also, the mass density of the concrete is believed to be determined.

Assuming a lognormal distribution for the aforementioned variables and a coefficient of vari-

ation(COV) equal to 15%, 1000 number of simulations were generated using the Latin hypercube sampling (LHS) method assuming that these parameters have zero correlation with each other. The 1000 thermal models were generated based on those simulations for which the temperature of 6 node inside the dam body for 2 months is shown in figure 10.4. As seen in the plot, the maximum inside dam temperature is occurring around mid October which stems from the thermal inertia phenomenon which is a description for the delay in the inside dam body temperature to feel the temperature increase of the surrounding fluid. This fact can also be interpreted from the seasonal water temperatures demonstrated in table 10.1 taken from the (Hatch, 2015) report.

Table 10.1: Water temperature (Hatch, 2015)

Depth (m)	**Jan**	**Feb**	**Mar**	**Apr**	**May**	**Jun**	**Jul**	**Aug**	**Sep**	**Oct**	**Nov**	**Dec**
0.0	3.9	3.9	4.4	-	-	12.2	17.2	22.2	20.0	15.6	12.8	8.9
1.6	5.6	6.1	6.7	-	-	11.7	16.1	21.7	20.0	15.6	12.2	8.3
4.6	6.7	7.2	7.2	-	-	10.0	14.4	18.9	19.4	15.0	11.7	8.3
7.7	6.9	7.5	7.5	-	-	9.4	11.7	12.2	13.3	14.4	11.7	8.3
19.8	7.2	7.8	7.8	-	-	8.9	10.0	10.6	11.1	10.6	11.1	8.3
35.1	7.2	7.8	7.8	-	-	8.9	8.9	8.9	9.4	9.4	9.4	8.3
80.8	7.8	8.3	8.3	-	-	8.3	8.3	8.3	8.3	8.3	8.3	8.3

As seen in this table, around depth 7.7 [m], which corresponds to the depth of our point of interest, the maximum temperature of the whole year is measured in October.

10.1.1 Procedure

The procedure itself is algorithmically implemented through a sequence of Matlab® files, Fig. 10.3. Note that this procedure is tied to the computer program used (Merlin).

10.1.2 Observations

Figure 10.4 explains the most important conclusions from this thermal uncertainty quantification:

- First of all this is showing that the results of the sensitivity analysis for the dam cannot

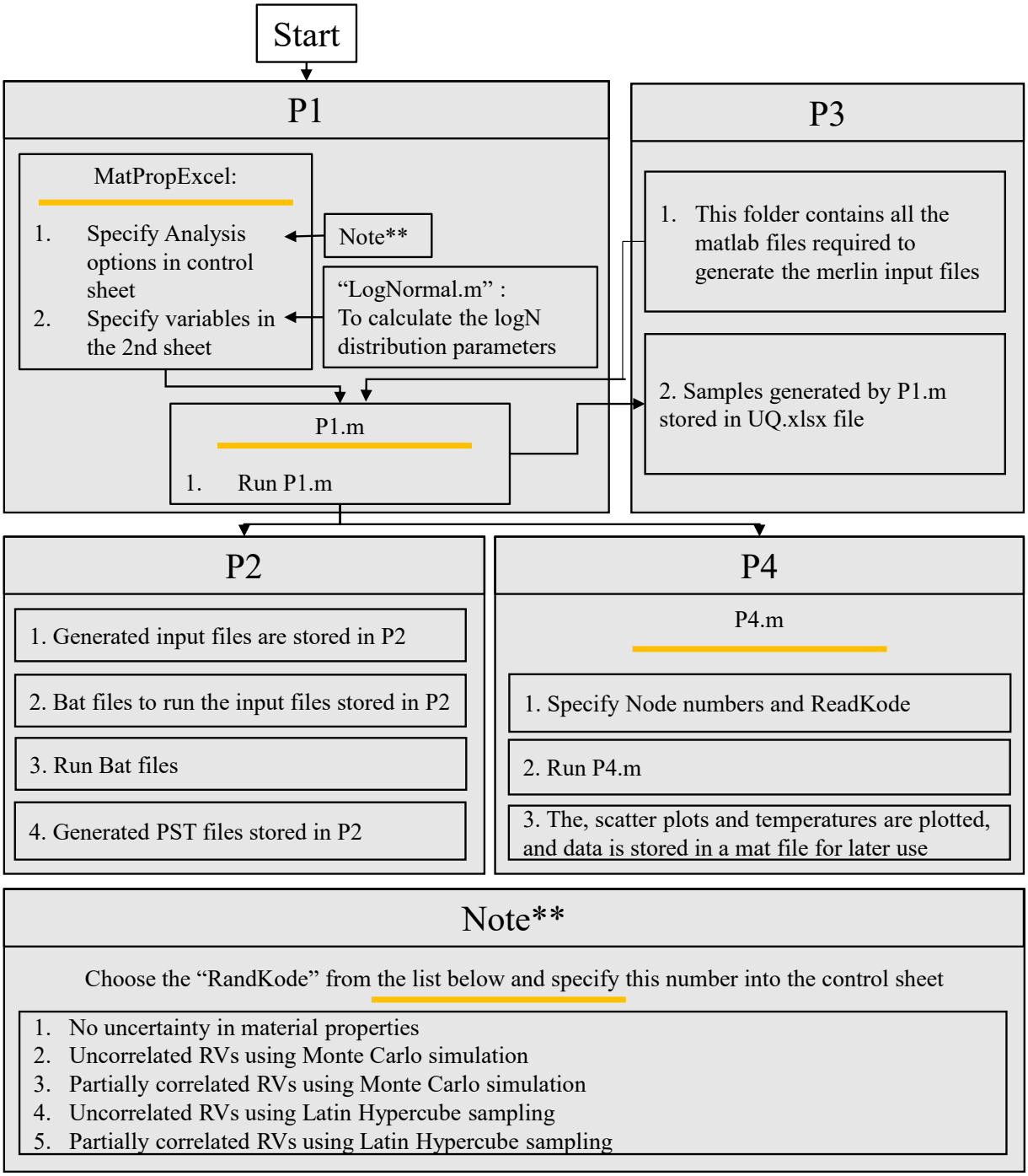

Figure 10.3: Uncertainty Quantification Flowchart

be generalized to the whole dam body and throughout the year. In other words, there is a temporal and spacial variation in the results of thermal analysis.

- While at the top of the dam, which is exposed to the air, the air temperature is the most effective variable at the bottom of the dam close to the upstream face the temperature is more sensitive to the specific heat value.
- Even at the bottom of the dam the temperature is more sensitive to the top water temperature rather than bottom water temperature which is due to the higher variation of top temperature compared to bottom.
- The temperatures of the nodes below water level are more sensitive to the conductivity at the upstream face and to air temperature at the downstream side.

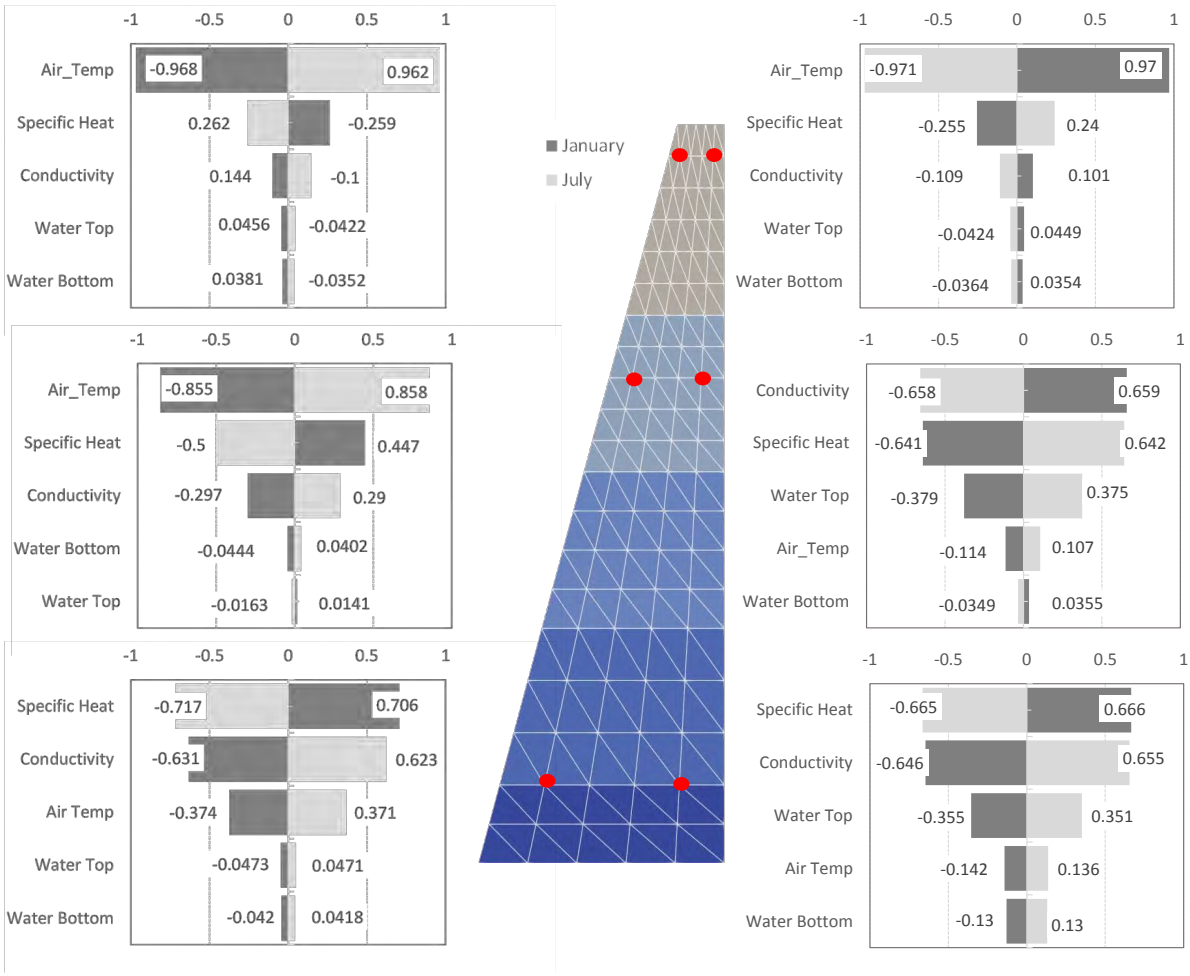

Figure 10.4: Correlation of nodal temperatures and variables at 6 different nodes in January and July

Figure 10.5 is showing the monthly temperature variation and the resullting temperature mean and

standard deviation at the 6 nodes. as seen, the maximum temperature moves as the node goes into the depth.

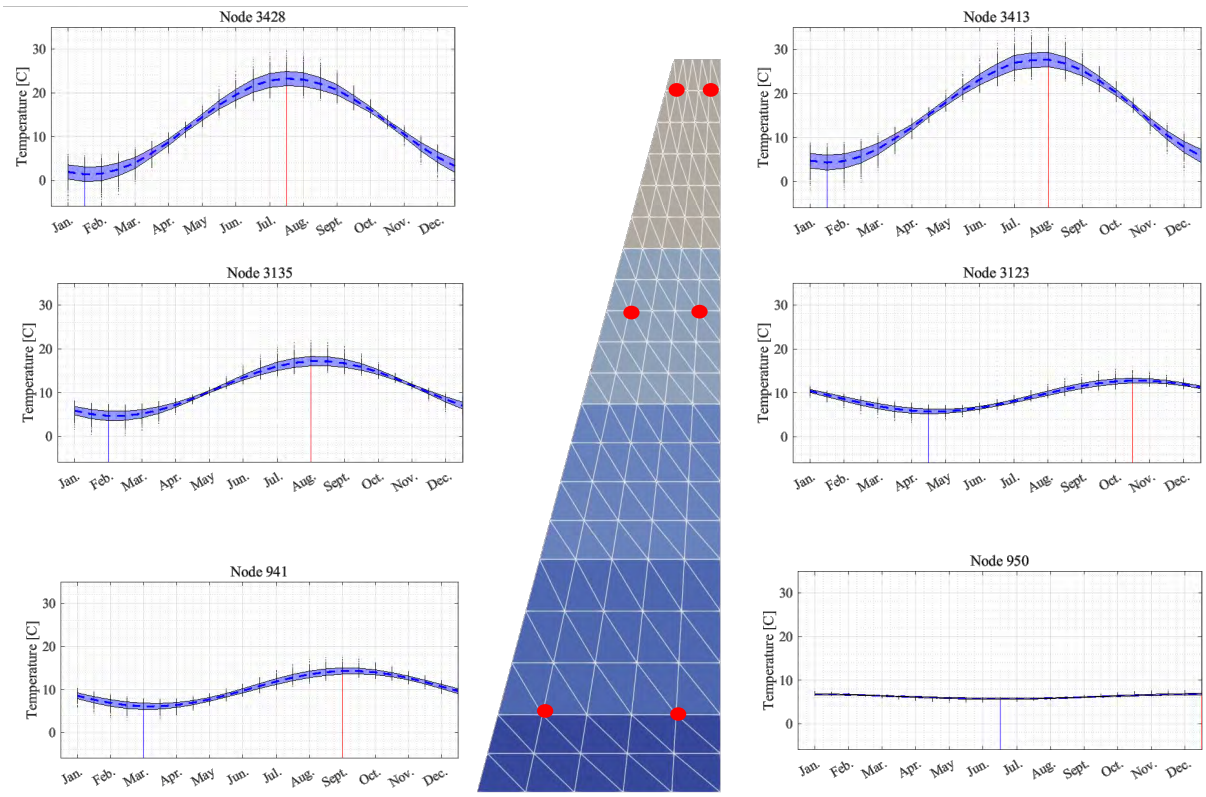

Figure 10.5: Monthly variation of temperature at 6 nodes throughout a year

Taking another point inside dam body as a point of interest, the scatter plots of each variable versus the nodal temperature can be presented for every month of the year. Figure C.1 through C.4 show the correlation plots of each variable versus the resulted nodal temperature at the point of interest. There are correlations associated with the thermal parameters and thermal results. As expected the conductivity has negative correlation with the temperature through almost the whole year.

As seen in figure 10.6 the correlation between the air temperature amplitude and the concrete internal temperature is positive during the colder months of the year and is negative during the warmer months. Figure C.3 and C.4, show almost zero correlation between the nodal temperature

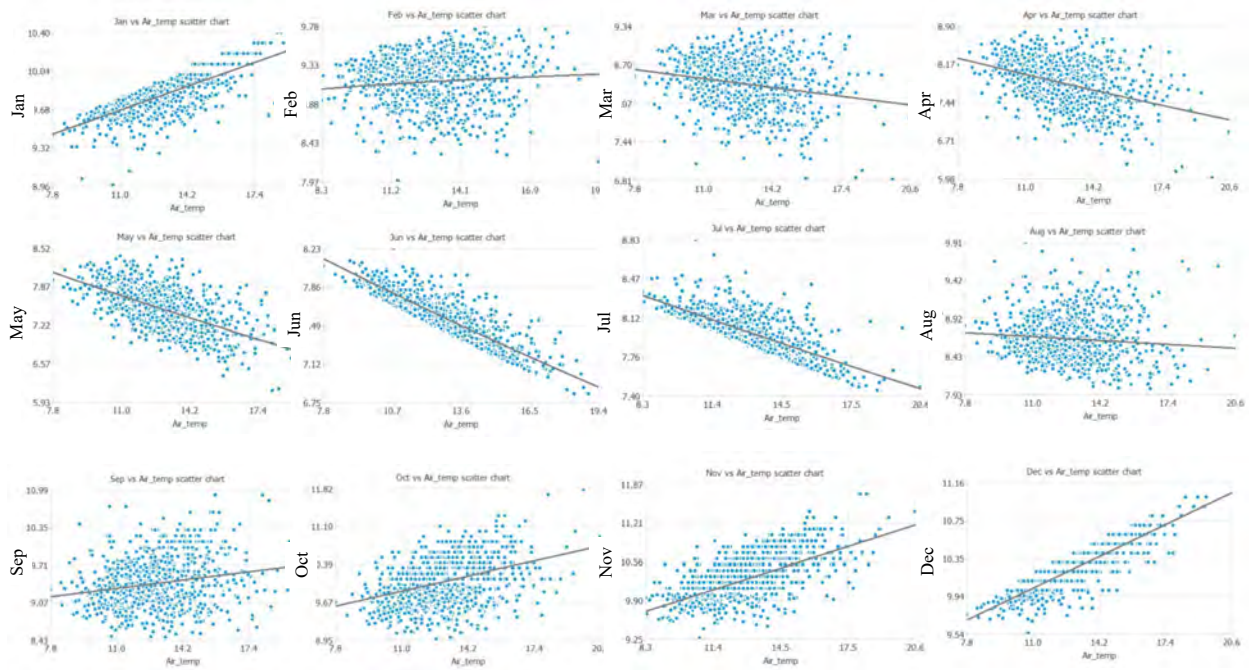

Figure 10.6: Monthly air temperature correlation coefficients at node 944 (PoI)

at the point of interest and water temperature amplitude. While air temperature amplitude has noticeable correlation with the internal node temperature. This shows that the point of interest is more under the influence of the air temperature rather than water. It is noted that the temperature amplitudes are considered as the random variable and thus are constant values for each analysis. Therefore, the possibility of phase lag is eliminated. Since, our data on the reservoir temperature was limited, this observation underlines the fact that the lack of data is not affecting the results significantly as the point of interest is selected to be an internal node below the water level.

The nodal temperature distribution, figure 10.7, resulted from thermal UQ analysis will be eventually incorporated into the stress uncertainty quantification(UQ) analysis.

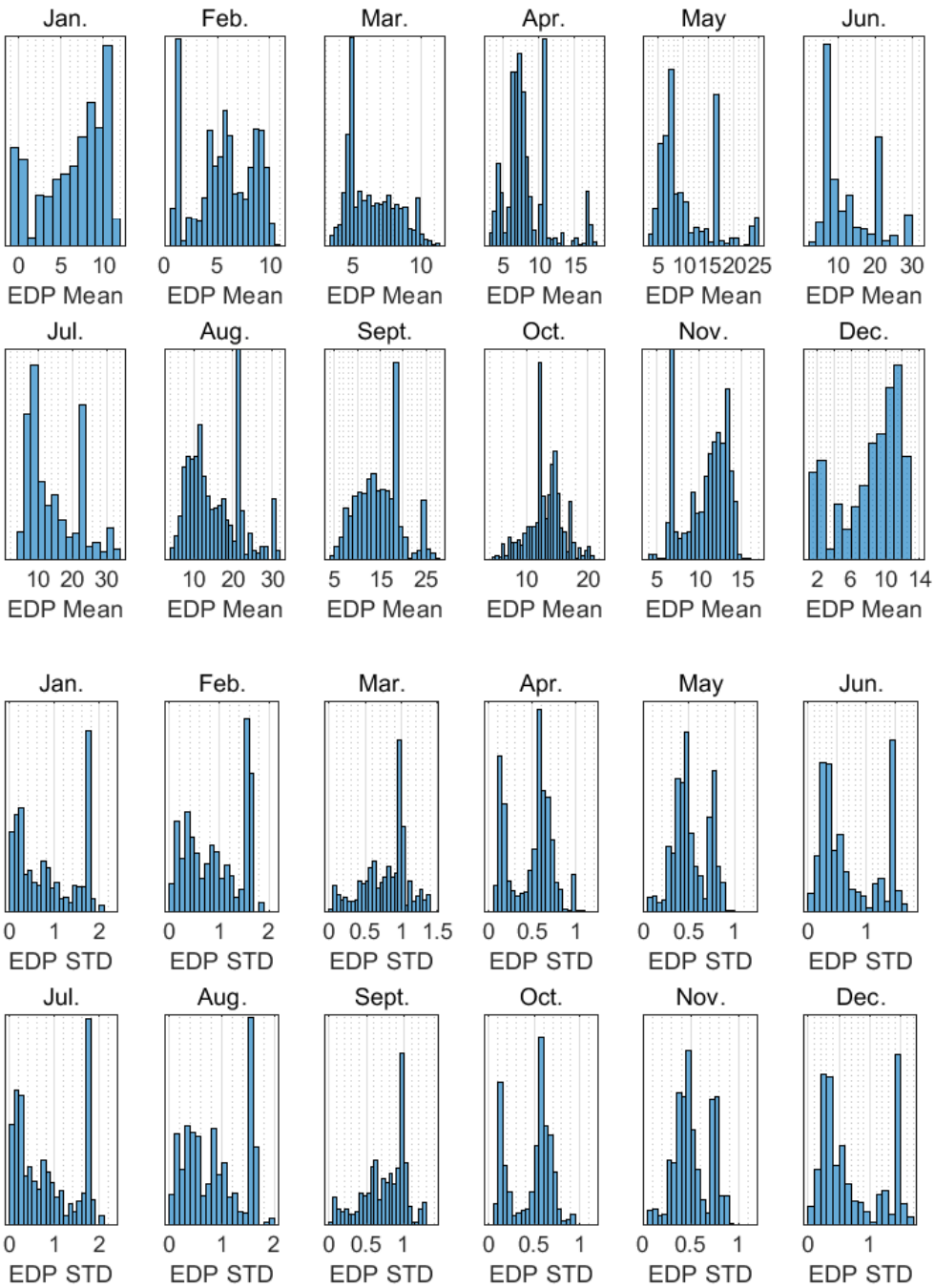

Figure 10.7: Monthly mean and standard deviations histograms for temperatures inside entire mesh

10.2 Stress Analysis

Determination of the AAR model parameters can introduce uncertainties into our stress responses. As shown schematically in figure 10.8, considering a distribution for each parameter every point on these curves will result in a different AAR expansion curve and in turn a unique response with time for multiple analyses. Therefore, the uncertainty quantification of the stress analysis through propagation of the uncertainty sources associated with the AAR model parameters is of great importance.

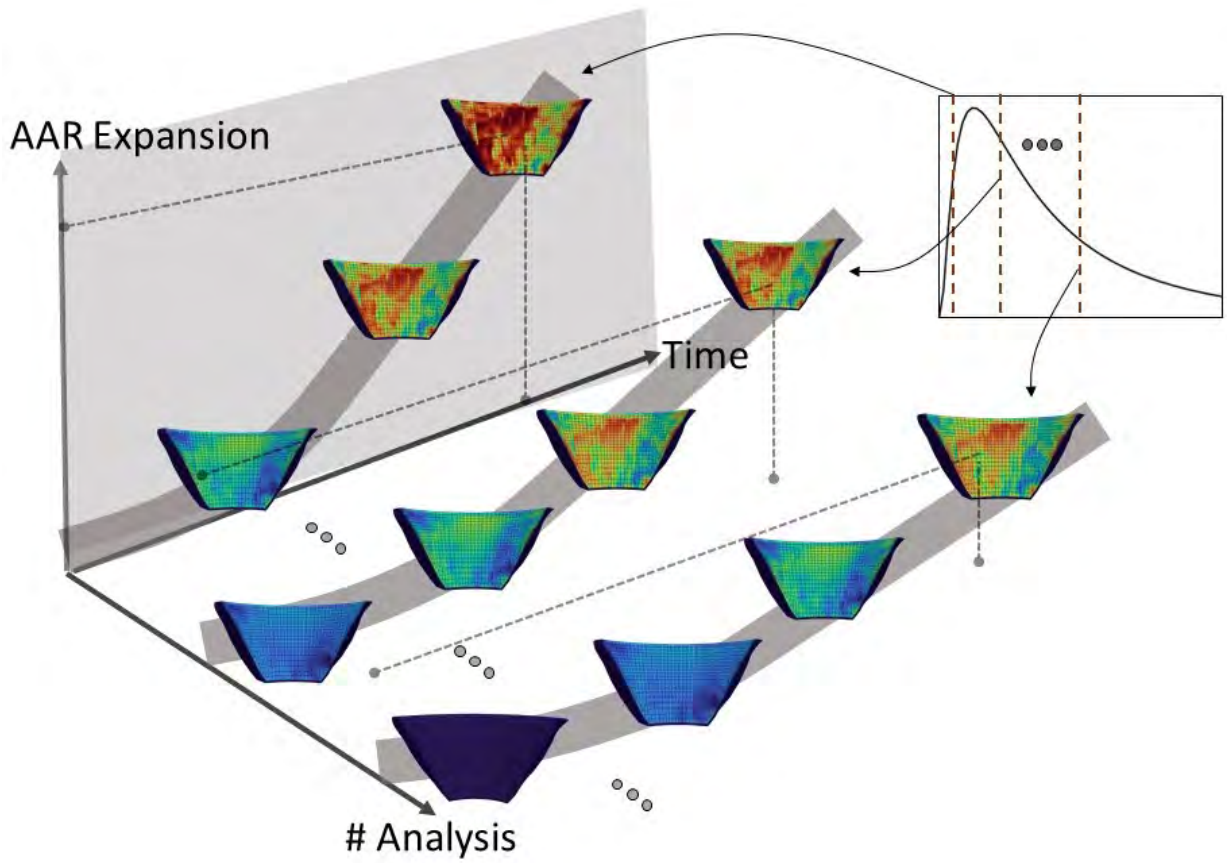

Figure 10.8: Uncertainty in AAR modeling

The uncertainty quantification of the dam stress analysis is also a function of temperature variability and depends on the uncertainties associated with the uncertainty in the dam internal temperatures. Therefore, the uncertainty quantification of the stress analysis requires performing

a number of thermal analysis as well. As such, 13 variables have been selected as the input random variables which are as follows:

(1) Specific heat

(2) Conductivity

(3) Air temperature amplitude

(4) Reservoir top temperature amplitude

(5) Reservoir bottom temperature amplitude

(6) Elastic modulus of Concrete (Top)

(7) Elastic modulus of Concrete (middle)

(8) Elastic modulus of Concrete (bottom)

(9) AAR maximum volumetric strain

(10) Characteristic time (τ_c)

(11) Latency time (τ_l)

(12) Activation energy associated with τ_c (U_c)

(13) Activation energy associated with τ_l (U_l)

As seen, the random variables can be categorized as concrete material properties, Air and water temperature inputs and the AAR model properties. It should be noted that the modulus of elasticity of concrete is considered to be variable through the height of the dam and thus, 3 different values have been considered for that. Figure 10.9 shows a matrix plot for the 13 random variables and their correlations. As seen the random variables each have a log-normal distribution with almost zero correlations.

In order to investigate the effect of sample size on the results, 3 samples with 50, 100 and 200 models are selected, analyzed, and the results are compared. Each model is analyzed for 50 years starting from 1980 when the first AAR effects was observed.

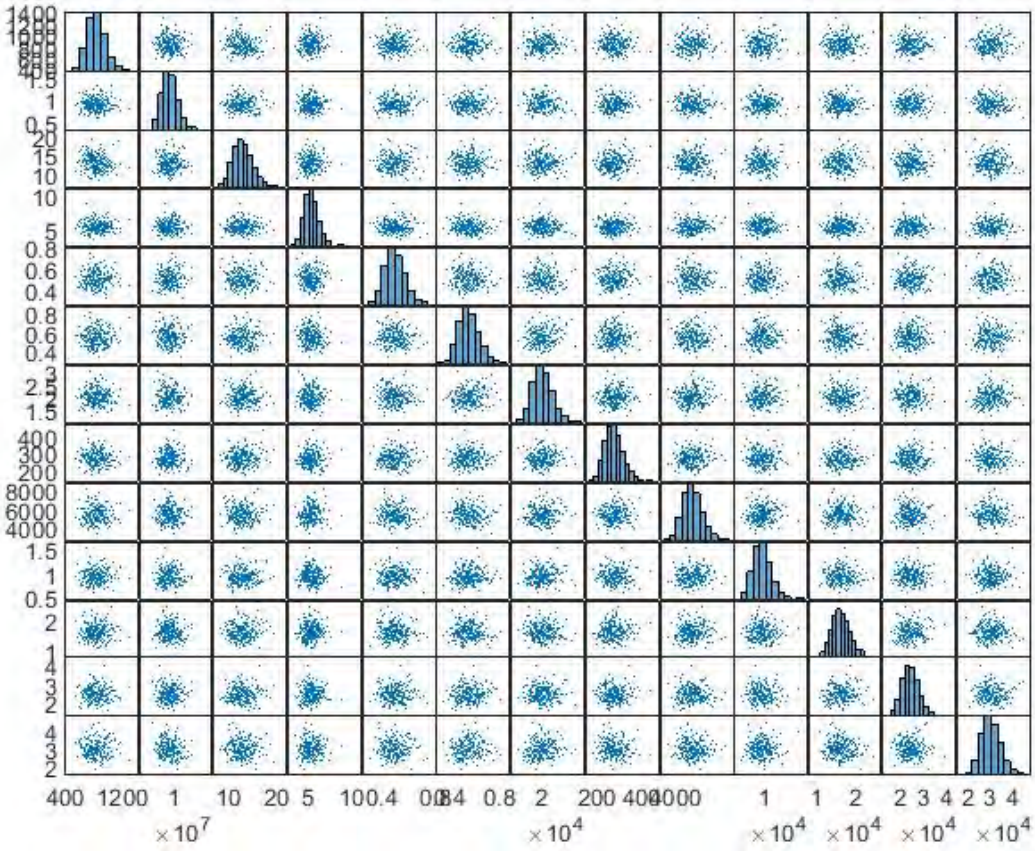

Figure 10.9: Matrix plot of the 13 input variables

Uncertainty Quantification of Stress Analysis

Step1:Thermal Analysis

P1

- Set variables and number of samples in "MatPropExcel.xlsx"
- Run "P1.m" to generate the input files

P2

- Set the number of input files and batch files in "GenerateThermalBat.m" and run to generate the batch files
- Run all of the generated batch files

P3

The variables of each file are saved into "UQ˙Thermal.xlsx", "UQ˙Thermal.mat"

P4

- Run P4.m to read the results and save them into "NEWTEMP.mat"
- Copy the mat file and paste into Stress/P3/Mat-Files

Step2:Stress Analysis

P1

- Set variables and number of samples in "MatPropExcel.xlsx"
- Run "P5.m" to generate the input files

P2

- Set the number of input files and batch files in "GenerateStressBat.m" and Run to generate the batch files
- Run all of the generated batch files

P3

The variables of each file are saved into UQ˙Stress.xlsx, UQ˙Stress.mat

P4

Read the results and plot

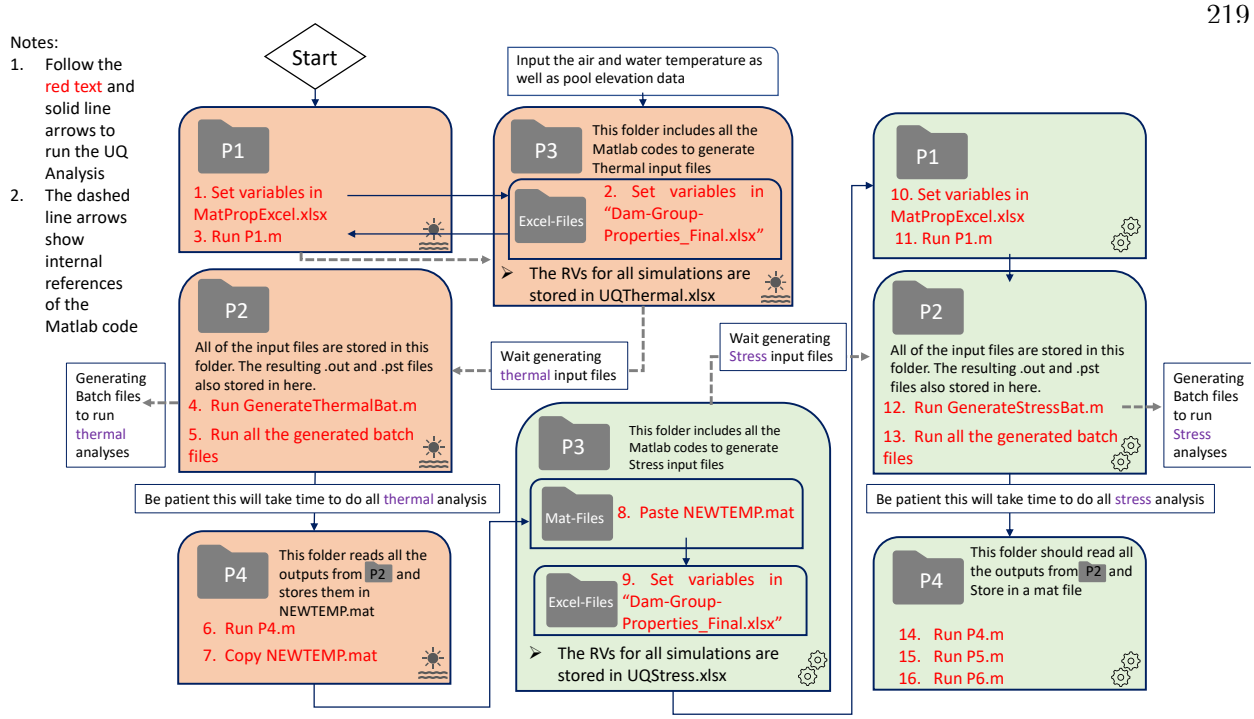

Figure 10.10: Flowchart of UQ Procedure

In order to present the displacements results 18 points at the rock-concrete interface and 2 points at the Crest are selected and to record the stresses in the body of the dam, in total 14 nodes have been chosen on the upstream and downstream sides which are shown in figure 10.11.

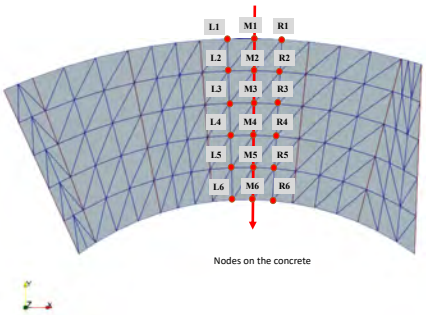

(a) COD

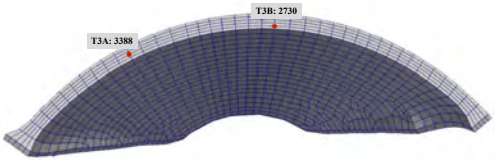

(b) Crest Displacement

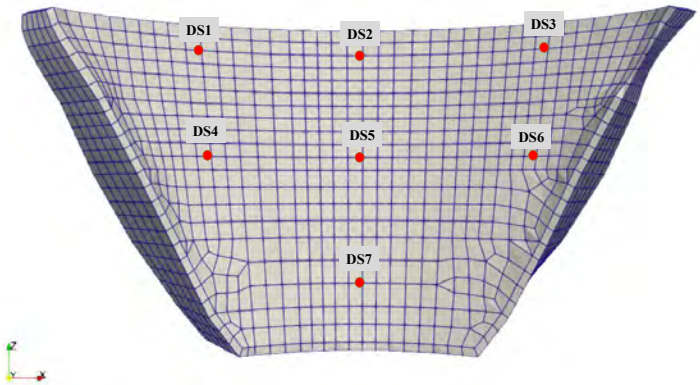

(c) Downstream,Stresses

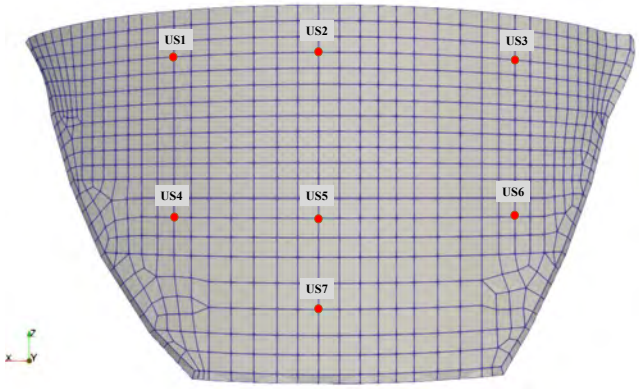

(d) Upstream, Stresses

Figure 10.11: Location of recorded nodes

10.2.1 Results

In this section the results of the uncertainty quantification, using 200 analysis sample, are demonstrated in terms of crest displacements and maximum principal stresses.

10.2.1.1 Displacements

Figure 10.12 shows the variation of the response of the nodes corresponding to the location of the T3A and T3B instruments in terms of the 2 horizontal and 1 vertical displcements as well as the mean and mean $\pm$ 1 standard deviation. As seen, the mean value of the most reliable recording (T3B in radial direction) is about 25 cm at the end of the analysis time which is in the December of 2030.

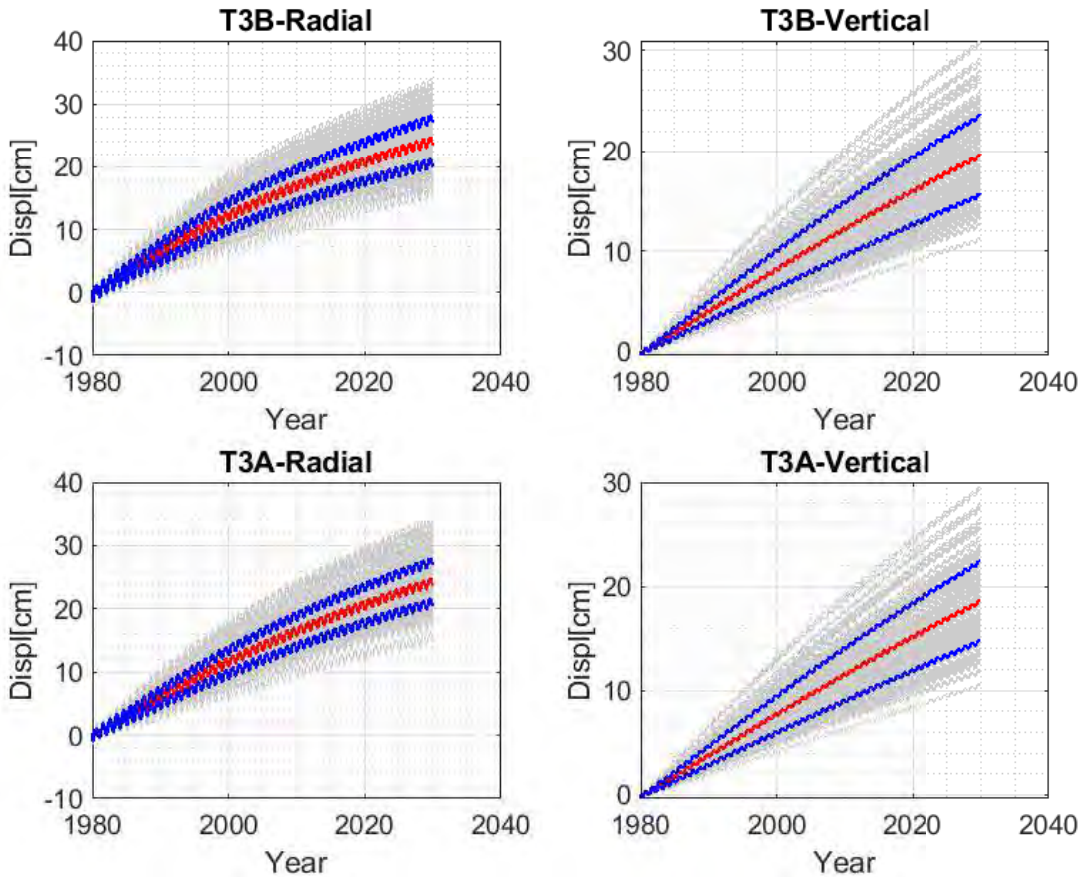

Figure 10.12: Crest Displacements (stream and vertical directions); (+ve is toward the upstream and upward)

10.2.1.2 Stresses

The maximum principal stresses for the 7 points on each side are shown separately in figure 10.13 and 10.14. The results suggest an overall higher stresses on the downstream side compared to the upstream.

It should be noted that the positive stress values indicates tension and thus at the points with higher stresses cracking can be expected. However, for the more detailed assessment of cracking a full nonlinear analysis is required.

To have a more clear interpretation of the results, the normalized maximum principal stresses with respect to the tensile strength of the concrete is plotted in figures 10.15 and 10.16. The higher

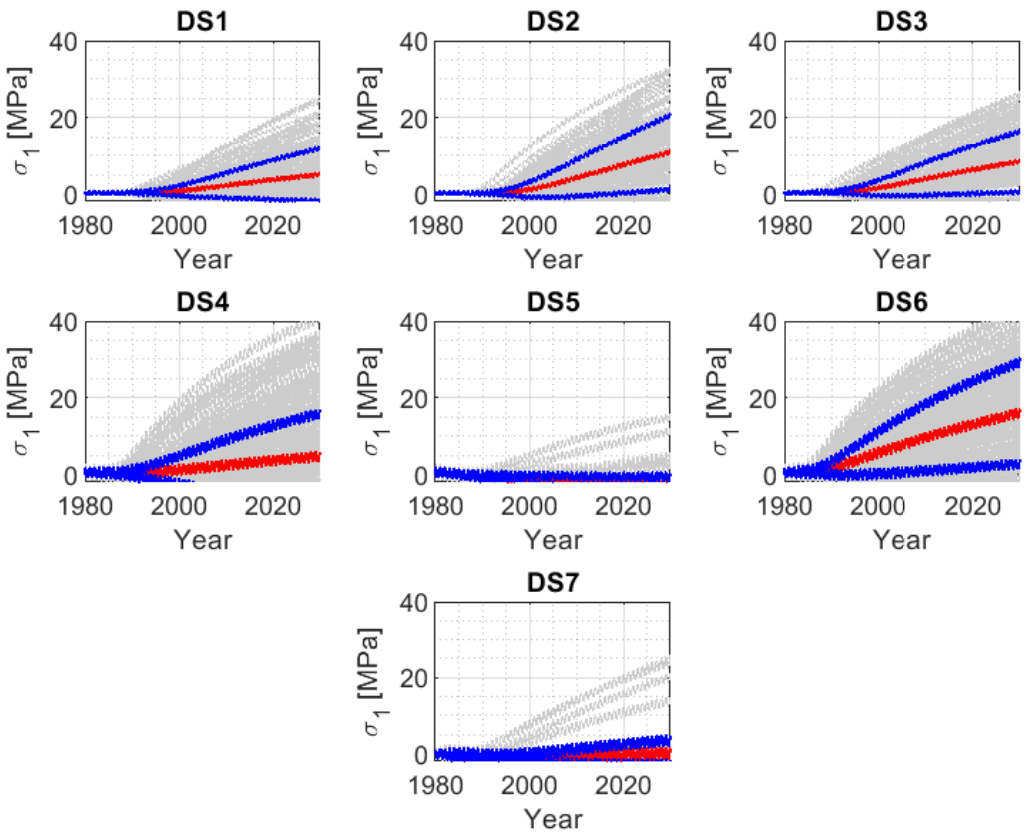

Figure 10.13: Maximum Principal Stress (+ve indicates tension); Downstream

ratios on the downstream side and the top nodes indicates that the concrete in that section will experience the cracking and as seen this is happening at earlier times for the top of the downstream side.

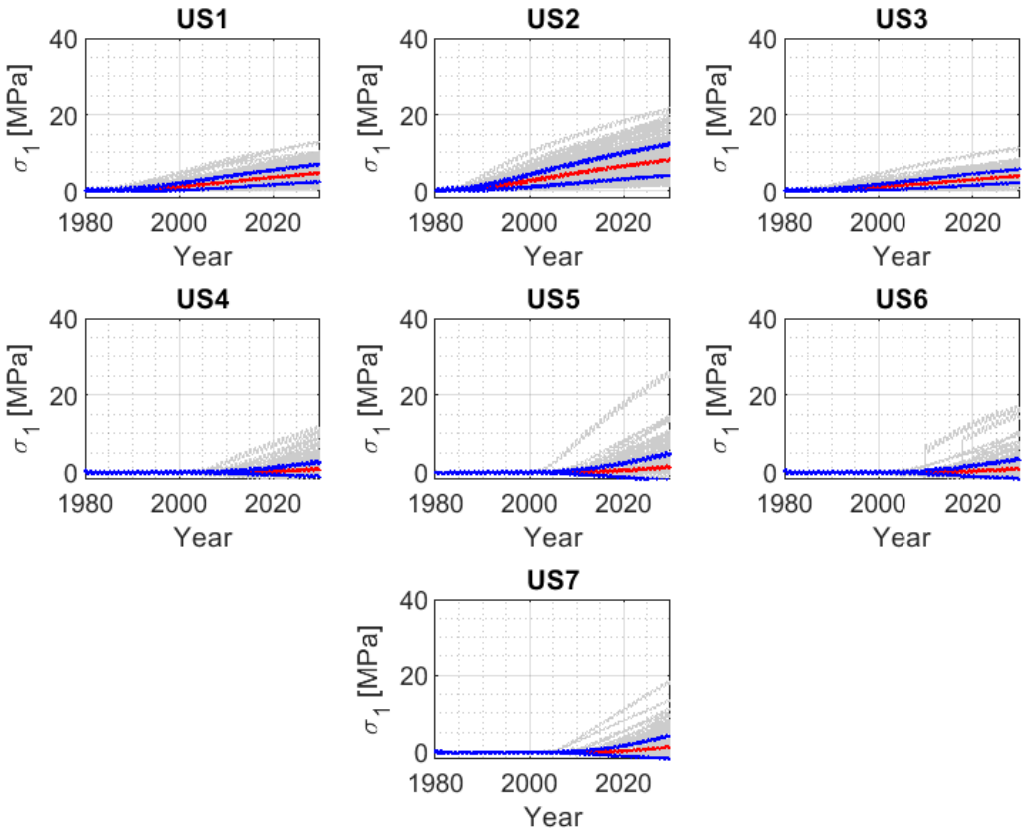

Figure 10.14: Maximum Principal Stres (+ve indicates tension)s; Upstream

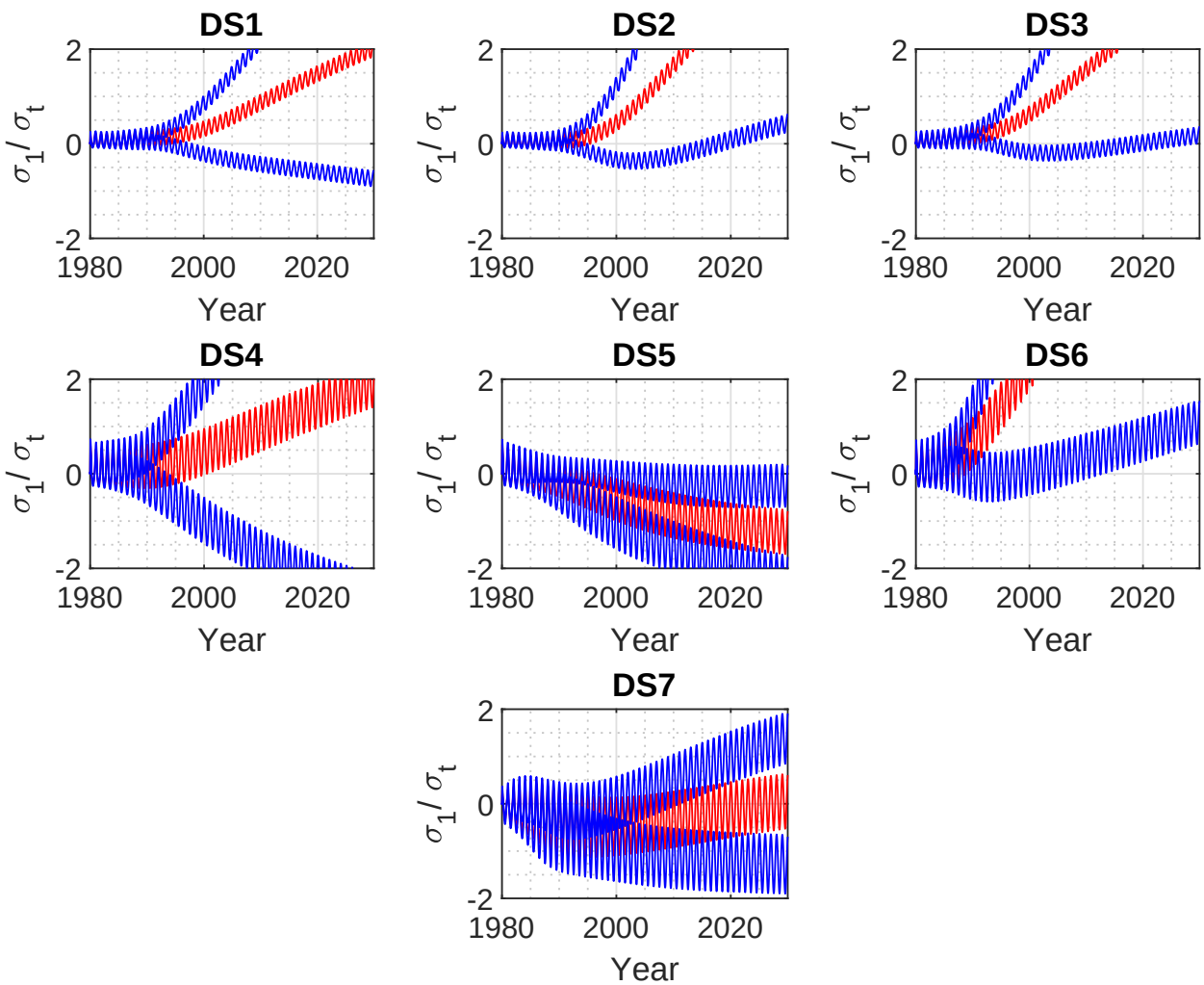

Figure 10.15: Normalized Maximum Principal Stress with respect to Tensile Strength(+ve indicates tension); Downstream

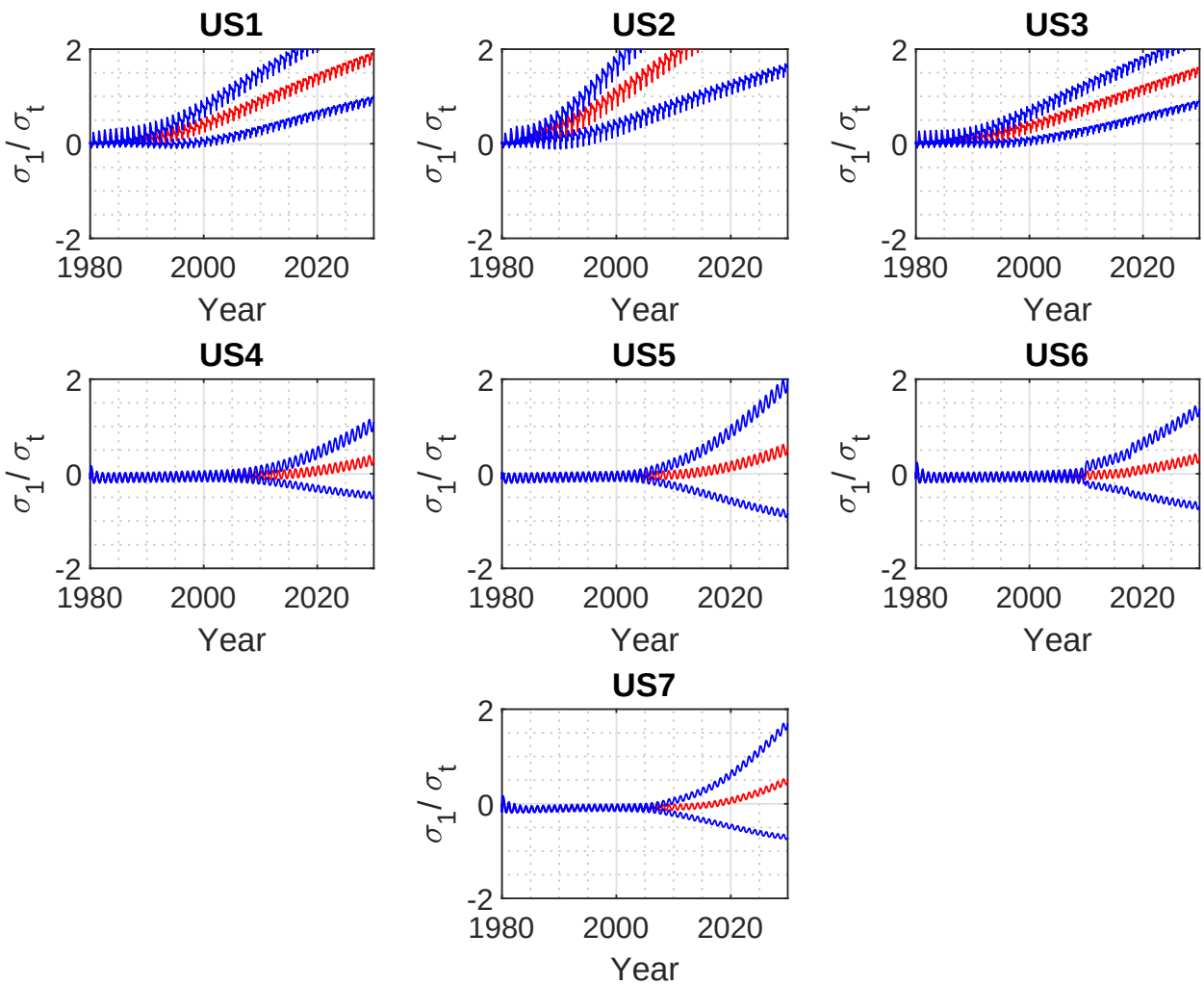

Figure 10.16: Normalized Maximum Principal Stress with respect to Tensile Strength (+ve indicates tension); Upstream

10.2.1.3 Probability of Exceedance

In order to determine the probability of exceedance from a certain limit state, the 2 methods have been selected to determine the fitting function using(Baker, 2015):

- Maximum likelihood Estimation: In this method the parameters are determined such that a certain distribution is most likely to produce the observed data. In the current study, the maximum likelihood estimation is used to fit a log-normal cumulative distribution function to the stress ratios in time (figure 10.17). In other words, the objective is to find the probability of the principal stresses exceeding the tensile strength at different time steps. For each specific point on the dam, at each time step t_j, a number of analysis out of total (200 analyses in this study) would result in the stress to exceed the threshold(tensile strength). Assuming 2 possible event: 1. exceed the threshold and 2. Not to exceed the threshold, the probability of observing z_j exceedance out of n_j analyses at each x_j can be determined by the binomial distribution:

$$P(z_j \text{exceedance in } n_j \text{ analyses}) \equiv \begin{pmatrix} n_j \\ z_j \end{pmatrix} p_j^{z_j}(1-p_j)^{n_j-z_j} \tag{10.1}$$

where p_j is the probability that an analysis at time t_j will exceed the threshold. In order to find the likelihood of the whole data, the probabilities at all time steps are multiplied:

$$\text{Likelihood} \equiv \prod_{j=1}^{m} \begin{pmatrix} n_j \\ z_j \end{pmatrix} p_j^{z_j}(1-p_j)^{n_j-z_j} \tag{10.2}$$

where m is the number of time steps. substituting the equation for log-normal CDF into the equation above We then have:

$$\text{Likelihood} \equiv \prod_{j=1}^{m} \begin{pmatrix} n_j \\ z_j \end{pmatrix} \Phi\left(\frac{\ln(x_j/\theta)}{\beta}\right)^{z_j} \left[1-\Phi\left(\frac{\ln(x_j/\theta)}{\beta}\right)\right]^{n_j-z_j} \tag{10.3}$$

As mentioned above the goal is to find the parameters so that the the distribution has the highest likelihood of representing the data. Thus the next step is to find the parameters

that maximize the logarithm of the likelihood funtion, since it is easier, therefore we have:

$$\left\{\hat{\theta},\hat{\beta}\right\} \equiv \underset{\theta,\beta}{\operatorname{argmax}} \sum_{j=1}^{m} \left\{ \ln \begin{pmatrix} n_i \\ z_j \end{pmatrix} + z_j \ln \Phi\left(\frac{\ln(x_j/\theta)}{\beta}\right) + (n_j - z_j) \ln \left[1 - \Phi\left(\frac{\ln(x_j/\theta)}{\beta}\right)\right]\right\} \tag{10.4}$$

All these procedure is followed using the code by (Baker, 2015).

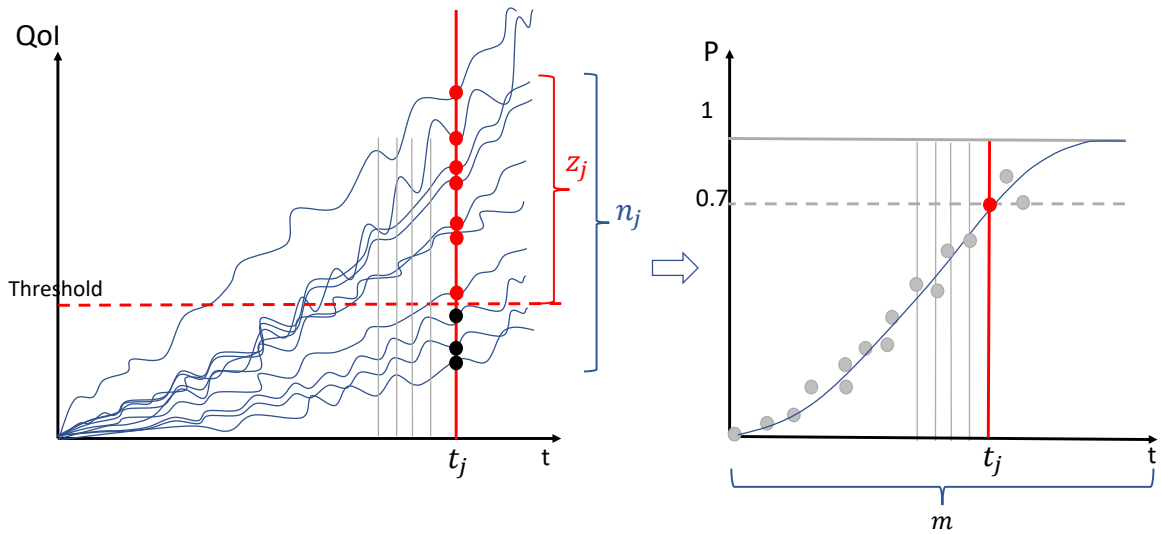

Figure 10.17: Schematic curve fitting procedure

- Sum of squared errors: This method is based on minimizing the sum of squared errors (SSE) between the observed data and predicted ones.

$$\left\{\hat{\theta},\hat{\beta}\right\} \equiv \underset{\theta,\beta}{\operatorname{argmin}} \sum_{j=1}^{m} \left[\frac{z_j}{n_j} - \Phi\left(\frac{\ln(x_j/\theta)}{\beta}\right)\right]^2 \tag{10.5}$$

In the current study the probability of exceedance of maximum principal stresses from the tensile strength is shown in figures 10.18 and 10.19.

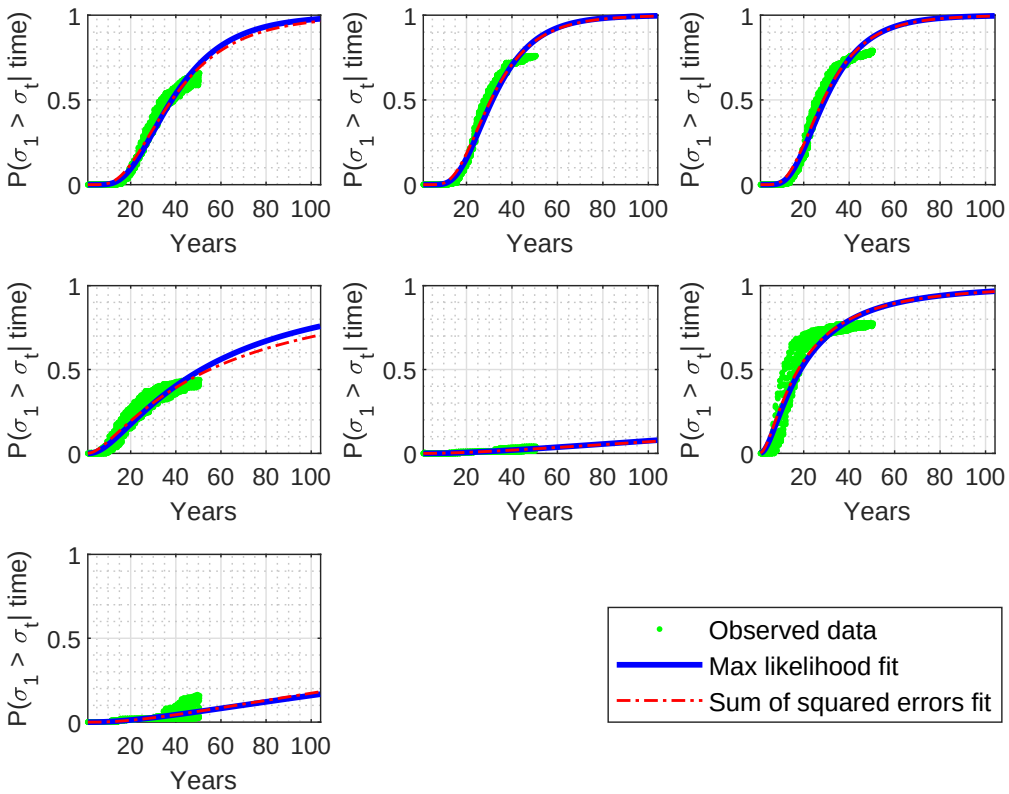

Figure 10.18: Probability of Exceedance; Downstream

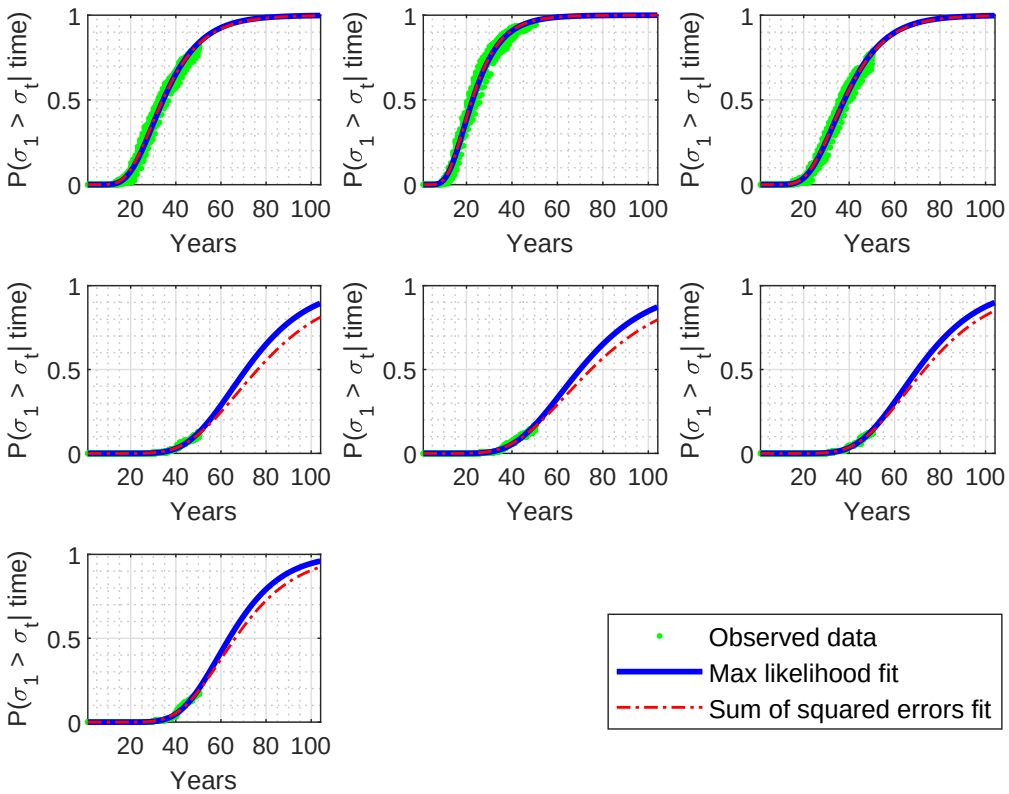

Figure 10.19: Probability of Exceedance; Upstream

10.2.1.4 Comparison of 3 sample sizes

As stated in the previous sections the uncertainty quantification was performed for 3 different samples with 50, 100 and 200 models. The standard error in terms of crest displacement and nodal stresses is calculated and plotted as a function of time. The standard error is a measure of how close the mean of each sample is likely to be to the true data mean. When the standard error increases, it is more likely that the sample mean is not a correct representation of the true data mean which can be determined using the following equation (James et al., 2013):

$$SE = \frac{\sigma}{\sqrt{n}} \tag{10.6}$$

Where n is the sample size and σ is the standard deviation.

looking at the standard errors, shown in figure 10.20 of crest displacements and stresses, one can conclude that the 100 analysis is providing a far better estimation of the real model compared to the 50 analysis while the 200 analysis is less effective in improving the results of 100 analysis. Furthermore, the analyses indicate that, as expected, the 3 samplings result in similar mean value curve while their standard deviations are different.

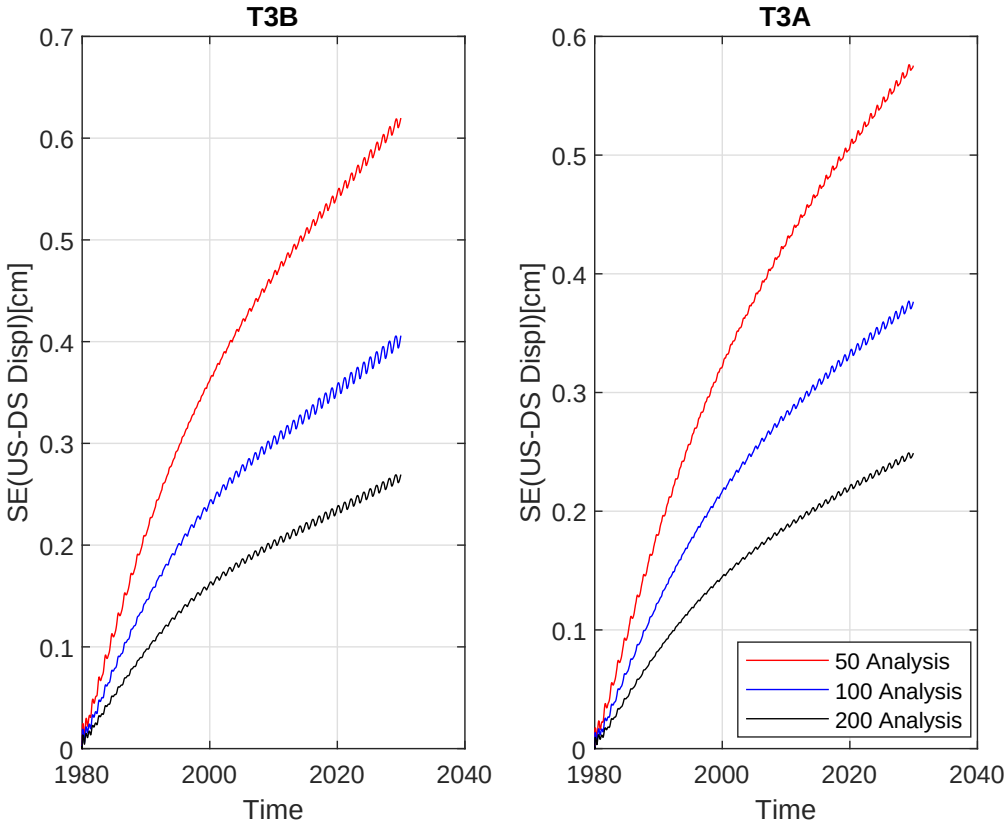

(a) Standard error

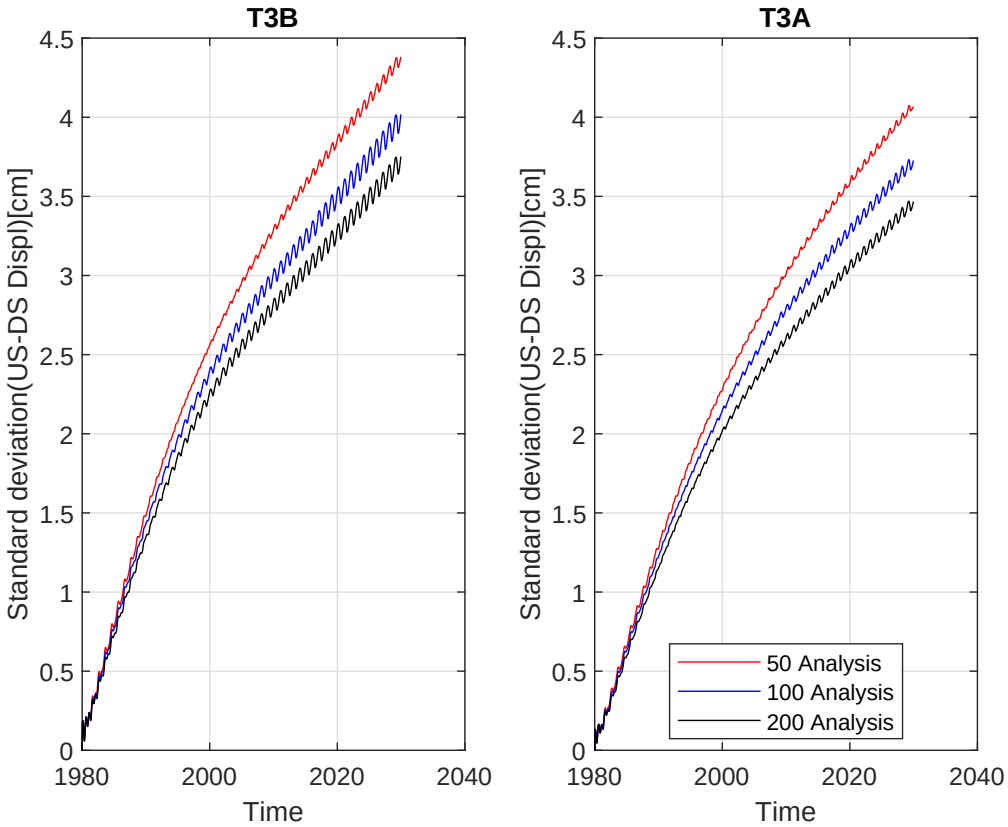

(b) Mean

Figure 10.20: Standard Error and Standard deviation curves of T3A and T3B US-DS displacements

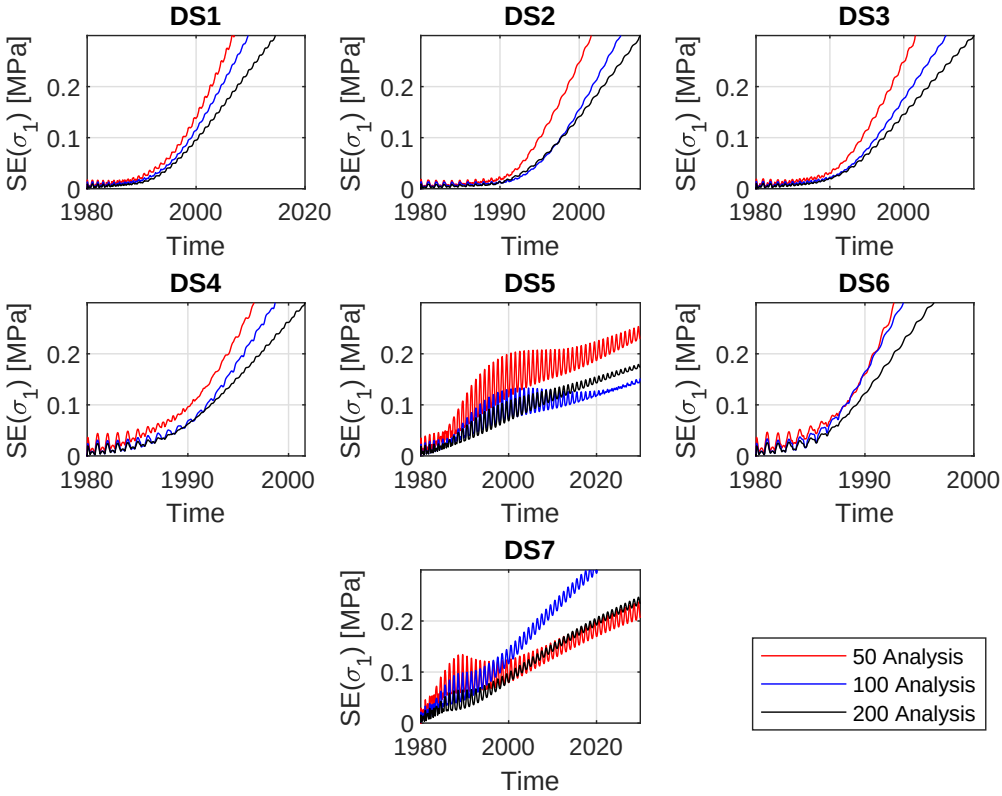

Figure 10.21: Standard Deviation; Downstream

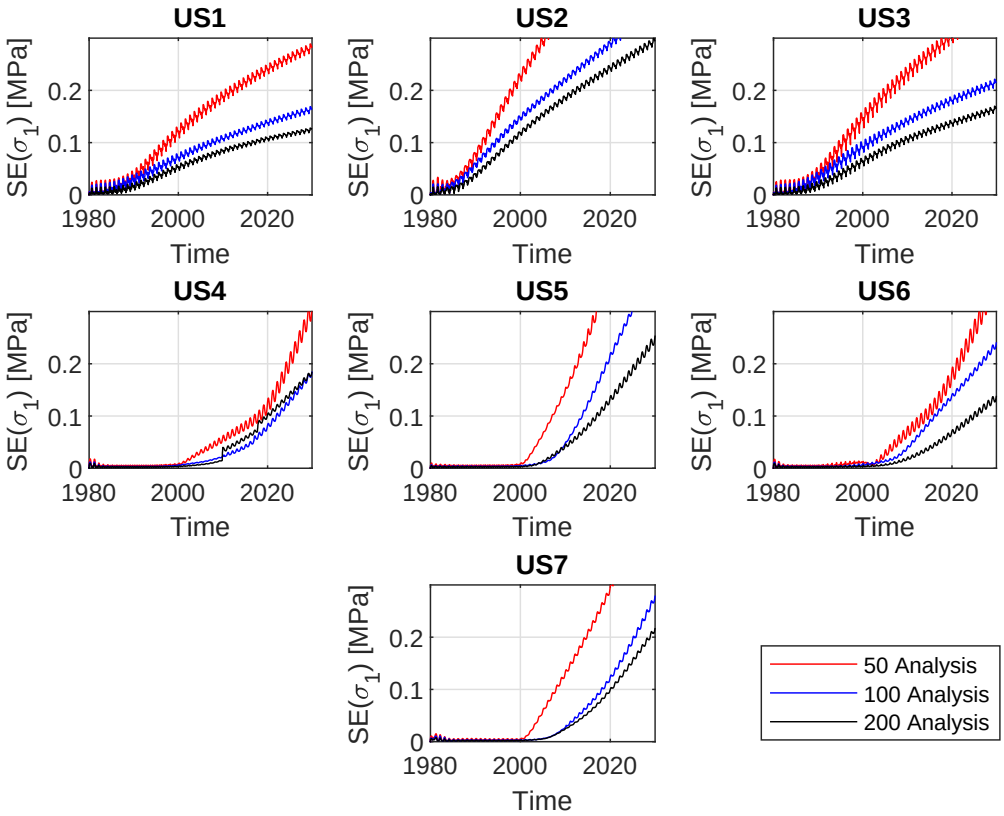

Figure 10.22: Standard Deviation; Upstream

Chapter 11

Seismic Analyses Results

11.1 Intensifying Artificial Acceleration

For the purpose of seismic analysis, three sets of intensifying artificial accelerations (IAAs) are selected and applied horizontally to the dam in the stream direction which are shown in Figure 11.1 along with the their envelopes demonstrating the peak ground acceleration up to each equivalent time. Though, the three IAA envelopes are relatively close to each other, as seen in the last plot of this figure, the selection of three records will allow for the considerations of curve to curve variability of the IAAs.

To facilitate further understanding of the selected IAAs, the acceleration response spectra at 4 different times of the analysis for all three IAAs are plotted in figure 11.2. As seen, there is a corresponding response spectrum to each equivalent time of the analysis for every IAA. As a matter of fact, as the equivalent time increases the response spectrum shifts to higher S_a values maintaining the overall shape of the spectrum.

Using the USGS hazard tool, a target response spectrum is determined for each of the three return periods of 2475, 975 and 475 years which are shown as the red smoothed curves in figure 11.2 and are referred to as "target" response spectra. While various methods may be used to match the matching IAA response spectra to the target one, two methods are represented in this study. One method is to simply match the PGAs (figure 11.3). The other method is to step further to match the spectral acceleration in the shaded area ranging from $0.2T1$ up to $1.5T1$, where $T1$ is fundamental period of the dam as shown in figure 11.4. Based on these two methods, for the

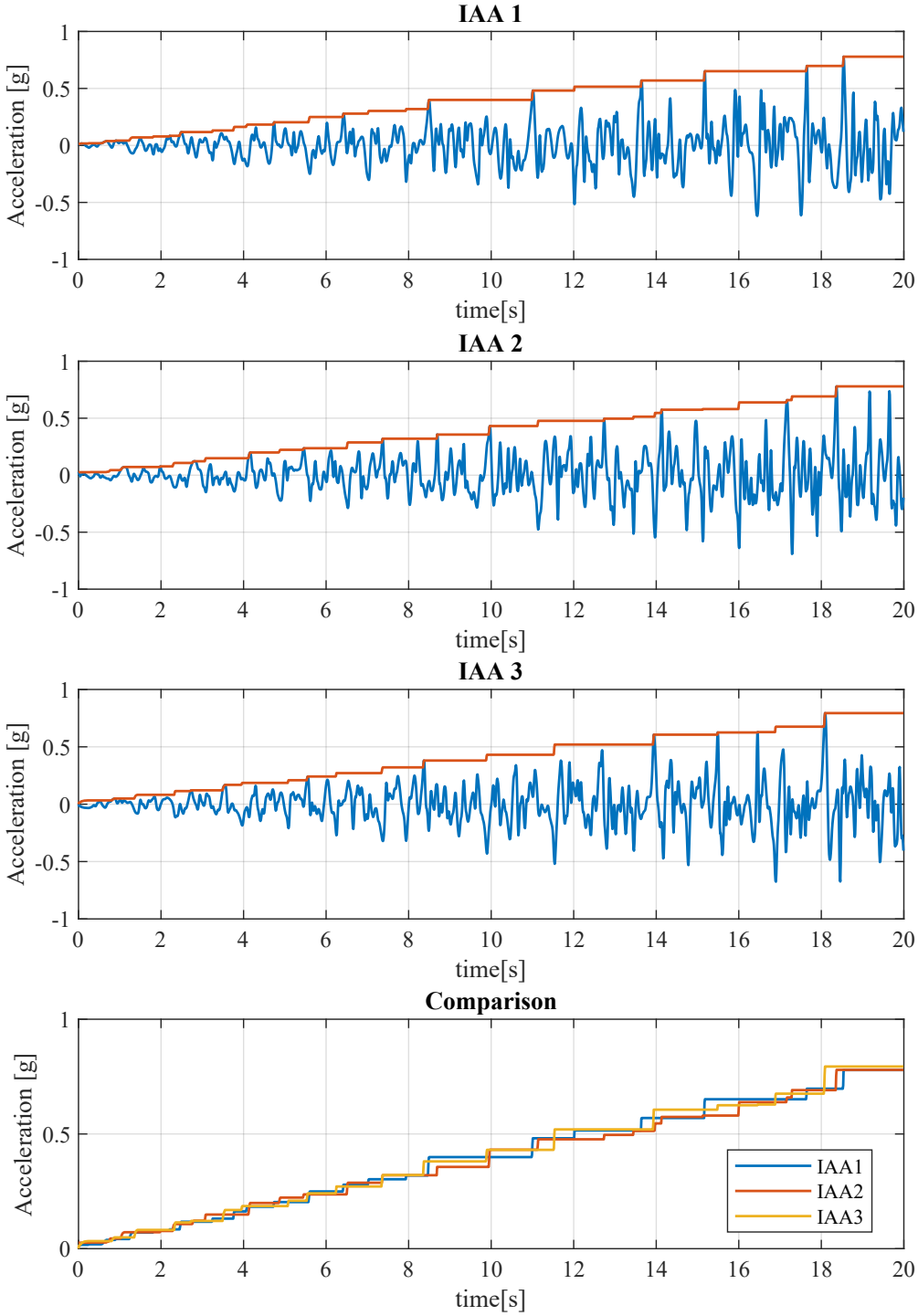

Figure 11.1: Intensifying Artificial Accelerations

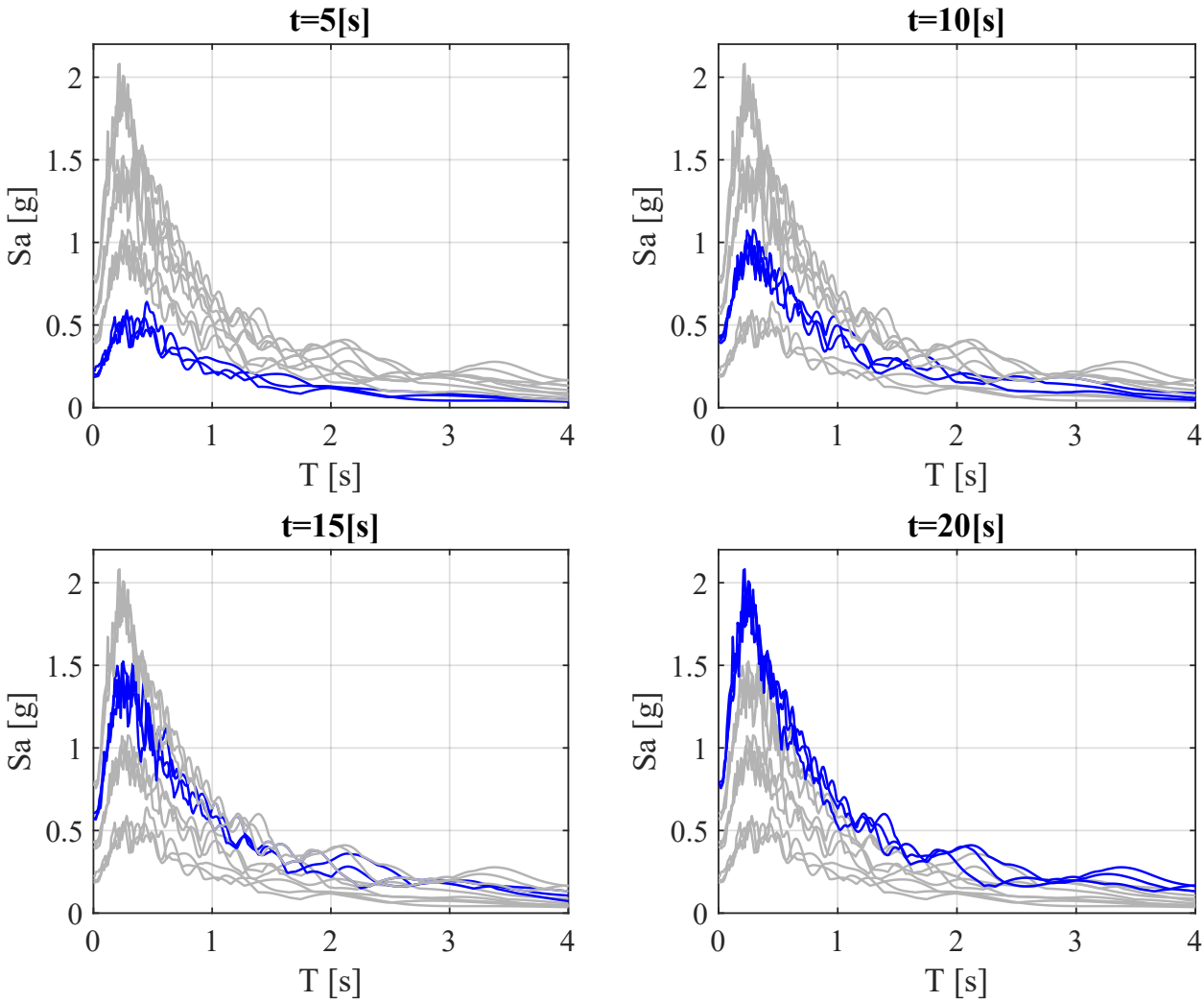

Figure 11.2: Intensifying artificial accelerations response spectra at different analysis equivalent times

interpretation purposes, all of the figures in this chapter are presented in terms of both PGA and $S_a(T1)$.

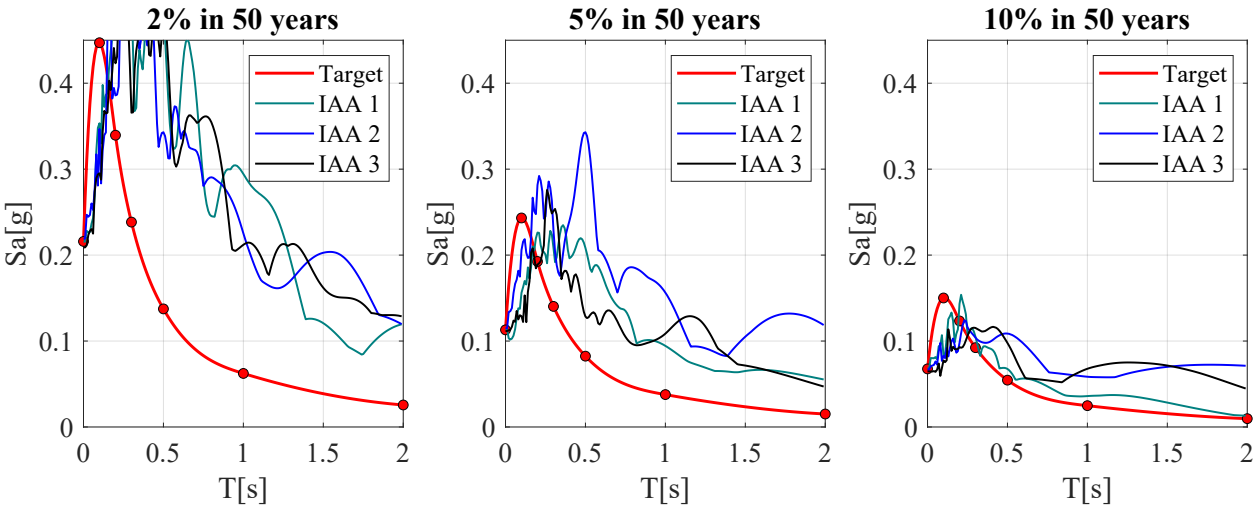

Figure 11.3: Matching PGA for different return periods

11.2 Seismic Analyses Results

Different assumptions in considering the effect of soil-structure interaction will result in drastic differences in the results of seismic analysis. Therefore, for the comparison purposes, three different types of boundaries were considered which are as follows:

- No Boundaries; The acceleration applied at the base of the foundation with no dashpots at the boundaries
- Absorbing Boundaries; Dashpots are used at the four sides and below the dam foundation
- Free-Field; Dashpots are defined similar to the previous model and in addition to that the effect of surrounding free field is considered on the sides.

A summary of the performed analysis and the presented results are shown in figure 11.5. Three IAAs are applied to each of the three SSI assumptions once after 50 years of AAR analysis and another time prior to the start of AAR. The response of the dam is illustrated in terms of crest horizontal and vertical displacements, joint opening displacements as well as maximum principal

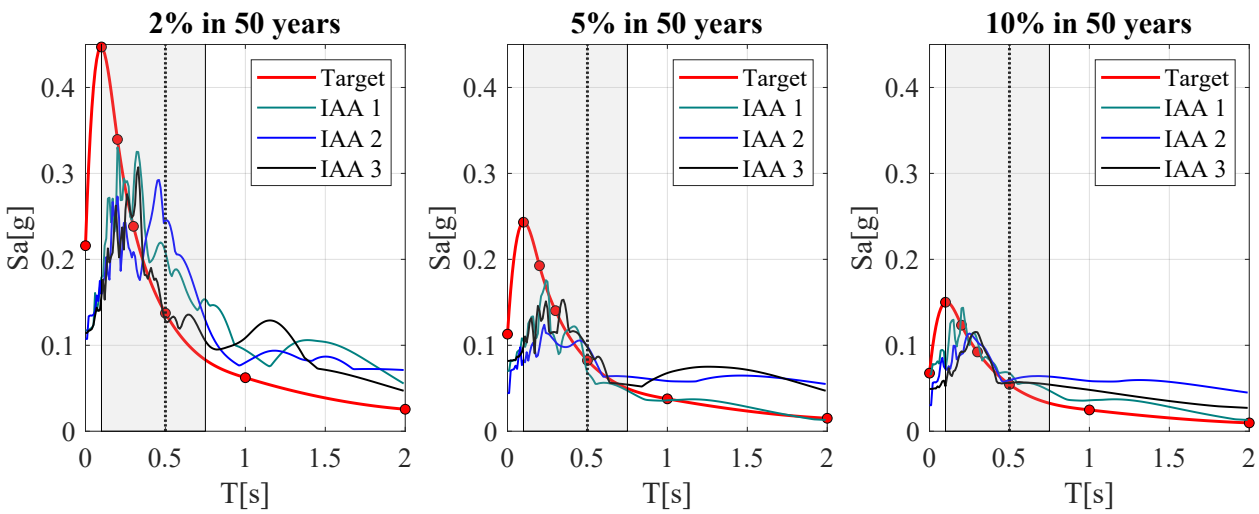

Figure 11.4: Matching acceleration response spectra in [0.2T,1.5T] for different return periods

stresses at several points on the dam upstream and downstream faces. In the first section the responses of the AAR- affected dam is compared with it's sound counterpart model. Then in the next section, responses are compared for the three SSI models with and without AAR separately, to compare the effect of SSI modeling assumptions.

11.2.1 Seismic Response of the Dam; Effect of AAR

Since modeling the soil-structure interaction is as essential step to the dynamic analysis of dams, the most advanced model among the three that are compared in this study is used to compare the effect of AAR on the seismic response of the case study dam and results are presented in this section. Figure 11.6 is showing the recorded crest displacements at the center of the crown cantilever during the dynamic analysis for both with and without AAR cases. As shown in the AAR static analysis results, in the previous chapters, the dam experiences about 24 cm in horizontal and 20 cm in vertical crest displacements due to AAR expansion and therefore the dynamic displacements start at an offset on the y axis compared to the without AAR case. It is shown through the envelope of the displacements that the dam can experience close to 50cm in horizontal displacements at the analysis equivalent time of 20 seconds. Figure 11.7 can provide a better understanding of the ground motion intensity that can cause such high amounts of displacements to the dam. In this figure the horizontal and vertical displacements are plotted against PGA and $S_a(T1)$ suggesting that in order for the dam to experience the above mentioned maximum displacements a ground motion with a PGA of 0.8g or $S_a(T1)$ of about 1.4g should hit the structure. It is more realistic to look at the PGA and $S_a(T1)$ of the dam determined from probabilistic seismic hazard analysis (PSHA) of the dam site for different return periods (figures 11.3 and 11.4). Based on these figures the $S_a(T1)$ is considered to be 0.14g, 0.09g and 0.06g and the PGAs to be 0.22g, 0.11g and 0.067g for the three return periods, respectively. As such considering the PGA as an intensity measure, the top left plot in figure 11.7 suggests that a ground motion with the return period of 2475 years will result in about 31cm of horizontal displacements in the AAR-affected dam while this amount in its sound counterpart (blue curve) is about 7cm. These displacements are translated into drift

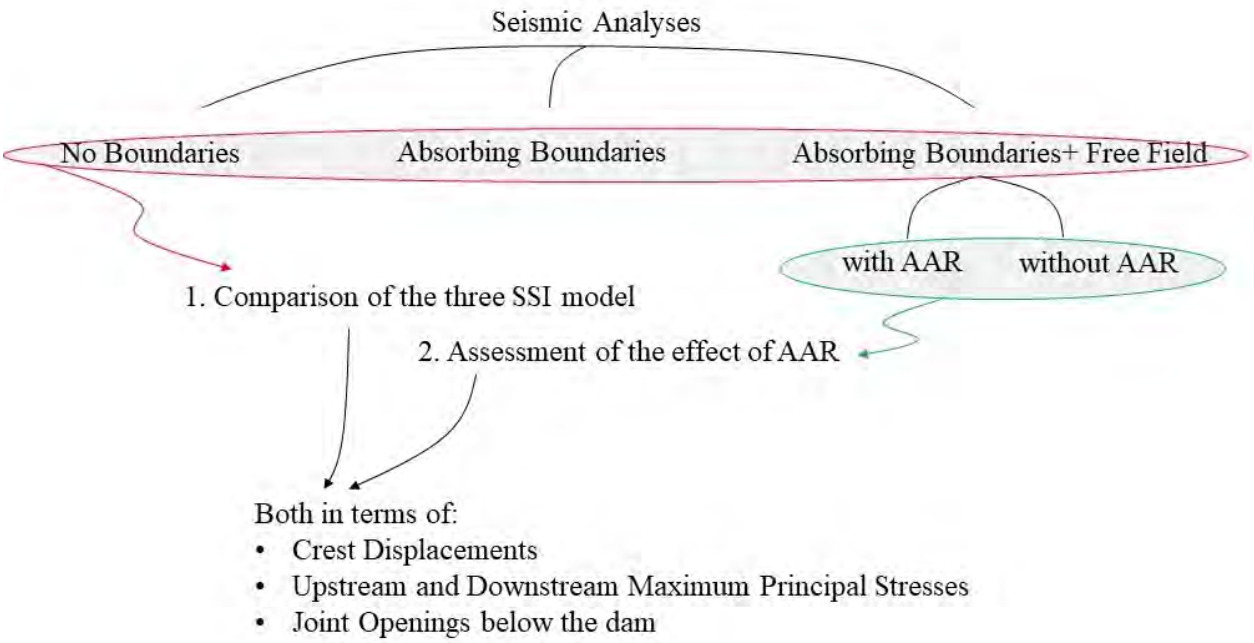

Figure 11.5: Different types of analyses

ratios of about 0.4% and 0.095% for the two cases, respectively. On the other hand, considering the $S_a(T1)$ as the intensity measure which provides a more realistic response compared to PGA, suggests about 26 cm (drift ratio equal to 0.3%) and 6 cm (drift ratio equal to 0.08%) in horizontal displacements for the AAR affected dam and its sound counterpart, respectively.

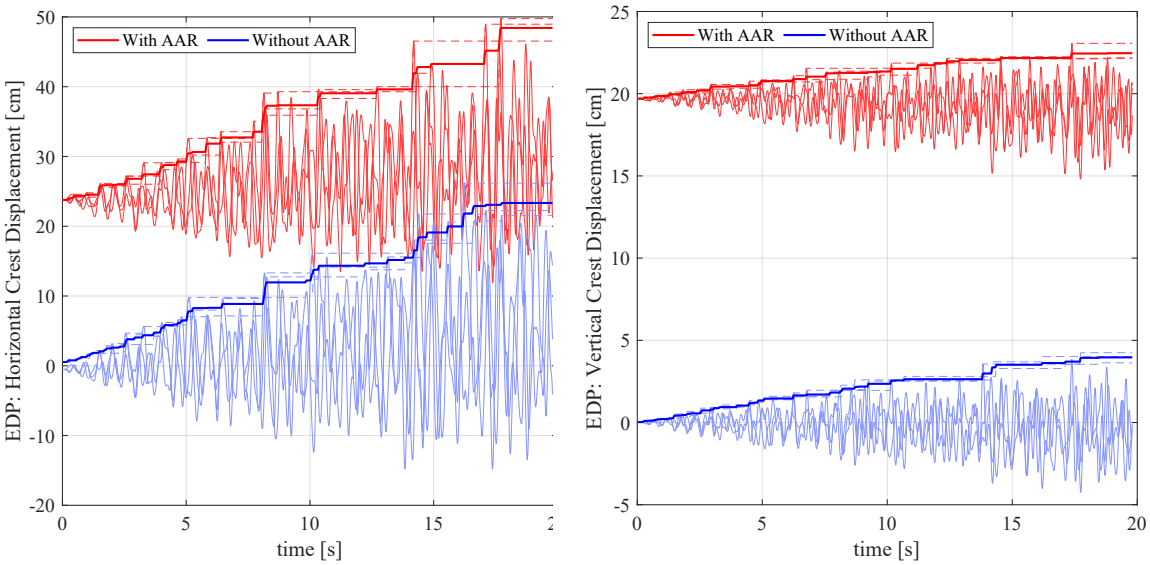

(a) Stream Direction (b) Vertical direction

Figure 11.6: Comparison of crest displacement with and without AAR for Free field model with respect to analysis time

Figure 11.8 is comparing the joint opening below the dam at the dam toe and heel. As shown, that at the studied intensity levels the joint opening is rather small and the thus uncontrolled release of water may not be a reason for concern.

Figures 11.9 and 11.10 illustrate the maximum principal stresses in the upstream and downstream sides of the dam comparing the with and without AAR cases. In this figure each row corresponds to a specific height of the dam body, the top one showing the stresses at the crest level. The two horizontal dashed lines in these figures show the threshold of concrete tensile strength and two times this value. It can be seen that the tensile stresses in the AAR affected dam has already passed the two thresholds before the start of the dynamic analysis.

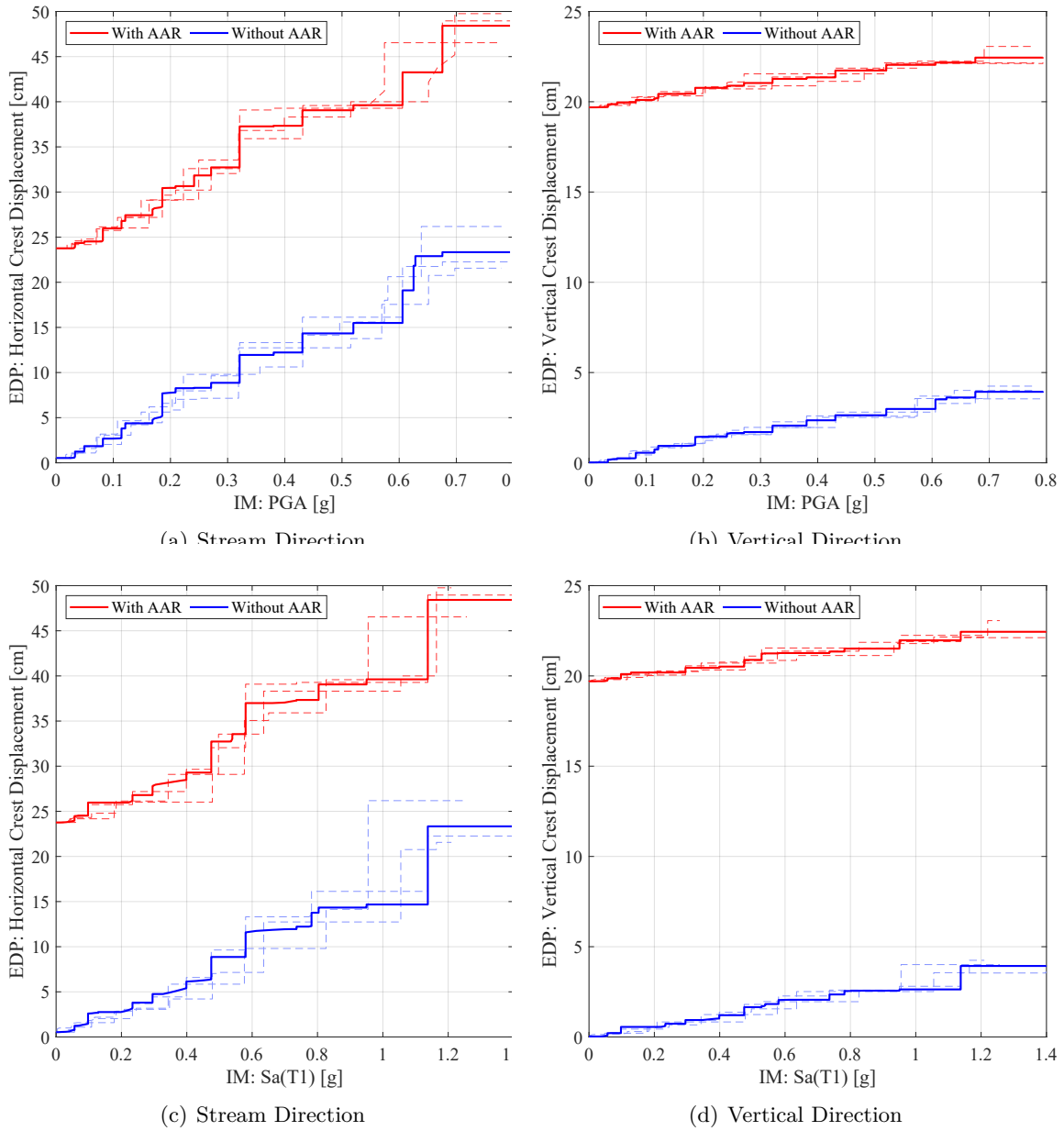

(a) Stream Direction (b) Vertical Direction

(c) Stream Direction (d) Vertical Direction

Figure 11.7: Comparison of Crest Displacements with and without AAR for Free field model with respect to PGA and Sa(T1)

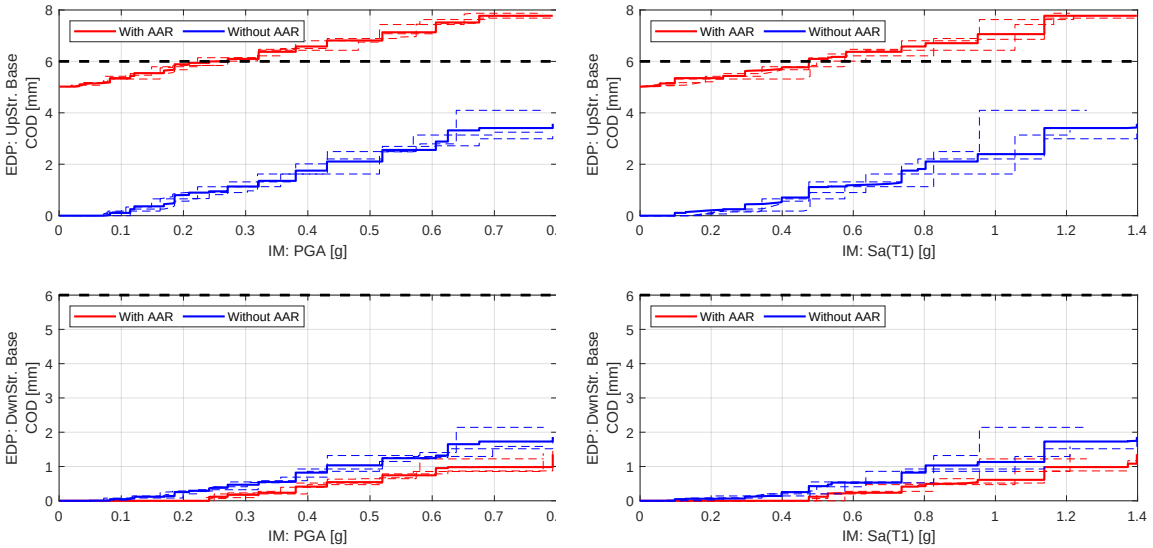

Figure 11.8: Comparison of joint opening displacement with and without AAR for Free field model versus PGA and Sa(T1)

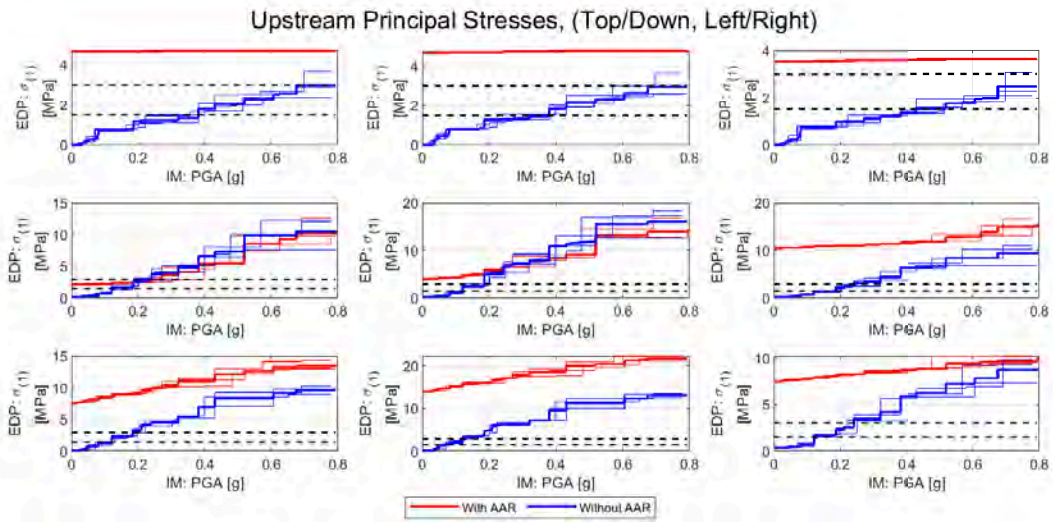

(a) Upstream

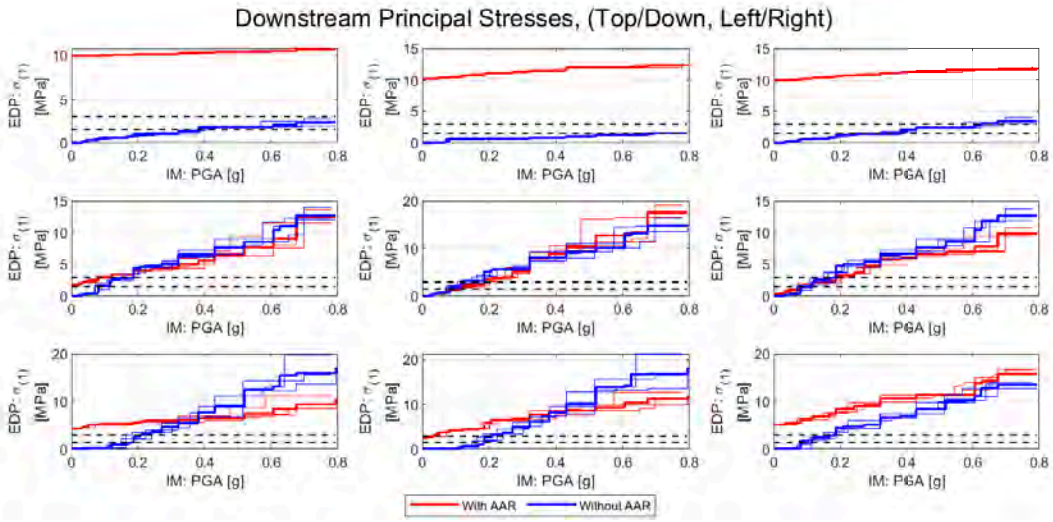

(b) Downstream

Figure 11.9: Comparison of maximum principal with and without AAR for Free field model with respect to PGA

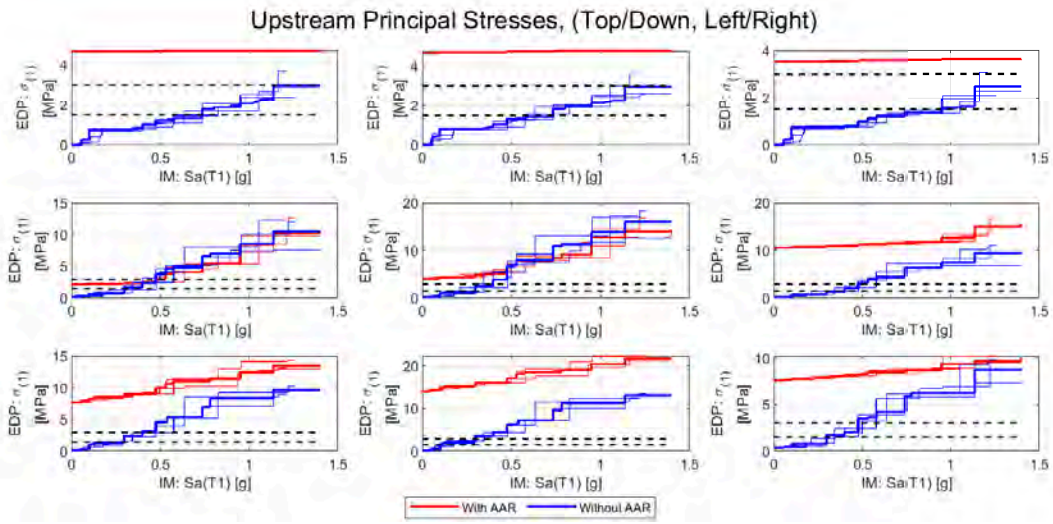

(a) Upstream

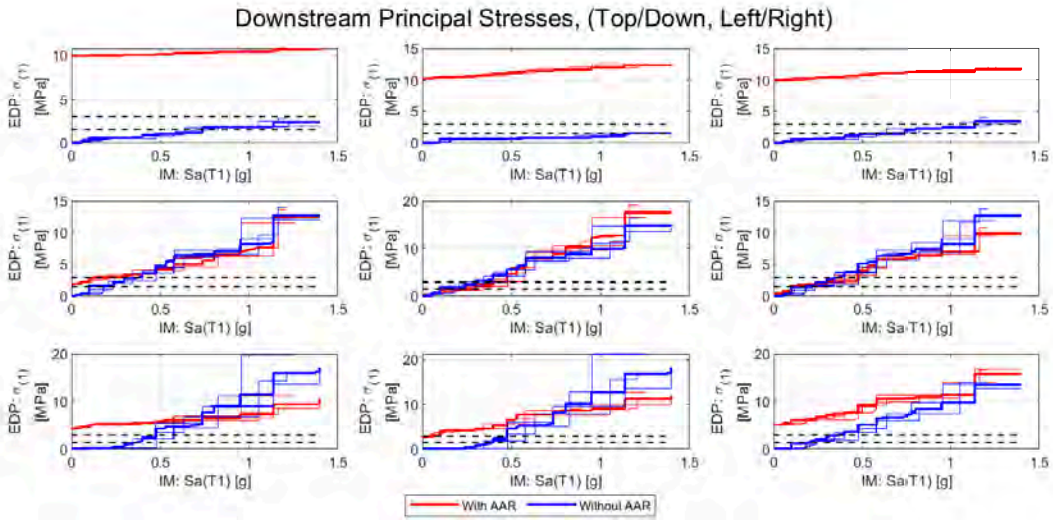

(b) Downstream

Figure 11.10: Comparison of maximum principal with and without AAR for Free field model with respect to Sa(T1)

11.2.2 Comparison of Different SSI Models

In the following section the results from the three different dam-foundation modeling assumptions are compared once for sound condition dam and another time for AAR affected dam. It is worth noting that for the interpretation purposes all of the responses are plotted against the two discussed intensity measure.

While the crest displacements with respect to the analysis equivalent time is shown in figure 11.11, and 11.16, the plots in figure 11.12 can provide a better understanding of the differences in terms of PGA and $S_a(T1)$. It is shown that the massless foundation with no consideration of absorbing boundaries provides highly overestimated responses in terms of displacements compared to the other two models. While using dashpots to absorb the outgoing waves will also result in unrealistically lower displacements. Similar observations are made by looking at the displacements of AAR-affected dam in figure 11.17.

Figure 11.13 and, 11.18 shows that at the dam heel after exceeding a certain intensity level, the free field model results in higher joint opening displacements than the two other models.

However, the maximum principal stress plots shown in figure 11.14, 11.15 and 11.19, 11.20 show that the free field model stresses especially at the crest level are considerably higher than the two other cases. This observation underlines the importance of considering the effect of the free field motion on the dam-foundation system. It is worth noting that all of the above observations are made specific for the case study dam and may not apply to other dams.

11.2.3 Dam Deformed Shape

Figure 11.21 and 11.22 show the AAR affected dam deformations at various equivalent analysis times. As seen, at intensity levels of interest which correspond to figure 11.21, there are small joint openings at the crest in contraction joints, while more openings are observed at the dam-rock interface joints. However, figure 11.22 shows that at the very high intensity levels (i.e. towards the end of the analysis equivalent time), the cantilevers may start moving independent of each other

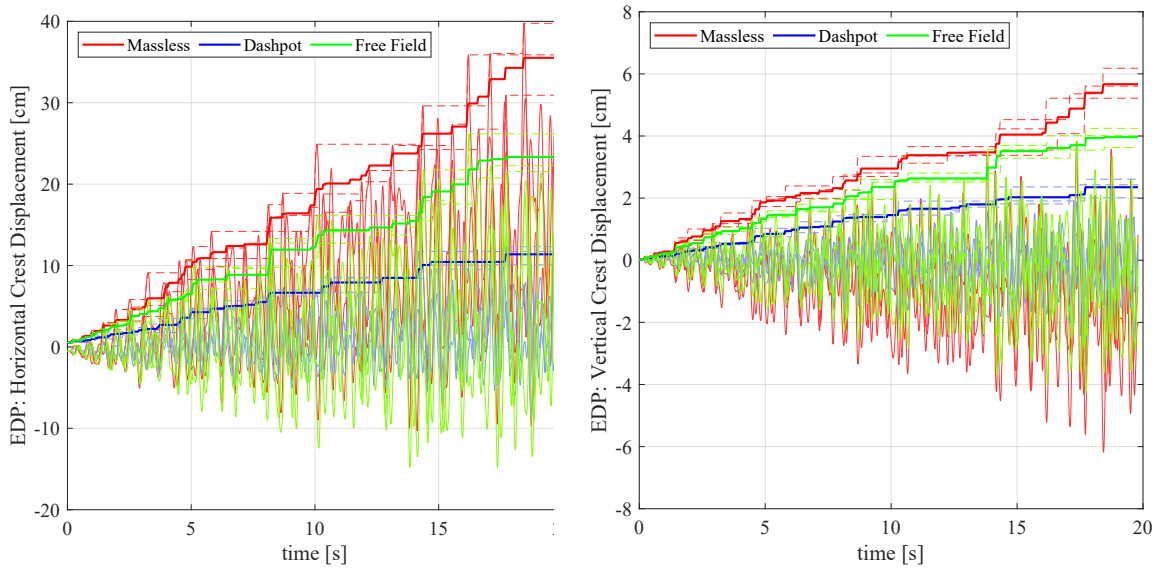

(a) Stream Direction

(b) Vertical direction

Figure 11.11: Comparison of crest displacement without AAR for three SSI models with respect to analysis time

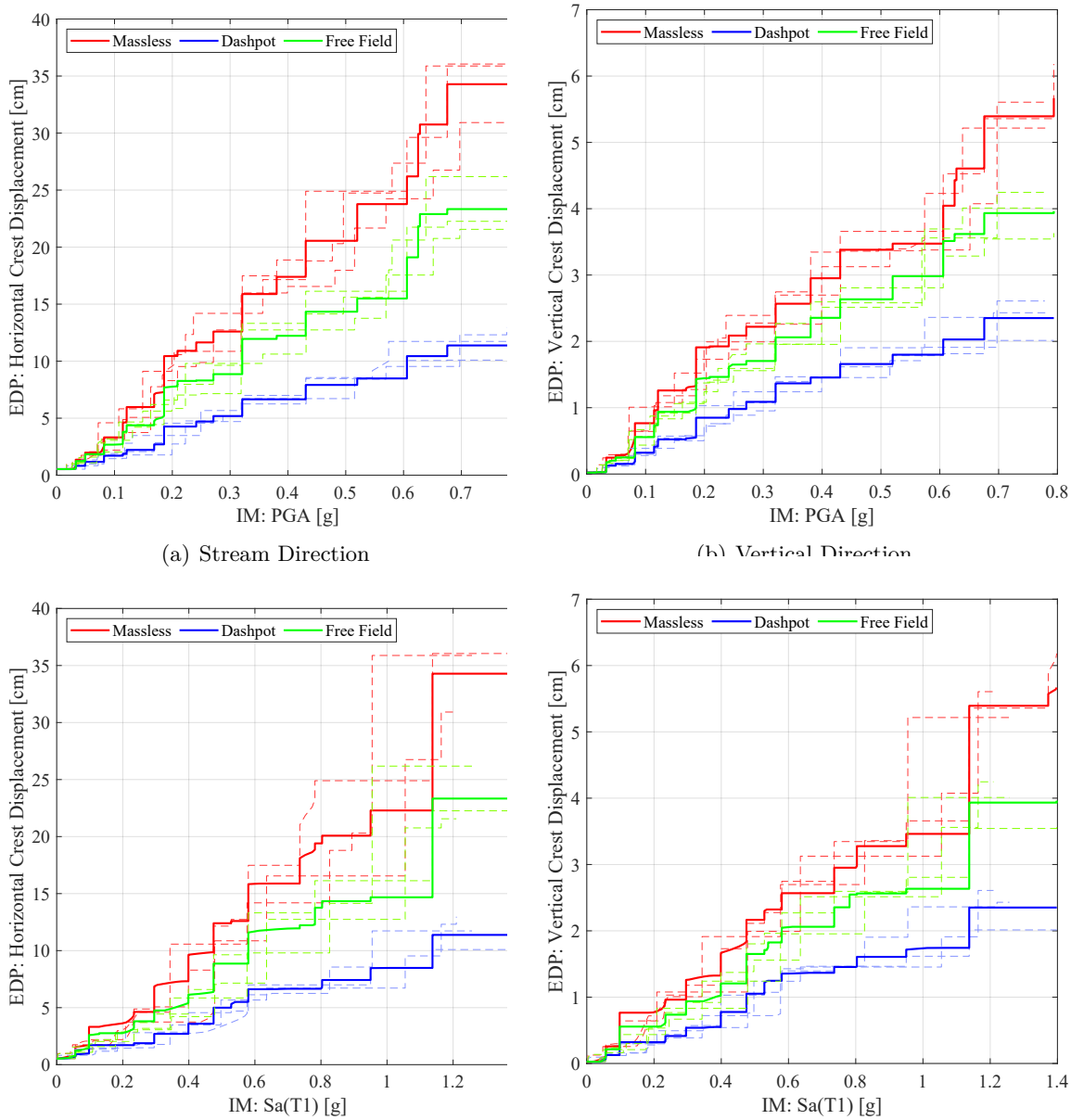

(a) Stream Direction

(b) Vertical Direction

(c) Stream Direction

(d) Vertical Direction

Figure 11.12: Comparison of Crest Displacements without AAR for three SSI models versus PGA and Sa(T1)

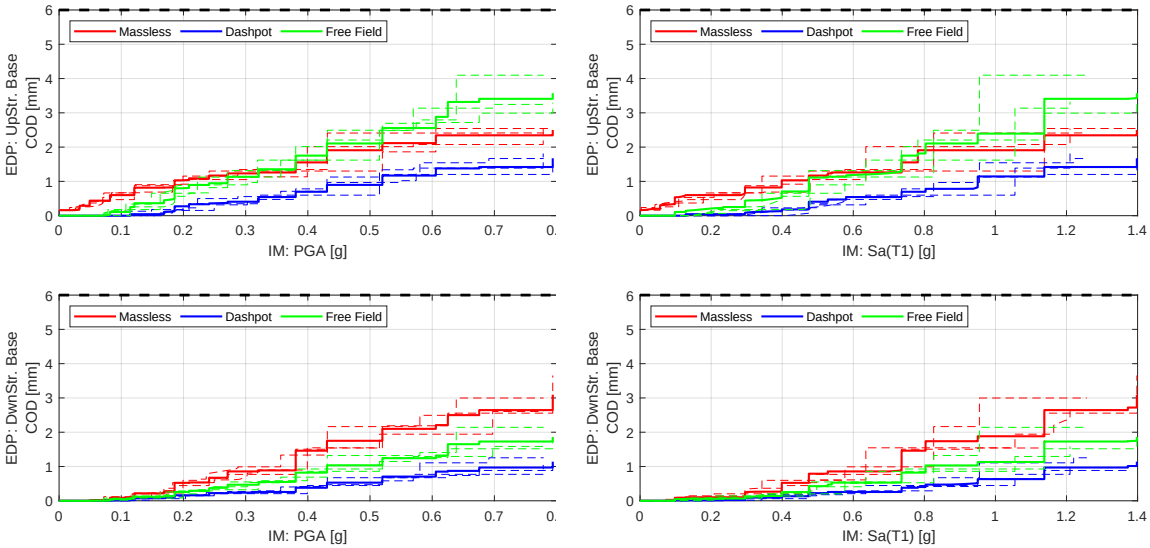

Figure 11.13: Comparison of joint opening displacement without AAR for three SSI models versus PGA and Sa(T1)

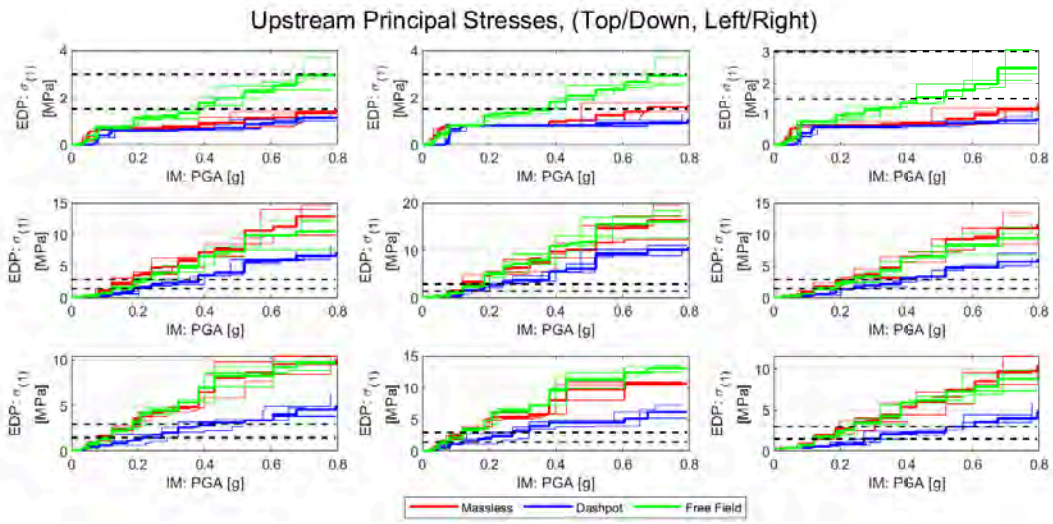

(a) Upstream

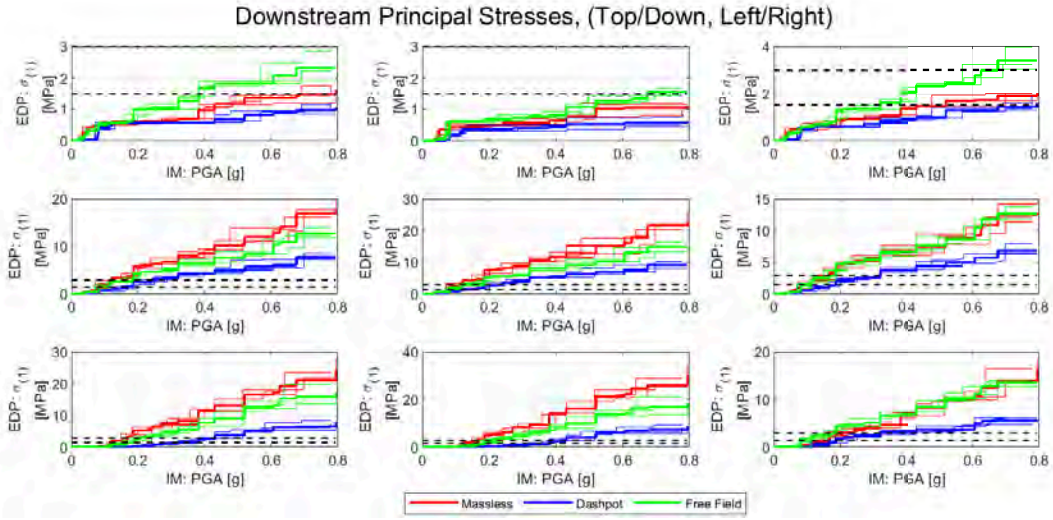

(b) Downstream

Figure 11.14: Comparison of maximum principal stresses without AAR for three SSI model with respect to PGA

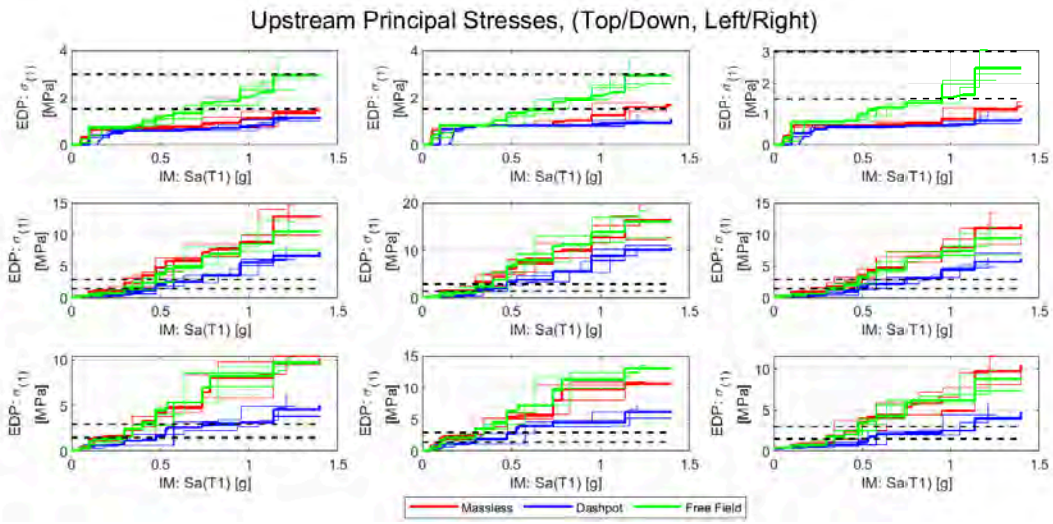

(a) Upstream

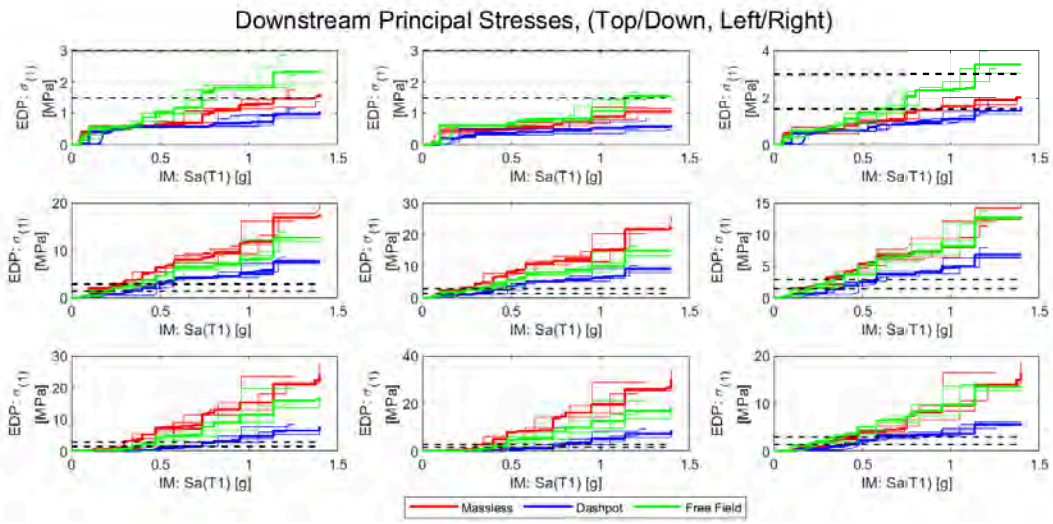

(b) Downstream

Figure 11.15: Comparison of maximum principal stresses without AAR for three SSI models with respect to Sa(T1)

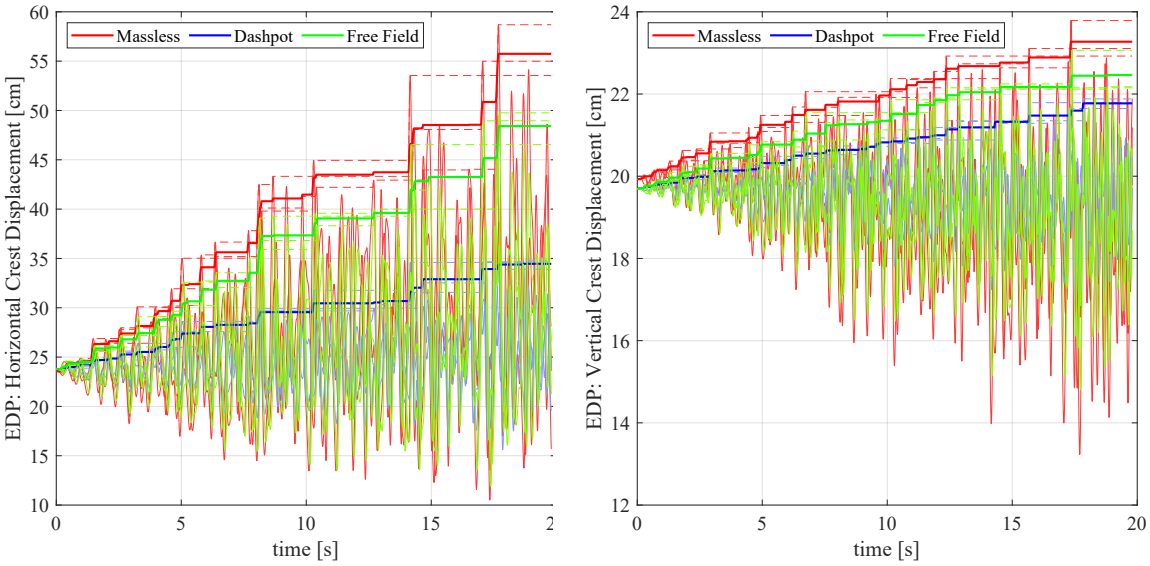

(a) Stream Direction

(b) Vertical direction

Figure 11.16: Comparison of crest displacement with AAR for three SSI models with respect to analysis time

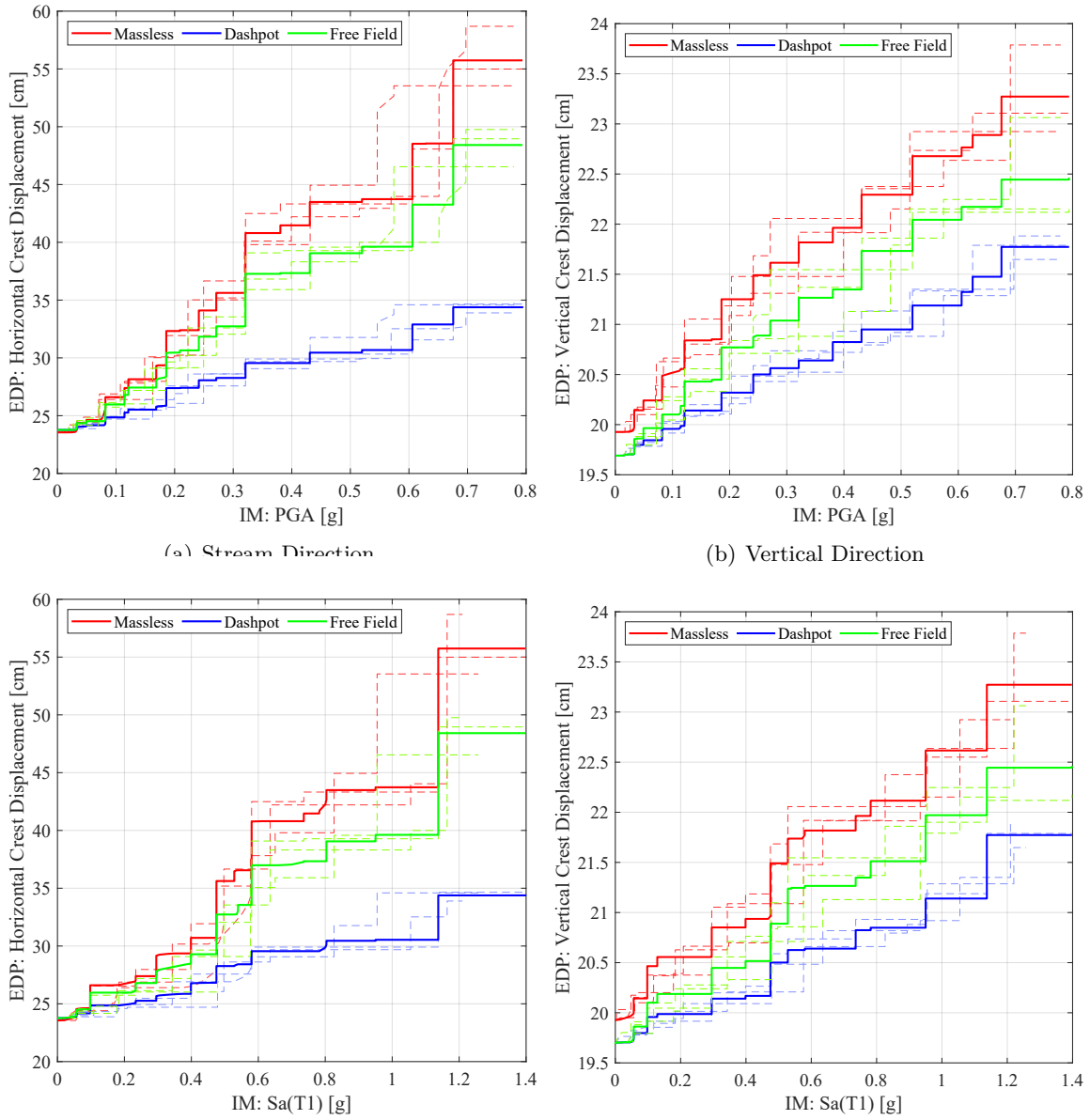

(a) Stream Direction

(b) Vertical Direction

(c) Stream Direction

(d) Vertical Direction

Figure 11.17: Comparison of Crest Displacements with AAR for three SSI models versus PGA and Sa(T1)

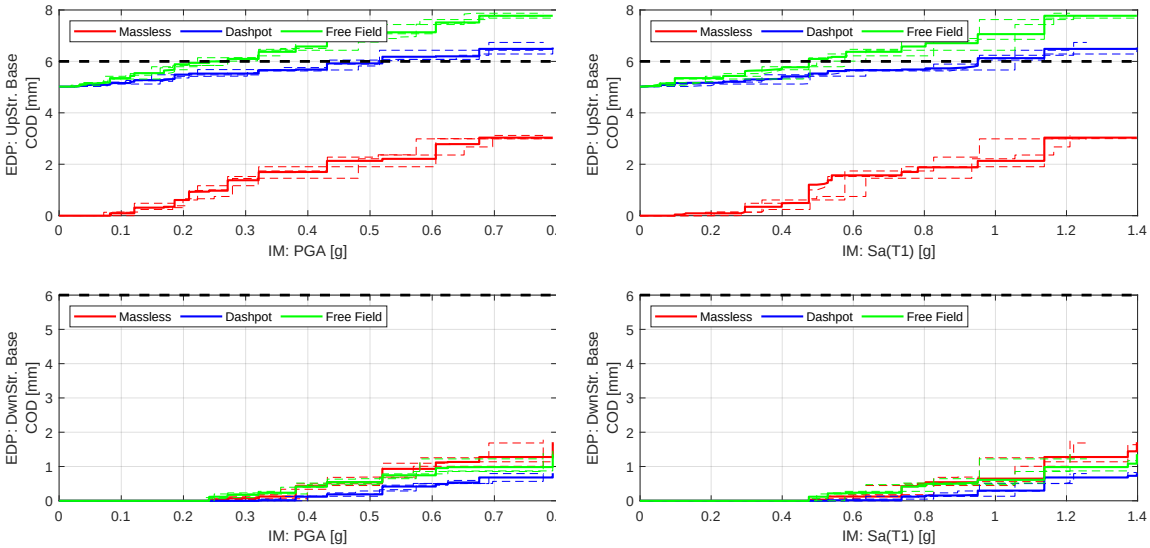

Figure 11.18: Comparison of joint opening displacement with AAR for three SSI models versus PGA and Sa(T1)

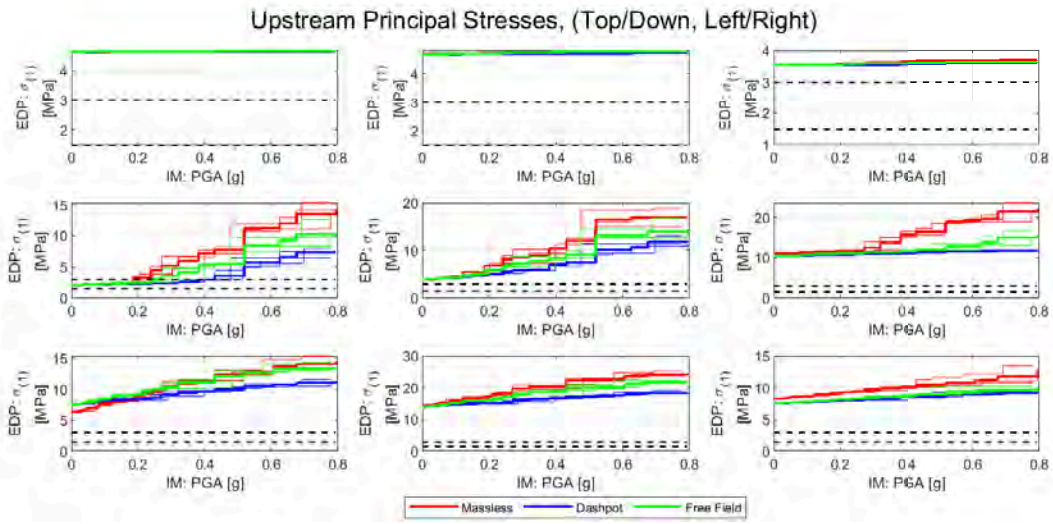

(a) Upstream

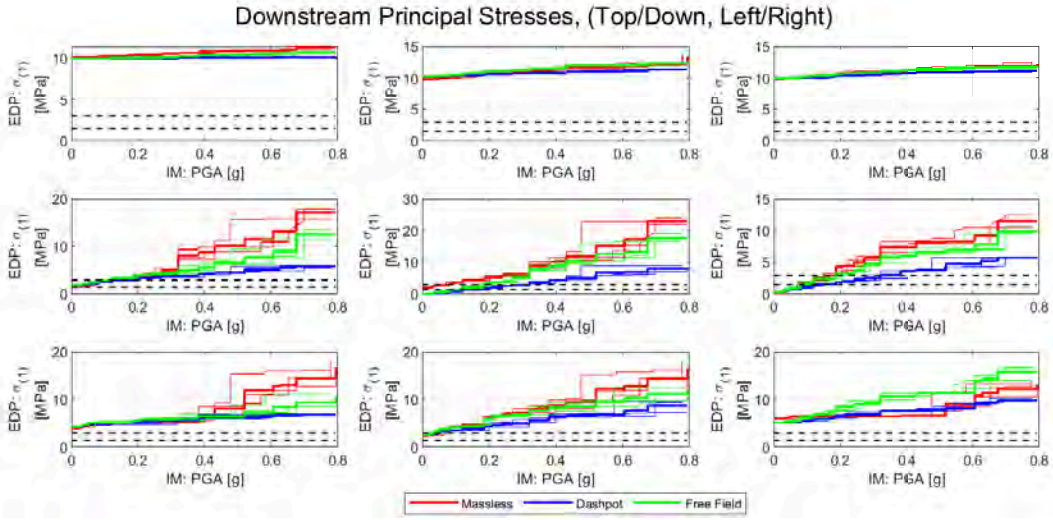

(b) Downstream

Figure 11.19: Comparison of maximum principal stresses with AAR for three SSI model with respect to PGA

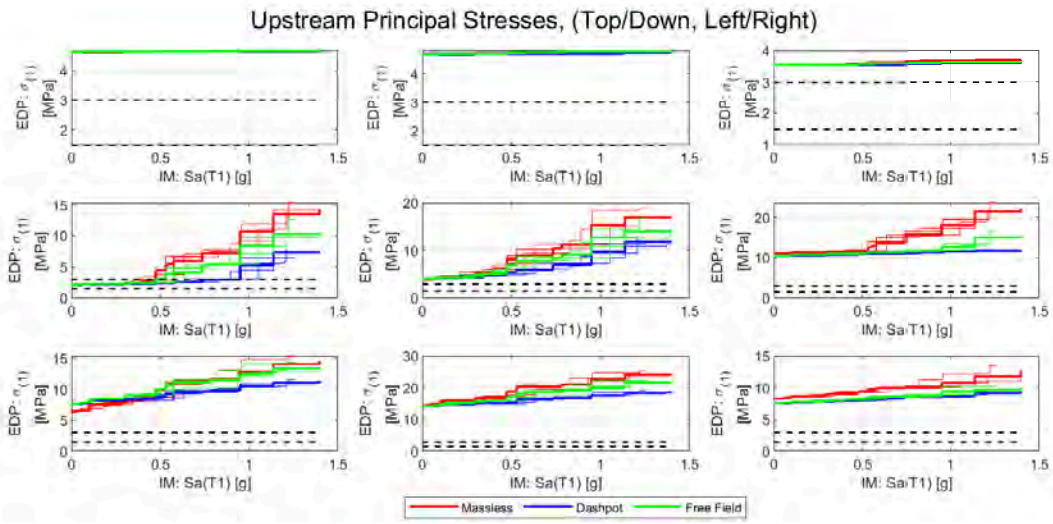

(a) Upstream

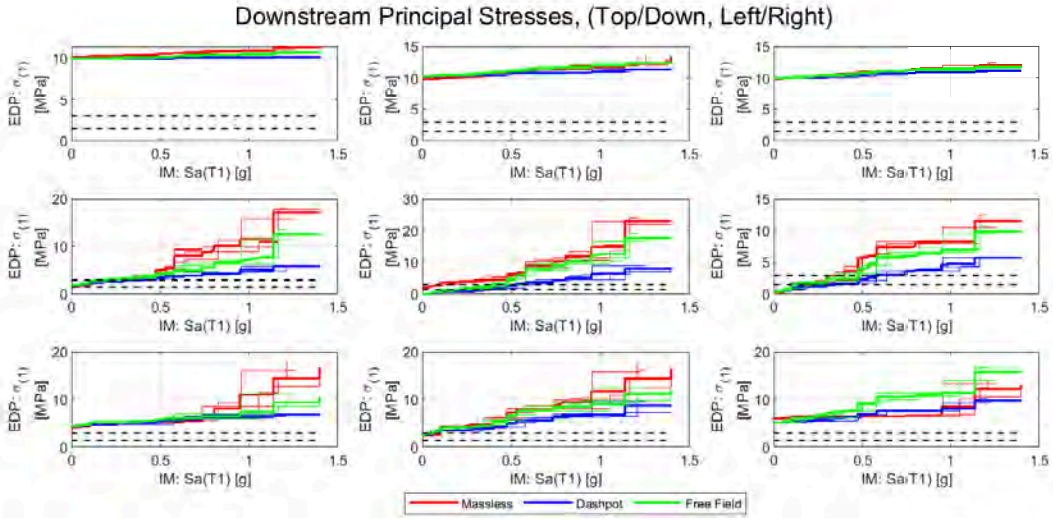

(b) Downstream

Figure 11.20: Comparison of maximum principal stresses with AAR for three SSI models with respect to Sa(T1)

resulting in the loss of arch effect.

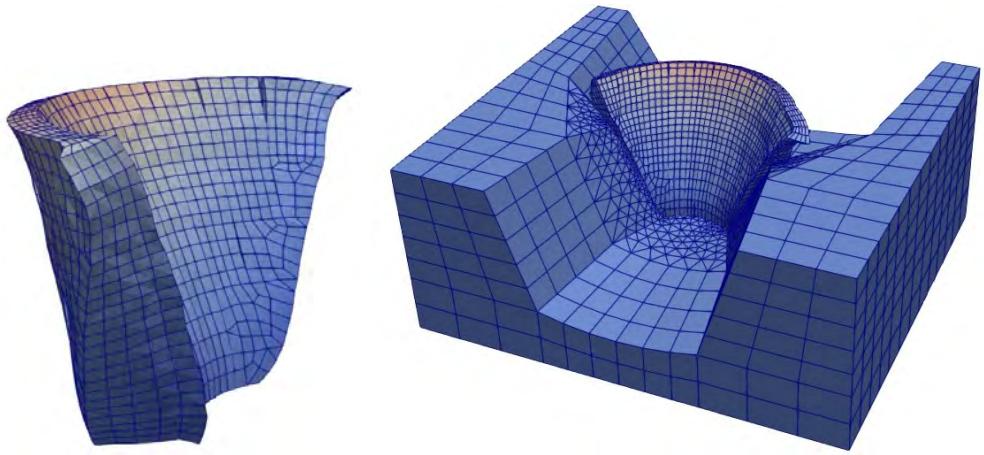

(a) t=3 second

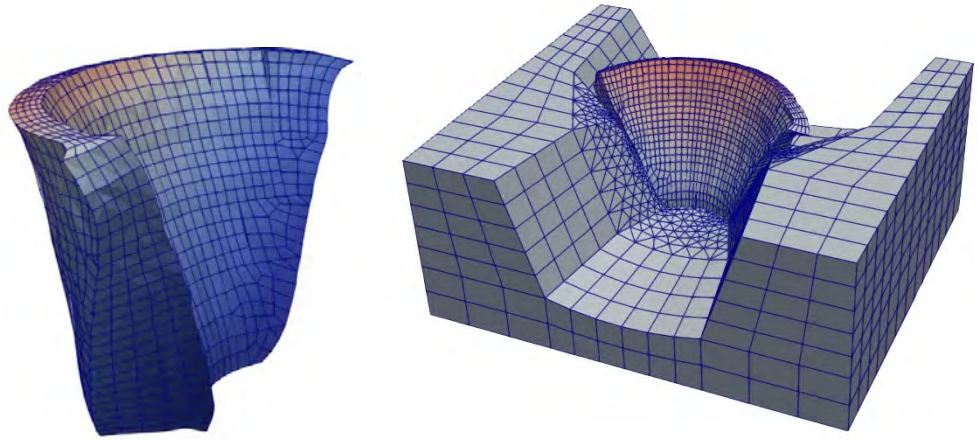

(b) t=5 second

Figure 11.21: Comparison of Dam deformed shape at 3 and 5 seconds of equivalent time

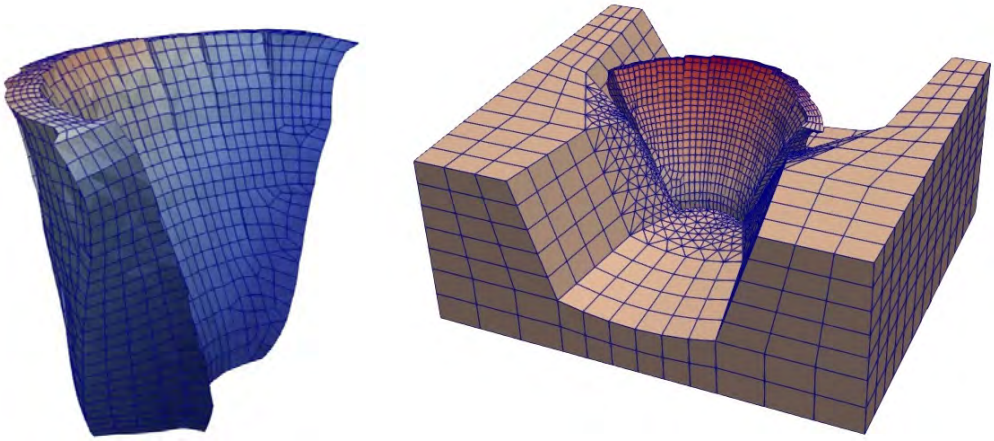

(a) t=10 second

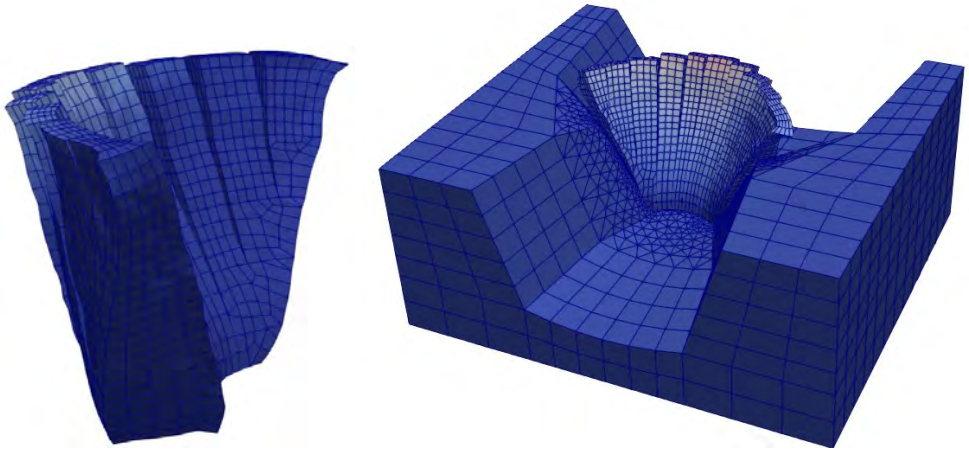

(b) t=20 second

Figure 11.22: Comparison of Dam deformed shape at 10 and 20 seconds of equivalent time

Chapter 12

Conclusion and Recommendation for Future Work

Abstract

This final chapter will, very succinctly, summarize the findings of this research and make few recommendations for future work.

12.1 Conclusion

As discussed in the previous chapters from a deterministic nonlinear AAR analysis it can be concluded that:

- The cracking is mostly occurred on the lower portion and inside the dam.
- In general there is more AAR at the downstream side of the dam compared to the upstream.
- Downstream side of the dam is more in tension which can be an indicative of potential cracking.

The findings of the uncertainty quantification can be summarized as follows:

- Stresses : Mean values of the normalized stresses with respect to the tensile strength on the downstream and upstream sides indicate that there is a possibility of cracking occur:
  - at the top center and right side of the downstream starting about year 2005
  - at the top left side of the downstream starting about year 2015
  - at the mid height right side of the downstream starting about year 2020
  - at the mid height left side of the downstream starting about year 2020

while it wouldn't be a concern at other heights of the center of the dam on the downstream.

  * at the top right side of the upstream starting about year 2020
  * at the top left side of the upstream starting about year 2015
  * at the top center of the upstream starting about year 2000

  while the stresses are lower than our concerning limit in the mid-height and bottom of the upstream.

- Probability of Exceedance
  * The probability of exceednace of the maximum principal stress (σ_1) from the concrete tensile strength can be interpreted as a possibility of cracking at a certain point. As seen the 50% probability of exceedance at the top mid portion of the dam happens after about 30 years of analysis (year 2010) on the downstream and after 20 years of analysis (year 2000) on the upstream. Overall, the stress values have higher probability of exceeding the threshold on the upstream compared to downstream at the top of the dam. However, the mid-height of the dam is showing a higher probability of exceedance on the downstream side while on the upstream side the 50 % probability of exceednace is likely to occur around 70 years of analysis(year 2050)
- Effect of Sample size
  * The number of analysis chosen for the uncertainty quantification has to be determined to be a good representative of the true data. To this aim, the uncertainty quantification has been repeated with 3 different sample sizes of 50, 100 and 150 analyses. The comparison of the results from the 3 samples indicate that the 100 analyses sample can provide a relatively better estimation compared to the 50 analyses sample however this improvement is not as significant when it comes to the comparison of the 200 and 100 analyses samples. As seen in figure 10.20 the T3B and T3A horizontal displacement have standard error of about 2.5 mm at the end of the analysis time which can be even more reduced by increasing the number of analyses.

∗ Comparing standard errors for stress (figures 10.21 and 10.22) shows that the 200 analyses sample is slighlty better than the 100 and thus increasing the number of analysis will not probably improve the accuracy of the model.

12.2 Recommendation for Future work

- Horizontal joints
- Laboratory Data for AAR compatible with finite element analysis
- Reliable field measurement of water temperature from top to bottom
- Field measurements of *in-situ* stresses
- Seismic fragility curve
- Complete detailed risk assessment, Fig. 12.1
- Uncertainty quantification with nonlinear analysis (though this may require extensive computational support).
- Add downstream tensile stresses to the list of parameters that have to be reconciled between analysis and field cracking observations.

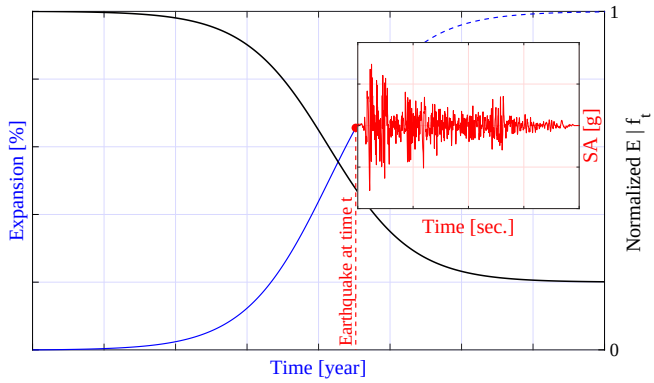

Figure 12.1: Earthquake occurring after substantial AAR expansion

Bibliography

Ake, J., J. Pires, and C. Munson (2015). "Current and Future Application of Seismic Research Activities at the NRC in Response to the Accident at the Fukushima Dai-ichi Nuclear Power Plant". In: **International Experts Meeting on Strengthening Research and Development Effectiveness in the Light of the Accident at the Fukushima Daiichi Nuclear Power Plant**. Last Retrieved, June 2016. Vienna, Austria.

Alembagheri, Mohammad (2019). "A study on structural safety of concrete arch dams during construction and operation phases". In: **Geotechnical and Geological Engineering** 37.2, pp. 571–591.

Amberg, F, R Stucchi, and N Brizzo (2013). "The effect of temperature on the development of the Alkali Aggregate Reaction at the Pian Telessio dam". In: **9th ICOLD European Club Symposium**.

Ardito, Raffaele, G Maier, and G Massalongo (2008). "Diagnostic analysis of concrete dams based on seasonal hydrostatic loading". In: **Engineering Structures** 30.11, pp. 3176–3185.

Arrhenius, S. (1889). "On the Reaction Velocity of the Inversion of Cane Sugar by Acids". In: **Zeitschrift für physikalische Chemie** 4, p. 226.

Baker, Jack W (2015). "Efficient analytical fragility function fitting using dynamic structural analysis". In: **Earthquake Spectra** 31.1, pp. 579–599.

Basu, U. (2009). "Explicit finite element perfectly matched layer for transient three-dimensional elastic waves". In: **International Journal for Numerical Methods in Engineering** 77, pp. 151–176.

Basu, U. and A.K. Chopra (2004). "Perfectly Matched Layers for Time-Harmonic Elastodynamics of Unbounded Domains: Theory and Finite Element Implementation". In: **Computer Methods in Applied Mechanics and Engineering** 192, pp. 1337–1375.

Bažant, Ž., G. Zi, and C. Meyer (2000). "Fracture Mechanics of AAR in Concretes with Waste Glass Particles of Different Sizes". In: **J. of Engineering Mechanics, ASCE** 126.3, pp. 226–232.

Ben-Ftima, M., H. Sadouki, and E. Bruhwiler (2016). "Development of a computational multi-physical framework for the use of nonlinear explicit approach in the assessment of concrete structures affected by alklai-aggregate reaction". In: **9th International Conference on Fracture Mechanics of Concrete and Concrete Structures; FraMCoS-9**. Ed. by V.E. Saouma, J. Bolander, and E. Landis. Berkeley, CA.

Ben Haha, M. (2006). "Mechanical effects of alkali silica reaction in concrete studied by SEM-image analysis". Thèse EPFL 3516. PhD thesis. Ecole Polytechnique Federale de Lausanne.

Bielak, J. and P. Christiano (1984). "On the Effective Seismic Input for Non-Linear Soil-Structure Interaction Systems". In: **Earthquake Engineering and Structural Dynamics** 12, pp. 107–119.

Bielak, J. et al. (2001). "Domain Reduction Method for Three Dimensional Earthquake Modeling in Localized Regions, Part I: Theory". In: **Bulletin of Seismological Society of America** 93.2, pp. 817–824.

Blanco, A et al. (2018). "Expansions with different origins in a concrete dam with bridge over spillway". In: **Construction and Building Materials** 163, pp. 861–874.

Bofang, Z and L Zhanmei (1990). "Thermal stress". In: **Arch dams. Rotterdam: Balkema**, pp. 217–25.

Brand, Bruce and Larry K. Nuss (2021). "FAILURE MECHANISM DERIVED ARCH DAM STABILITY EVALUATION". In: **USSD Annual Conference 2021**. United States Society of Dams.

Bureau of Reclamation (1981). **Control of Cracking in Mass Concrete Structures**. Tech. rep. EM34. U.S. Bureau of Reclamation.

Capra, B. and J.P. Bournazel (1998). “Modeling of induced mechanical effects of alkali-aggregate reactions”. In: **Cement and Concrete Research** 28.2, pp. 251–260.

Cervenka, J. and V.K. Papanikolaou (2008). “Three Dimensional Combined Fracture-Plastic Material Model for Concrete”. In: **International Journal of Plasticity** 24.12, pp. 2192–2220.

Charlwood, RG, SV Solymar, and DD Curtis (1992). “A review of alkali aggregate reactions in hydroelectric plants and dams”. In: **Proceedings of the international conference of alkali-aggregate reactions in hydroelectric plants and dams**. Vol. 129.

Chulliat, O., E. Grimal, and E. Bourdarot (2017). “Chambon Dam”. In: **Swelling Concrete in Dams and Hydraulic Structures: DSC 2017**. Ed. by Alain Sellier et al. John Wiley & Sons.

Cima, J. and B. Reinicker (2015). “Concrete Growth at Roanoke Rapis Dam”. In: **Hydro Review**.

Clough, R.W. and Penzien, J. (1993). **Dynamics of Structures**. McGraw-Hill Inc., London, UK.

Comi, C, R Fedele, and U Perego (2009a). “A chemo-thermo-damage model for the analysis of concrete dams affected by alkali-silica reaction”. In: **Mechanics of Materials** 41.3, pp. 210–230.

Comi, C., R. Fedele, and U. Perego (2009b). “A chemo-thermo-damage model for the analysis of concrete dams affected by alkali-silica reaction”. In: **Mechanics of Materials** 41.3, pp. 210 –230.

Comi, Claudia, Beatrice Kirchmayr, and Rossella Pignatelli (2012). “Two-phase damage modeling of concrete affected by alkali–silica reaction under variable temperature and humidity conditions”. In: **International Journal of Solids and Structures** 49.23-24, pp. 3367–3380.

Coubard, G. and J. Sausse (2017). “Swelling Arch Dams with Thrust Blocks”. In: **Swelling Concrete in Dams and Hydraulic Structures: DSC 2017**. Ed. by Alain Sellier et al. John Wiley & Sons.

Cundall, P. A. et al. (1979). “Solution of Infinite Dynamic Problems by Finite Element Modelling in the Time Domain”. In: **Proceedings of the 2nd International Conference on Applied Numerical Modelling**. Pentech Press, pp. 341–351.

Cundall, P.A. et al. (1980). **NEESI Soil Structure Interaction Program for Dynamic and Static Problems**. Tech. rep. 51508-9. Norwegian Geotechnical Institute.

Curtis, D. et al. (2005). "Updated Assessment of Concrete Growth Effects on a TVA Dam". In: **USSD 2005 Conference, Salt Lake City, UT, June**.

Dennis, J.E. and R.B. Schnabel (1983). **Numerical Methods for Unconstrained Optimization and Nonlinear Equations**. Englewood Cliffs.

DOE EnergyPlus^{TM} 9.3.0 (2020). **Input Output Reference**. Tech. rep. U.S. Department of Energy.

Dressel, W.D. (2011). **Digitized data for the BCL3 (vertical), T3A (upstream/downstream and vertical), and T3B (upstream/downstream and vertical)**. email Excel files received 11/10/20.

El Mohandes, F. and F.J. Vecchio (2013). **VecTor3: A. User's Manual; B. Sample Coupled Thermal and Structural Analysis**. Dept. of Civil Engineering, University of Toronto. Toronto, Canada.

Estekanchi, H.E., A. Vafai, and M. Sadeghazar (2004). "Endurance time method for seismic analysis and design of structures". In: **Scientia Iranica** 11, pp. 361–370.

Estekanchi, Homayoon E et al. (2020). "A state-of-knowledge review on the Endurance Time Method". In: **Structures** 27, pp. 2288–2299.

Fairbairn, Eduardo MR et al. (2006). "Modelling the structural behaviour of a dam affected by alkali–silica reaction". In: **International Journal for Numerical Methods in Biomedical Engineering** 22.1, pp. 1–12.

Farage, MCR, JLD Alves, and EMR Fairbairn (2004). "Macroscopic model of concrete subjected to alkali–aggregate reaction". In: **Cement and Concrete Research** 34.3, pp. 495–505.

Ferreira, Anna Paula Guida, Michèle Cristina Resende Farage, and Flávio de Souza Barbosa (2013). "Modelling of the mechanical behavior of concrete affected by alkali-aggregate reaction". In: **Rem: Revista Escola de Minas** 66.1, pp. 35–40.

Ghanem, Roger and Masanobu Shinozuka (1995). "Structural-system identification. I: Theory". In: **Journal of Engineering Mechanics** 121.2, pp. 255–264.

Ghrib, Faouzi and Rene Tinawi (1995). "An application of damage mechanics for seismic analysis of concrete gravity dams". In: **Earthquake Engineering & Structural Dynamics** 24.2, pp. 157–173.

Gunn, R., K. Scrivener, and A. Leemann (2017). "The Identification, Extent and Prognosis of Alkali-Aggregate Reaction Related to Existing Dams in Switzerland". In: **Swelling Concrete in Dams and Hydraulic Structures: DSC 2017**. Ed. by Alain Sellier et al. John Wiley & Sons.

Hariri-Ardebili, M.A. and H. Mirzabozorg (2014). "Estimation of probable damages in arch dams subjected to strong ground motions using endurance time acceleration functions". In: **KSCE Journal of Civil Engineering** 18, pp. 574–586.

Hariri-Ardebili, M.A. and V.E. Saouma (2015). "Quantitative failure metric for gravity dams". In: **Earthquake Engineering and Structural Dynamics** 44, pp. 461–480.

Hariri-Ardebili, MA and VE Saouma (2016). "Probabilistic seismic demand model and optimal intensity measure for concrete dams". In: **Structural Safety** 59, pp. 67–85.

Hariri-Ardebili, M.A. and V.E. Saouma (2017). "Single and multi-hazard capacity functions for concrete dams". In: **Soil Dynamics and Earthquake Engineering** 101, pp. 234–249.

Hariri-Ardebili, M.A., V.E. Saouma, and C. Merz (2018). "Risk-Informed Conditional Assessment of a Bridge with Alkali Aggregate Reaction". In: **ACI Structural Journal** 115.2, pp. 475–487.

Hariri-Ardebili, M.A. et al. (2016). "A new class of seismic damage and performance indices for arch dams via ETA method". In: **Engineering Structures** 110, pp. 145–160.

Hariri-Ardebili, Mohammad Amin, Hasan Mirzabozorg, and M Reza Kianoush (2013). "Seismic analysis of high arch dams considering contraction-peripheral joints coupled effects". In: **Central European Journal of Engineering** 3.3, pp. 549–564.

Hariri-Ardebili, Mohammad Amin and Siamak Sattar (2023). "Uncertainty and bias in fragility estimates by intensifying artificial accelerations". In: **Probabilistic Engineering Mechanics** 74, p. 103545.

Hashemi, A. (2012). **Soil Structure Interaction Effects on a Nuclear Containment Structure**. Tech. rep. Redacted Report. Bechtel National, Inc.

Hatch (2015). [redacted] **Dam ASR Structural Analysis**. Tech. rep. H346991-0000-10-124-0001. ACRES.

Huang, H. and B. Spencer (2016). "Grizzly model for fully coupled heat transfer, moisture, diffusion, alkali-silica reaction and fractureing process in concrete". In: **9th International Conference on Fracture Mechanics of Concrete and Concrete Structures; FraMCoS-9**. Ed. by V.E. Saouma, J. Bolander, and E. Landis. Berkeley, CA.

Huang, H., B. Spencer, and G. Cai (2015). **Grizzly Model of Multi-Species Reactive Diffusion, Moisture/Heat Transfer, and Alkali-Silica Reaction in Concrete**. Tech. rep. INL/EXT-15-36425. Idaho Falls, Idaho 83415: Idaho National Laboratory.

Hudson, M., I.M. Idriss, and M. Beikae (1994). **QUAD4M A Computer Program to Evaluate the Seismic Response of Soil Structures Using Finite Element Procedures and Incorporating a Compliant Base**. Tech. rep. Center for Geotechnical Modeling Department of Civil & Environmental Engineering University of California Davis.

James, Gareth et al. (2013). **An introduction to statistical learning**. Vol. 112. Springer.

Japan Society of Civil Engineers (2000). **Dynamic Analysis and Earthquake Resistant Design; Volume 2 Methods of Dynamic Analysis**. Section 4.2. Balkema.

Joshi, Nirmal R et al. (2021). "Time-Dependent Deformation of a Concrete Arch Dam in Thailand-Numerical Study on Effect of Alkali Silica Reaction on Deflection of Arch". In: **Journal of Advanced Concrete Technology** 19.3, pp. 181–195.

Kenkyusho, K.K. (1995). **SuperFLUSH/3D**.

Kreider, J. and A. Rabl (1994). **Heating and Cooling of Buildings**. Hightstown, NJ: McGraw-Hill, Inc.

Lamea, M and H Mirzabozorg (2015). "Evaluating Sensitivity of an AAR-Affected Concrete Arch Dam to the Effects of Structural Joints and Solar Radiation". In: **Strength of Materials** 47.2, pp. 341–354.

Larive, C. (1998). *Apports Combinés de l'Experimentation et de la Modélisation à la Comprehension del'Alcali-Réaction et de ses Effets Mécaniques*. Tech. rep. *In French*. Paris: *Ecole Normale des Ponts et Chaussées*.

Lebon, G., V.E. Saouma, and Y. Uchita (2010). "3D rock-dam seismic interaction". In: **Dam Engineering** 21.

Lemos, J.V. (1999). "Discrete Element Analysis of Dam Foundations". In: **Distinct Element Modelling in Geomechanics**. Ed. by K.R. Saxena, V.M. Sharma, and R. Woods. Balkema, pp. 89–115.

Leroy, R. et al. (2011). "Re-assessment and treatment-design of an ASR-affected gravity dam". In: **Dams and reservoirs under changing challenges**. Ed. by Anton J Schleiss and Robert M Boes. CRC press.

Løkke, Arnkjell and Anil K Chopra (2019). "Direct finite element method for nonlinear earthquake analysis of concrete dams: Simplification, modeling, and practical application". In: **Earthquake Engineering & Structural Dynamics** 48.7, pp. 818–842.

Lysmer, J. and L.A. Drake (1972). "A Finite Element Method for Seismology". In: **Methods in Computational Physics** 11, pp. 181–216.

Lysmer, J. and R.L. Kuhlemeyer (1969). "Finite Element Model for Infinite Media". In: **ASCE Journal of Engineering Mechanics** 95.EM 4, pp. 859–877.

Lysmer, J., T. Udaka, and H.B. Seed (1975). **FLUSH A computer Program for Approximate 3D Analysis of Soil-Structure Interaction Problems**. Tech. rep. UCB/EERC-75/30. Earthquake Engineering Research Center, University of California: Berkeley, CA.

Malm, Richard, Manouchehr Hassanzadeh, and Rikard Hellgren (2017). "Proceedings of the 14th ICOLD International Benchmark Workshop on Numerical Analysis of Dams". In: **14th ICOLD**

International Benchmark Workshop on Numerical Analysis of Dams. KTH Royal Institute of Technology.

Mashayekhi, M. and H.E. Estekanchi (2013). "Investigation of strong-motion duration consistency in endurance time excitation functions". In: **Scientia Iranica** 20, pp. 1085–1093.

Mashayekhi, M. et al. (2018). "Development of hysteretic energy compatible endurance time excitations and its application". In: **Engineering Structures** 177, pp. 753–769.

Metalssi, O. et al. (2014). "Modeling the cracks opening–closing and possible remedial sawing operation of AAR-affected dams". In: **Engineering Failure Analysis** 36, pp. 199–214.

Mirzabozorg, H. (2013). Personal Communication.

Mirzabozorg, H. et al. (2014). "Mathematical Modeling and Numerical Analysis of Thermal Distribution in Arch Dams Considering Solar Radiation Effect". In: **The Scientific World Journal** 2014.

Miura, F. and H. Okinaka (1989). "Dynamic Analysis Method for 3D Soil-Structure Interaction Systems with the Viscous Boundary Based on the Principle of Virtual Work". In: **Japanese Journal of Civil Engineering**, pp. 395–404.

Miura, F. and K. Toki (1987). "Estimation of Natural Frequency and Damping Factor for Dynamic Soil Structure Interaction Systems". In: **Proceedins of the 3rd Int. Conf. on Soil Dynamics and Earthquake Engineering**, pp. 73–87.

Multon, S. (2004). "Evaluation expérimentale et théorique des effets mécaniques de l'alcali-réaction sur des structures modèles". PhD thesis. Université de Marne la Vallée, France.

Nik-Azizan, N.Z. et al. (2017). "Numerical prediction of stress and displacement of ageing concrete dam due to alkali-aggregate and thermal chemical reaction". In: **Structural Engineering and Mechanics** 64.6, pp. 793–802.

Nocedal, Jorge and Stephen Wright (2006). **Numerical optimization**. Springer Science & Business Media.

Nozari, A. and H.E. Estekanchi (2011). "Optimization of endurance time acceleration functions for seismic assessment of structures". In: **International Journal of Optimization in Civil Engineering** 1, pp. 257–277.

Oliveira, Sérgio, Anca-Maria Toader, and Paulo Vieira (2012). "Damage identification in a concrete dam by fitting measured modal parameters". In: **Nonlinear Analysis: Real World Applications** 13.6, pp. 2888–2899.

Pan, J. et al. (2013). "Numerical prediction of swelling in concrete arch dams affected by alkaliaggregate reaction". In: **European Journal of Environmental and Civil Engineering** 17.4, pp. 231–247.

Rodriguez, J. et al. (2011). "Contribution to Theme A of the Benchmark Workshop: Effect of Concrete Swelling on the Equilibrium and Displacements of an Arch Dam". In: **Proceedings of the XI ICOLD Benchmark Workshop on Numerical Analysis of Dams**. Valencia, Spain.

Rypl, D. (2021). **T3D Mesh Generator**.

Salamon, J., W. Dressel, and D. Liechty (2021). "Monitoring of Dams Suffering from ASR at the Bureau of Reclamation". In: **Diagnosis & Prognosis of AAR Affected Structures**. Ed. by V.E. Saouma. Springer, pp. 95–116.

Saouma, V.E. (2013). **Numerical Modeling of Alkali Aggregate Reaction**. 320 pages. CRC Press.

— ed. (2020). **Diagnosis & Prognosis of AAR Affected Structures; State-of-the-Art Report of the RILEM Technical Committee 259-ISR**. Springer Nature.

Saouma, V.E., M.A. Hariri-Ardebili, and L. Graham-Brady (2020). "Stochastic analysis of concrete dams with alkali aggregate reaction". In: **Cement and Concrete Research** 132, p. 106032.

Saouma, V.E. and M.Amin Hariri-Ardebili (2021a). **Road Map for the Probabilistic Static and Dynamic Assessment of Concrete Dams Suffering from AAR**. Tech. rep. Report #2 Submitted to Bureau of Reclamation under Cooperative Agreement N0. R18AC00055. University of Colorado, Boulder.

Saouma, V.E. and M.Z. Hariri-Ardebili (2021b). **Aging, Shaking and Cracking of Infrastructures; From Mechanics to Concrete Dams and Nuclear Structures**. Springer-Nature.

Saouma, V.E. and L. Perotti (2006a). "Constitutive Model for Alkali Aggregate Reactions". In: **ACI Materials Journal** 103.3, pp. 194–202.

Saouma, V.E., L. Perotti, and T. Shimpo (2007a). "Stress Analysis of Concrete Structures Subjected to Alkali-Aggregate Reactions". In: **ACI Materials Journal** 104.5, pp. 532–541.

Saouma, V.E., J. Červenka, and R.W. Reich (2010). **Merlin Finite Element User's Manual**.

Saouma, V.E. et al. (2011). "A Simplified 3D Model for Rock-Structure Interaction with Radiation Damping and Free Field Input". In: **Bulletin of Earthquake Engineering** 9, pp. 1387–1402. DOI: s10518-011-9261-7.

Saouma, Victor and Luigi Perotti (2006b). "Constitutive model for alkali-aggregate reactions". In: **ACI materials journal** 103.3, p. 194.

Saouma, Victor, Luigi Perotti, and Takashi Shimpo (2007b). "Stress analysis of concrete structures subjected to alkali-aggregate reactions". In: **ACI structural journal** 104.5, p. 532.

Saouma, Victor E and M Amin Hariri-Ardebili (2021c). **Aging, Shaking, and Cracking of Infrastructures: From Mechanics to Concrete Dams and Nuclear Structures**. Springer Nature.

Saouma, V.E. (2014). **Numerical Modeling of AAR**. 324 pages. CRC Press.

Schnabel, P. B., J. Lysmer, and H.B. Seed (1972). **SHAKE A Computer Program for Earthquake Response Analysis of Horizontally Layered Sites**. Tech. rep. UCB/EERC-72/12. Earthquake Engineering Research Center, University of California: Berkeley, CA.

Sellier, A. et al. (2009b). "Combination of structural monitoring and laboratory tests for assessment of alkali aggregate reaction swelling: application to gate structure dam". In: **ACI Material Journal**, pp. 281–290.

— (2009a). "Combination of structural monitoring and laboratory tests for assessment of alkali-aggregate reaction swelling: application to gate structure dam". In: **ACI materials journal** 106.3, pp. 281–290.

Selvadurai, A. (2013). **Partial differential equations in mechanics 1: Fundamentals, Laplace's Equation, Diffusion Equation, Wave Equation**. Springer.

Smith, W.D. (1974). "A nonreflecting Plane Boundary for Wave Propagation Problems". In: **Journal of Computational Physics** 15, pp. 492–503.

Struble, L. and S. Diamond (1981). "Swelling Properties of Synthetic Alkali Silica Gels". In: **Journal of the American Ceramic Society** 64.11, pp. 652–655.

Tatin, M et al. (2018). "Statistical modelling of thermal displacements for concrete dams: Influence of water temperature profile and dam thickness profile". In: **Engineering Structures** 165, pp. 63–75.

Thonstad, T. et al. (2021). **Structural Performance of Nuclear Power Plant Concrete Structures Affected by Alkali-Silica Reaction (ASR); Task 2: Assessing Bond and Anchorage of Reinforcing Bars in ASR-Affected Concrete**. NIST Technical Note 2127. US Department of Commerce, National Bureau of Standards.

Ulm, F. et al. (2000). "Thermo-Chemo-Mechanics of ASR Expansion in Concrete Structures". In: **ASCE J. of Engineering Mechanics** 126.3, pp. 233–242.

Vamvatsikos, Dimitrios and C Allin Cornell (2004). "Applied incremental dynamic analysis". In: **Earthquake spectra** 20.2, pp. 523–553.

Westergaard, H.M. (1933). "Water Pressures on Dams During Earthquakes". In: **Transactions ASCE** 59.8, pp. 418–433.

Whitman, F.H. et al. (1988). "Fracture Energy and Strain Softening of Concrete as Determined by Means of Compact Tension Specimens". In: **Materials and Structures** 21, pp. 21–32.

Wolf, J.P. (1988). **Soil-Structure Interaction Analysis in Time Domain**. New York: Prentice-Hall Inc.

Zhang, Ruifu et al. (2021). "Generating high spectral consistent endurance time excitations by a modified time-domain spectral matching method". In: **Soil Dynamics and Earthquake Engineering** 145, p. 106708.

Zhang, Y. et al. (2003). “Treatment of Seismic Input and Boundary Conditions in Nonlinear Seismic Analysis of a Bridge Ground System”. In: **16th ASCE Engineering Mechanics Conference**. University of Washington, Seattle.

Zienkiewicz, O.C., D. Kelly, and P. Bettess (1979). “The sommerfeld (radiation) condition on infinite domains and its modelling in numerical procedures”. In: **Computing Methods in Applied Sciences and Engineering, 1977, I**. Ed. by R. Glowinski, J. Lions, and Iria Laboria. Vol. 704. Lecture Notes in Mathematics. Springer Berlin / Heidelberg, pp. 169–203.

Zienkiewicz, O.C., R. L. Taylor, and J.Z. Zhu (2005). **The Finite Element Method for Solid and Structural Mechanics**. 6th. Elsevier Butterworth-Heinemann.

Appendix A

Thermal Load; Verification

Abstract

It is of great significance to validate the utilized method on a simple model prior to conducting any thermal analysis on a complicated mesh. This chapter includes three main parts in the first section a comprehensive study is conducted to determine and regenerate the pool temperature at different elevations for seven dams that their data was available from Bureau of Reclamation, 1981 report in order to evaluate the ability of the utilized formula for approximation of the pool temperature.

In the second part, the thermal analysis is conducted on a single column and results are compared with the numerical solution, also the stability condition is discussed. last but not least, the calculations of solar radiation is validated on a cantilever and an arch.

A.1 Pool Temperature

ASR expansion being a thermodynamically reaction, expansion is very sensitive to water temperature in the dam reservoir. Whereas air temperature is usually well recorded, reservoir temperature is not. At best, we may have air and surface temperature. Hence, this section will make a best estimate determination of reservoir temperature at the dam based on recorded reservoir

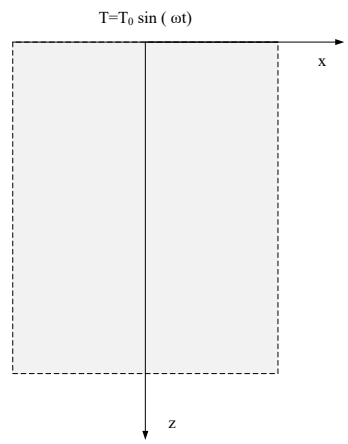

Figure A.1: Semi infinite plate subjected to surface harmonic temperature

temperature in terms of depths at other dams. The governing equation for thermal diffusion is

$$\frac{\partial T}{\partial t} = \underbrace{\frac{k}{\rho c_p}}_{\mu} \frac{\partial^2 u}{\partial x^2} \tag{A.1}$$

where μ is the thermal diffusivity and describes the rate of temperature spread through a material.

A.1.1 Heat conduction in a semi-infinite plate

Considering a semi-infinite solid, Fig A.1, with its free surface is subjected to a periodic temperature variation $T(x,t)$

$$T(0,t) = T_m + T_0 \sin(\omega t) \tag{A.2}$$

Solution for $T(0,t) = T_M$ is well known, and is given by

$$T(x,t) = T_m \text{erfc}\left(\frac{x}{2\sqrt{\mu t}}\right) \tag{A.3}$$

Solution for $T(0,t) = T_0 \sin(\omega t)$ is given by (Selvadurai, 2013), Fig. A.1. as

$$T(z,t) = T_0 \exp\left\{-\left(\frac{\omega}{2\mu}\right)^{\frac{1}{2}} z\right\} \sin\left[\omega t - \left(\frac{\omega}{2\mu}\right)^{\frac{1}{2}} z\right] \tag{A.4}$$

To visualize the temperature distribution in 1-D "column", we consider a top variation with amplitude ± 10, Fig. A.2(a); a bottom variation of ± 2.5, Fig. A.2(c); and the sum of the two Fig. A.2(e).

A.1.2 Pool water temperature distribution

A.1.2.1 Empirical Solution

An empirical equation for the temperature distribution was first given by Bofang and Zhanmei (1990) in term of a mean top and bottom water temperatures and calibrated for a specific dam. The equation was later extended by Ardito, Maier, and Massalongo (2008).

$$T_w(y_w, t) = T_{bot}(t).\frac{1 - e^{-\phi y_w}}{1 - e^{-\phi H}} + T_{top}(t).\frac{e^{-\phi y_w} - e^{-\phi H}}{1 - e^{-\phi H}} \tag{A.5}$$

where T_{bot} is the time sequence of temperature measurements at $y_w = H$ (reservoir bottom); T_{top} is the time sequence of temperature measurements at $y_w = 0$ (reservoir top), Figure A.3(a); and most importantly ϕ is an empirical parameter that must be properly determined for the specific dam. For illustration, Figure A.3 shows the water temperature for a dam 100 m high, and $\phi = 0.04$.

A.1.2.2 Model comparisons

Figure A.2 qualitatively (and not quantitatively) compares the two previously described models for a 100 m high dam with a mean top and bottom temperatures of 20 and 6 °C, and a harmonic varioton with 10 and 2 °C respectively.

Whereas it is indeed expected that the analytical of solution (Selvadurai, 2013) has equal impact for the top and bottom temperature diffusion (albeit with different weight due to difference in temperature), this is not the case in the empirical equation of Ardito, Maier, and Massalongo (2008).

This is most apparent in Figure A.2(d) where the bottom temperature has far greater impact on the top than the other way around. This can be simply explained by the fact that, contrarily to the analytical equation, there is inherent in this equation the notion of “bottom” and “top”, and that heat simply moves upward.

Hence, the bottom reservoir temperature has a much greater impact that the top one, and should be recorded in as much as possible. In the absence of measurements, it can be argued that the temperature can not be lower than 4°C when the maximum water density is reached (except

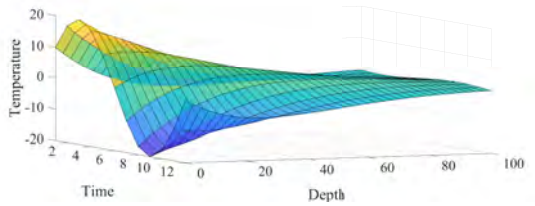

(a) Analytical; Top harmonic temperature ±10 (Selvadurai, 2013)

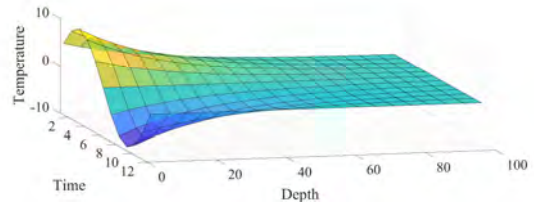

(b) Emperical; Top harmonic temperature ±10 (Ardito, Maier, and Massalongo, 2008)

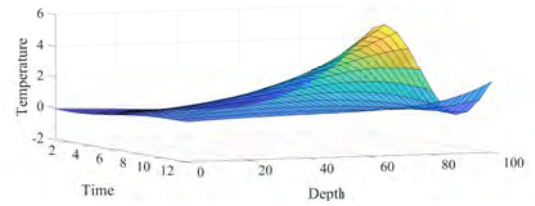

(c) Analtical; Bottom harmonic temperature ±2.5 (Selvadurai, 2013)

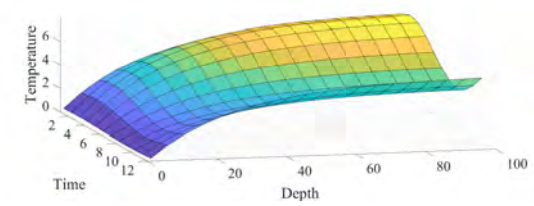

(d) Emperical; Bottom harmonic temperature ±2.5 (Ardito, Maier, and Massalongo, 2008)

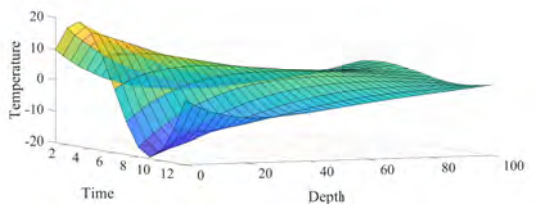

(e) Analytical; Net temperature distribution (Selvadurai, 2013)

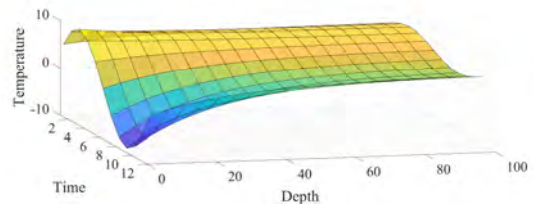

(f) Emperical; Net temperature distribution (Ardito, Maier, and Massalongo, 2008)

Figure A.2: Analytical and emperical solution for water temperature distribution

in particular conditions i.e. when the reservoir is covered by ice, or near water intake structures) (Tatin et al., 2018).

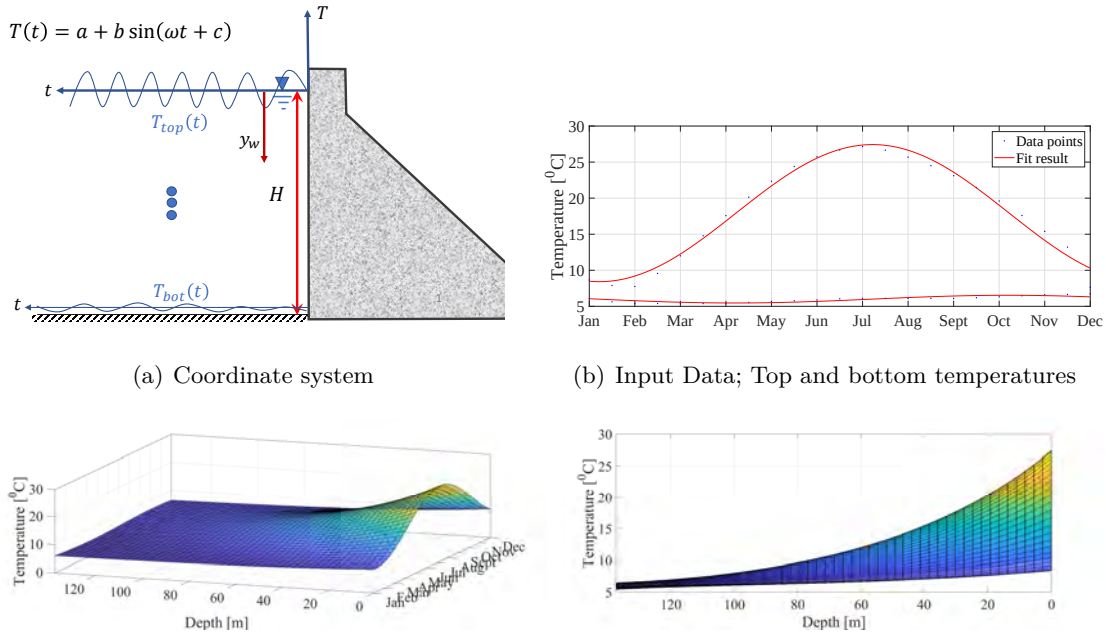

(a) Coordinate system

(b) Input Data; Top and bottom temperatures

(c) Fitted Model

Figure A.3: Fitted model of Ardito, Maier, and Massalongo (2008)

A.1.2.3 Application

Bureau of Reclamation (1981) reports the temporal and spatial (in terms of depth) water temperature for seven dams including shown in Figure A.4.

Those plots have been digitized, and are shown in Figure A.5.

In the next step we seek to fit the data reported in Figure A.5 into Eq. A.5. First, all digitized data are fitted into harmonic equation

$$T(t, y) = A(y) + B(y)\sin(\omega t + C(y)) \tag{A.6}$$

Then two approaches are pursued

Model I Using T_{bot} and T_{top}, determine ϕ from all other curves.

Model II Use the entire set of curves to determine the coefficients for T_{bot}, T_{top}, and ϕ

Results for the fitted surfaces based on Model II are shown in Figure A.6 and table B.1.

The goodness of fit (based on R^2) is shown in the last two columns of this table for the two methods which is clearly better for model II which is the reason for demonstrating only the results

of model II.

As for the case study dam the same approach is followed herein using the available pool temperature data within the upper 100 ft and the results shown in figure A.7 indicate the lack of sufficient data to utilize this method to estimate the parameters of Eq. A.5. Also, the values based on model II are shown in table B.2. As seen in this table the goodness of fit is not in an acceptable range.

A.2 Numerical Solution with Merlin; Concrete

A.2.1 Stability Condition

The Courant–Friedrichs–Lewy or CFL condition is a condition for the stability of unstable numerical methods that model convection or wave phenomena.

It states that the distance that any information travels during the time-step length within the mesh must be lower than the distance between mesh elements. In other words, information from a given cell or mesh element must propagate only to its immediate neighbors. This results in

$$\frac{\mu \Delta t}{h^2} \leq \frac{1}{2} \tag{A.7}$$

where μ is the diffusivity defined in Equation A.1.

A.2.2 Verification Problems

Before a comprehensive thermal study is undertaken, it is important to validate the ability of the finite element code (Merlin) to properly conduct linear transient thermal analysis of concrete subjected to: a) temperature, b) flux; and c) solar radiation. For this purpose a $1[m] \times 1[m] \times 100[m]$ concrete column is analyzed under various thermal load conditions in which the temperature is applied at one end of the column. The studied columns are shown in figure A.8. For this study, material properties of the concrete were taken from Hatch (2015) presented in table 6.1 and the air-concrete film coefficient was taken to be equal to $20[\mathrm{W\,m^{-2}\,K^{-1}}]$ also obtained from Hatch (ibid.) . The whole verification procedure presented in this section is summarized in figure A.9

A.2.2.1 Temperature

At first, the temperature is applied directly to the concrete column considering once a constant temperature which does not change with time and then a harmonic temperature that is defined using a sine function such that $T = -12.6\sin(\frac{2\pi}{12}t)$ which represents the harmonic term of the air temperature at the dam location. It is worth mentioning that the air temperature at the dam was estimated as $T = -12.6\sin(\frac{2\pi}{12}t)+12.6$ based on the available data. Then, the results of the thermal analysis of this column from Merlin is compared to that of the analytical solution. The analytical solution for constant and harmonic temperatures are given by equation A.3 and A.4 respectively.

Constant The constant temperature of 12.6 $[^oC]$ is applied directly at the end of the column the value considered for the temperature was obtained from the constant term of the equation representing the air temperature at the dam location. The results for both Merlin and analytical solutions are shown in figure A.10 and A.11. figure A.10 shows the temperature variation of the first 20[m] of the column within 4 years.

Figure A.11 shows that the 2 solutions are in good agreement and they have slight difference at the beginning of the thermal loading and gradually converging to a constant value in 4 years.

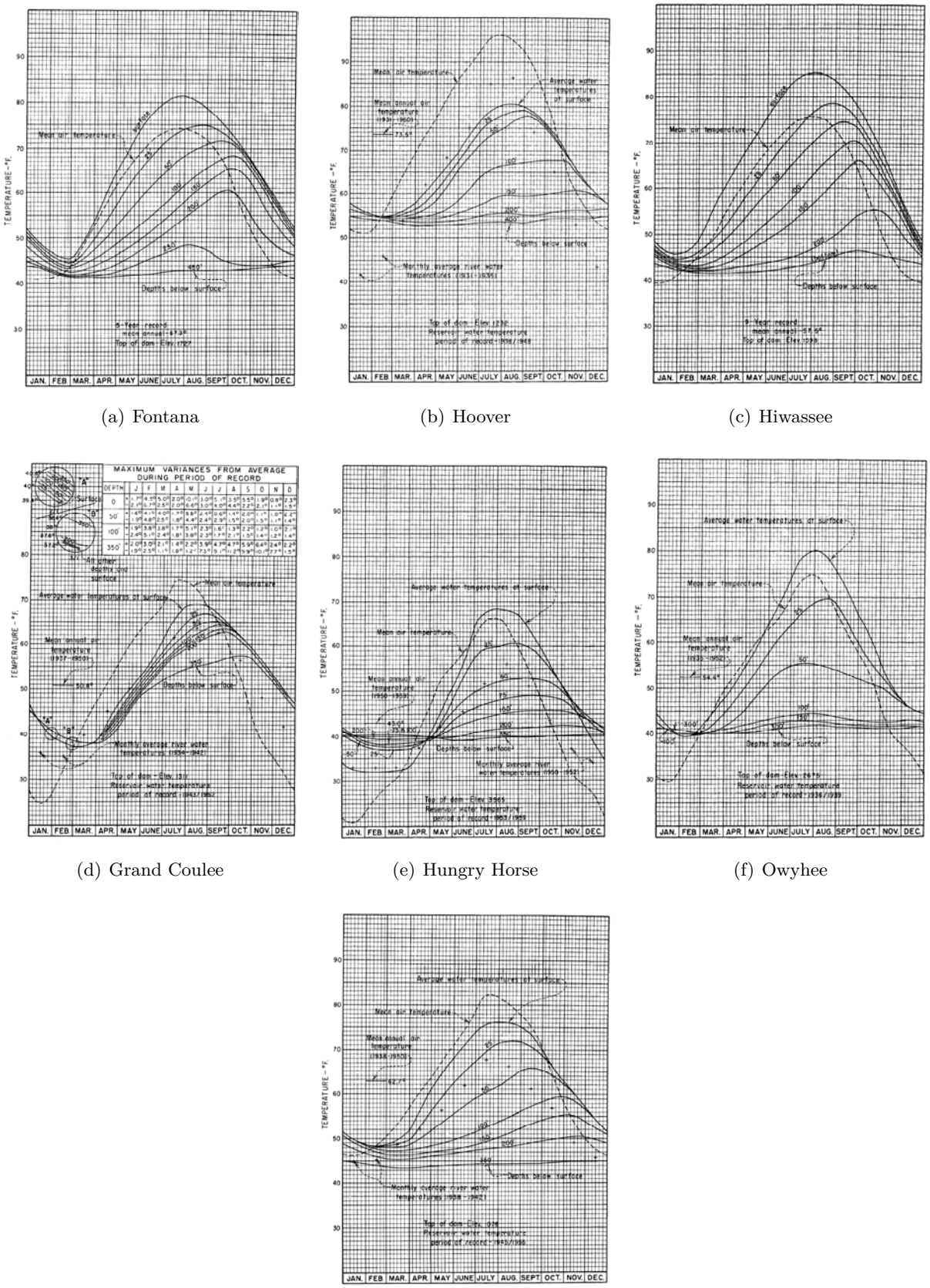

(a) Fontana

(b) Hoover

(c) Hiwassee

(d) Grand Coulee

(e) Hungry Horse

(f) Owyhee

(g) Shasta

Figure A.4: Recorded pool temperatures (Bureau of Reclamation, 1981)

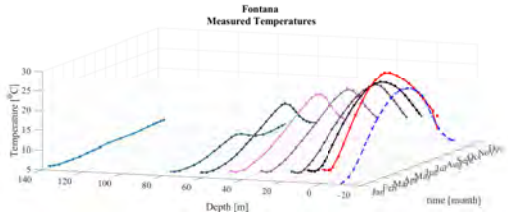

(a) Fontana

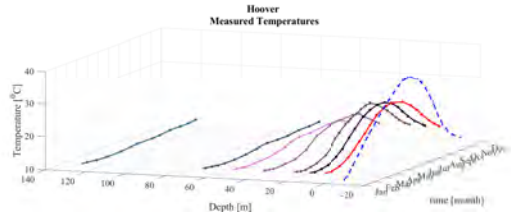

(b) Hoover

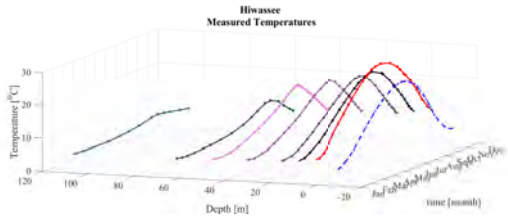

(c) Hiwassee

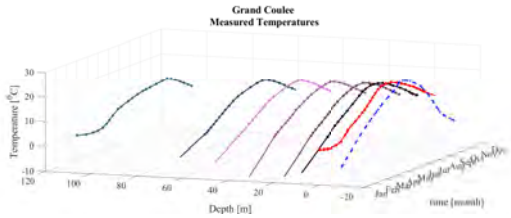

(d) Grand Coulee

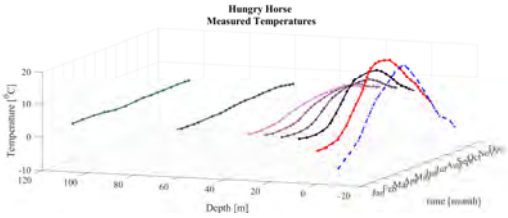

(e) Hungry Horse

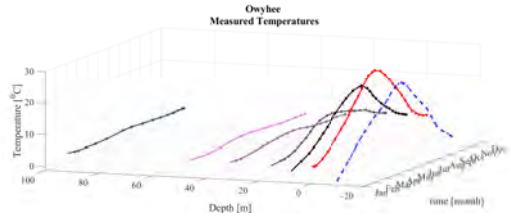

(f) Owyhee

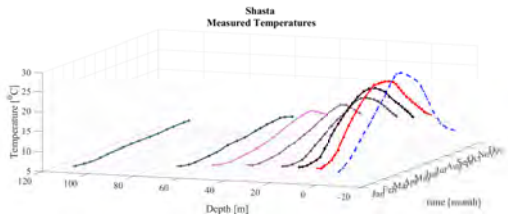

(g) Shasta

Figure A.5: Digitized data from Figure A.4

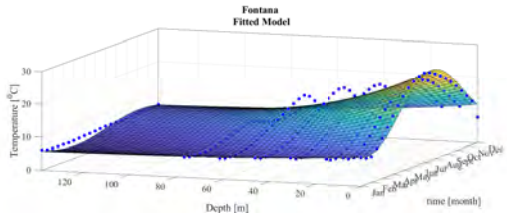

(a) Fontana

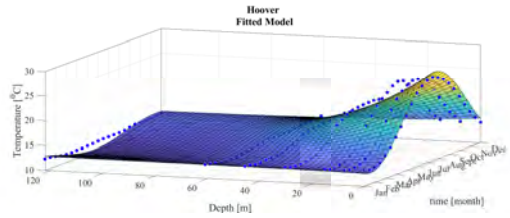

(b) Hoover

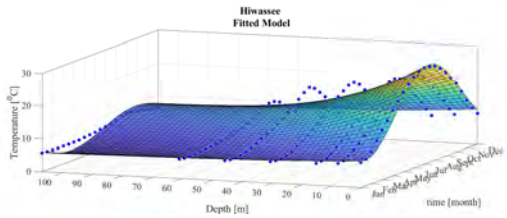

(c) Hiwassee

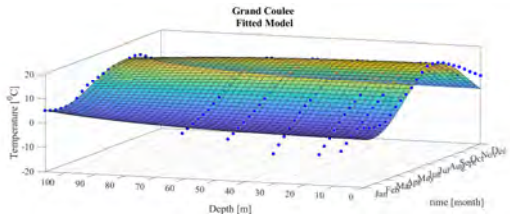

(d) Grand Coulee

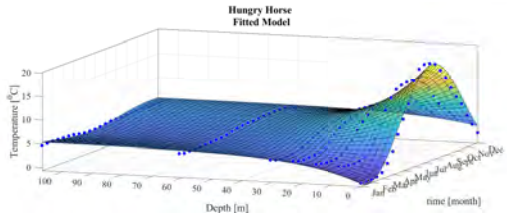

(e) Hungry Horse

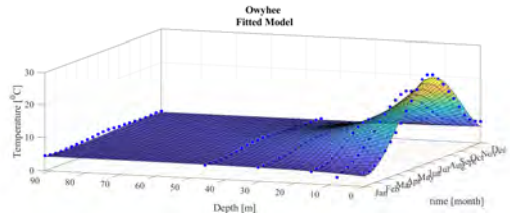

(f) Owyhee

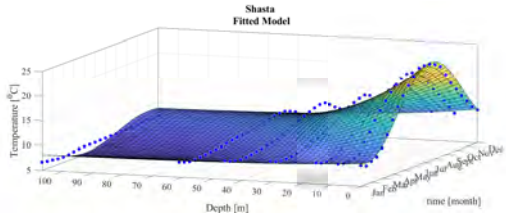

(g) Shasta

Figure A.6: Fitted dam temperatures from (Model II) Figure A.5

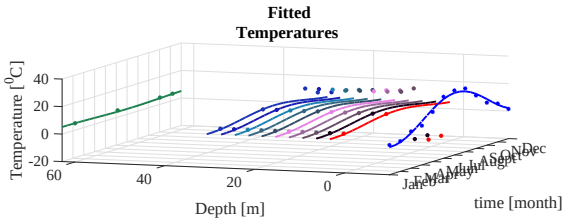

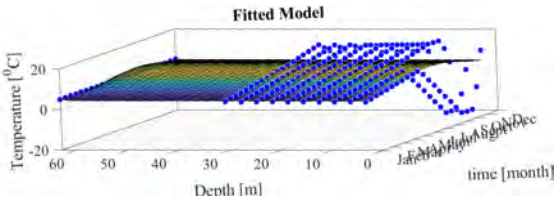

Figure A.7: Fitted dam temperature (from model II) for the case study dam

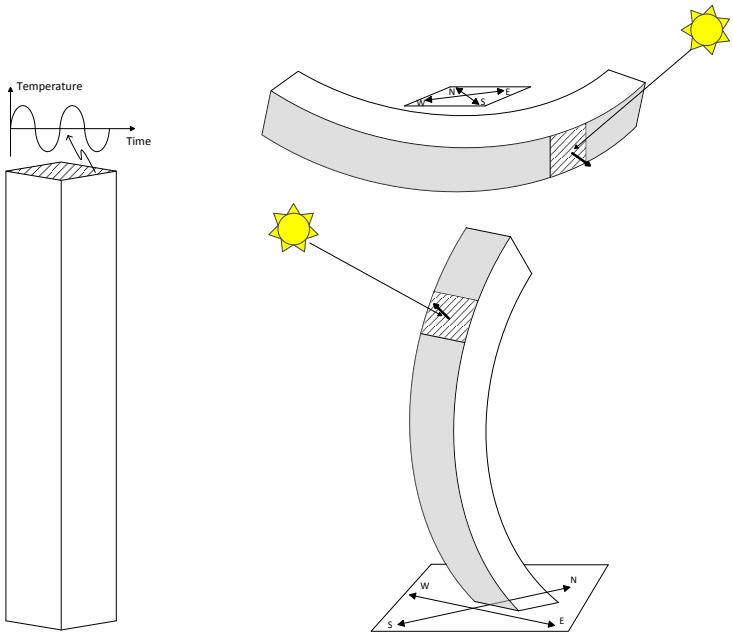

(a) Straight Column (b) Curved Column

Figure A.8: Thermal analysis results of constant temperature applied at the end of the column

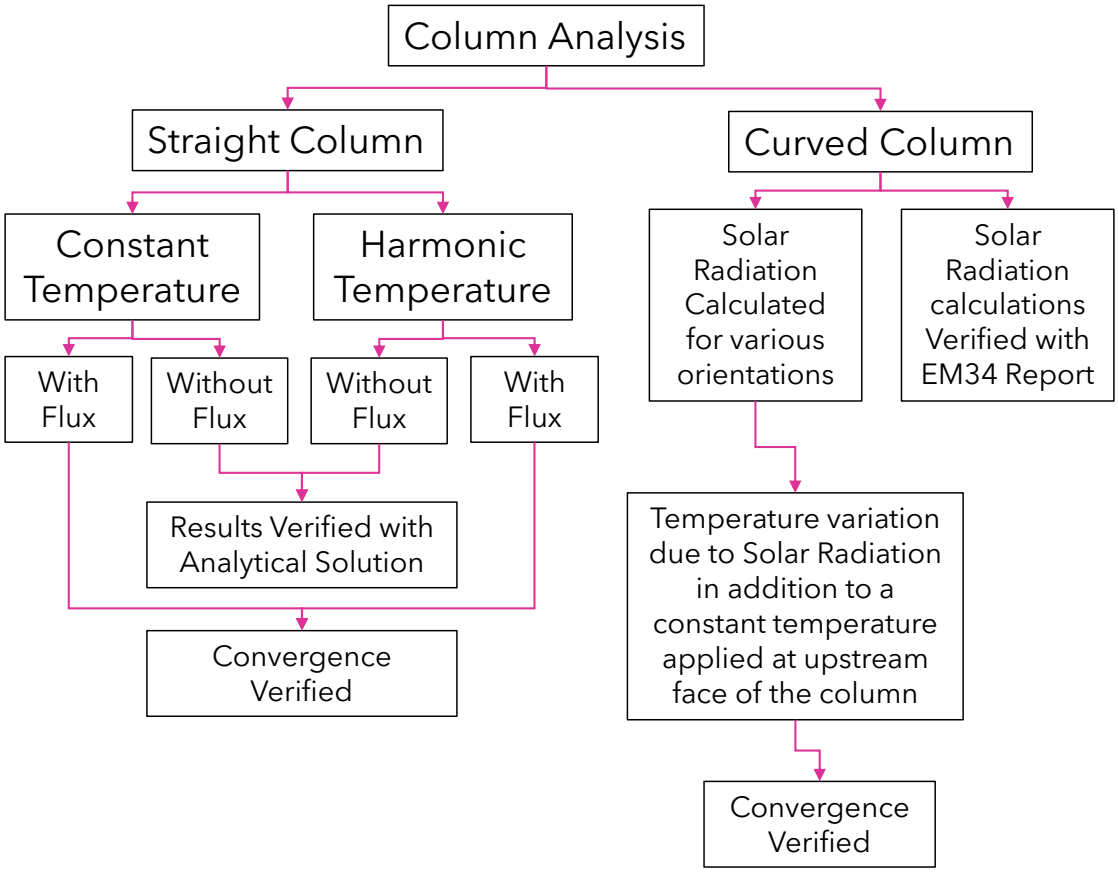

Figure A.9: Verification procedure

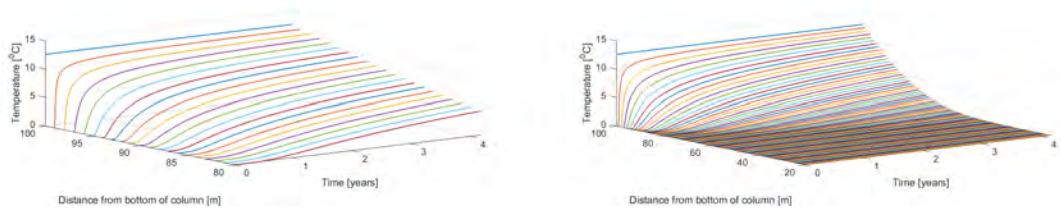

(a) analytical Solution (b) Merlin Solution

Figure A.10: Thermal analysis results of constant temperature applied at the end of the column

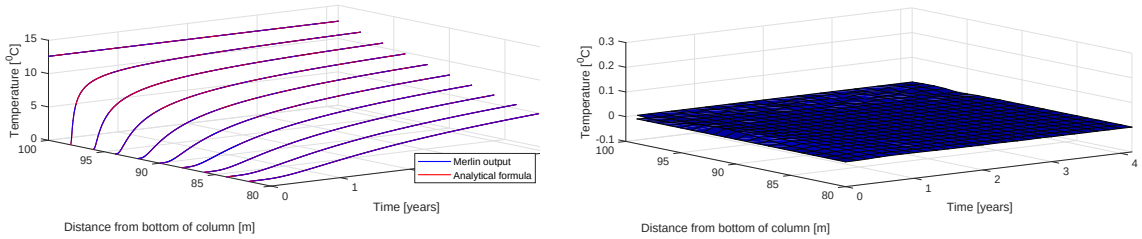

(a) Analytical vs. Merlin Solution

(b) Difference of 2 solutions

Figure A.11: Comparison of Analytical and Merlin solutions of constant temperature applied at the end of the column

Harmonic In order to have a more realistic simulation in this section the previously discussed constant temperature is replaced with a harmonic temperature ($T = -12.6\sin(\frac{2\pi}{12}t)$), plotted in figure A.12, varying with a sine function throughout the year. In figure A.13 the oscillation of temperature within 4 years is shown for Merlin and analytical solutions. It is shown that the temperature can travel almost about 15 [m] through the length of the column and its intensity is reduced within this distance. Figure A.14 also, suggests a good match between the analytical and Merlin solutions for applied harmonic temperature which underlines the accuracy of the finite element code. **Stability Condition evaluation** In order to evaluate the effect of CFL condition in convergence of the thermal analysis, the analysis is conducted considering 2 different time steps. As shown in table A.1 the time step is once considered to be equal to 0.1[month] in which $\frac{\mu\Delta t}{h^2} = 0.435$ which is less than $\frac{1}{2}$ and therefore conforms to the CFL condition. Then, The time step is increased to 1 [month] keeping the mesh size h constant, $\frac{\mu\Delta t}{h^2} = 4.35$ and becomes greater than $\frac{1}{2}$ which in turn does not conform to the CFL condition. figure A.15 shows the results of these 2 analyses compared to the analytical solution. As seen the difference of the analytical and Merlin solutions, although decreasing, lasts for CFL non-conforming analysis after 4 years.

Results show that the difference between the analytical and Merlin solutions are greater in Non-conforming analysis. In other words, failing to conform to the CFL condition had resulted in a delay in the convergence of the analysis.

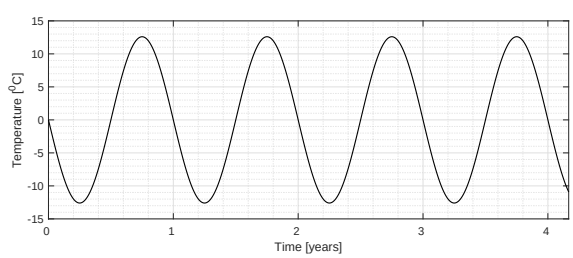

Figure A.12: Applied harmonic temperature

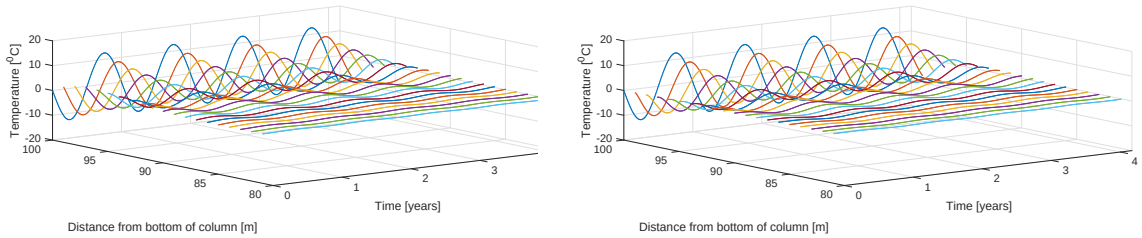

(a) analytical Solution (b) Merlin Solution

Figure A.13: Thermal analysis results of harmonic temperature applied at the end of the column

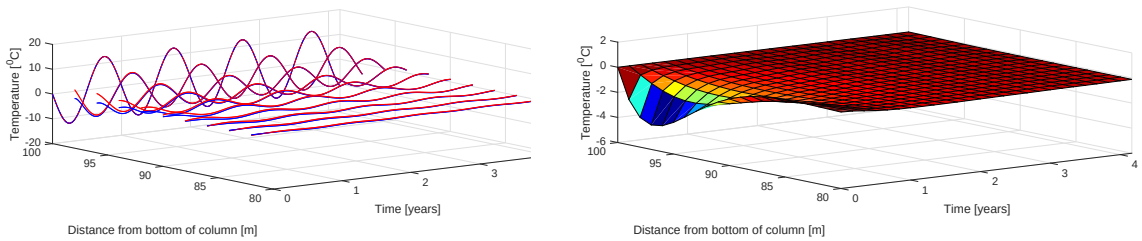

(a) Analytical vs. Merlin Solution (b) Difference of 2 solutions

Figure A.14: Comparison of Analytical and Merlin solutions of harmonic temperature applied at the end of the column

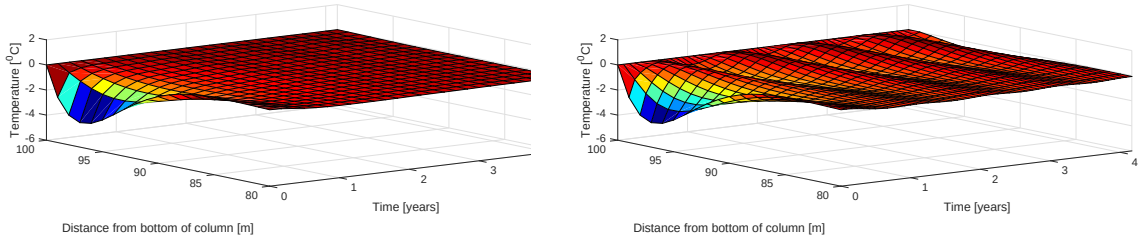

(a) Difference of 2 solutions, CFL Conforming (b) Difference of 2 solutions,CFL Non-conforming-Case 2

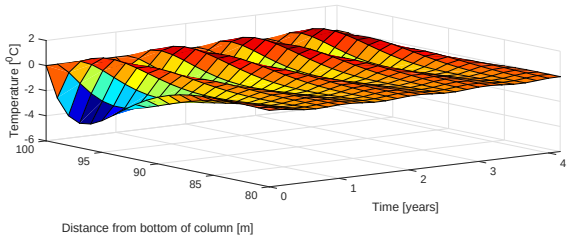

(c) Difference of 2 solutions,CFL Non-conforming-Case 3

Figure A.15: Comparison of results of CFL condition conforming and non conforming thermal analysis with harmonic temperature applied at the end of the column

Table A.1: CFL conforming and non-conforming conditions

	μ $[m^2mo^{-1}]$	$\Delta t[mo]$	$h[m]$	$\frac{\mu\Delta t}{h^2}$
Case1	4.35	0.1	1	0.435
Case2	4.35	1	1	4.35
Case3	4.35	2	1	8.7

A.2.2.2 Flux

In reality the temperature transfer from surrounding fluid cannot be simulated by applying the temperature directly to a material. In other words, there is a heat convection between the fluid and material and should be taken into account. In this study the fluid is considered to be air and, thus, the air-concrete film coefficient is used to apply the temperature using a flux rather than direct application. Therefore, the aforementioned constant and harmonic temperatures are repeated here to assess the effect of heat flux. **Constant** Results for the heat flux with a constant temperature of 12.6 $[^oC]$ is shown in figure A.16. **Harmonic** In this section the heat flux of a harmonic temperature is evaluated. Figure A.14 shows the Merlin solutions for the thermal analysis of column under harmonic temperature

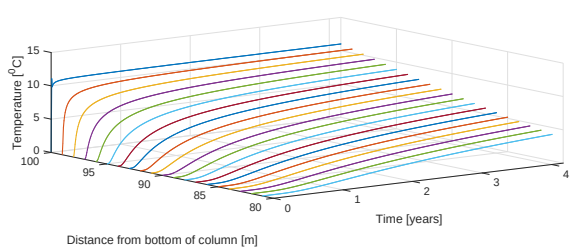

Figure A.16: Thermal analysis results of constant water temperature using flux applied at the end of the column

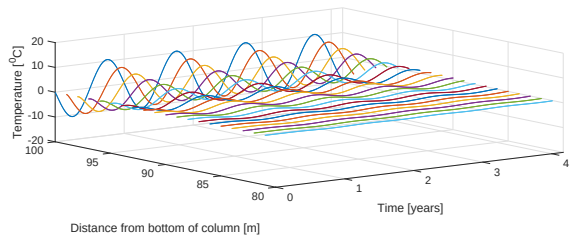

Figure A.17: Thermal analysis results of harmonic water temperature using flux applied at the end of the column

A.3 Solar radiation

In order to investigate the effect of solar radiation, a curved column presented in figure A.18, is first considered as an arch located at the upstream face of the dam and then once again it is studied as a cantilever at the same location which is shown in figure A.18.

In this study only the location and the orientation of the dam with respect to the south is used for solar radiation calculations and therefore the existence of water is omitted for the cantilever and solar radiation is calculated through the whole height of the column as this might be the case for other dams.

As previously stated the model is a $1[m] \times 1[m] \times 100[m]$ concrete column and there are 100 elements through it's length. For the solar radiation study, only the elements on the convex side of the column were assumed to receive the solar radiation as they are facing the South.

Studying the arch and cantilever will let us investigate both the effect of orientation and inclination of the surface in the received amount of solar radiation. Because the column has a curvature, the arch elements each have different orientations with respect to the South direction and cantilever elements each have different inclinations with respect to horizon, therefore, will receive different amount of solar radiations.

Figure A.19 shows the temperature variation due to solar radiation through the length of the column within a year for both arch and cantilever. As seen in the figure, in the arch, the temperature increase is maximum at the center of the arch which is facing the South direction almost directly. As for the cantilever also the maximum tempertaure increase happens at the top

of the cantilever as it is inclined upward and in turn receives the maximum direct solar radiation throughout the whole year.

The temperature increase due to solar radiation is then added to the constant temperature of 12.6[^oC], which is the constant term of the air temperature at the dam location, and thermal analysis is conducted using Merlin. The temperatures through the central axis of the column is shown in figure A.20 for about 3 years which is showing good stability even after a year. It should be noted that the distance between mesh elements that the information is expected to travel is 0.5[m] herein and therefore, in order to conform to the CFL condition, the analysis time step was set to 0.02[$month$]. Figure A.21 is showing the procedure to calculate the temperature due to solar radiation to be applied on the curved column.

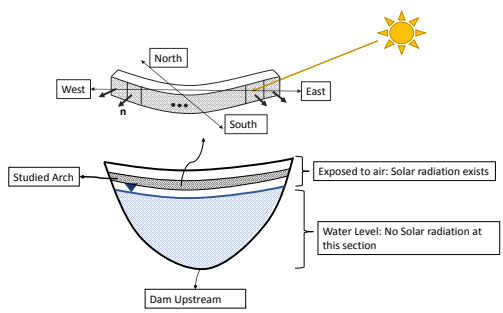

(a) Arch

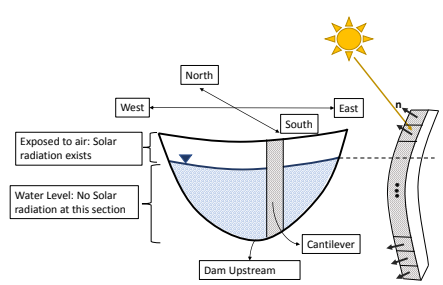

(b) Cantilever

Figure A.18: Studied arch and cantilever located at dam upstream

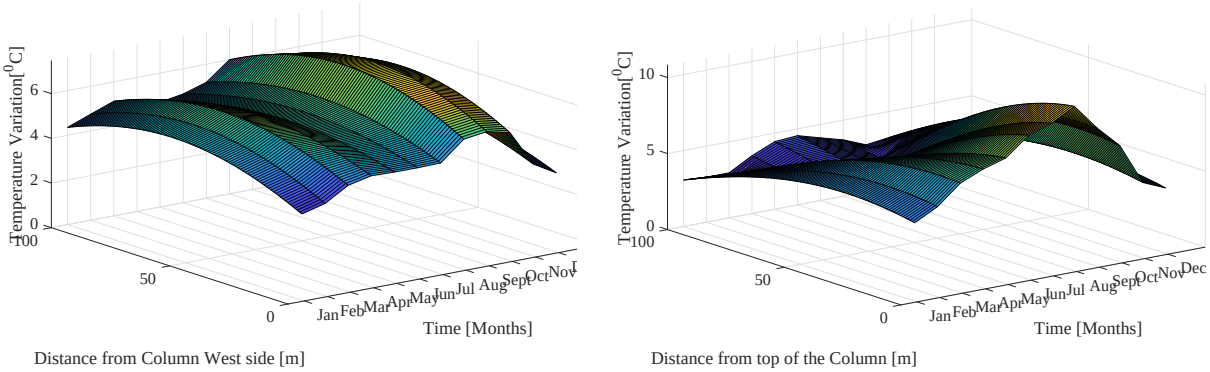

(a) Arch (b) Cantilever

Figure A.19: Temperature variation due to solar radiation throughout the curved column within 1 year

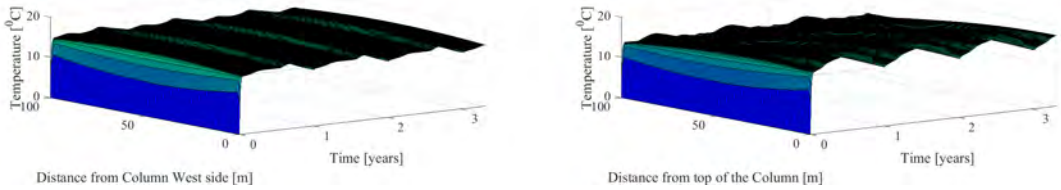

(a) Arch (b) Cantilever

Figure A.20: Thermal analysis result for nodes on the central axis of the curved column considering solar radiation effect

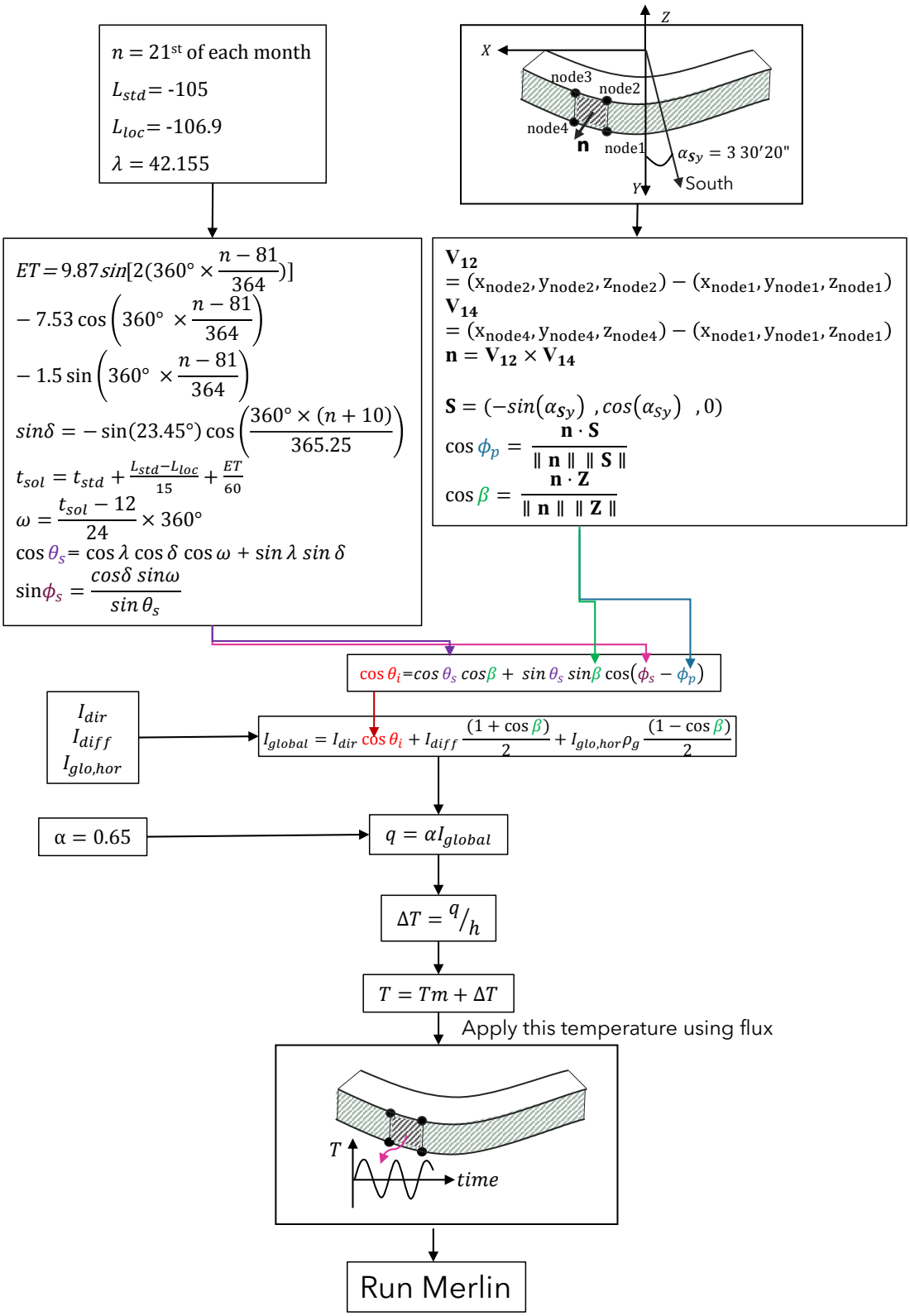

Figure A.21: Solar radiation calculation procedure for curved column

A.4 Conclusion

This chapter presented the smaller scale of the main thermal analysis to be conducted in the subsequent chapters. As described in this chapter, the thermal analysis of a single straight column was conducted using constant and harmonic temperatures applied directly to the top of the column and results compared to the numerical solution. Once the results validated the finit element method by showing a good match between the finite element and numerical solution, the stability of the solution was then assessed and thermal analysis was conducted using film coefficients to apply the temperatures to get closer to the real situation. In the next section, the purpose was to validate the solar radiation calculation presented in previous chapter, and therefore, two curved cantilever and arch were studied to determine their temperatuer increase due to solar radiation for which the results are shown and discussed.

Appendix B

Verification Study for Pool and Concrete Temperatures

Table B.1: Temperature data fitting

	a	b	c	ϕ	Method I	Method II
			Fontana			
Top	17.7415	-9.49679	0.70389	0.015827	0.902	0.994
Bot	5.612374	1.833289	8.823558			
Air	14.08135	9.601167	4.390997			
			Hoover			
Top	20.01634	-7.83074	0.714605	0.022716	0.936	0.984
Bot	12.04701	-1.22955	5.073473			
Air	23.07812	-12.0916	7.539764			
			Hiwassee			
Top	18.8469879	-11.0046	0.8444	0.02161	0.912	0.953
Bot	6.302679	-3.10449	12.13985			
Air	14.18313	10.17568	4.402833			
			Grand Coulee			
Top	9.224278	-10.6	0.645757	-0.02681	0.67548	0.78859
Bot	8.848105	-5.29629	19.1146			
Air	10.43781	-12.3562	1.258763			
			Hungry Horse			
Top	9.465751	-10.1285	0.694353	0.047607	0.933082	0.964424
Bot	4.733725	-0.93688	5.089331			
Air	6.051459	-11.8553	-5.05113			
			Owyhee			
Top	14.45718	-11.3601	0.977942	0.057675	0.965436	0.969316
Bot	4.37022	-0.3687	5.535384			
Air	11.16966	-11.0676	1.300982			
			Shasta			
Top	17.07467	-7.7792	0.75023	0.027206	0.910388	0.960983
Bot	7.115839	-1.81833	5.165946			
Air	17.13336	-9.66453	1.184623			

Table B.2: Temperature data fitting for the case study dam

	a	b	c	ϕ	Method I	Method II
			The case study dam			
Top	-10.6406	-30.2534	9.053441	0.237732	-0.024	0.596
Bot	-0.60584	-12.9162	2.650509			
Air	12.58733	-12.6138	0.974763			

Appendix C

Complementary Figures

Abstract

In the course of this research, multiple secondary figures were generated. It was deemed preferable to include them in this report so as not to confuse reading of the report with too many of them.

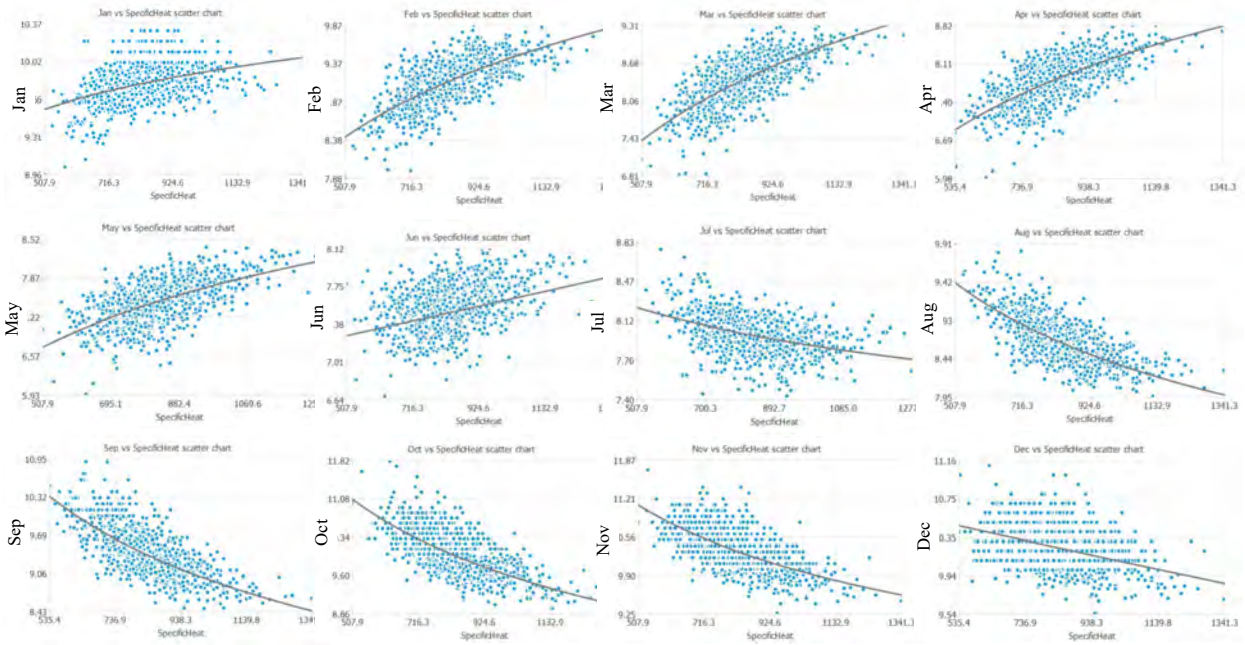

Figure C.1: Monthly specific heat correlation coefficients at node 944 (PoI)

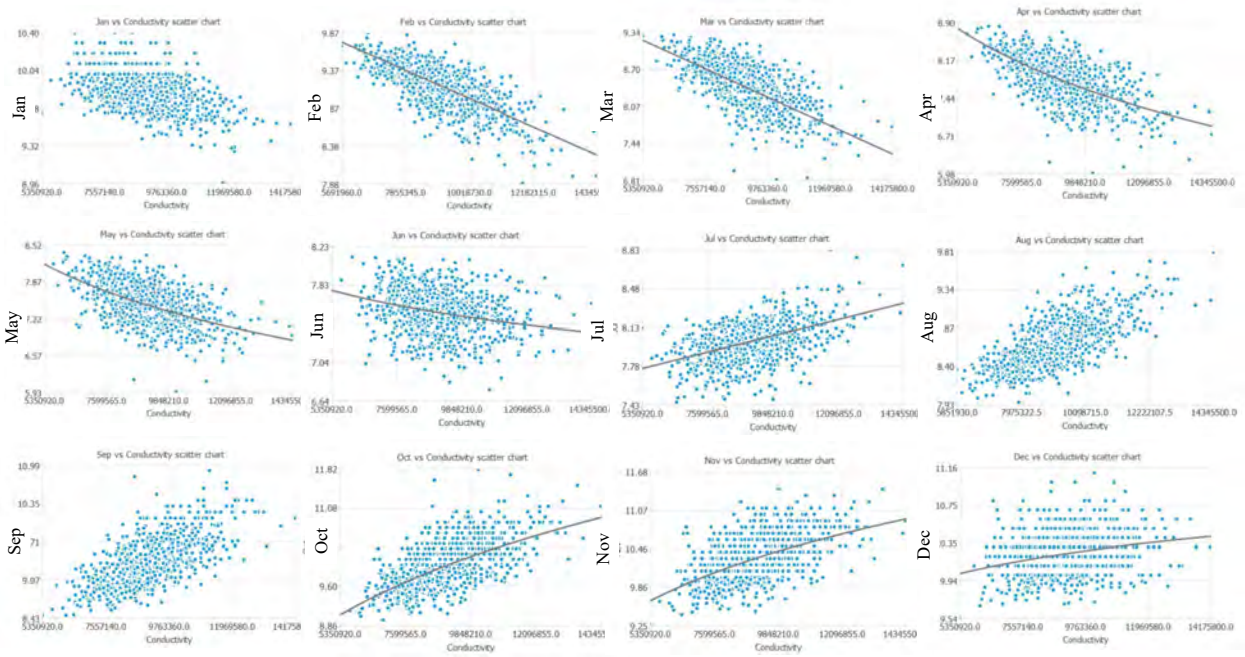

Figure C.2: Monthly conduction correlation coefficients at node 944 (PoI)

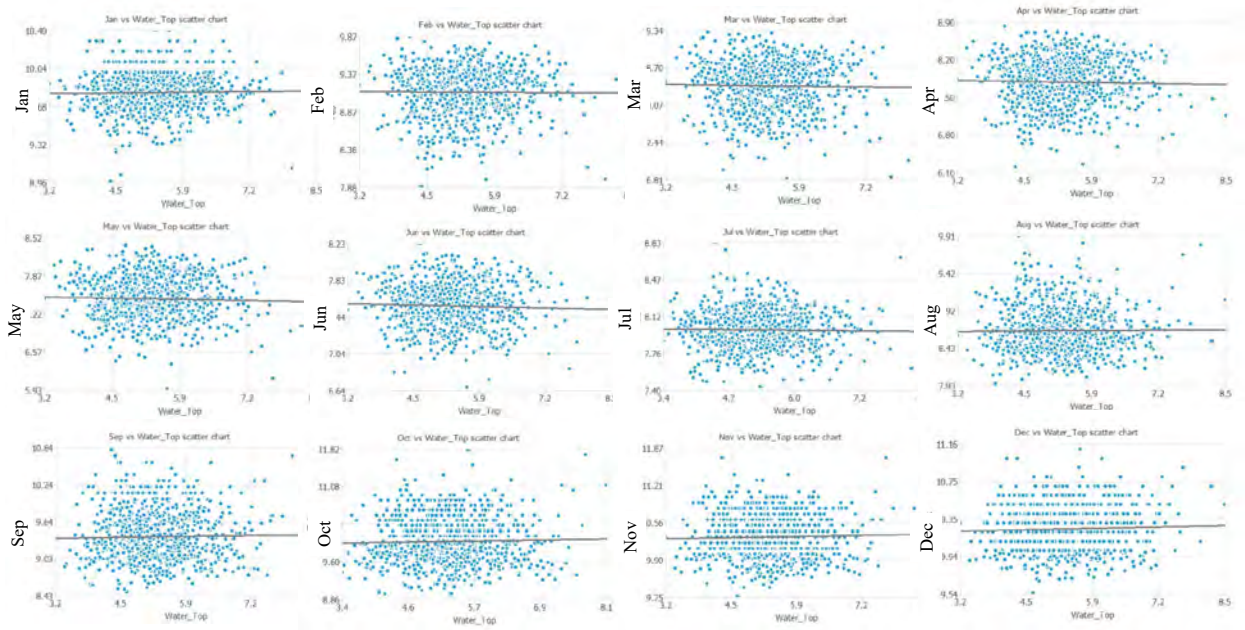

Figure C.3: Monthly top water temperature correlation coefficients at node 944 (PoI)

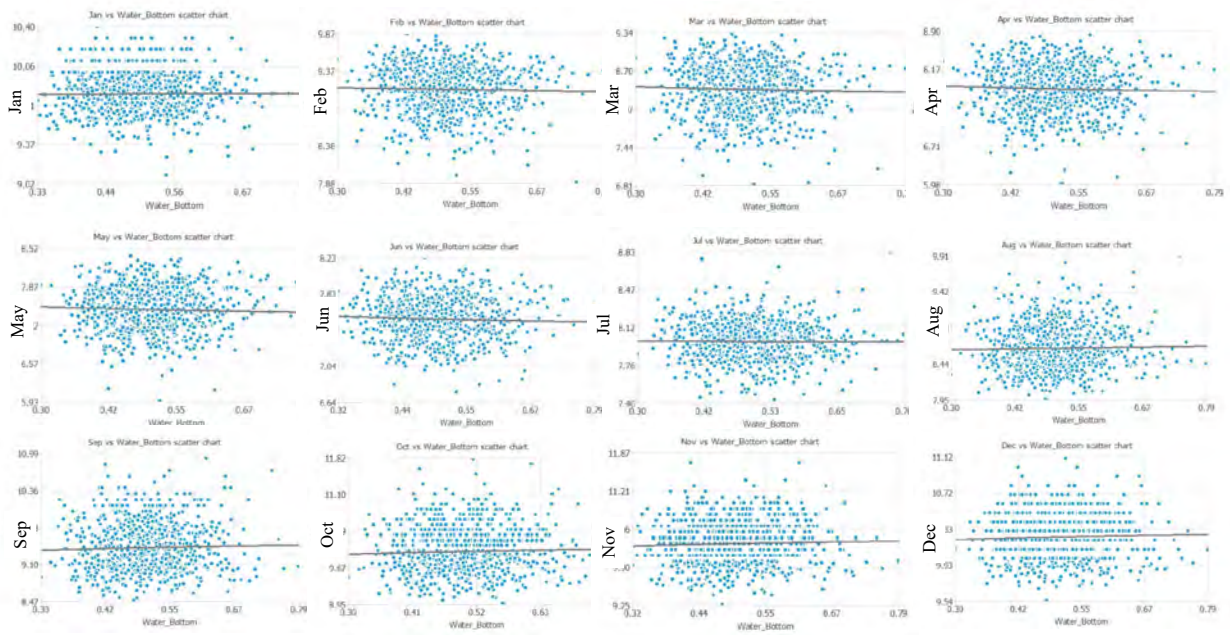

Figure C.4: Monthly bottom water temperature correlation coefficients at node 944 (PoI)

Appendix D

Additional Uncertainty Quantification Results

Abstract

The uncertainty quantification (UQ) study was conducted with 50, 100, and 200 analyses. We have retained results of the last one in the report, and this chapter will simply report the figures associated with the 50 and 100 analyses UQ studies.

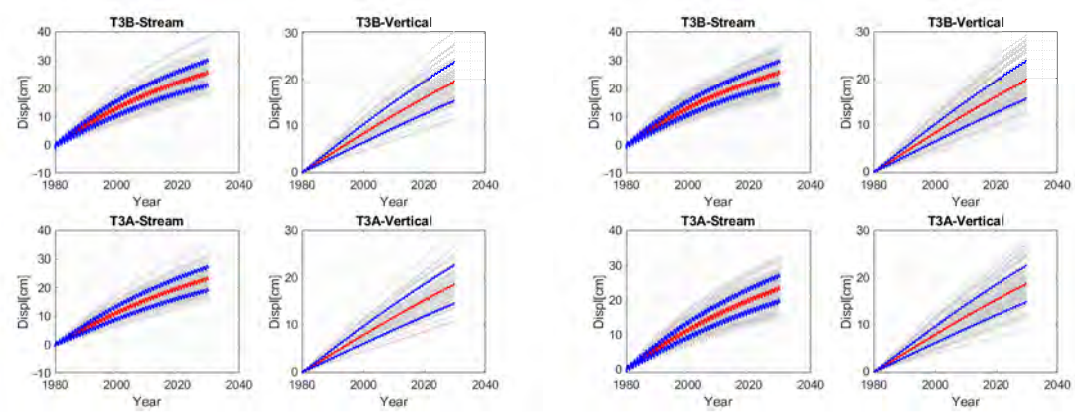

(a) 50 Analysis

(b) 100 Analysis

Figure D.1: Crest Displacements (Stream and vertical directions)

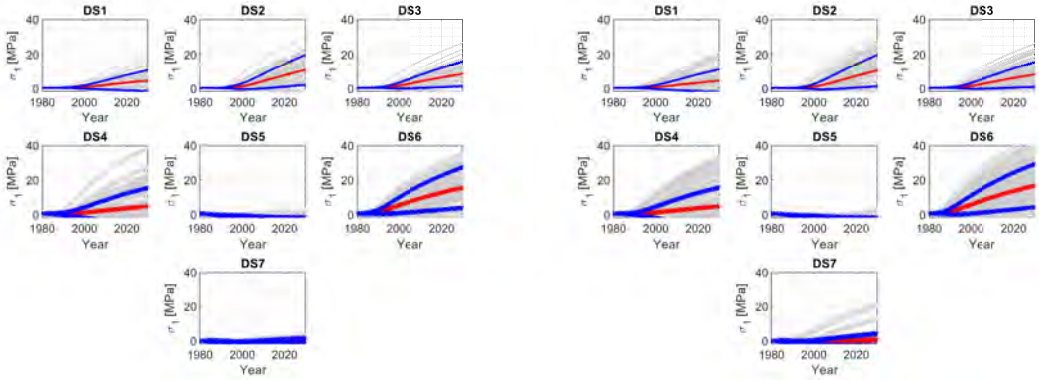

(a) 50 Analysis

(b) 100 Analysis

Figure D.2: Maximum Principal Stress; Downstream

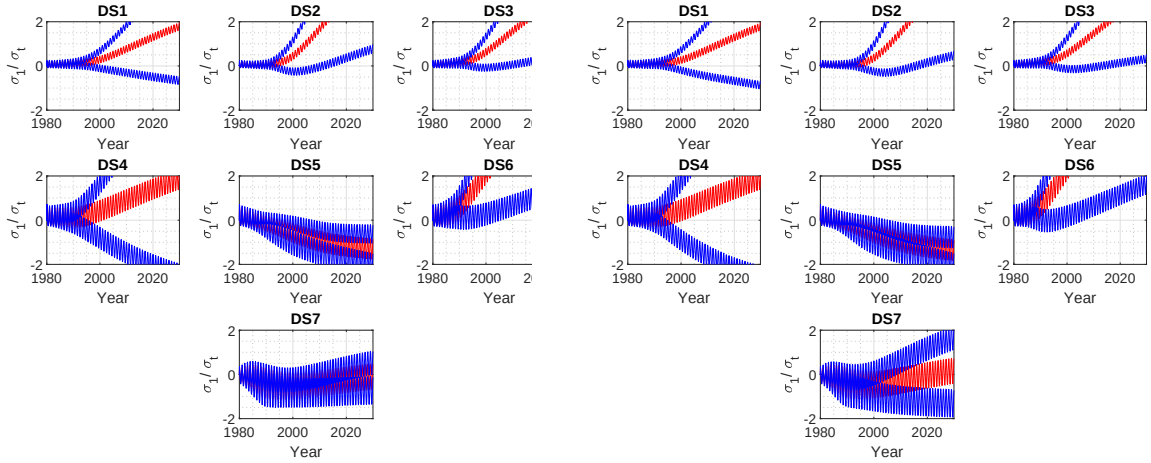

(a) 50 Analysis

(b) 100 Analysis

Figure D.3: Ratio of Maximum Principal Stress to Tensile Strength; Downstream

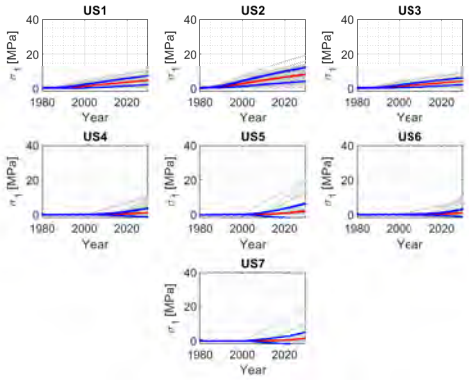

(a) 50 Analysis

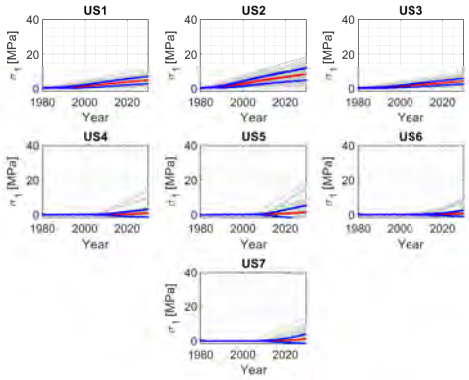

(b) 100 Analysis

Figure D.4: Maximum Principal Stress; Upstream

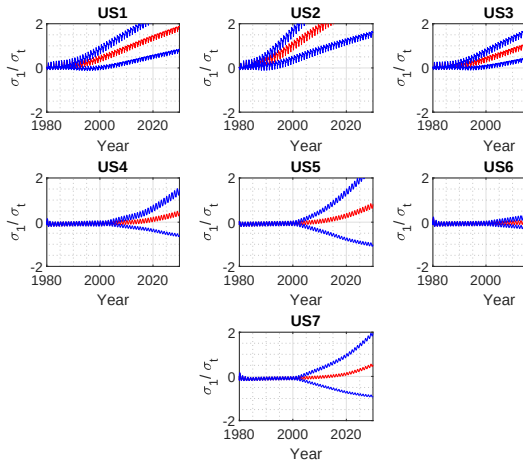

(a) Analysis 50

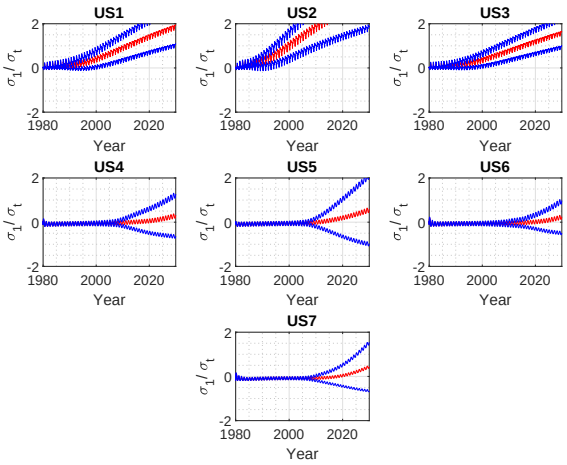

(b) Analysis 100

Figure D.5: Ratio of Maximum Principal Stress to Tensile Strength; Upstream

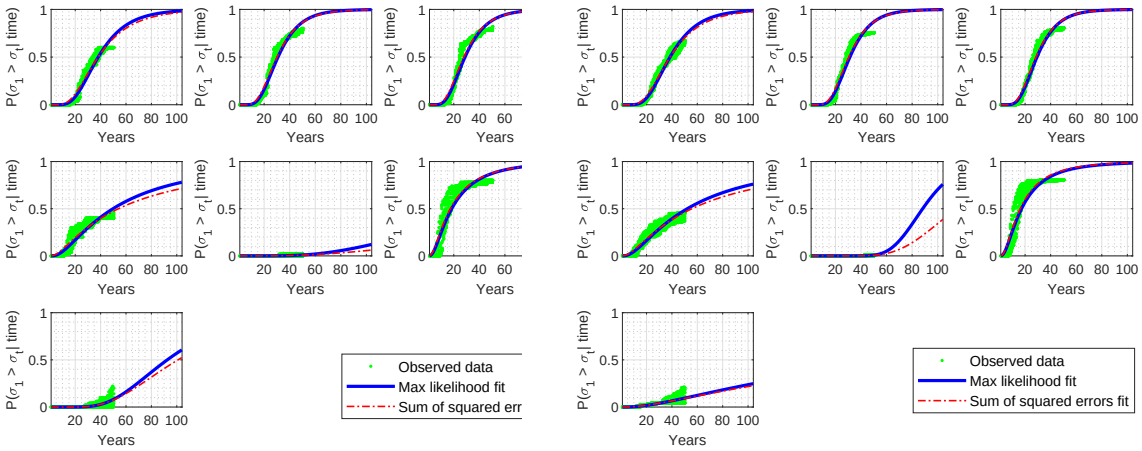

(a) 50 Analysis (b) 100 Analysis

Figure D.6: Probability of Exceedance; Downstream

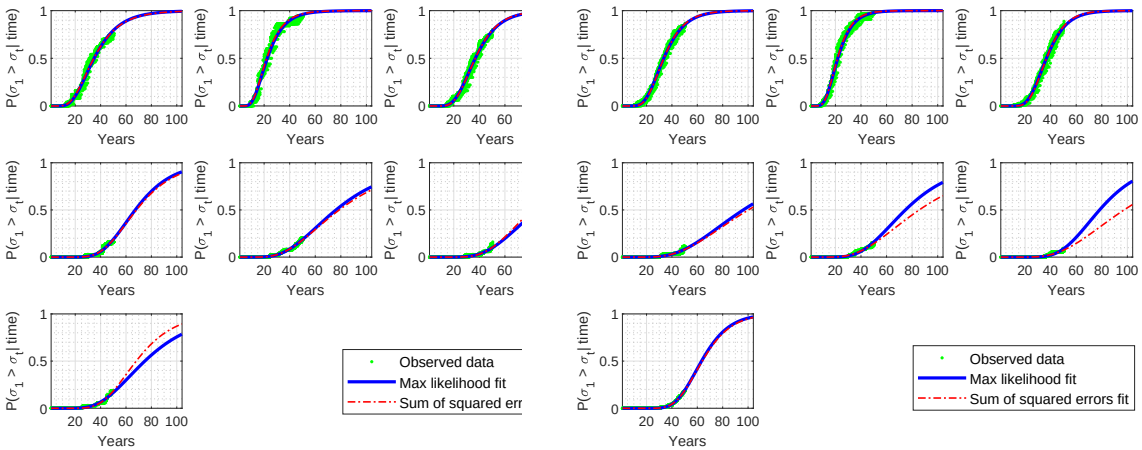

(a) Analysis 50 (b) Analysis 100

Figure D.7: Probability of Exceedance; Upstream

Appendix E

Modeling Dam-Foundation

Abstract

Modeling of the foundation proved to be slightly problematic. At first the presence of the massive shear key was ignored, and given the (typical) deformed shape of the arch dam, this would have resulted in joint openings in the downstream face.

Reclamation commented that this was not observed, and the massive shear key ensured that there would be no slip nor rotation at the base. Hence, all the analyses in the report accounted for this massive shear key (modeled by drastically increasing the joint properties at the base of the dam).

This appendix, however reports the results previously obtained for academic interest as this may indeed occur in other arch dams suffering from AAR. So far the illustrated results were based

on the assumption of the full rock-concrete bond below the dam. However, this might not be the case for other arch dams. Therefore, the analysis results assuming a rock-concrete joint below the dam are presented in this chapter. the crack opening displacements at the bottom of the dam is shown in figure E.1 using 6 nodes in a row from upstream to downstream in order to assess the potential for the uncontrolled release of water. As seen the the crack is closing on the upstream side while opening on the downstream which denies the likelihood of the release of water from bottom of the dam.

Figure E.2 also demonstrates the same finding for 7 different time steps and at 6 different

locations suggesting that the crack opening displacement is close to zero at the upstream and greater at the downstream and is increasing with time. This observation suggests the deformations as shown in figure E.3. In other words the dam is tilting towards the upstream resulting in the opening of the crack on the downstream side. The angles β and α can be a rough indication of the dam tilt which are also plotted in figure E.4.

The 200 analysis shows that the mean value of the rotation of the dam wall is greater than the mean of the dam bottom rotation while these 2 values are approaching to each other with time. At the end of the analysis the mean value of the α and β are about 0.0035 and 0.0015 radians.

In addition to the crack opening on the downstream side of the dam, the abovementioned figure is also supporting the fact that sliding is occuring at the bottom of the dam as plotted in figure E.5. Since in the finite element model, the joint elements have finite stiffness to prevent closure there are negative displacements reported In figure E.1.

Upstream

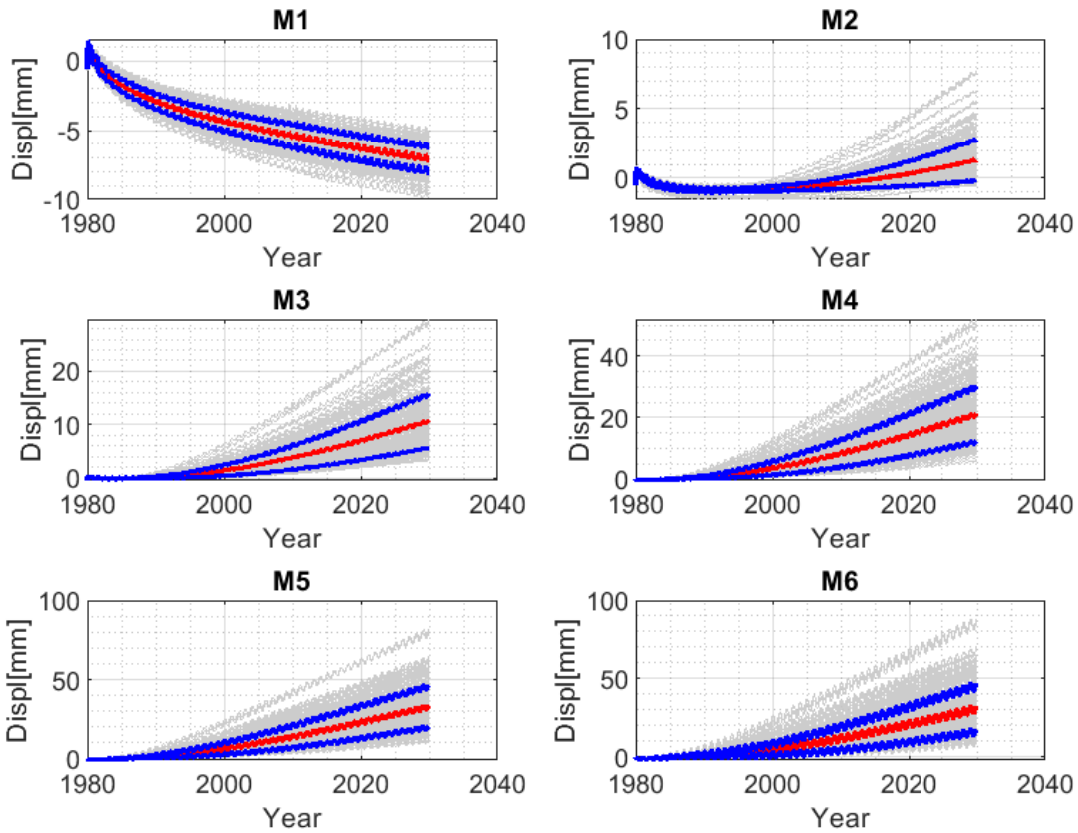

Downstream

Figure E.1: Concrete Rock interface crack opening displacements for 6 nodes from upstream to downstream for all increments

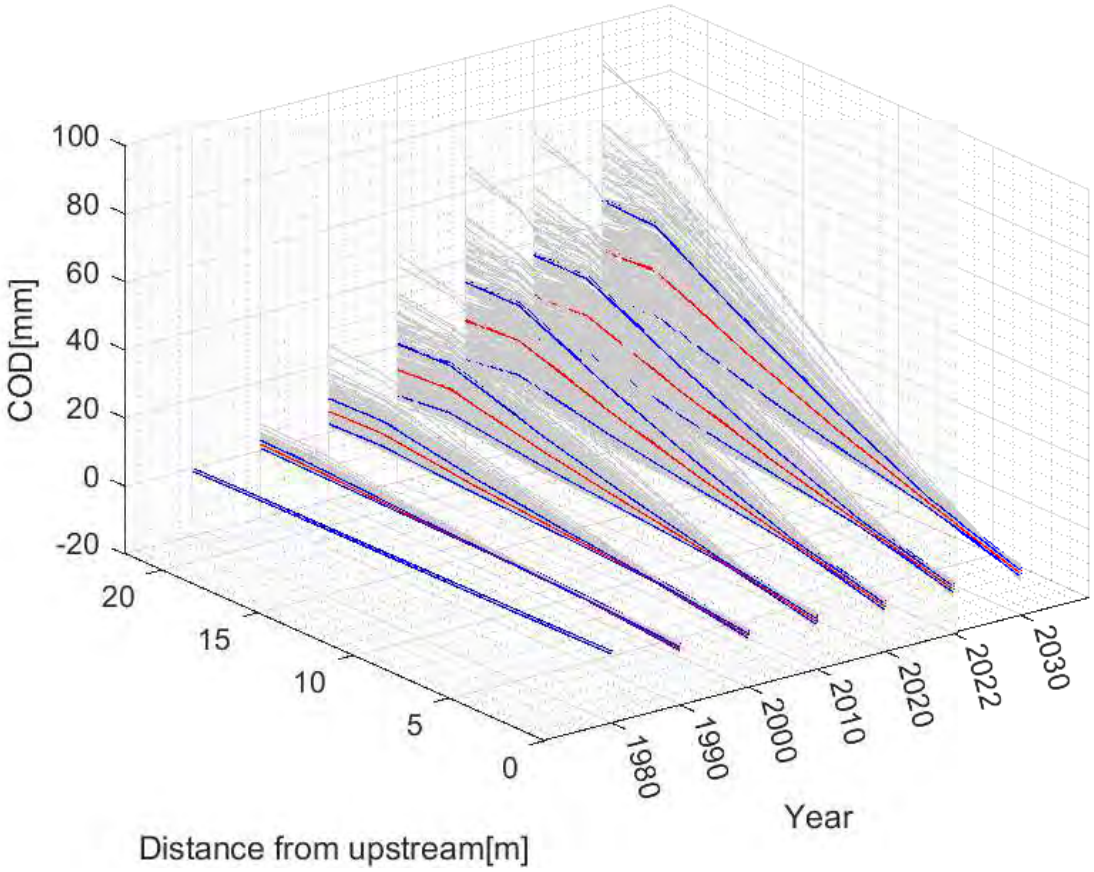

Figure E.2: Concrete Rock interface crack opening displacements for 6 nodes from upstream to downstream for 5 different increments

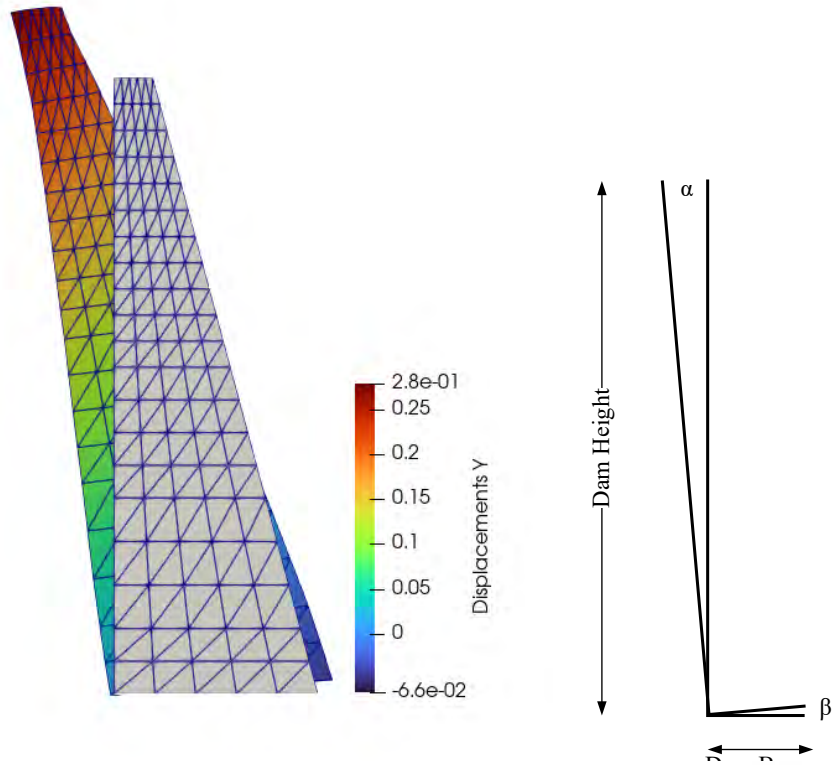

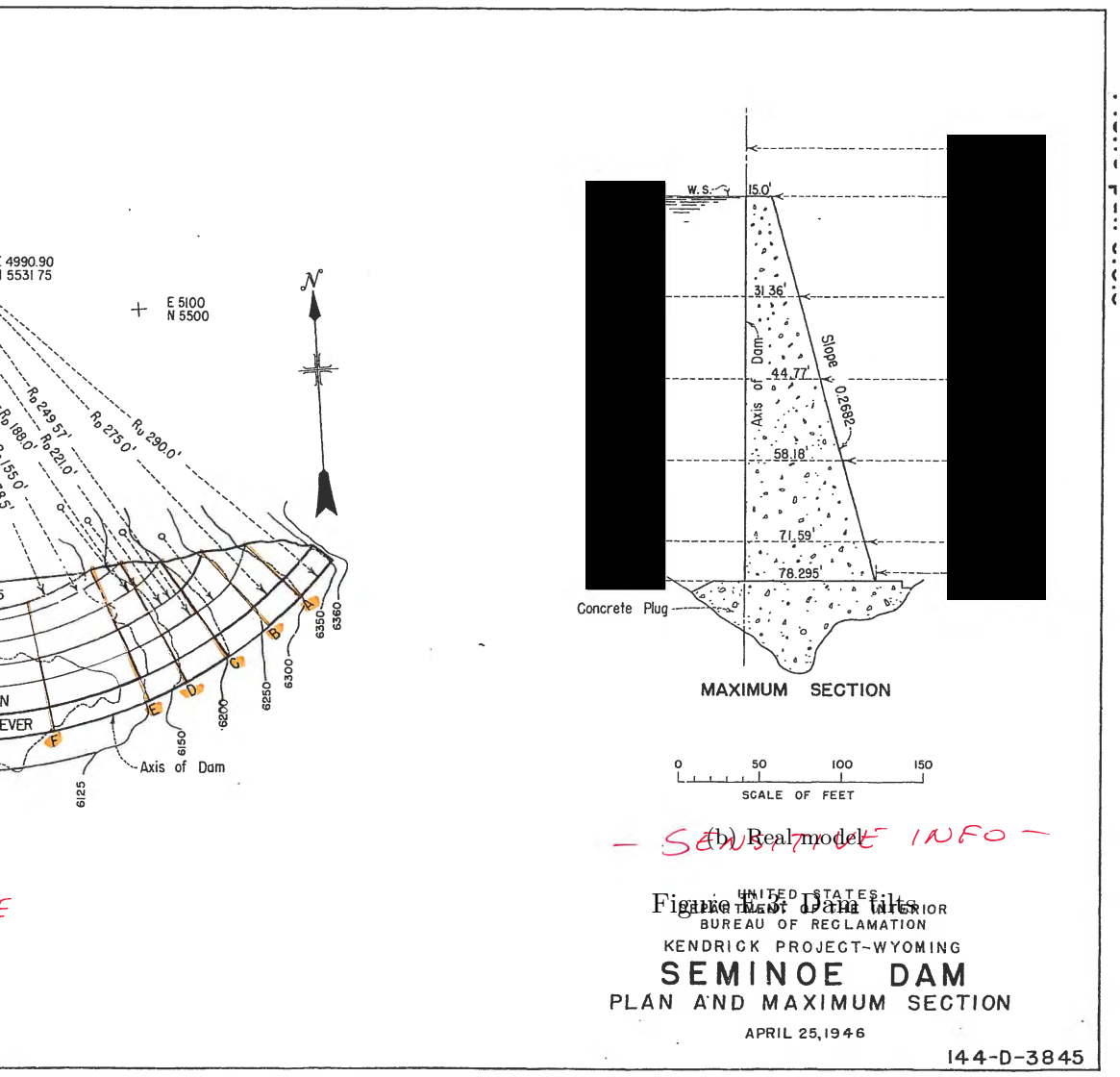

(b) Real model

Figure 1. Dam data inputs

— SENSITIVE INFO —

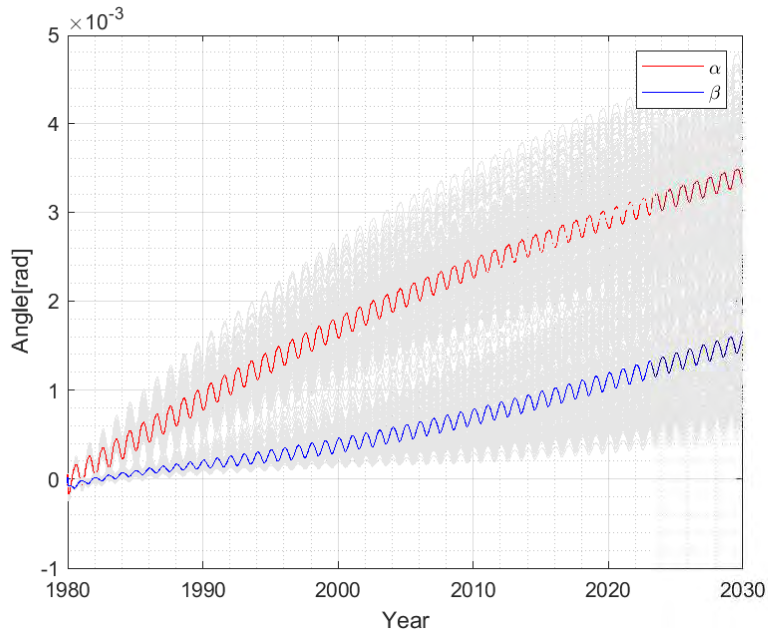

Figure E.4: angles

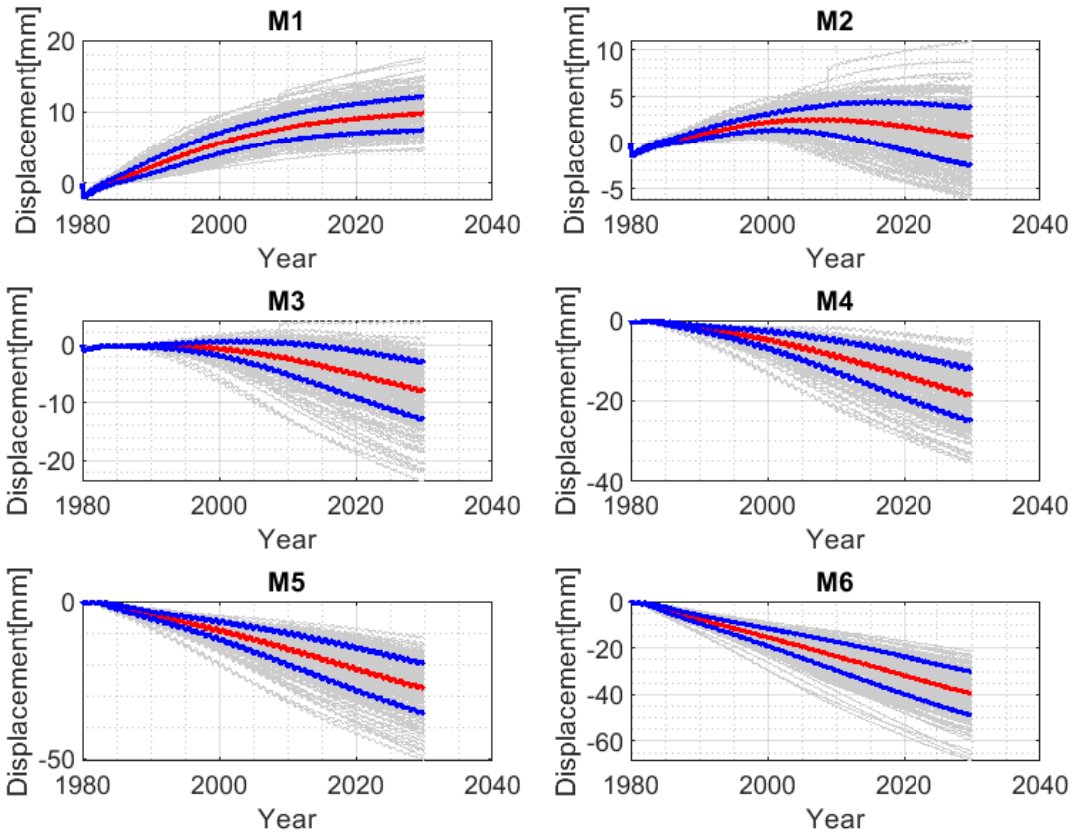

Figure E.5: Sliding; (+ve) Upstream

Appendix F

Fourier Transform

F.1 Basic Equations

Fourrier transforms enables us to transfer a signal from the time domain to the frequency domain through the following equation:

$$X(\omega) = \int_{-\infty}^{\infty} x(t)e^{-2i\pi\omega t}\mathrm{d}t \tag{F.1}$$

$$x(t) \xrightarrow{\text{FFT}} X(\omega) \tag{F.2}$$

while the inverse FFT takes us back from the frequency domain to the time domain through:

$$x(t) = \int_{-\infty}^{\infty} X(\omega)e^{2i\pi\omega t}\mathrm{d}\omega \tag{F.3}$$

$$X(\omega) \xrightarrow{\text{FFT}^{-1}} x(t) \tag{F.4}$$

F.2 Butterworth Filter

Spider has the following filters implemented in its de-convolution feature, figure F.1.

$$|H(j\omega)|^2 = \begin{cases} \text{Low pass} & \frac{1}{1+\left(\frac{\omega}{\omega_L}\right)^{2n}} \\ \text{High pass} & \frac{1}{1+\left(\frac{\omega_U}{\omega}\right)^{2n}} \\ \text{Band pass} & \frac{1}{1+\left(\frac{\omega}{\omega_L}\right)^{2n}}\frac{1}{1+\left(\frac{\omega_U}{\omega}\right)^{2n}} \\ \text{Band stop} & \frac{1}{1+\left(\frac{\omega_L}{\omega}\right)^{2n}}\frac{1}{1+\left(\frac{\omega}{\omega_U}\right)^{2n}} \end{cases} \tag{F.5}$$

where ω, ω_L, ω_U and n are the frequency, the lower and upper filter frequencies, and the order of the filter, respectively.

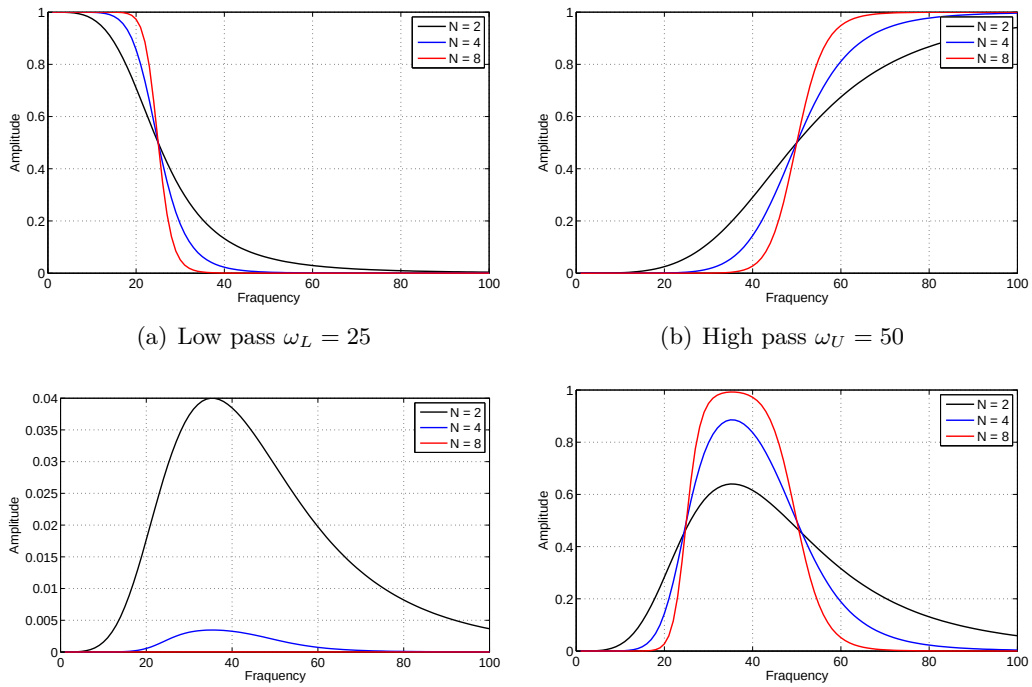

(a) Low pass $\omega_L = 25$

(b) High pass $\omega_U = 50$

(c) Band pass $(\omega_L = 25, \omega_U = 50)$

(d) Band stop $(\omega_L = 25, \omega_U = 50)$

Figure F.1: Comparison of filters

F.3 Transfer Function

In dynamic event, we can define an input record $i(t)$ which is amplified by $h(t)$ resulting in an output signal $o(t)$, figure F.2. Similarly, the operation can be defined in the frequency domain. This output to input relationship is of major importance in many disciplines. The transfer function is the "Laplace" transform of the output divided by the Laplace transform of the input. Hence, in 1D, we can determine the transfer function as follows:

(1) $i(t) \xrightarrow{\text{FFT}} I(\omega)$

(2) $o(t) \xrightarrow{\text{FFT}} O(\omega)$

(3) Transfer Function is $TF_{I-O} = \frac{O(\omega)}{I(\omega)}$

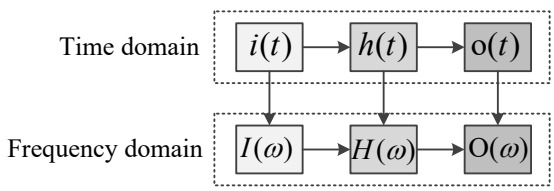

Figure F.2: Transfer function

Appendix G

Wave Equation

Reference will be made to the wave equation in both the derivation of the Lysmer model in soil structure interaction, as well as in the derivaiton of the hydrodynamic force in Westergaard's model.

Considering an infinitesimal element at rest, figure G.2, with elastic modulus E, and mass density ρ, we seek to determine the governing differential equation under dynamic condition.

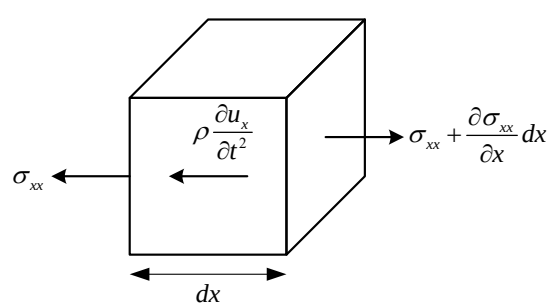

Figure G.1: Infinitesimal element subjected to elastic wave

Thinking in terms of equilibrium of forces, it is more appealing to invoke D'Alembert's principle of **dynamic equilibrium** rather than Newton's second law of motion. This principle is based on the notion of a fictitious **inertia force**, equal to the product of mass times acceleration and acting in a direction opposite to the acceleration. Hence, the element force equilibrium requirements of a typical differential element are, using D'Alembert's principle which states that with inertia forces included, a system is in equilibrium at each time instant.

$$\frac{\partial \sigma_{xx}}{\partial x}\mathrm{d}x - \rho\frac{\partial^2 u_x}{\partial t^2}\mathrm{d}x = 0 \tag{G.1}$$

Since $\sigma_{xx} = \lambda\varepsilon_{xx} = \lambda\frac{\partial u_x}{\partial x}$, substituting, we obtain

$$\frac{\partial^2 u_x}{\partial t^2} - V_p^2\frac{\partial^2 u_x}{\partial x^2} = 0 \tag{G.2}$$

where $V_p = \sqrt{\frac{\lambda}{\rho}}$

The solution of this equation, for harmonic wave propagation in the positive x-direction, is

$$u(t,x) = U\left[\sin(\omega t - \frac{\omega x}{V_p}) + \cos(\omega t - \frac{\omega x}{V_p})\right] \tag{G.3}$$

where ω is the arbitrary frequency of the harmonic motion. The velocity, $\frac{\partial u}{\partial t}$ of a particle at location x is

$$\dot{u}(t,x) = U\omega\left[\cos(\omega t - \frac{\omega x}{V_p}) - \sin(\omega t - \frac{\omega x}{V_p})\right] \tag{G.4}$$

and the strain in the x direction is

$$\varepsilon(x,t) = \frac{\partial u}{\partial x} = -\frac{\dot{u}(x,t)}{V_p} \tag{G.5}$$

The corresponding stress is now

$$\sigma(x,t) = \lambda\varepsilon(x,t) = -V_p\rho\dot{u}(x,t) \tag{G.6}$$

Thus, the compressive stress is equal to the force on a viscous damper with constant damping coefficient equal to ρV_p per unit area of boundary. It can be easily shown that the shear wave radiation boundary condition parallel to a free boundary, is satisfied if damping value is equal to ρV_s.

When modeling the wave motion in a spatial domain, it is essential to introduce artificial boundaries to limit the bounded domain to a reasonable size. The simple Dirichlet boundary condition, in which displacements are fixed, is unsuitable as substantial reflection (through Snell's law) will occur at the boundary and reflected waves will degrade the solution. A solution to this nagging problem could be to enlarge the numerical mesh, thus delaying the side reflections.

Obviously this solution considerably increases the expense of computation and is not viable unless artificial damping can be introduced in the material near the far field, (Hudson, Idriss, and Beikae, 1994). Thus, a numerical model (finite element in our case) should absorb the incoming waves just as they would be absorbed by the free field physically.

G.1 Deconvolution

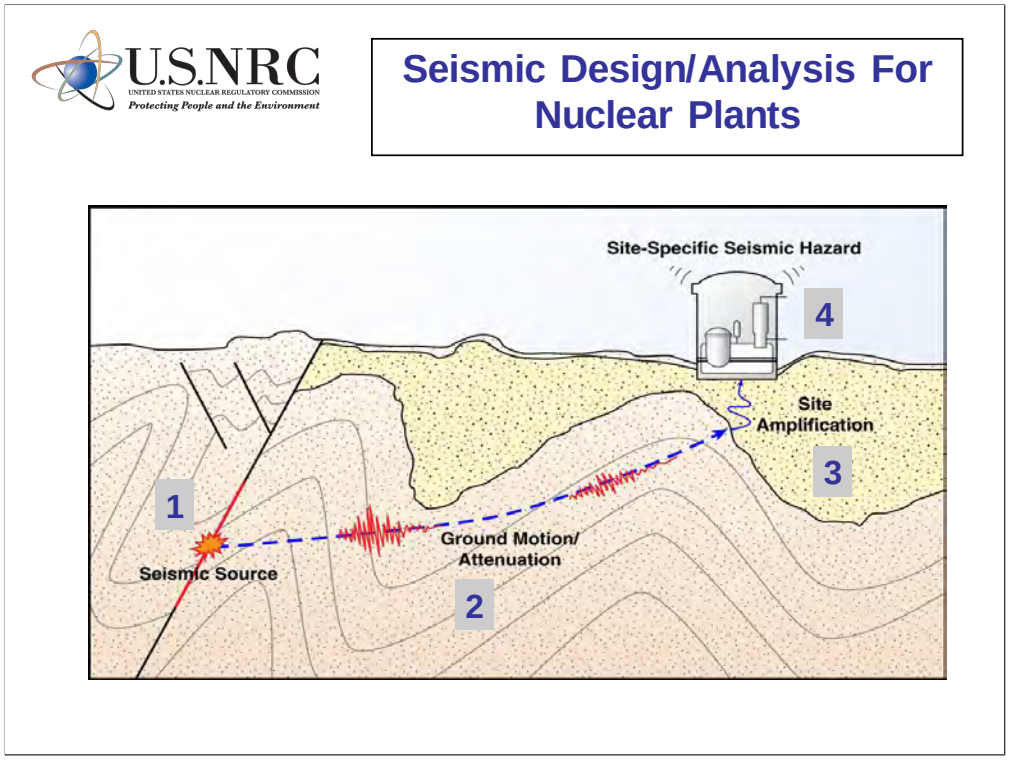

Figure G.2: Seismic Attenuation/Amplification (Ake, Pires, and Munson, 2015)

G.1.1 Introduction

Seismic events originate through tectonic slips and elastic (p- and s-) waves traveling through rock/soil foundation up to the surface. Hence, the seismographs (usually installed at the foot of the dam) record only the manifestation of the event.

On the other hand, modeling the foundation is essential for proper and comprehensive analysis of the dam, and as such the seismic excitation will have to be applied at the base of the foundation.

However, figure G.3, if we were to apply at the base the accelerogram recorded on the surface $I(t)$, the output signal $A(t)$ at the surface will be different than the one originally recorded (unless we have rigid foundation). Hence, the accelerogram recorded on the surface must be de-convoluted into a new one $I'(t)$, such that when the new signal is applied at the base of the foundation, the computed signal at the dam base matches the one recorded by the accelerogram.

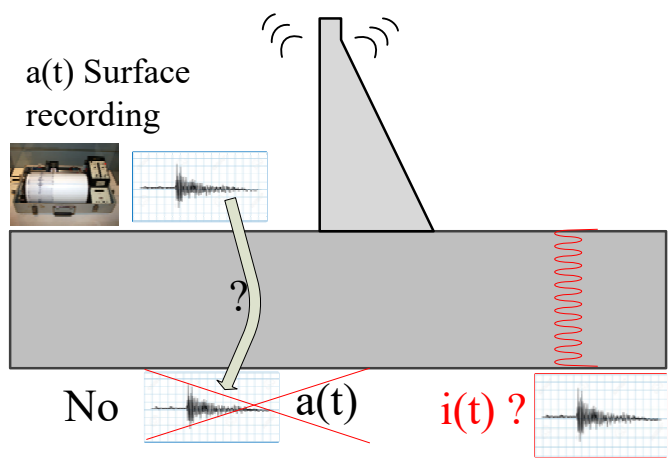

Figure G.3: Deconvolution

G.1.2 Algorithm

G.1.2.1 One-Dimensional

Extending our discussion one step further, we introduce the concept of deconvolution which addresses the dilemma posed above, and will now require one (or more) finite element analyses. With reference to figure G.4.

(1) Record the earthquake induced acceleration on the surface $a'(t)$, and apply it as $i'(t)$ at the base of the foundation.

(2) Perform a transient finite element analysis.

(3) Determine the surface acceleration $a(t)$ (which is obviously different from $i(t)$).

(4) Compute the following FFTs:

$$i'(t) \xrightarrow{\text{FFT}} I'(\omega) = A'(\omega) \tag{G.7}$$

$$a(t) \xrightarrow{\text{FFT}} A(\omega) \tag{G.8}$$

(5) Compute transfer function from the base to surface as

$$TF_{I'-A} = A(\omega)/I'(\omega) \tag{G.9}$$

(6) Compute the inverse transfer function $TF^{-1}_{I'-A}$.

(7) Determine the updated excitation record in the frequency domain

$$I(\omega) = TF^{-1}_{I'-A} \times A'(\omega) = \frac{I'(\omega)}{A(\omega)} A'(\omega) \tag{G.10}$$

(8) Determine the updated excitation in the time domain

$$I(\omega) \xrightarrow{\text{FFT}^{-1}} i(t) \tag{G.11}$$

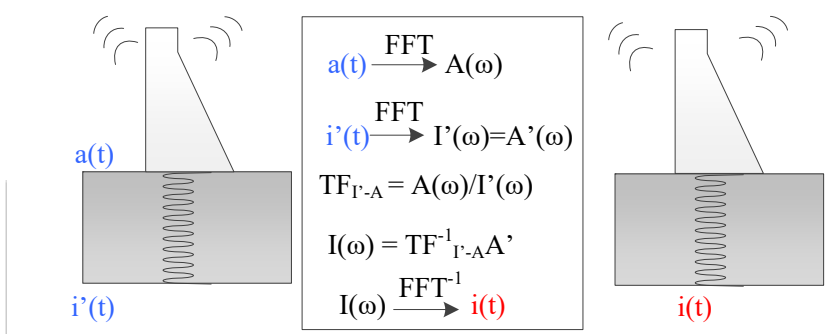

Figure G.4: Deconvolution applied in finite element analysis

G.1.2.2 Three-Dimensional

In 3D applications, the transfer function is a 3×3 matrix, each row corresponds to the response to an excitation in a given direction, and each column corresponds to the response in a given direction. Hence, three separate analysis must be performed $\lfloor\ I'_x \quad I'_y \quad I'_z\ \rfloor$ and for each

excitation, we must determine the three components of the surface acceleration. Then, we will compute the 3D transfer function:

$$[TF] = \underbrace{\begin{bmatrix} TF_{xx} & TF_{xy} & TF_{xz} \\ TF_{yx} & TF_{yy} & TF_{yz} \\ TF_{zx} & TF_{zy} & TF_{zz} \end{bmatrix}}_{TF_{I'-A}} = \begin{bmatrix} \frac{A_{xx}(\omega)}{I'_x(\omega)} & \frac{A_{xy}(\omega)}{I'_x(\omega)} & \frac{A_{xz}(\omega)}{I'_x(\omega)} \\ \frac{A_{yx}(\omega)}{I'_y(\omega)} & \frac{A_{yy}(\omega)}{I'_y(\omega)} & \frac{A_{yz}(\omega)}{I'_y(\omega)} \\ \frac{A_{zx}(\omega)}{I'_z(\omega)} & \frac{A_{zy}(\omega)}{I'_z(\omega)} & \frac{A_{zz}(\omega)}{I'_z(\omega)} \end{bmatrix} \tag{G.12}$$

Hence, the excitation to be applied in the frequency domain is given by:

$$\begin{Bmatrix} I_x(\omega) \\ I_y(\omega) \\ I_z(\omega) \end{Bmatrix} = [TF_{I'-A}]^{-1} \begin{Bmatrix} A'_x(\omega) \\ A'_y(\omega) \\ A'_z(\omega) \end{Bmatrix} \tag{G.13}$$

while in the time domain it is

$$\begin{Bmatrix} I_x(\omega) \\ I_y(\omega) \\ I_z(\omega) \end{Bmatrix} \xrightarrow{\text{FFT}^{-1}} \begin{Bmatrix} i_x(t) \\ i_y(t) \\ i_z(t) \end{Bmatrix} \tag{G.14}$$

G.1.2.3 Simplification

The preceding 3D generalized procedure can be simplified by ignoring the off-diagonal terms

$$[TF] = \begin{bmatrix} TF_{xx} & 0 & 0 \\ 0 & TF_{yy} & 0 \\ 0 & 0 & TF_{zz} \end{bmatrix} = \begin{bmatrix} \frac{A_{xx}(\omega)}{I'_x(\omega)} & 0 & 0 \\ 0 & \frac{A_{yy}(\omega)}{I'_y(\omega)} & 0 \\ 0 & 0 & \frac{A_{zz}(\omega)}{I'_z(\omega)} \end{bmatrix} \tag{G.15}$$

which will greatly simplify the inversion of the transfer function.

$$\begin{Bmatrix} I_x(\omega) \\ I_y(\omega) \\ I_z(\omega) \end{Bmatrix} = [TF_{I'-A}]^{-1} \begin{Bmatrix} A'_x(\omega) \\ A'_y(\omega) \\ A'_z(\omega) \end{Bmatrix} = \begin{bmatrix} \frac{I'_x(\omega)}{A_{xx}(\omega)} & 0 & 0 \\ 0 & \frac{I'_y(\omega)}{A_{yy}(\omega)} & 0 \\ 0 & 0 & \frac{I'_z(\omega)}{A_{zz}(\omega)} \end{bmatrix} \begin{Bmatrix} A'_x(\omega) \\ A'_y(\omega) \\ A'_z(\omega) \end{Bmatrix} \tag{G.16}$$

and finally,

$$\begin{Bmatrix} I_x(\omega) \\ I_y(\omega) \\ I_z(\omega) \end{Bmatrix} = \begin{bmatrix} \frac{I'_x(\omega)}{A_{xx}(\omega)} A'_x(\omega) & 0 & 0 \\ 0 & \frac{I'_y(\omega)}{A_{yy}(\omega)} A'_y(\omega) & 0 \\ 0 & 0 & \frac{I'_z(\omega)}{A_{zz}(\omega)} A'_z(\omega) \end{bmatrix} \xrightarrow{\text{FFT}^{-1}} \begin{Bmatrix} I_x(t) \\ I_y(t) \\ I_z(t) \end{Bmatrix} \tag{G.17}$$